



저작자표시-비영리-변경금지 2.0 대한민국

이용자는 아래의 조건을 따르는 경우에 한하여 자유롭게

- 이 저작물을 복제, 배포, 전송, 전시, 공연 및 방송할 수 있습니다.

다음과 같은 조건을 따라야 합니다:



저작자표시. 귀하는 원저작자를 표시하여야 합니다.



비영리. 귀하는 이 저작물을 영리 목적으로 이용할 수 없습니다.



변경금지. 귀하는 이 저작물을 개작, 변형 또는 가공할 수 없습니다.

- 귀하는, 이 저작물의 재이용이나 배포의 경우, 이 저작물에 적용된 이용허락조건을 명확하게 나타내어야 합니다.
- 저작권자로부터 별도의 허가를 받으면 이러한 조건들은 적용되지 않습니다.

저작권법에 따른 이용자의 권리는 위의 내용에 의하여 영향을 받지 않습니다.

이것은 [이용허락규약\(Legal Code\)](#)을 이해하기 쉽게 요약한 것입니다.

[Disclaimer](#)

Doctoral Thesis

Silver Nanowire Transparent Electrodes for Soft Optoelectronic and Electronic Devices

Seungse Cho

School of Energy and Chemical Engineering
(Energy Engineering)

Ulsan National Institute of Science and Technology

2021

Silver Nanowire Transparent Electrodes for Soft Optoelectronic and Electronic Devices

Seungse Cho

School of Energy and Chemical Engineering
(Energy Engineering)

Ulsan National Institute of Science and Technology


Silver Nanowire Transparent Electrodes for Soft Optoelectronic and Electronic Devices

A thesis/dissertation submitted to
Ulsan National Institute of Science and Technology
in partial fulfillment of the
requirements for the degree of
Doctor of Philosophy

Seungse Cho

01. 11. 2021

Approved by



Advisor

Hyunhyub Ko

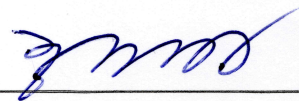
Silver Nanowire Transparent Electrodes for Soft Optoelectronic and Electronic Devices

Seungse Cho

This certifies that the thesis/dissertation of Seungse Cho is approved.

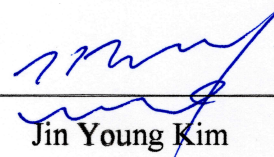
01. 11. 2021

Signature



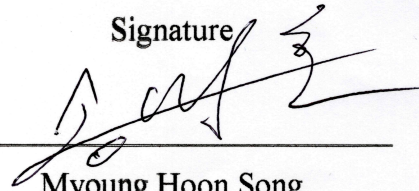
Advisor: Hyunhyub Ko

Signature



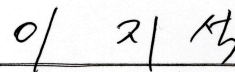
Jin Young Kim

Signature



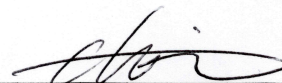
Myoung Hoon Song

Signature



Jiseok Lee

Signature



Moon Kee Choi

Abstract

Recently, with an increasing importance of human-machine interface along with the rapid growth of Internet of Things (IoT), various flexible and stretchable electronic and optoelectronic devices have been developed for the wide range of multifunctional and wearable applications such as touch screen panels, organic solar cells, organic light-emitting diodes, thin-film loudspeakers, microphones, interactive displays, and electronic skins. High mechanical flexibility/stretchability, optical transparency, and electrical conductivity are the critical properties that transparent conductive electrodes (TCEs) should possess for the realization of high-performance flexible/stretchable electronics and optoelectronics. While indium tin oxide (ITO) has been widely used in commercial TCEs, the further development and application of ITO have been limited by the high cost and inherent brittleness of the material. One promising alternative to ITO as a TCE material is silver nanowire (AgNW) networks having good flexibility and stretchability, which can provide lower sheet resistance (R_s) and higher optical transmittance (T) than other TCE candidates such as carbon nanotubes, graphene, and conducting polymers. Moreover, AgNW networks can be readily prepared by low-cost solution-based process, enabling the mass production of next-generation optoelectronic and electronic applications. The integration of AgNW networks with the flexible/stretchable substrates can provide powerful platforms to realize highly stable and high-performance soft optoelectronic and electronic devices with the superior transparency and stable supply of electrical conductivity during mechanical deformations.

This thesis covers our recent studies about flexible/stretchable AgNW TCEs and their applications in various soft optoelectronic and functional electronic devices. First, chapter 1 introduces research trends in flexible/stretchable transparent electrodes and several issues of AgNW networks that should be carefully considered for their future soft optoelectronic and electronic device applications. In chapter 2, we demonstrated a simple and efficient assembly strategy for the large-area, highly cross-aligned AgNW arrays for TCE applications through a modified bar-coating assembly. As opposed to conventional solvent-evaporation-induced assemblies, which are slow and produce nonuniform conductive networks, our modified bar-coating strategy enables fast, efficient, and uniform alignment of AgNWs in a large-area by simply dragging the Meyer rod over the AgNW solution on the target substrates. For the potential applications, we demonstrated large-scale, flexible, and transparent resistive-type touch screens and force-sensitive mechanochromic touch screens using cross-aligned AgNW transparent electrodes which exhibited highly uniform and precise touch sensing performance across the entire region. In chapter 3, we introduced ultrathin, transparent, and conductive hybrid nanomembranes (NMs) with nanoscale thickness, consisting of the orthogonal AgNW arrays embedded

in a polymer matrix. Here, we present a skin-attachable NM loudspeaker and wearable transparent NM microphone, which can emit thermoacoustic sound and can provide excellent acoustic sensing capabilities. In chapter 4, solution-processable, high-performance flexible alternating-current electroluminescent (ACEL) devices are developed based on high- k nanodielectrics and cross-aligned AgNW transparent electrodes. The solution-processed La-doped barium titanate (BTO:La) nanocuboids are fabricated as high dielectric constant nanodielectrics, which can enhance the dielectric constant of an ACEL devices, enabling the fabrication of high-performance flexible ACEL devices with a lower operating voltage as well as higher brightness. In chapter 5, we fabricated transparent, flexible, and self-healable thermoacoustic loudspeakers based on AgNW/poly(urethane-hindered urea) (PUHU) conductive electrodes. Our self-healable AgNW/PUHU electrodes exhibit a great self-healing property for the surface damages by means of the dynamic reconstruction of reversible bulky urea bonds in PUHU. In chapter 6, synesthetic bimodal generation of sound and color is demonstrated by stretchable sound-in-display devices consisting of strain-insensitive stretchable AgNW electrodes and field-induced inorganic EL phosphor emissive layers. The stretchable sound-in-display devices show highly robust and reliable EL and sound generating performances that can be repeatedly stretched and released without severe performance degradation because of the use of strain-insensitive AgNW electrodes. Finally, in chapter 7, we summarize this thesis along with the future perspective of flexible/stretchable transparent electrodes that should be considered for next-generation soft electronic and optoelectronic device applications. In this thesis, studies on flexible/stretchable AgNW transparent electrodes and their device applications could be further expanded for diverse soft and wearable optoelectronic and electronic applications such as wearable sensors, healthcare monitoring devices, and human-machine interfaces with better convenience, appearance, and reusability.

Contents

Abstract	1
Contents	4
List of Figures	6
List of Tables	25
Nomenclature	26
Chapter 1. Introduction	29
1.1 Flexible/stretchable transparent electrodes	29
1.1.1 Nanostructured transparent conducting materials	30
1.2 Transparent AgNW networks	33
1.2.1 Conductive percolation networks	36
1.2.2 Junction resistance	37
1.2.3 Alignment of AgNW networks	38
1.3 Flexible and transparent AgNW electrodes and device applications	40
1.3.1 Touch screen panels	40
1.3.2 Flexible loudspeakers	45
1.3.3 Acoustic sensors	47
1.4 Stretchable and transparent AgNW electrodes and device applications	49
1.4.1 Electroluminescence	53
1.5 Challenges of current flexible/stretchable transparent electrodes	56
Chapter 2. Large-scale AgNW alignment technique for flexible force-sensitive mechanochromic touch screens	59
2.1 Introduction	59
2.2 Experimental Details	61
2.3 Results and Discussion	64
2.4 Conclusions	95
Chapter 3. Orthogonal AgNW-embedded hybrid nanomembranes (NMs) for skin-attachable acoustic device applications	96
3.1 Introduction	96
3.2 Experimental Details	98

3.3 Results and Discussion	99
3.4 Conclusions	128
Chapter 4. High-performance flexible electroluminescent (EL) devices based on high- k nanodielectrics and cross-aligned AgNW electrodes	129
4.1 Introduction	129
4.2 Experimental Details	131
4.3 Results and Discussion	135
4.4 Conclusions	156
Chapter 5. Self-healable and flexible thermoacoustic loudspeakers with AgNW/poly(urethane-hindered urea) PUHU electrodes	157
5.1 Introduction	157
5.2 Experimental Details	160
5.3 Results and Discussion	162
5.4 Conclusions	183
Chapter 6. Highly stretchable sound-in-display electronic devices with strain-insensitive AgNW electrodes.....	184
6.1 Introduction	184
6.2 Experimental Details	186
6.3 Results and Discussion	187
6.4 Conclusions	216
Chapter 7. Summary and Future perspective	217
7.1 Summary	217
7.2 Future perspective	220
References	222
Appendix A: List of Achievements	248
Acknowledgements	251

List of Figures

Figure 1.1. Diverse soft optoelectronic and electronic device applications based on flexible/stretchable transparent electrodes. (C. Larson et al. *Science* **2016**, *351*, 1071, M. S. Lim et al. *Nano Lett.* **2020**, *20*, 1526, X. Zhang et al. *Energy Environ. Sci.* **2018**, *11*, 354, J. Lee et al. *Nanoscale* **2012**, *4*, 6408, L.-Q. Tao et al. *Nat. Commun.* **2017**, *8*:14579, A. G. Nasibulin et al. *ACS Nano* **2011**, *5*, 3214, T. Kim et al. *Adv. Funct. Mater.* **2013**, *23*, 1250, A. Miyamoto et al. *Nat. Nanotechnol.* **2017**, *12*, 907).

Figure 1.2. Various next-generation conducting nanomaterials. (a) Sheet resistance versus optical transmittance for various transparent electrodes (W. Xiong et al. *Adv. Mater.* **2016**, *28*, 7167). (b) Conducting polymer (N. Kim et al. *Adv. Mater.* **2014**, *26*, 2268). (c) Graphene (J. C. Meyer et al. *Nature* **2007**, *446*, 60). (d) Metal mesh (A. Khan et al. *Small* **2016**, *12*, 3021). (e) Carbon nanotube (F. Mirri et al. *ACS Nano* **2012**, *6*, 9737). (f) Electrospun nanotrough (B. W. An et al. *Nano Lett.* **2016**, *16*, 471). (g) Metallic nanowire (Y. Sun et al. *Nat. Electron.* **2019**, *2*, 513).

Figure 1.3. Synthesis of AgNWs based on the polyol process. (a) Schematic illustration of the mechanism proposed to account for the growth of AgNWs with pentagonal cross sections (Y. Sun et al. *Nano Lett.* **2003**, *3*, 955). (b) TEM images of as-synthesized AgNWs (Y. Sun et al. *Nano Lett.* **2002**, *2*, 165).

Figure 1.4. Various coating methods of AgNW networks. (a) Drop casting (X. Guo et al. *RSC Adv.* **2015**, *5*, 24953). (b) Spray coating (D. Y. Choi et al. *Nanoscale* **2013**, *5*, 977). (c) Spin coating (S. Xie et al. *Opt. Express* **2013**, *21*, A355). (d) Vacuum filtration (W. Xiong et al. *Adv. Mater.* **2016**, *28*, 7167). (e) Blade coating (X. Zhang et al. *ACS Appl. Mater. Interfaces* **2016**, *8*, 34630). (f) Bar coating (S. Ye et al. *Adv. Mater.* **2014**, *26*, 6670).

Figure 1.5. Conductive percolation network of randomly oriented AgNWs. (a) Sample networks of AgNWs for $140 \mu\text{m} \times 140 \mu\text{m}$ domain with concentration just above critical percolation concentration ($C \sim C_p$) (left) and concentration much above critical percolation concentration ($C \gg C_p$) (right) (M. Jagota & N. Tansu *Sci. Rep.* **2015**, *5*:10219). (b) Transmittance (550 nm) plotted as a function of sheet resistance for thin films prepared from different conducting nanomaterials (S. De et al. *ACS Nano* **2010**, *4*, 7064).

Figure 1.6. Nanowire junction resistance. (a) Schematic showing a percolated network of monodisperse rods in which the resistance at nanowire-nanowire junctions dominates (R. M. Mutiso et al. *ACS Nano* **2013**, *7*, 7654). (b) Illustration of the measurement setup for resistance of single nanowire and junction resistance (F. Selzer et al. *Appl. Phys. Lett.* **2016**, *108*, 163302).

Figure 1.7. Various AgNW assembly techniques. (a) Langmuir-Blodgett assembly (A. Tao et al. *Nano Lett.* **2003**, *3*, 1229). (b) Capillary printing (S. Kang et al. *Nano Lett.* **2015**, *15*, 7933). (c) Water-bath assisted convective assembly (S.-k. Duan et al. *Phys. Chem. Chem. Phys.* **2015**, *17*, 8106). (d) H-dip coating (B. Park et al. *Sci. Rep.* **2015**, *6*, 19485). (e) Spray-assisted assembly (H. Hu et al. *Nanoscale* **2017**, *9*, 1307) (f) Conical fibers array brushing (L. Meng et al. *Adv. Mater.* **2018**, *30*, 1706938) (g) Agitation-assisted alignment (H. Hu et al. *Adv. Funct. Mater.* **2019**, *29*, 1902922).

Figure 1.8. Resistive-type touch screen panel applications using the AgNW networks. (a) Demonstration of applying a very long AgNW transparent conductor for a touch screen panel (J. Lee et al. *Nanoscale* **2012**, *4*, 6408). (b) Demonstration for exact writing input using the uniform AgNW TCE-based flexible touch screen panel (Y. Jia et al. *ACS Appl. Mater. Interfaces* **2016**, *8*, 9865). (c) Demonstration of touch screen panel using the Ag/NW-GFRHybrimer films (J. Jang et al. *ACS Appl. Mater. Interfaces* **2016**, *8*, 27035). (d) Demonstration of healable touch screen panel using AgNW healable conductor on the LCD monitor (J.-S. Bae et al. *Adv. Mater. Technol.* **2018**, *3*, 1700364).

Figure 1.9. Capacitive-type touch screen panel applications using the AgNW networks. (a) Spray coated flexible AgNW electrode-based capacitive touch screen panel (C. Mayousse et al. *Nanotechnology* **2013**, *24*, 215501). (b) Capacitive touch screen panel with diamond patterns fabricated by selective laser ablation of AgNW percolation networks (S. Hong et al. *J. Nanosci. Nanotechnol.* **2015**, *15*, 2317). (c) Screen printed AgNW TCE-based capacitive touch screen panel (S. Yao & Y. Zhu *Nanoscale* **2014**, *6*, 2345). (d) Capacitive AgNW PDMS touch screen panel (H. Lee et al. *Adv. Funct. Mater.* **2014**, *24*, 3276). (e) Healable transparent capacitive touch screen panel based on healable AgNW-polymer composite electrodes (J. Li et al. *ACS Nano* **2014**, *8*, 12874). (f) Transparent and stretch-unresponsive capacitive touch screen panel with selectively patterned AgNW/rGO electrodes (T. Y. Choi et al. *ACS Appl. Mater. Interfaces* **2017**, *9*, 18022).

Figure 1.10. Various flexible loudspeakers using the AgNW networks. (a) The acoustic device consists of transparent graphene/AgNW TCEs and PVDF piezoelectric layer (S. Xu et al. *CrystEngComm* **2014**, *16*, 3532). (b) Flexible and transparent sound-emitting devices using AgNW electrodes (H. Tian et al. *Appl. Phys. Lett.* **2011**, *99*, 253507). (c) The thermoacoustic loudspeaker made of AgNW random networks on a polyimide substrate (P. L. Torraca et al. *J. Appl. Phys.* **2017**, *121*, 214502).

Figure 1.11. Acoustic sensors using the AgNW networks. (a) Self-powered microphone assembled with Mxene/AgNW hybrid electrodes (W. Chen et al. *ACS Nano* **2020**, DOI: 10.1021/acsnano.0c01635). (b) Flexible acoustic sensor using AgNW/PDMS film with mass block-beam structure (Q. Zhang et al. *Soft Robot.* **2020**, DOI: 10.1089/soro.2020.0030).

Figure 1.12. Two representative strategies can be applied to realize soft electronics. The materials innovation, by developing novel materials that are intrinsically stretchable; structural design, by making nonstretchable materials into specific structures that absorbs externally applied strain without fracturing (C. Wang et al. *Adv. Mater.* **2018**, *30*, 1801368). Hydrogel (H. Yuk et al. *Nat. Mater.* **2016**, *15*, 190). Liquid metal (C. Ladd et al. *Adv. Mater.* **2013**, *25*, 5081). Polymer (M. Kaltenbrunner et al. *Nat. Commun.* **2012**, *3*, 770). Nanomaterial (Y. Kim et al. *Nature* **2013**, *500*, 59.). Interlock (C. Pang et al. *Nat. Mater.* **2012**, *11*, 795). Crack (Z. Liu et al. *ACS Appl. Mater. Interfaces* **2014**, *6*, 13487). Kirigami (S. J. P. Callens and A. A. Zadpoor *Mater. Today* **2018**, *21*, 241). Origami (S. J. P. Callens and A. A. Zadpoor *Mater. Today* **2018**, *21*, 241). Textile (J. Chen et al. *Nat. Energy* **2016**, *1*, 16138). Serpentine (J. A. Fan et al. *Nat. Commun.* **2014**, *5*, 3266). Wave/wrinkle (D.-H. Kim et al. *Science* **2008**, *320*, 507).

Figure 1.13. Transparent and stretchable electrodes using AgNW-based conducting networks. (a) Stretchable and transparent electrodes based on AgNW-crosslinked-polyacrylate composites (W. Hu et al. *Nanotechnology* **2012**, *23*, 344002). (b) Stretchable and transparent electrodes using graphene-AgNW hybrid structures (M.-S. Lee et al. *Nano Lett.* **2013**, *13*, 2814). (c) Stretchable and transparent AgNW/PDMS electrode (S. Hong et al. *Adv. Mater.* **2015**, *27*, 4744). (d) Stretchable, transparent, and adhesive AgNW electrodes (J.-H. Kim et al. *Nano Lett.* **2018**, *18*, 4531).

Figure 1.14. Stretchable ACEL devices based on AgNW electrodes. (a) Stretchable and self-deformable ACEL devices (J. Wang et al. *Adv. Mater.* **2015**, *27*, 2876). (b) Stretchable and waterproof EL devices (B. You et al. *ACS Appl. Mater. Interfaces* **2017**, *9*, 5486). (c) Bright stretchable ACEL devices based on high permittivity composites (F. Stauffer and K. Tybrandt *Adv. Mater.* **2016**, *28*, 7200). (d) Bright stretchable EL devices based on AgNW electrodes and high-*k* thermoplastic elastomers (Y. Zhou et al. *ACS Appl. Mater. Interfaces* **2018**, *10*, 44760).

Figure 2.1 (a) Photographs of various kinds of Meyer rods (#2, #3, #6, #10, and #15) and (b) corresponding optical microscope images. The scale bar is 200 μm . (c) Schematic illustration of the specifications of various Meyer rods. The rod number determines the diameter of wrapped wires and the open area.

Figure 2.2 Large-scale bar-coating alignment of unidirectional and cross-aligned AgNW arrays. (a) A photograph of the solution-processed bar-coating alignment of the AgNWs on a $20 \times 20 \text{ cm}^2$ PET substrate and (b) a schematic showing the alignment process of AgNWs during the bar-coating assembly of the AgNW solution. The combined interaction between shear stress alignment and the electrostatic pinning produced highly aligned and uniform AgNW arrays during the dragging of a confined meniscus between the rod and substrate. (c) Dark-field optical microscope images of the unidirectionally aligned and (d) cross-aligned AgNW arrays. Insets are the fast Fourier transform (FFT) analyses of the optical

micrographs indicating the direction and uniformity of the aligned AgNW structures. The scale bars are 40 μm . (e) Distribution of the alignment degrees of 150 NWs in Fig. 1c with a full width at half maximum (FWHM) value of 21.4. (f) Mapping image showing the highly uniform distribution of FWHM values of each pixel in a 4×4 array over a large-area ($20 \times 20 \text{ cm}^2$) of aligned AgNWs. The FWHM values were calculated by fitting the radial summation of the pixel intensities of the FFT analysis.

Figure 2.3 Schematic of an overall procedure for the solution-processed bar-coating assembly to fabricate unidirectionally and cross-aligned AgNW arrays. Before the bar-coating assembly, poly-L-lysine (PLL) solution is coated on O_2 plasma-treated target substrate to form amine groups on the surface. Consecutively, the meniscus dragging produces highly aligned AgNW arrays. The cross-aligned AgNW array is formed by repeating the bar-coating assembly in a perpendicular direction to that of the pre-aligned AgNW arrays.

Figure 2.4 Dark-field optical micrographs of the unidirectionally aligned AgNWs coated with AgNW ink dispersed in different kinds of solvents; (a) isopropyl alcohol (IPA), (b) water, and (c) ethanol. During the bar-coating assembly, #2 bar, 3 μl of volume, and 10 mm s^{-1} of coating speed were used in all experiments. The scale bar is 40 μm .

Figure 2.5 Dark-field optical micrographs of the aligned AgNW networks coated on substrates modified with different types of functional groups; (a) PLL ($-\text{NH}_2$), (b) hexamethyldisilazane (HMDS) ($-\text{CH}_3$), and (c) O_2 plasma ($-\text{OH}$). During the bar-coating assembly, #2 bar, 3 μl of volume, and 10 mm s^{-1} of coating speed were used in all experiments. The scale bar is 40 μm .

Figure 2.6 X-ray photoelectron spectroscopy (XPS) survey to investigate the interactions between AgNWs and the substrate surface pretreated with different functional groups with PLL, HMDS, and O_2 plasma. (a) High resolution N 1s spectra of the pristine AgNW, PLL, PLL/AgNW, HMDS/AgNW, and O_2 plasma/AgNW. (b) High resolution C 1s spectra of the pristine AgNW, HMDS/AgNW, and O_2 plasma/AgNW. (c) High resolution Ag 3d spectra of the pristine AgNW, PLL/AgNW, HMDS/AgNW, and O_2 plasma/AgNW.

Figure 2.7 The radial summations of the pixel intensities of the fast Fourier transform (FFT) analysis data as a function of radial angle (0 - 180°) of the unidirectional AgNW array, cross-aligned AgNW arrays, and random AgNW network. Contrary to aligned and cross-aligned AgNWs networks which show clear Gaussian peaks, random AgNW network shows uncertain spectra of radial summations due to the lack of directionality.

Figure 2.8 Dark-field optical micrograph of the random AgNW networks fabricated by conventional bar-coating process. Inset shows the corresponding FFT analysis data. The scale bar is 40 μm .

Figure 2.9 Large-area ($20 \times 20 \text{ cm}^2$) alignment of the AgNWs by bar-coating assembly. 16 dark-field optical micrographs of the aligned large-area AgNW arrays in a large-area PET film and the corresponding FFT analysis images in the insets. For the bar-coating assembly, #2 bar, 100 μl of volume, and 10 mm s^{-1} of coating speed were used in the experiment. The FWHM values of 16 AgNW arrays confirm the high uniformity and the scalability of the bar-coating assembly process as shown in Figure 1f. The scale bar is 40 μm .

Figure 2.10 Unidirectional bar-coating alignment of the AgNW arrays and the anisotropic optical properties. (a-c) FWHM values according to the variation in the bar-coating parameters, including the amount of solution (2-40 μl), coating speed (10-70 mm s^{-1}), and substrate temperature (23-60 $^{\circ}\text{C}$). (d-f) Anisotropic optical properties of the unidirectional AgNW arrays. (d) Schematic showing the polarized absorption test as a function of the angle θ between the direction of the polarized incident light and the NW alignment. (e) Polarized UV-vis absorption spectra of unidirectionally aligned AgNW arrays as a function of polarization angle (0-90 $^{\circ}$). (f) Optical dichroic property of unidirectionally aligned AgNW array. Polarized optical microscope images of “UNIST” patterns with different AgNW alignment directions exhibits invisible AgNW arrays when the light was polarized parallel to the direction of AgNW alignment ($\theta = 0^{\circ}$) and clearly visible AgNW array when the light was polarized perpendicular to the direction of AgNW alignment ($\theta = 90^{\circ}$). The scale bar is 100 μm .

Figure 2.11 Dark-field optical micrographs of the aligned AgNW networks fabricated by the bar-coating assembly with different coating conditions; (a) volume of solution (2-40 μl), (b) coating speed (10-70 mm s^{-1}), and (c) substrate temperature (23-60 $^{\circ}\text{C}$). All insets show the corresponding FFT analysis images. The scale bar is 40 μm .

Figure 2.12 The effect of the amount of AgNW dispersion on the formation of contact area between the meniscus and the substrate. Schematics and close-up photographs show the meniscus between the rod and substrate with a different volume of dispersion (2-40 μl). As the volume of dispersion increases, the contact area becomes broader. The scale bars are 500 μm (top) and 1000 μm (bottom).

Figure 2.13 In the meniscus dragging process, the shear force gradient is generated as a function of the height of the meniscus in a Couette flow. Therefore, the AgNWs located far from the dragging bar have a high probability of misalignment due to a reduced shear force. In thick meniscus film, many of AgNWs are located far from the dragging bar and thus have a high probability of misalignment. In thin

meniscus film, most of AgNWs are near the dragging bar, which results in the high probability of alignment.

Figure 2.14 The effect of spacer thickness for the alignment of AgNWs. (a) Schematics showing the different height of the meniscus between the rod and the substrate depending on the thickness of spacer. As the thickness of spacer increases, the height of meniscus increases. (b) Dark-field optical micrographs showing the alignment of AgNWs depending on the variation of spacer thickness (20-120 μm). During the bar-coating assembly, #2 bar and 10 mm s^{-1} of coating speed were used in all experiments. The scale bar is 40 μm .

Figure 2.15 Polarized UV-Vis absorption spectra of the random AgNW networks as a function of polarization angle (θ) from 0 to 90°. As compared to aligned AgNW arrays, random AgNW networks without any anisotropic optical properties do not show any noticeable change in their absorption peaks as the polarization angle increases.

Figure 2.16 Schematics showing the polarized optical microscope modes according to the direction between the polarizing filter and the AgNW alignment direction; (a) $\theta = 0^\circ$, (b) $\theta = 90^\circ$. When the polarizing filter and the aligned AgNW array have the same vertical polarization direction ($\theta = 0^\circ$), vertically polarized light passes through the aligned AgNW film. However, when the polarizing filter and aligned AgNW array have the perpendicular polarization direction ($\theta = 90^\circ$), polarized light cannot penetrate the aligned AgNW film.

Figure 2.17 Dark-field optical micrographs of cross-aligned AgNW arrays by varying the number of cross-coatings for bar-coating conditions of (a) #2 bar and 3 μl , (b) #3 bar and 4 μl , and (c) #6 bar and 8 μl . All of the cross-aligned AgNW arrays were fabricated at the coating speed of 10 mm s^{-1} . The scale bar is 40 μm .

Figure 2.18 Optical and electrical performance of the large-area transparent conductive electrodes (TCEs) using the cross-aligned AgNW networks. (a) UV-vis spectra and corresponding sheet resistance, R_s , of cross-aligned AgNW arrays with different numbers of cross-coatings. The substrate was used as a reference in all UV-vis experiments. (b) R_s versus optical transmittance, T , at 550 nm for the cross-aligned and random AgNW networks fitted by percolative regime. (c) R_s versus T performance of various AgNW TCEs. (d) A photograph of large-scale ($20 \times 20 \text{ cm}^2$) TCE coated with uninform cross-aligned AgNW arrays (top), and schematic showing its 4×4 pixels for analysis (bottom). (e) 4×4 pixels mapping images showing the R_s distribution of cross-aligned and (f) random AgNW networks over a large substrate area ($20 \times 20 \text{ cm}^2$). The average R_s was set so as to be similar in both films. (g) 4×4 pixels mapping images showing the T distribution of cross-aligned and (h) random AgNW networks over a large substrate area ($20 \times 20 \text{ cm}^2$).

Figure 2.19. Mechanical stability of cross-aligned AgNW based TCEs on PET substrate. (a) Variation in resistance of cross-aligned AgNW TCEs as a function of bending radius. (b) Resistance change of cross-aligned AgNW TCEs during 1000 bending cycles at the bending radius of 1.5 mm.

Figure 2.20 Large-scale, flexible, and transparent touch screens using cross-aligned AgNW TCEs. (a) Schematic showing the structure of the large-scale, flexible, and transparent touch screen using the cross-aligned AgNW arrays on a PET substrate connected to a laptop computer through a controller board. (b) A photograph of the large-scale, flexible, and transparent touch screen ($20 \times 20 \text{ cm}^2$) using cross-aligned AgNW TCEs. (c) Demonstration of writing alphabet letters on the transparent touch screen, which have been recorded on the computer monitor. (d) Demonstration of tracing a picture of a butterfly placed under the transparent touch screen.

Figure 2.21 (a-f) Output images of touch signal and (g) normalized gap distance between adjacent touch signals, generated by two touch points pressed with different gap distance of (a) $0 \mu\text{m}$, (b) $50 \mu\text{m}$, (c) $100 \mu\text{m}$, (d) $200 \mu\text{m}$, (e) $500 \mu\text{m}$, and (f) $1000 \mu\text{m}$ on touch screen based on cross-aligned AgNW TCEs. Our touch screen can detect touch location with the resolution of $100 \mu\text{m}$, which corresponds to the resolution of touch controller board. L_0 is defined as minimum gap distance between two touch signals that can be distinguished by touch screen.

Figure 2.22 Demonstration of large scale, flexible touch screen fabricated by cross-aligned AgNW based TCEs. Handwritten letters “FNL” was precisely written on top of curved surface.

Figure 2.23 Flexible, transparent, and force-sensitive touch screens. (a) Schematic illustration of the device structure of a force-sensitive touch screen showing simultaneous force and touch sensing in response to dynamic writings. (b) Schematic illustration of the mechanochromic touch screen system with the color analysis using a spectroradiometer. (c) Normalized luminance at 448 nm wavelength as a function of the writing force. A fitted line shows a linear relationship between the normalized luminance and the writing force. (d) Photographs of mechanochromic color changes on the touch screen as a function of different dynamic writing force. The blue color intensity of the written letters “FNL” on the touch screen increases with the writing force. The scale bar is 1 cm. (e) Normalized luminance spectra of blue color letters “FNL” in visible range (380-520 nm). Based on the linear curve in Figure 5c, the applied forces can be determined to be from $F_1 = 4.3 \pm 0.2 \text{ N}$ to $F_5 = 14.9 \pm 3.4 \text{ N}$. (f) Representation of the color coordinates on the CIE 1931 color space according to the different writing force. The X-Y coordinates move to the deep blue region with the increase of applied force. (g) A photograph of the written letter “A” on the mechanochromic touch screen (left) and its 10×10 pixels array of applied force mapping data showing the local force distribution (right). The scale bar is 1 cm.

Figure 2.24 The investigation of the relationship between the color intensity and the applied writing force using a spectroradiometer. (a) The photographs of the different lines on the mechanochromic touch screen as a function of writing force and (b) its normalized luminance spectra in visible range (380-520 nm). The horizontal lines are drawn by a stylus as a function of dynamic writing force.

Figure 2.25 The resolution of line width drawn by using different tip size of stylus on mechanochromic SP-PDMS film. (a,b) The stylus with small size of tip can generate very thin blue line with the thickness of $\sim 79 \mu\text{m}$. (c,d) Stylus with large size of tip generates blue line with the thickness of $\sim 147 \mu\text{m}$.

Figure 2.26 Real time monitoring images of mechanochromic colors on the touch screen (a) and its touch signals on the laptop monitor (b). The red dotted squares show the alphabet “A” written by the smallest force during the writing on the mechanochromic touch screen. The scale bar is 2 cm.

Figure 3.1 Fabrication of free-standing hybrid NMs with orthogonal AgNW array. (a) Schematic of fabrication procedure for free-standing hybrid NMs with orthogonal AgNW array embedded in polymer matrix. (b) Free-standing AgNW composite NMs floating on a surface of water. The scale bar indicates 1 cm. (c) Dark-field optical microscope image of orthogonal AgNW arrays. The inset shows a fast Fourier transform (FFT) image of the optical micrograph, corresponding to its surface geometric structure. The scale bar indicates $40 \mu\text{m}$. (d) Cross-sectional SEM image of hybrid NM as-fabricated on a ZnO/Si substrate. The scale bar indicates 100 nm. (e) Optical transmittance of polymer NMs, hybrid NM, bare PET, and bare glass in visible range of 400-800 nm. The glass is used as a reference. (f) Photograph of hybrid NM on surface of water under compressive force applied by a glass rod. The scale bar indicates 3 mm. (g) Free-standing hybrid NM supported by a wire loop. Inset shows the high transparency of the hybrid NM. The scale bar indicates 1 cm. (h) Hybrid NMs transferred onto curvilinear surface and (i) onto human skin.

Figure 3.2 Fabrication of free-standing hybrid NM with orthogonal AgNW array by removing the sacrificial layer.

Figure 3.3 Total thickness of hybrid NMs measured by atomic force microscopy.

Figure 3.4 Transmittance in visible range of 400–800 nm and corresponding sheet resistance, R_s , of the orthogonal AgNW array with different numbers of orthogonal coatings.

Figure 3.5 The structural design of the hybrid NM for the calculation of the bending stiffness with geometrical parameters illustrated.

Figure 3.6 SEM images of the hybrid NM folded in half.

Figure 3.7 Conformal contact of AgNW composite hybrid NMs on 3D microstructures. (a) Schematic of conformal contact of NMs on the skin surface. (b) Hybrid NMs attached to a thumb. The inset shows a micrograph of a hybrid NM on the skin of a fingertip. The scale bar indicates 1 mm. (c) and (d) SEM images of the hybrid NMs transferred on line-patterned 3D PDMS microstructures with a line width of (c) 20 and (d) 120 μm . The scale bars indicate 10 and 20 μm , respectively. The insets show a magnification images with the scale bars indicating (c) 10 and (D) 50 μm . SEM images of the hybrid NMs with different thickness of (e) 40, (f) 100, and (g) 200 nm transferred on micropyramid-patterned 3D PDMS microstructures with diameter of 10 μm and height of 7 μm . All scale bars indicate 5 μm .

Figure 3.8 High magnitude SEM images of the hybrid NM transferred on the line-patterned PDMS with a line width of 20 μm .

Figure 3.9 Estimated step surface coverage of the hybrid NMs with different thickness placed on a micropyramid-patterned PDMS substrate.

Figure 3.10 Mechanical properties of hybrid NMs with orthogonal AgNW array. (a) Free-standing hybrid NMs with different densities of orthogonal AgNW arrays floating on the water surface. NMs are wrinkled by a water droplet of radius $a \approx 0.3$ mm. The number of wrinkles decreases as the density of AgNWs increases. All scale bars indicate 200 μm . (b) Young's modulus (E) of NMs as calculated from the wrinkle tests. (c) Comparison of calculated and experimental bending stiffness of hybrid NMs with different density of orthogonal AgNW arrays. Measured bending stiffness was calculated by using Young's modulus experimentally obtained from capillary wrinkling method. (d) Applied indentation load versus displacement of free-standing hybrid NMs as a function of density of orthogonal AgNW array. (e) Maximum indentation load versus displacement of hybrid NMs as a function of orthogonal AgNW arrays.

Figure 3.11 Number of wrinkles generated from a pure parylene NM and hybrid NMs.

Figure 3.12 Variation in the number of wrinkles N as a function of $N \sim a^{1/2}h^{-3/4}$.

Figure 3.13 Indentation test for measuring the mechanical properties of NMs.

Figure 3.14 Loading-unloading indentation test.

Figure 3.15 Skin-attachable NM loudspeaker. (a) Schematic of skin-attachable NM loudspeaker with orthogonal AgNW array. Sound is generated by temperature oscillation produced by applying an AC voltage. (b) Acoustic measurement system where sound emitted from NM loudspeaker is collected by a commercial microphone with a dynamic signal analyzer. (c) Variation in sound pressure (SP) generated from NM loudspeaker and thick film loudspeaker as a function of the input power at 10 kHz. (d) Experimental and theoretical values of sound pressure level (SPL) versus sound frequency

for NM and thick PET film loudspeakers. (e) Skin-attachable NM loudspeaker mounted on the back of a hand. The scale bar indicates 1 cm.

Figure 3.16 Infrared (IR) images of the orthogonal AgNW array with AC 10 V applied at a frequency of 10 kHz.

Figure 3.17 SPL versus distance between the commercial microphone and thermoacoustic loudspeaker using an orthogonal AgNW array on a PET substrate.

Figure 3.18 Theoretical values of SPL as a function of sound frequency for (a) 100 nm-thick and (b) 220 μ m-thick loudspeakers with different substrates.

Figure 3.19 Wearable and transparent NM microphone. (a) Schematic of wearable NM microphone device. (b) Transparent NM microphone placed over “UNIST” logo, illustrating its transparent and unobtrusive appearance. The scale bar indicates 1 cm. (c) Sensing measurement system for NM microphone. Variation in the output voltages as a function of (d) sound frequency and (e) SPL for NM microphone and thin-film microphone. (f) Waveform and short-time Fourier transform (STFT) signals of original sound (“There’s plenty of room at the bottom”, left) extracted by the sound wave analyzer, the signal read from the NM-based microphone (middle), and thin-film microphone (right)

Figure 3.20 Comparison of adhesion force of various micro-patterned PDMS films.

Figure 3.21 Schematic of (a) NM and (b) thin-film microphone devices. In the NM microphone, NMs are mounted to the “holey” PDMS film as a free-standing geometry. In the thin-film microphone, a hybrid NM mounted to a planar PDMS film without a hole is fully laminated with the surface of PDMS film, where NMs cannot be free-standing.

Figure 3.22 Waveform and short-time Fourier transform (STFT) signals of original sound (“There’s plenty of room at the bottom”) extracted by the sound wave analyzer, where the signal was read from a commercial microphone.

Figure 3.23 Personal voice-based security system. (a) Schematic of voice security system (left) and photograph of authorization process using free-standing NM microphone (right). (b) Sound waveforms and (c) voiceprints collected from registrant, authorized user, and denied user using NM microphone. (d) Matching probability of voiceprint for authorized user using NM microphone and commercial microphone. (e) Matching probability of voiceprints obtained from different users including registrant, man, and two women.

Figure 3.24 FFTs extracted from the sound wave of the word “Nanomembrane” obtained from voices of different subjects including the registrant, authorized user and denied users.

Figure 3.25 FFTs extracted from the sound wave, obtained from the voice of a registrant by using (upper) NM microphone and (bottom) commercial microphone (40PH, G.R.A.S.).

Figure 3.26 FFTs for repeated test of 10 times, extracted from the sound wave of the word “hello” obtained from various voices of different subjects including the registrant, a man, and two women.

Figure 4.1 (a) A photograph of ZnS:Cu/PDMS slurry in ambient light and (b) under a UV lamp. (c) Rheological behavior of slurry prepared with varying shear rate sweeps.

Figure 4.2 (a) SEM micrograph of ZnS:Cu particles with a mean particle size of $\mu = 26 \mu\text{m}$ and standard deviation of $\sigma = 5.5 \mu\text{m}$. The scale bar is $100 \mu\text{m}$. (b) Photoluminescence mechanism in ZnS doped with Cu impurity. (c) A photograph of ZnS:Cu particles placed on a glass plate and in a glass vial (dispersed in methanol). (d) X-ray diffraction pattern of hexagonal ZnS matched with standard JCPDS card (JCPDS card no.: 79-2204). (e) Photoluminescence spectra of ZnS:Cu recorded at room temperature with an excitation wavelength of 400 nm, which resulted in a green emission spectrum with peak emission wavelength at 500 nm.

Figure 4.3 Schematic representation of the overall procedure used to fabricate flexible ACEL devices using screen printing. i) The orthogonal AgNWs are formed by repeating the barcoating assembly in a perpendicular direction to that of the pre-aligned AgNW arrays. ii) Afterward, a BTO:La dielectric layer is screen printed on top of the AgNWs. iii) This is followed by a ZnS/PDMS layer. iv) Finally, the top electrode of AgNWs was deposited to obtain sandwich-like flexible ACEL device structure.

Figure 4.4 Flexible alternating-current electroluminescent (ACEL) devices. (a) Schematic representation of flexible ACEL device consisting of top and bottom crossaligned AgNW electrodes, ZnS emissive material, and high- k BTO:La nanodielectrics. (b) Photographs of the flexible ACEL device before and (c) after lighting up under applied bias. The scale bars are 2 cm. (d) A cross-sectional SEM image of flexible ACEL devices showing the homogeneous distribution of ZnS particles in the PDMS matrix. The scale bar is $100 \mu\text{m}$. (e) Partially enlarged cross-section view of top AgNWs. The scale bar is $20 \mu\text{m}$. (f) Partially enlarged tilted view of nanodielectrics. The scale bar is $5 \mu\text{m}$.

Figure 4.5 Band structure diagram showing EL mechanism for flexible ACEL devices caused by impact-excitation of Cu^{2+} in ZnS EL particles.

Figure 4.6 Synthesis and structural characterization of hydrothermally prepared bare and La-doped BTO nanodielectrics. (a) SEM images of tetragonal BTO:La nanodielectrics. The scale bar is 200 nm. The inset shows the particle size distribution histogram. (b) FETEM image of BTO:La nanodielectrics showing distinct tetragonal shape and the inset shows the selected area electron

diffraction (SAED) pattern showing bright diffraction spots. The scale bar is 100 nm. (c) Room temperature X-ray diffraction patterns for the La-doped BTO. Inset shows a magnified view of the region corresponding to the diffraction angles $2\theta = 44^\circ\text{--}46^\circ$ and (200) planes showing the peak splitting indicative of a tetragonal phase. (d) High resolution XPS spectra for La 3d showing two peaks at 834 and 851 eV, indicating La insertion into the BTO crystal structure.

Figure 4.7 FETEM image of La doped BTO nanocuboids and magnified FETEM image showing inter-planer spacing. The scale bar is 50 nm.

Figure 4.8 Structural characterization of hydrothermally prepared bare and La-doped BTO nanodielectrics. (a) Room temperature X-ray diffraction patterns for the La-doped BTO. (b) Magnified view (dashed rectangle of a) of the region corresponding to the diffraction angles $2\theta = 44\text{--}46^\circ$ and (200) planes showing peak splitting indicative of the tetragonal phase. (c) Evolution of lattice parameters vs. La content. (d) Dependence of tetragonality on La content and effect of La content on BTO nanoparticle size.

Figure 4.9 (a) FESEM images of undoped and La-doped BTO nanocuboids with different La concentrations. All scale bars are 1 μm . (b) Effect of La doping on BTO nanoparticle size variations.

Figure 4.10 XPS spectra showing Ba 3d, Ti 2p, O 1s and La 3d peaks of xLa: BTO samples.

Figure 4.11 (a) Dark field optical microscopy image of orthogonally aligned AgNW network and corresponding FFT images showing orthogonal alignment of nanowires. The scale bar is 20 μm . (b) Optoelectrical properties of AgNW films. Transmittance (at 550 nm) is plotted as a function of sheet resistance. Photograph of a thin AgNW network with $T = 95\%$. The scale bar in the inset photo is 2.5 cm.

Figure 4.12 Comparison of brightness between flexible ACEL devices with random AgNW electrodes and with cross-aligned AgNW electrodes.

Figure 4.13 Dielectric constant of BTO:La/PDMS nanocomposite. The plot is fitted with theoretical Lichteneker's mixing rule. which is shown with a solid line.

Figure 4.14 SEM images showing the fractured cross-sections of two types of composites containing $\phi\text{BTO:La} = 8.0, 14.8, 25.8, \text{ and } 47.0 \text{ vol.}\%$. More agglomeration of the filler was observed at higher La concentration (47.0 vol. %) BTO:La. All scale bars are 5 μm .

Figure 4.15 Dielectric permittivity and EL spectroscopic studies of flexible ACEL devices. (a) Frequency dependence of dielectric constant of PDMS, PDMS/ ZnS, PDMS/ZnS/BTO, PDMS/ZnS/BTO:La (0.5), and PDMS/ZnS/BTO:La (1.0). (b) EL intensity comparison spectra of

flexible ACEL devices with and without BTO:La nanodielectrics, showing that La doping enhances the device brightness when driven at an AC bias of 200 V and 1 kHz. (c) Brightness comparison of the devices under various applied voltages and under an applied fixed frequency of 1 kHz. (d) Brightness of flexible ACEL devices under varying frequencies and fixed applied AC voltage. (e) EL spectrum of La-doped flexible ACEL device driven at a high frequency of 5 kHz frequency exhibiting emission color tuning as the peak position is shifted from green to blue emission wavelength. The right inset shows a comparison of EL spectra at low and high frequencies. (f) CIE 1931 color space chromaticity diagram showing CIE coordinates (x , y) of light emission calculated from the EL spectra obtained by varying the applied frequency.

Figure 4.16 (a) Schematic illustration of setup used to characterize flexible ACEL devices. (b) Optical photograph of flexible ACEL device driven with 200 V and 1 kHz of AC bias. The scale bar is 3 cm.

Figure 4.17 Schematic illustration of the ACEL device with the corresponding simplified equivalent circuit model, where V_T and Q_T are the total voltage and charge, C_{die} and V_{die} are capacitance and voltage of the BTO:La high- k nanodielectric layer, and C_{emit} and V_{emit} are capacitance and voltage of emitting layer, respectively. When an external voltage of V_T is applied to the circuit, V_T is dropped into V_{die} and V_{emit} , that are in inverse proportion to the capacitance values. Now that Q_T is same for both components in this series circuit, a higher dielectric constant or C_{die} means a lower V_{die} , resulting in the increase of V_{emit} .

Figure 4.18 (a) Schematic of the model showing the mesh structure of a flexible ACEL device consisting of top and bottom electrodes, ZnS layer, and high- k dielectric layer. (b) Electrical potential distribution in a flexible ACEL device. The finite element models show 2D maps of the electric field (c and e) and charge density distribution (d and f) in flexible ACEL devices with different dielectric strengths. The materials used were undoped BTO and BTO:La. The dielectric constants of undoped and BTO:La were taken as 11 and 21, respectively.

Figure 4.19 Local field strength variation with high dielectric matrix.

Figure 4.20 Relationship between voltage and device brightness fitted with Lehmann model (red squares and black circles are experimental data points and solid lines are fits to the Lehmann model).

Figure 4.21 Device uniformity and flexibility. (a) Normalized brightness as a function of distance from the contact for high-aspect-ratio flexible ACEL devices, as shown in Figure 4.4c. (b) Sequential optical photographs of a flexible ACEL device undergoing increasing bending. The flexible ACEL device was bent into a convex shape, demonstrating excellent mechanical stability in terms of flexibility and bendability of the device. All scale bars are 1 cm. (c) Device operation under different bending

radii. (d) Normalized EL intensity under cyclic bending tests showing excellent brightness retention.

Figure 4.22 (a) Schematic of Joule heating test using an orthogonal AgNW network as a transparent electrode. (b) IR camera images of orthogonal AgNW networks at an applied voltage of 7 V. The scale bar is 2 cm.

Figure 5.1 Self-healable and transparent AgNW/PUHU electrodes. (a) Synthetic scheme and chemical structure of the self-healable PUHU polymer (Hindered urea bond is indicated in blue lines). (b) Mechanism of the self-healing process of the PUHU polymer. (c) Photograph of the fabricated self-healable AgNW electrode. The scale bar is 1 cm. (d) SEM image of self-healable AgNW/PUHU electrodes. The scale bar is 1 μm . (e) Optical transmittance of AgNW-coated self-healable electrodes in the visible range of 400 to 800 nm. The air was used as standard reference.

Figure 5.2 FT-IR spectra of IPDI, HU-IPDI, and PUHU. Isocyanate peak disappeared in PUHU (at $\nu = 2,250 \text{ cm}^{-1}$).

Figure 5.3 Surface morphology of the bare PUHU film. (a) OM image of the PUHU film after scratching and (b) after the healing process; the scale bars are 30 μm . (c) SEM image of the PUHU film after scratching and (d) after the healing process; the scale bars are 5 μm and 2.5 μm , respectively.

Figure 5.4 Tensile test result of PUHU and control sample synthesized by ethylenediamine. The modulus was 59 MPa for PUHU and 63 MPa for the control sample, respectively.

Figure 5.5 Confocal OM images of a PUHU film on a PEN substrate (a) before healing, (b) after healing, and (c) depth profile of a and b. Confocal OM images of a control sample synthesized with ethylenediamine on a PEN substrate. (d) before healing, (e) after healing, and (f) depth profile of d and e. All scale bars are 30 μm .

Figure 5.6 OM images of self-healing processes of PUHU polymers at (a) ambient air condition and 40°C and (b) RH 80% and 40°C. All scale bars are 30 μm .

Figure 5.7 Fabrication process of self-healable AgNW/PUHU electrode.

Figure 5.8 Self-healing behavior of the AgNW/PUHU electrodes. (a) Schematic illustration of the self-healing process of the presence of the healable AgNW/PUHU electrode. (b) AFM images of the self-healable AgNW/PUHU electrode before scratching (pristine), after scratching, and after the self-healing process. All scale bars are 3 μm . (c) Surface height profiling of the self-healable AgNW/PUHU electrode before scratching (pristine), after scratching, and after the self-healing process. (d) Plot of resistance after repetitive scratching and self-healing processes. (e) Plot of resistance after repetitive scratching and self-healing processes.

Figure 5.9 DSC curves of PUHU polymers after humid treatment at 95 °C and RH 80%. The glass transition temperature appeared near -19.5 °C.

Figure 5.10 OM and SEM images of the AgNW/PUHU electrode after scratching (left) and the healing process (right). The scale bars are $2\ \mu\text{m}$ for (OM) and $1\ \mu\text{m}$ for (SEM).

Figure 5.11 SEM and EDS images of self-healable AgNW/PUHU electrodes (a) after scratching and (b) after the healing process. The scale bars are $2.5\ \mu\text{m}$ for (a) and $1\ \mu\text{m}$ for (b).

Figure 5.12 FT-IR spectra of AgNW/PUHU electrode after repetitive healing processes at 95 °C and RH 80%.

Figure 5.13 OM images showing the repeatedly healed AgNW/PUHU electrode surface.

Figure 5.14 Photograph of the self-healable AgNW/PUHU electrode connected to the LED lamp during scratching and self-healing processes. All scale bars are 1 cm.

Figure 5.15 Adhesion properties of the AgNWs on the PUHU film. (a) Schematic illustration of the semi-embedded AgNW networks on the PUHU film surface. (b) SEM image of semi-embedded AgNW networks. The scale bar is 500 nm. (c) Change in the resistance of the AgNW networks on various substrates including glass, TPU, PEN, PDMS, and PUHU during the taping test for 1,000 times. (d,e) SEM images of the AgNW networks on the PUHU film (d) before and (e) after performing the taping test for 1,000 times. The scale bars are $2\ \mu\text{m}$. Insets show enlarged SEM images. The scale bars in insets are 500 nm.

Figure 5.16 Mechanical properties of the self-healable AgNW/PUHU electrodes. (a) Plot of the change in resistance when the bending radius is changed from 8 to 1.4 mm. (b) Plot of the change in resistance when 10,000 bending cycles are performed at a fixed bending radius of 5 mm. (c) Photographs of self-healable AgNW/PUHU electrodes connected to the LED lamp during 10,000 bending cycles. The scale bars are 1 cm.

Figure 5.17 Self-healable AgNW/PUHU electrode-based TA loudspeakers. (a) Photograph of self-healable TA loudspeaker with microphone for sound measurements. The scale bar is 1 cm. (b) Schematic mechanism of the TA loudspeaker. (c) Schematic representation of the acoustic measurement system. (d) Variation in sound pressure level (SPL) generated from the self-healable TA loudspeaker as a function of input power at different frequencies. (e) Plot of temperature change of the TA loudspeaker against the increasing power input on the speaker device. Inset shows the infrared image of the TA loudspeaker while applying power. (f) Experimental values of the SPL versus sound frequency for the self-healable TA loudspeaker before scratching (pristine), after scratching, and after self-healing process.

Figure 5.18 Plot of the sound pressure of the TA loudspeaker with different frequencies against varying distances, which is obtained by using a commercial microphone.

Figure 5.19 Plot of SPL inside an anechoic room without the TA loudspeaker, showing an ambient noise level of below 25 dB.

Figure 5.20 Photographs showing the surface and resistance of the TA loudspeaker at different stages: (a) before scratching, (b) after scratching, and (c) after scratching and self-healing. All scale bars are 1 cm.

Figure 6.1 Stretchable sound-in-display electronics. (a) Concept of a stretchable sound-in-display device and (b) schematic image showing device geometry. (c) Cross-sectional SEM image of the device. Scale bar is 20 μm . (d) SEM image of stretchable AgNW electrode. Scale bar is 5 μm . (e) Operation of the sound-in-display device with sound-synchronized EL under bending, twisting, and stretching on the index finger. An audible sound and blue luminescence are generated (AC 60 V and 5 kHz). All scale bars are 1.5 cm. (f) Schematic operation mechanism of the sound-in-display device.

Figure 6.2 Investigation of size distribution of ZnS:Cu phosphors. (a) SEM images of ZnS:Cu phosphors. The scale bar is 25 μm . (b) Size distribution of ZnS:Cu phosphors. The average diameter of ZnS:Cu phosphors is around 18.2 μm .

Figure 6.3 Investigation of AgNWs. (a) TEM images of single AgNW. The scale bar is 10 nm. (b) SEM images of AgNW networks. The scale bar is 1 μm .

Figure 6.4 Photograph of the fabricated stretchable EL loudspeaker device placed on the background UNIST logo. The scale bar is 1.5 cm.

Figure 6.5 Schematic of an overall procedure for the fabrication of strain-insensitive stretchable AgNW electrodes. Firstly, the liquid state PDMS prepolymer is partially-cured. Before the coating of AgNWs, partially-cured PDMS was pre-strained and pre-treated with O_2 plasma. After the coating of AgNWs, pre-strained PDMS was released and cured completely.

Figure 6.6 Observation of strain-insensitive stretchable AgNW electrodes. (a) A photograph of a stretchable and transparent AgNW electrode. (b) SEM image of stretchable AgNW electrode. The scale bar is 100 μm . (c, d) The magnified SEM images of the stretchable AgNW electrode. The scale bars are 10 μm and 3 μm , respectively.

Figure 6.7 The SEM images for the comparison between stretchable AgNW electrodes fabricated by using partially-cured and fully-cured PDMS. (a, b) The SEM images of stretchable AgNW electrodes using partially-cured PDMS. The scale bars are 10 μm and 2 μm , respectively. (c, d) The

SEM images of stretchable AgNW electrodes using fully-cured PDMS. The scale bars are 5 μm and 2 μm , respectively.

Figure 6.8 The taping test for the comparison of adhesion property between stretchable AgNW electrodes fabricated by using partially-cured and fully-cured PDMS. Compared to the partially-cured PDMS based electrodes, fully-cured PDMS based stretchable electrodes show dramatic increase in resistance after two times of taping tests.

Figure 6.9 Characterization of strain-insensitive stretchable AgNW electrodes. (a) Resistance as a function of tensile strain for different initial resistances. (b) Resistance evolution during repetitive stretching to 100% for 1000 cycles. Inset: photograph of the stretching system. (c) SEM images of stretchable AgNW electrodes during stretching to 150%. All scale bars are 20 μm . Insets illustrate the wrinkle structures of stretched electrodes. (d) Enlarged SEM images of stretchable AgNW electrodes during stretching to 150%. All scale bars are 10 μm .

Figure 6.10 Effect of the number of coatings on (a) the electrical resistance of stretchable AgNW electrodes and (b) AgNW density.

Figure 6.11 Effect of strain on the resistance of stretchable AgNW electrodes fabricated without pre-straining.

Figure 6.12 Photographs showing the behavior of LED circuits connected to strain-insensitive stretchable AgNW electrodes upon the increase of tensile strain up to 150%. All scale bars equal 2 cm.

Figure 6.13 Photographs of a stretchable electrode during stretching to 150%. All scale bars equal 1 cm.

Figure 6.14 Mechanical stability of strain-insensitive stretchable AgNW electrodes. (a) Effect of bending radius on electrode resistance. (b) Electrode resistance change during 1000 bending cycles at a bending radius of 1 mm.

Figure 6.15 Band structure diagram showing the ACEL mechanism for the stretchable EL loudspeaker. Emission originates from the impact excitation of Cu^{2+} in $\text{ZnS}:\text{Cu}$ phosphors.

Figure 6.16 Photograph of the setup used to measure EL by a spectroradiometer. The applied AC voltage from the function generator was amplified by a high-voltage amplifier.

Figure 6.17 (a) Sinusoidal, square, and ramp waves. (b) Luminance intensity obtained for various excitation waveforms at 100 V and 10 kHz.

Figure 6.18 Light emission characteristics and mechanical properties of stretchable EL loudspeaker. (a) Effects of voltage on the luminance of stretchable EL loudspeaker at different frequencies and the corresponding fits. (b) EL spectra of stretchable EL loudspeaker recorded at different applied voltages and a fixed frequency of 10 kHz. (c) Representation of color coordinates in CIE 1931 color space according to voltage- and frequency-dependent emission color change. White arrows (V) indicate the change of color coordinates upon the increase of applied AC voltage from 20 to 180 V. Black arrow (f) indicates the change of color coordinates upon the increase of applied frequency from 100 Hz to 50 kHz. (d) Photographs of EL loudspeaker stretched to strains of 0, 60, 100, and 150% (AC 100 V, 10 kHz). All scale bars are 1.5 cm. (e) Effect of stretching strain on the relative emission intensity of the stretchable EL loudspeaker. (f) Stretching stability test of the stretchable EL loudspeaker under repetitive straining to 100%. (g) Emission stability test of the stretchable EL loudspeaker under 5000 on-off cycles.

Figure 6.19 EL spectra as a function of applied frequency (50 Hz to 20 kHz) at a fixed applied voltage of 100 V.

Figure 6.20 Luminance of stretchable EL loudspeaker as a function of emission layer thickness (100 V, 10 kHz).

Figure 6.21 Characterization of the stretchable EL loudspeaker. (a) Photograph of the stretchable EL loudspeaker during sound recording using a microphone. Scale bar is 1.5 cm. (b) Acoustic measurement system in which sound emitted from the stretchable EL loudspeaker is collected by a microphone. (c) Effect of applied voltage on the SPL generated by the stretchable EL loudspeaker at an AC to DC voltage ratio of 3:1. (d) Sound performance of stretchable EL loudspeaker for different AC to DC voltage ratios. (e) Dependence of SPL on the distance between the microphone and the stretchable EL loudspeaker. (f) Effect of angle on the SPL of the stretchable EL loudspeaker at 100 V and 10 kHz. The distance between the loudspeaker and the microphone equaled 2.5 cm. (g) Dependence of loudspeaker SPL on tensile strain. (h) Stability of sound performance during 5000 cycles of stretching to 100% strain. (i) Sound performance stability of the stretchable EL loudspeaker during repeated 5000 on-off cycles.

Figure 6.22 Power spectrum of the background noise in the anechoic room.

Figure 6.23 Sound intensity under varying excitation waveforms (100 V, 10 kHz).

Figure 6.24 Sound performance under different DC to AC bias ratio ($V_{\max} = 200$ V, 10 kHz).

Figure 6.25 Experimental values of SPL versus sound frequencies for stretchable EL loudspeaker.

Figure 6.26 Sound intensity of stretchable EL loudspeaker as a function of emission layer thickness (100 V, 10 kHz).

Figure 6.27 Stretchable sound-in-display electronics. (a) Luminance and SPL as functions of the AC to DC voltage ratio ($V_{\text{max}} = 360$ V, frequency = 10 kHz) before and after the application of tensile strain (150%). (b) Schematic diagram showing the waveform of AC-DC combined signals used for music playing. (c) Wearable EL loudspeaker attached to a gloved index finger during music playing. Music sound was recorded by a commercial microphone. Scale bar is 1.5 cm. (d) Wearable EL loudspeaker during finger flexion. Scale bar is 1.5 cm. (e) Input signal of the sound wave (*Le Nozze di Figaro*). (f) Analyzed output sound wave (left) and its short-time Fourier transform (right) in the straightened state and (g) in the state of finger flexion.

List of Tables

Table 4.1 Comparison of results achieved in this study with performance of previously reported ACEL devices.

Table 6.1 Summary of recently reported works related to the light emission or sound generation.

Nomenclature

IoT	Internet of Things
TCE	Transparent conductive electrode
ITO	Indium tin oxide
AgNW	Silver nanowire
R_s	Sheet resistance
T	Transmittance
NM	Nanomembrane
ACEL	Alternating-current electroluminescent
BTO:La	La-doped barium titanate
PUHU	poly(urethane-hindered urea)
EL	Electroluminescent
OLED	Organic light-emitting-diodes
CNT	Carbon nanotube
PEDOT:PSS	poly(3,4-ethylenedioxythiophene) (4-styrenesulfonate)
CVD	Chemical vapor deposition
CuNW	Copper nanowire
PVP	poly(vinyl pyrrolidone)
PET	polyethylene terephthalate
PDMS	polydimethylsiloxane
FoMs	Figures of merit
rGO	Reduced graphene oxide
PU	Polyurethane
PVDF	poly(vinylidene fluoride)
PZT	$\text{Pb}[\text{Zr}_x\text{Ti}_{1-x}]\text{O}_3$
MXene	Transition metal carbide/carbonitride
DEA	Dielectric elastomer actuator
PUU	Polyurethane urea
TPU	Thermoplastic polyurethane
IPA	Isopropyl alcohol
PLL	Poly-L-lysine
XPS	X-ray photoelectron spectroscopy

HMDS	Hexamethyldisilazane
FFT	Fast Fourier transform
FWHM	Full width at half maximum
AI	Artificial intelligence
NP	Nanoparticle
NW	Nanowire
LbL	Layer-by-layer
ZnO	Zinc oxide
SEM	Scanning electron microscopy
<i>EI</i>	Bending stiffness
<i>E</i>	Young's modulus
<i>C_p</i>	Heat capacity
BTO	Barium titanate
FETEM	Field-emission transmission electron microscopy
XRD	X-ray diffraction
TA	Thermoacoustic
HCPUA	Heat capacity per unit area
RH	Relative humidity
SPL	Sound pressure level
PCD	Poly(carbonate diol)
DBTDL	Dibutyltin dilaurate
HDI	Hexamethylene diisocyanate
RF	Radio frequency
IPDI	Isophorone diisocyanate
FT-IR	Fourier-transform infrared spectroscopy
AFM	Atomic force microscope
PEN	Polyethylene naphthalate
OM	Optical microscopy
DSC	Differential scanning calorimetry
AFM	Atomic force microscopy
AC	Alternating current
DC	Direct current
ZnS:Cu	Copper-doped zinc sulfide
<i>S_{AC}</i>	Time-dependent actuation amplitude

STFT	Short-time Fourier transform
UV-vis	Ultraviolet-visible
PL	Photoluminescence
AAO	Anodic aluminum oxide
E-field	Electric field

Chapter 1. Introduction.

1.1 Flexible/stretchable transparent electrodes

Soft electronics, as an emerging and interesting research field, have attracted enormous attention in the past few years to integrate electronics with dynamic nonplanar surfaces by expanding the limited capabilities of conventional rigid electronics. The rapid evolution of wearable electronics with the growing importance of human-machine interfaces and internet of things (IoT) has inspired transition from current rigid systems to flexible and ultimately to stretchable electronics, enabling the conformal integration of electronic devices with skin/clothes of robots or human.^{1,2}

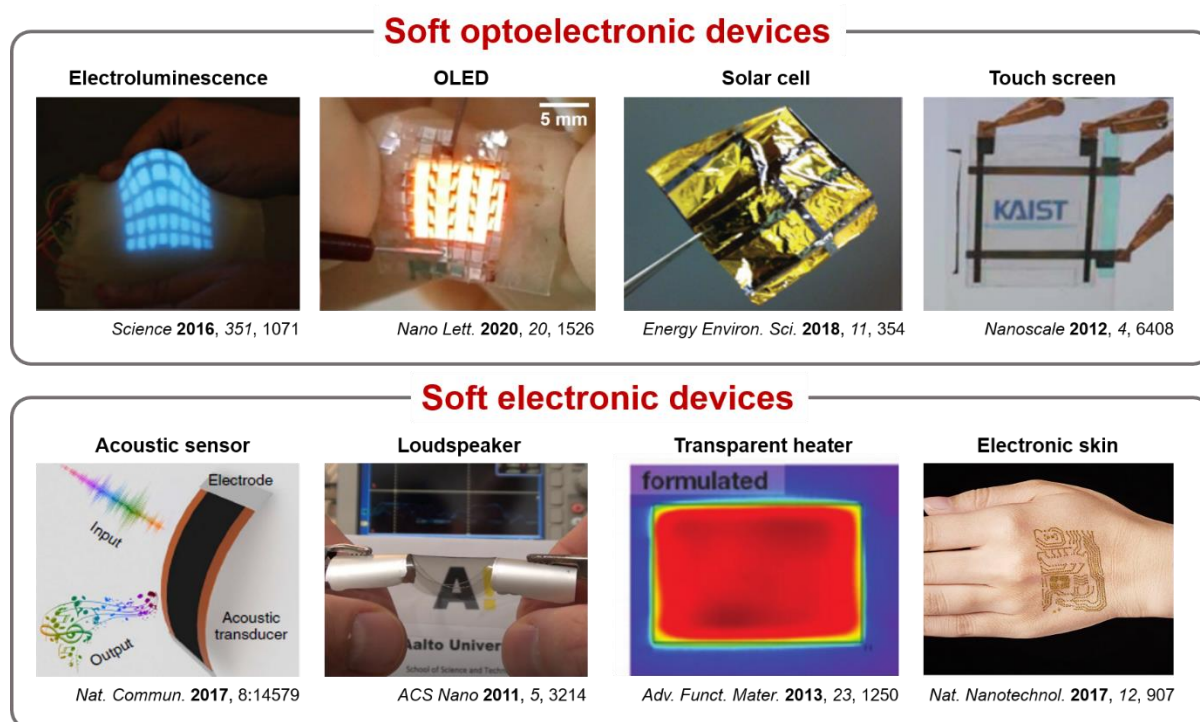


Figure 1.1. Diverse soft optoelectronic and electronic device applications based on flexible/stretchable transparent electrodes. (C. Larson et al. *Science* **2016**, 351, 1071, M. S. Lim et al. *Nano Lett.* **2020**, 20, 1526, X. Zhang et al. *Energy Environ. Sci.* **2018**, 11, 354, J. Lee et al. *Nanoscale* **2012**, 4, 6408, L.-Q. Tao et al. *Nat. Commun.* **2017**, 8:14579, A. G. Nasibulin et al. *ACS Nano* **2011**, 5, 3214, T. Kim et al. *Adv. Funct. Mater.* **2013**, 23, 1250, A. Miyamoto et al. *Nat. Nanotechnol.* **2017**, 12, 907).

Figure 1.1 shows the representative soft optoelectronic and electronic device applications using flexible or stretchable transparent electrodes in the last decade. With the increasing demand for

soft optoelectronic/electronic device applications, electroluminescent (EL) devices,³ organic light-emitting-diodes (OLEDs),⁴ organic solar cells,⁵ touch screens,⁶ acoustic sensors,⁷ loudspeakers,⁸ transparent heaters,⁹ and electronic skins¹⁰ have been developed with flexible or even stretchable form. With the intensive researches on soft electronics, flexible/stretchable optoelectronic and electronic devices show tremendous advances in device performance with high durability at strained states. Compared to the rigid electronics, flexible/stretchable electronics can provide opportunity to be used in wearable and conformable devices when being integrated into body parts or arbitrary curvilinear objects. For example, soft optoelectronic devices such as EL devices, OLEDs, solar cells, and touch screens can be conformably installed on the three-dimensionally curved non-planar surfaces or human skins, enabling the provision of visual information with higher user experience and the user-display interfaces. Besides, soft electronic devices with diverse functionalities such as acoustic sensors, loudspeakers, microphones, transparent heaters, and electronic skins can be further explored in various human-machine interface applications. In particular, the development of high-performance flexible or stretchable transparent conductors is critically important for the realization of highly robust and reliable soft optoelectronic and electronic devices. Despite the notable progress in the flexible/stretchable electronics, the development of flexible or stretchable transparent conductors having both high levels of electrical conductivity and optical transparency as well as high mechanical durability under repeated deformation is still challenging.¹¹

1.1.1. Nanostructured transparent conducting materials

Flexible or stretchable transparent electrodes play a pivotal role in a variety of future soft optoelectronic and electronic device applications. Next-generation transparent electrodes should possess three main physical properties: high electrical conductivity, optical transparency, and mechanical durability. Doped metal-oxide films, especially indium tin oxide (ITO) films, are the most widely used transparent conducting material because of its optical transparency and electrical conductivity. Although ITO has excellent sheet resistance and optical transparency, its brittleness causes failure under mechanical deformation, which is not compatible with the soft electronic applications.¹² In addition, price of raw indium material and high-cost manufacturing process based on vapor phase sputtering process make the ITO undesirable for the flexible or stretchable electronic applications.¹³ Given the fact that ITO has several limitations in manufacturing process and non-compatibility with soft electronics, nanostructured transparent conducting materials such as conducting polymer,¹⁴ graphene,¹⁵ metal mesh,¹⁶ carbon nanotube (CNT),¹⁷ electrospun nanotrough,¹⁸ and metallic nanowires¹⁹ have been thoroughly explored and investigated due to their promising properties in the past few years (Figure 1.2). Even though typical transparent conducting nanomaterials can be ideal for

designing transparent conductors, trade-off between electrical conductivity and optical transmittance should be considered for the optimal performances (Figure 1.2a).

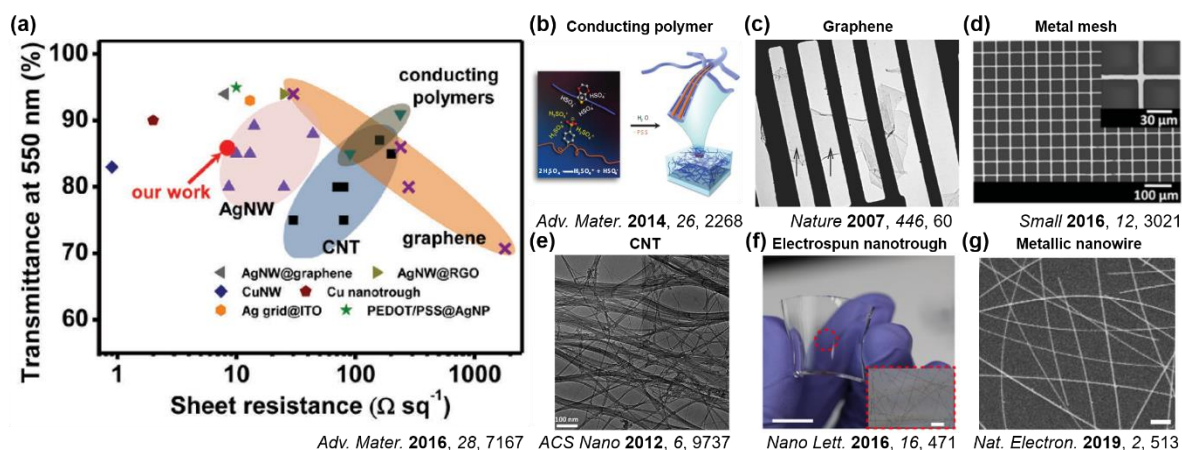


Figure 1.2. Various next-generation conducting nanomaterials. (a) Sheet resistance versus optical transmittance for various transparent electrodes (W. Xiong et al. *Adv. Mater.* **2016**, *28*, 7167). (b) Conducting polymer (N. Kim et al. *Adv. Mater.* **2014**, *26*, 2268). (c) Graphene (J. C. Meyer et al. *Nature* **2007**, *446*, 60).¹⁵ (d) Metal mesh (A. Khan et al. *Small* **2016**, *12*, 3021). (e) Carbon nanotube (F. Mirri et al. *ACS Nano* **2012**, *6*, 9737). (f) Electrospun nanotrough (B. W. An et al. *Nano Lett.* **2016**, *16*, 471). (g) Metallic nanowire (Y. Sun et al. *Nat. Electron.* **2019**, *2*, 513).

Conducting polymers are one of the most promising alternative material to ITO due to their solution-processability and high mechanical flexibility (Figure 1.2b).²⁰ A complex of poly(3,4-ethylenedioxythiophene) (PEDOT) and poly(4-styrenesulfonate) (PSS), in which PSS acts as counterion is the most widely used conducting polymer for flexible transparent electrodes that are often used in OLED and organic solar cells as hole transport layer.¹⁴ Despite high optical transparency (>85%) and mechanical flexibility of PEDOT:PSS, low electrical conductivity (>100 $\Omega \text{ sq}^{-1}$) limits its applications requiring high current carrying capacity.

From the discovery of single atomic layer of carbon, graphene has attracted enormous attention for replacing ITO films due to outstanding electrical, mechanical, and chemical properties in the past decade (Figure 1.2c).²¹ The atomically thin single-crystal graphene sheets have an excellent transparency in visible region. Although graphene sheets can be synthesized in large-scale using roll-to-roll process, the fabrication process is based on complicated wet-chemical doping and chemical vapor deposition (CVD) with high vacuum condition.²² Moreover, the electrical conductivity of graphene is still not comparable with metallic nanomaterials.

Recently metal mesh structures have been reported to replace ITO films for flexible transparent electrodes because of their superior optical transmittance and sheet resistance compared to ITO films (Figure 1.2d).^{16, 23} Due to the inherent light scattering and low haze factor of metal mesh structure, it can be readily applied to the flexible optoelectronic applications including solar cells and touch screens by enhancing optical path length of photons in solar cells and improving image quality of touch screen display.²⁴ However, fabrication process of metal mesh is mostly based on photolithography and laser-etching process for high precision patterning that involves complicated procedures.

Transparent conducting networks of CNTs have received increasing attention to replace ITO due to the flexibility, durability, and solution-processability (Figure 1.2e).^{17, 25} Especially, single-walled CNTs have been intensively utilized in flexible optoelectronic devices because of its high optical transparency compared to the multi-walled CNTs. Even though CNTs are easily coated on a large-area substrate by solution-based roll-to-roll coating processes, the electrical conductivity of CNT networks is not comparable to ITO films owing to the large junction resistance between CNT bundles.

More recently, electropun metal nanotrough networks having superior optoelectronic performances and mechanical durability have been presented for future flexible transparent electrodes (Figure 1.2f).^{18, 26} Thereafter, Cui research group further enhanced the optoelectronic performance ($0.36 \Omega \text{ sq}^{-1}$ at 92% transmittance) using hybrid of mesoscale and nanoscale metal nanowires synthesized by electrospinning methods.²⁷ Although the proposed metal nanotrough networks show excellent optical transparency and electrical conductivity, electrospinning process is not adequate to mass production with low production efficiency.

Among various alternatives to ITO film, metallic nanowires are currently the most promising material due to the solution-processability and comparable optoelectronic performance to ITO ($<30 \Omega \text{ sq}^{-1}$ at $>90\%$ transmittance) (Figure 1.2g).¹³ The metallic nanowires including copper nanowires (CuNWs)²⁸⁻³⁰ and silver nanowires (AgNWs)^{19, 31-33} have been intensively researched in the past decade for the fabrication of flexible and even stretchable transparent electrodes.

1.2. Transparent AgNW networks

Flexible and transparent conductive electrodes (TCEs) based on AgNW network have attracted great attention in a variety of optoelectronic and electronic devices because of its high optical transparency, electrical conductivity, and mechanical flexibility, which are critical properties that TCEs should possess for the realization of high-performance optoelectronic and electronic device applications. The scalable production of AgNW networks were developed by Xia group using a polyol process (Figure 1.3).³⁴ Using poly(vinyl pyrrolidone) (PVP) as a surfactant and ethylene glycol as a reducing agent during synthesis, solution-phase of large-scale AgNWs are synthesized, where diameters could be controlled in the range less than 60 nm and length could reach up to $\sim 50 \mu\text{m}$.³⁵ This extremely high aspect ratio of AgNWs provides much higher electrical conductivity because of the minimization of junction resistance.

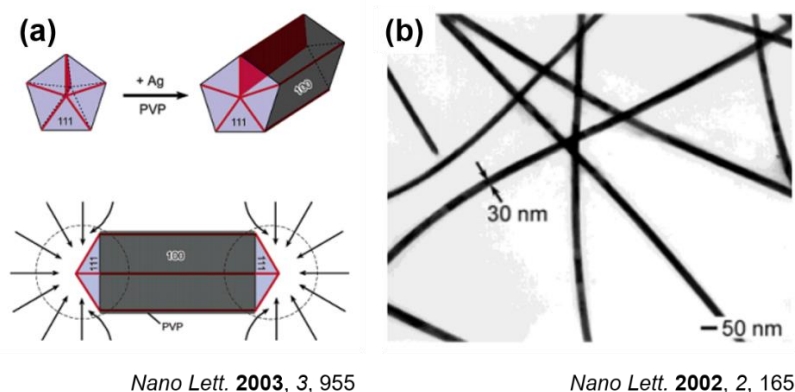


Figure 1.3. Synthesis of AgNWs based on the polyol process. (a) Schematic illustration of the mechanism proposed to account for the growth of AgNWs with pentagonal cross sections (Y. Sun et al. *Nano Lett.* **2003**, 3, 955). (b) TEM images of as-synthesized AgNWs (Y. Sun et al. *Nano Lett.* **2002**, 2, 165).

Because AgNWs are well dispersed in a variety of popular solvents such as deionized water, ethanol, isopropyl alcohol, and ethylene glycol, solution-phase coating processes are possible with the low cost and large-area fabrication. Various solution-based processes such as drop casting,³⁶ spray coating,³⁷ spin coating,³⁸ vacuum filtration,³⁹ blade coating,⁴⁰ and bar coating^{13, 31} have been widely used for fabricating AgNW-based TCEs (Figure 1.4). Drop casting of nanowire suspension on a desired substrate always results in a dense and randomly oriented nanowire networks by coffee ring effect with low optical transparency. Spray coating of nanowire suspension is frequently used method for the fabrication of large-area random AgNW networks.³⁶ Despite the ease of spray coating for applying

nanowires on the non-planar and large substrates, the adequate temperature control or delicate pressure control are needed for the uniform coating of sprayed droplet of nanowire suspension.^{37,41} Spin coating is a very popular nanowire coating method due to the rapid coating process. However, spin coating is hard to be used in large-area coating processes because of the fundamental limitation of setup that requires high speed of rotation of substrates. In addition, variation of spin rate and concentration of nanowire suspension is not very scalable to control the density of AgNW networks.³⁸ Vacuum filtration of nanowire dispersion is particularly utilized when the AgNW film needs to be transferred onto the desired substrates regardless of hydrophilicity or hydrophobicity such as polyethylene terephthalate (PET), glass, polydimethylsiloxane (PDMS) and so on. Obviously, a vacuum filtration method results in dense and random AgNW networks, which is not scalable and makes issues in the transfer process of AgNW thin films.³⁹ Doctor blade coating is one of the most widely used technique because of its large-area coating capability and simplicity. By simply moving a substrate under the blade, thin nanowire films are fabricated. However, very thin film fabrication is difficult by the blade coating compared with the bar coating.⁴⁰ Bar coating (or Meyer rod coating) is one of the most widely used method because of its simplicity and scalability for making AgNW thin films. Besides, bar coating is compatible with the roll-to-roll process for the large-area applications with high accuracy, cost-effectiveness, and good uniformity.⁴²

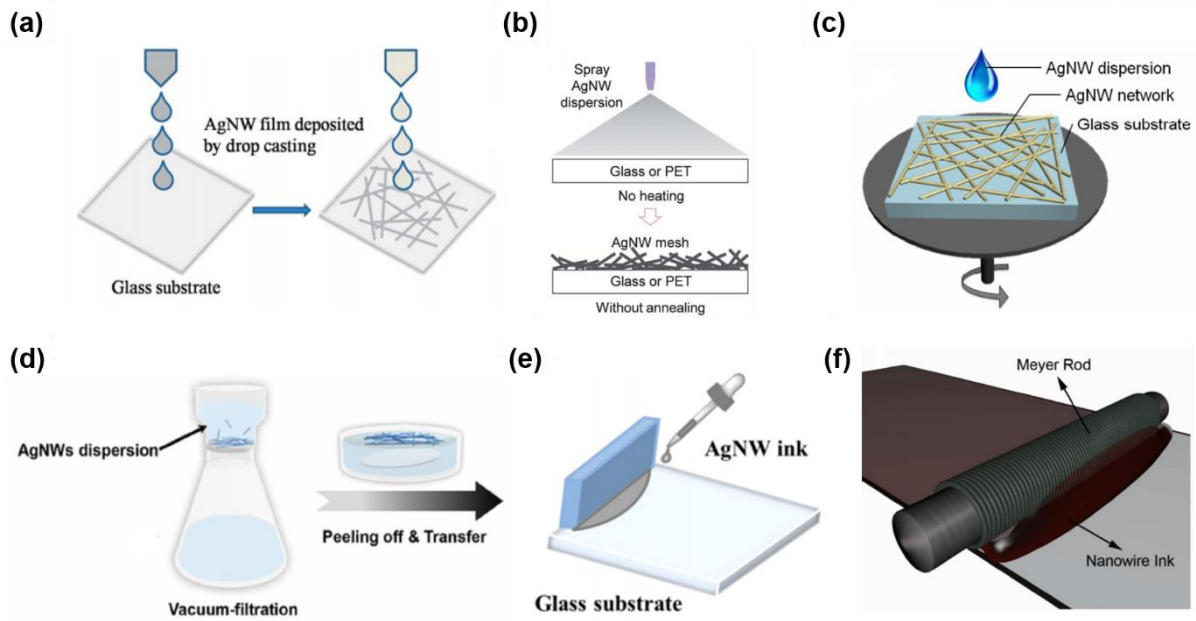


Figure 1.4. Various coating methods of AgNW networks. (a) Drop casting (X. Guo et al. *RSC Adv.* **2015**, *5*, 24953). (b) Spray coating (D. Y. Choi et al. *Nanoscale* **2013**, *5*, 977). (c) Spin coating (S. Xie et al. *Opt. Express* **2013**, *21*, A355). (d) Vacuum filtration (W. Xiong et al. *Adv. Mater.* **2016**, *28*, 7167). (e) Blade coating (X. Zhang et al. *ACS Appl. Mater. Interfaces* **2016**, *8*, 34630). (f) Bar coating (S. Ye et al. *Adv. Mater.* **2014**, *26*, 6670).

1.2.1 Conductive percolation networks

The solution processable AgNW-based coating methods enable the facile and simple large-scale fabrication of thin film AgNW networks. The random networks are spontaneously formed during conventional solution-based coating methods because of high aspect ratio of nanowires in the presence of polar solvents. For the efficient electrical current path through AgNW networks, construction and density control of nanowire network are important parameter for high-performance TCEs. Figure 1.5a shows the typical AgNW networks with concentration just above critical percolation concentration (C_p) (left) and concentration much above C_p (right).⁴³ In percolation theory, the C_p of conductive networks can be plotted as a power law dependence of conductivity form, $\sigma \sim (C - C_p)^\alpha$, where C is the concentration of AgNWs and α is the critical exponent that related to the spatial geometry of AgNW networks ranging from 1.33 for 2D network to 1.94 for 3D network.⁴⁴ Here, the effective percolation threshold of conductive networks can be reduced by efficiently constructing nanowire orientations or controlling the aspect ratio of individual nanowires.

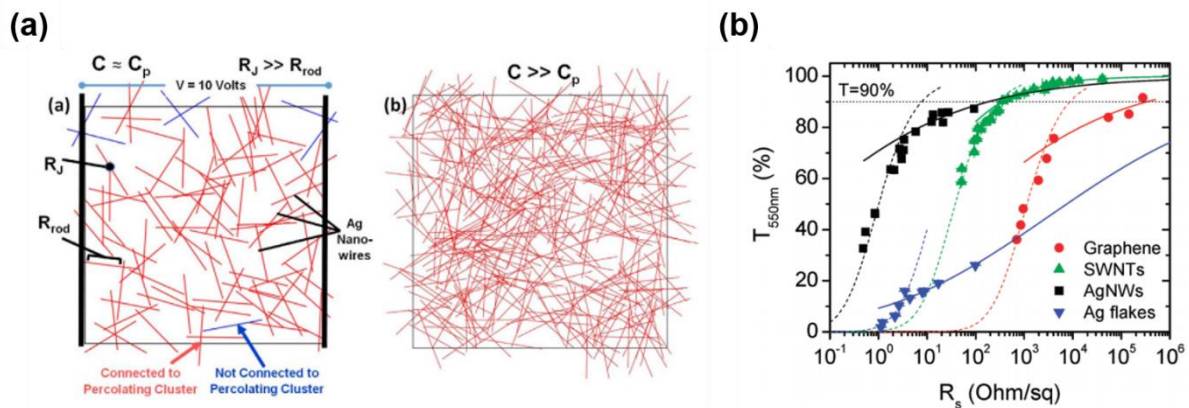


Figure 1.5. Conductive percolation network of randomly oriented AgNWs. (a) Sample networks of AgNWs for $140 \mu\text{m} \times 140 \mu\text{m}$ domain with concentration just above critical percolation concentration ($C \sim C_p$) (left) and concentration much above critical percolation concentration ($C \gg C_p$) (right) (M. Jagota & N. Tansu *Sci. Rep.* **2015**, 5:10219). (b) Transmittance (550 nm) plotted as a function of sheet resistance for thin films prepared from different conducting nanomaterials (S. De et al. *ACS Nano* **2010**, 4, 7064).

Along with the development of high-performance TCEs, it is necessary to benchmark the performance of transparent conductors. Recently, figures of merit (FoMs) has been widely used to estimate the electrical to optical conductivity of TCEs. To compare the trade-off between transmittance

(T) and sheet resistance (R_s), the equation $T = \left[1 + \frac{1}{\pi} \left\{ \left(\frac{Z_0}{R_s} \right) \right\}^{1/(n+1)} \right]^{-2}$, is used, where Z_0 is the

impedance of free space ($Z_0 = 377 \Omega$), n is the percolation exponent describing the power law relationship between R_s and the film thickness, and Π is the percolative FoM. Here, the Π is a dimensionless number where large values of Π means high electrical conductivity with high optical transparency.⁴⁵ When fitting the R_s and T data by FoM, the transparent conductors are fitted well with percolative regime (Figure 1.5b). By fitting T and R_s data, we can obtain the objective values of σ_{DC}/σ_{Op} with FoMs.

1.2.2 Junction resistance

In conductive percolation network of AgNWs, current flows along with individual nanowires and a lot of nanowire-nanowire junction points. Polyvinylpyrrolidone (PVP) capping layer is crucial surfactant during the synthesis process for the stabilization of the individual nanowires in suspension. Due to the presence of electrically insulating few nm-thick PVP layer on the surface of AgNWs, a large loss in electrical conductivity is unavoidable in the conductive percolation networks.⁴⁶ As a result, the overall sheet resistance of conductive networks is ultimately controlled by the junction resistance (Figure 1.6a). While the electrical resistance of a single nanowire is under a few $\Omega \mu\text{m}^{-1}$, the junction resistance values of non-annealed and annealed nanowire networks are $529 \pm 239 \Omega$ and $25.2 \pm 1.9 \Omega$, respectively.⁴⁷ Therefore, manipulation of conductive percolation networks by reducing junction resistance is necessary for efficient current flow.

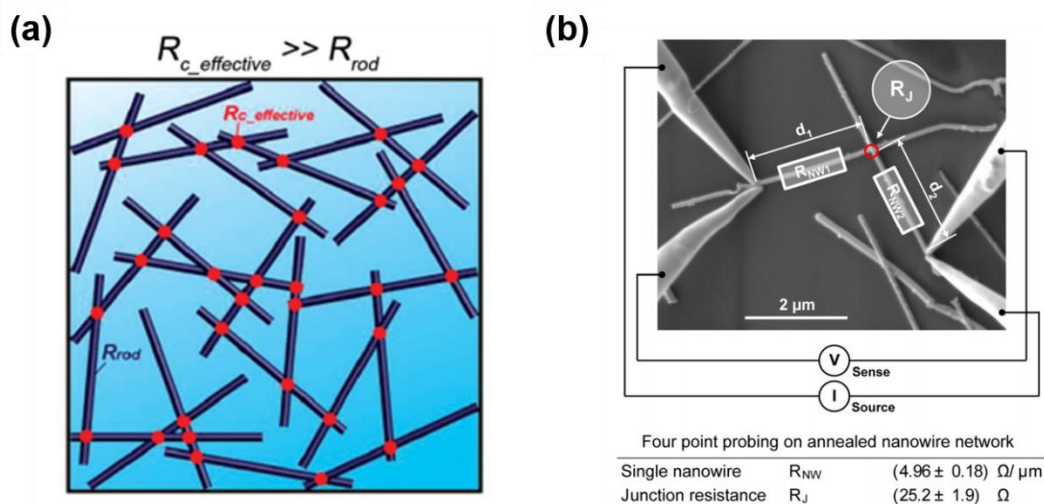


Figure 1.6. Nanowire junction resistance. (a) Schematic showing a percolated network of monodisperse rods in which the resistance at nanowire-nanowire junctions dominates (R. M. Mutiso et al. *ACS Nano* **2013**, *7*, 7654). (b) Illustration of the measurement setup for resistance of single nanowire and junction resistance (F. Selzer et al. *Appl. Phys. Lett.* **2016**, *108*, 163302).

The random network of AgNWs includes a lot of contact points between individual NWs where a few nm-thick PVP capping layers exist, resulting in a significant loss in electrical conductivity of overall conducting networks. To address this issue, various researches have been conducted to clearly remove the PVP residues and to weld junctions between individual NWs. Several post-treatment techniques have been proposed such as mechanical pressing,⁴⁸ plasmonic welding,⁴⁹ thermal annealing,⁵⁰ capillary-force-induced cold welding,⁵¹ and electrochemical Ostwald ripening.⁵² From the removal of PVP residues or fusion of AgNWs at the junctions, post-treatment techniques effectively enhance the overall electrical performance of random AgNW networks.

1.2.3. Alignment of AgNW networks

Despite the remarkable enhancement of electrical performance of random AgNW network-based TCEs enabled by various post-treatments, the fundamental problems are not solved due to the randomness of nanowire networks. To fundamentally address the trade-off between electrical conductivity and optical transmittance, manipulation of nanowire structures in the conductive percolation network is crucial to reduce junction resistance. Firstly, Yang group reported assembled monolayer of aligned AgNWs using Langmuir-Blodgett technique for the application in surface enhanced Raman spectroscopy substrates (Figure 1.7a).⁵³ From this technique, monolayer of aligned AgNWs can be transferred from the liquid-gas interface to large area solid supports. Previously, the capillary printing technique was introduced for the assembly of aligned AgNW network for highly conductive and transparent electrodes with low surface roughness (Figure 1.7b).³² Because the alignment of the AgNW networks significantly decreases the density of nanowire network, the electrical percolation threshold of the aligned AgNW networks is much lower than random AgNW networks. After this work, various kinds of alignment techniques have been demonstrated. The alignment technique using water-bath assisted convective assembly process at the temporary water/alcohol interface was demonstrated for fabricating hierarchical aligned AgNW networks (Figure 1.7c).⁵⁴ The horizontal-dip (H-dip) coating method was demonstrated for the oriented AgNW arrays (Figure 1.7d).⁵⁵ Here, the adjusted shear strain rate of the capillary flow in the Landau-Levich meniscus of the AgNW suspension induces the uniaxially oriented AgNW networks. Contrary to conventional spray coating method that leads to only random AgNW networks, Grazing Incidence Spraying technique allows the fabrication of aligned AgNW multilayers (Figure 1.7e).⁵⁶ The Grazing Incidence Spraying technique fabricates aligned AgNW arrays with a simple and versatile way that enables the tunable density and in-plane anisotropy. Recently, conical fibers array brushing-based liquid transfer technique was demonstrated for the fabrication of anisotropic AgNW networks (Figure 1.7f).⁵⁷ The brushing-based liquid transfer technique enables the fine control over the receding of the three-phase contact line when

the brush swept over the substrate. The layer-by-layer agitation-assisted alignment technique was introduced for the fabrication of stretchable and transparent AgNW electrodes (Figure 1.7g).⁵⁸ By simply controlling the agitation speed, duration, and the viscosity of solvent, this technique can fabricate the aligned multilayer of AgNW networks. In summary, variety of alignment techniques have been carried out for the controllable manipulation of AgNW networks enabling the improvement of optoelectronic performance of AgNW TCEs. However, there are still some drawbacks in the above methods, such as the requirement of additional processes (substrate pre-patterning, post-transfer, pre-growing of NWs), a slow evaporation, a slow coating speed, and incompatibility with large-scale development.

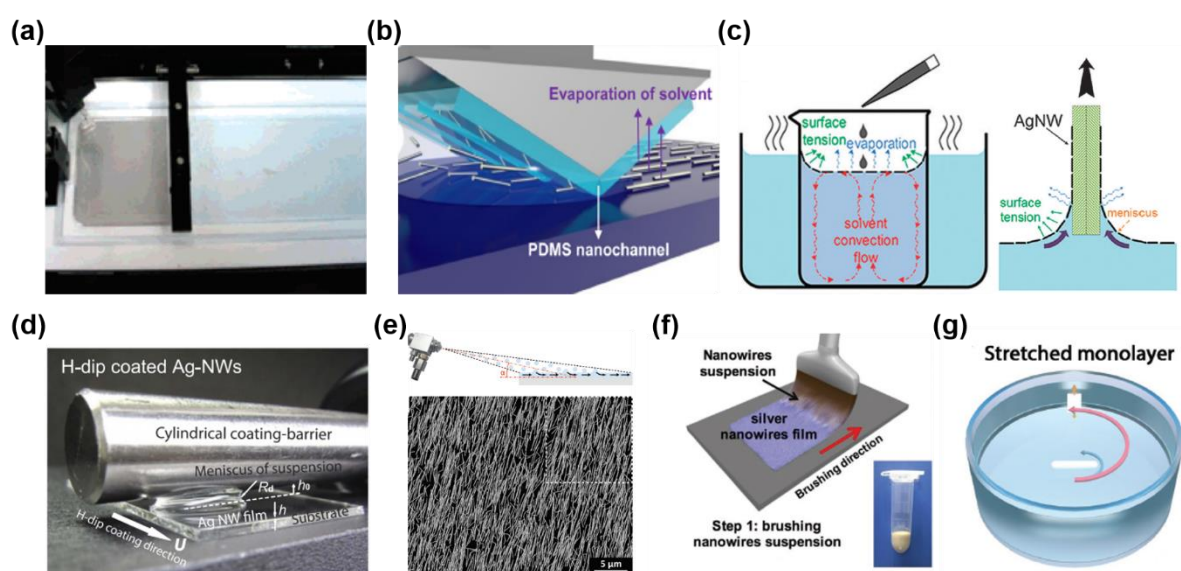


Figure 1.7. Various AgNW assembly techniques. (a) Langmuir-Blodgett assembly (A. Tao et al. *Nano Lett.* **2003**, *3*, 1229). (b) Capillary printing (S. Kang et al. *Nano Lett.* **2015**, *15*, 7933). (c) Water-bath assisted convective assembly (S.-k. Duan et al. *Phys. Chem. Chem. Phys.* **2015**, *17*, 8106). (d) H-dip coating (B. Park et al. *Sci. Rep.* **2015**, *6*, 19485) (e) Spray-assisted assembly (H. Hu et al. *Nanoscale* **2017**, *9*, 1307) (f) Conical fibers array brushing (L. Meng et al. *Adv. Mater.* **2018**, *30*, 1706938) (g) Agitation-assisted alignment (H. Hu et al. *Adv. Funct. Mater.* **2019**, *29*, 1902922).

1.3. Flexible and transparent AgNW electrodes and device applications

Over the last several years, a new platform of flexible electronics has been developed and commercialized rapidly by connecting smart devices and the internet to the people to communicate with each other. Besides, intense researches are now being conducted on flexible and transparent electronics that can be applied to the wearable forms attached to the human body or cloth. The AgNW is one of the most powerful next-generation candidate material owing to its superior electrical conductivity, optical transparency, and mechanical flexibility. Furthermore, AgNW shows high chemical stability in ambient condition and high thermal conductivity as well as mechanical strength that can be applied to the numerous flexible optoelectronic and electronic device applications including light-emitting devices, organic solar cells, displays, touch screen panels, transparent heaters, thin-film loudspeakers, microphones, strain sensors, and electronic skins. Despite the outstanding optoelectronic performance of AgNW-based TCEs, there are still some drawbacks for the successful device application such as operation stability, long-term stability, and device compatibility. Therefore, the most important thing that needs to be addressed is stable integration of AgNW-based TCEs with flexible optoelectronic and electronic devices.

1.3.1 Touch screen panels

With the development of portable smart appliances such as smart windows, smart televisions, smart phones, and tablet PCs, the demand for touch screen panels has been extensively increased and the TCEs become an essential components of touch screen panels. For flexible touch screen panel, the AgNW network is considered as promising TCEs thanks to its excellent mechanical flexibility, high optical transparency, and large-area applicability. Particularly, touch screen panels should be highly transparent due to the visibility of screens. In addition, the mechanical durability of the AgNW-based TCEs is another issue that should be addressed since touch screen panels have to be exposed to continuous physical stress. Consequently, plenty of AgNW TCE-based touch screen panels have been intensively researched.

While there are thousands of different touch screen panels on the market, most of them rely on either resistive- or capacitive-type of technology. The simplest design of a touch screen panels is a four-wire resistive-type touch sensor that is comprised of top and bottom TCEs facing each other. When the top electrode is depressed by an external force, both of electrodes meet and controller board captures the voltage change at the touch position along the *X-Y* coordination. Previously, Lee and co-workers demonstrated very long AgNW network conductors fabricated by low temperature laser nano-welding process for fabricating transparent touch screen panels (Figure 1.8a).⁶ The nano-welded very long

AgNW network electrodes showed high transparency with superior robustness. One of the most important factor of touch screen panel is the uniformity of the sheet resistance of TCEs. However, the uniformity of conventional AgNW networks are not comparable to that of ITO films. To address this issue, dynamic heating method based on infrared light was reported for the uniform sheet resistance (Figure 1.8b).⁵⁹ By overcoming the coffee ring effect during the drying process with dynamic heated method, highly uniform AgNW TCEs are fabricated for the realization of uniform touch screen panels with excellent stability. For the fabrication highly transparent and precise touch screen panels, Jang and co-workers reported high-performance TCE films using a silver grid (Ag grid)/AgNW hybrid structure (Ag/NW-GFRHybrimer) (Figure 1.8c).⁶⁰ The fabricated Ag/NW-GFRHybrimer shows good optoelectronic performance (R_s of $13 \Omega \text{ sq}^{-1}$ at 87%) with superior thermal, chemical, and mechanical stability, enabling the four-wire resistive-type touch screen panel with stable operation. Recently, a healable touch screen panel was demonstrated using healable and flexible AgNW electrodes (Figure 1.8d).⁶¹ The fabricated four-wire resistive-type touch screen panels with healable ability shows good touch accuracy with outstanding performance recovery after healing process.

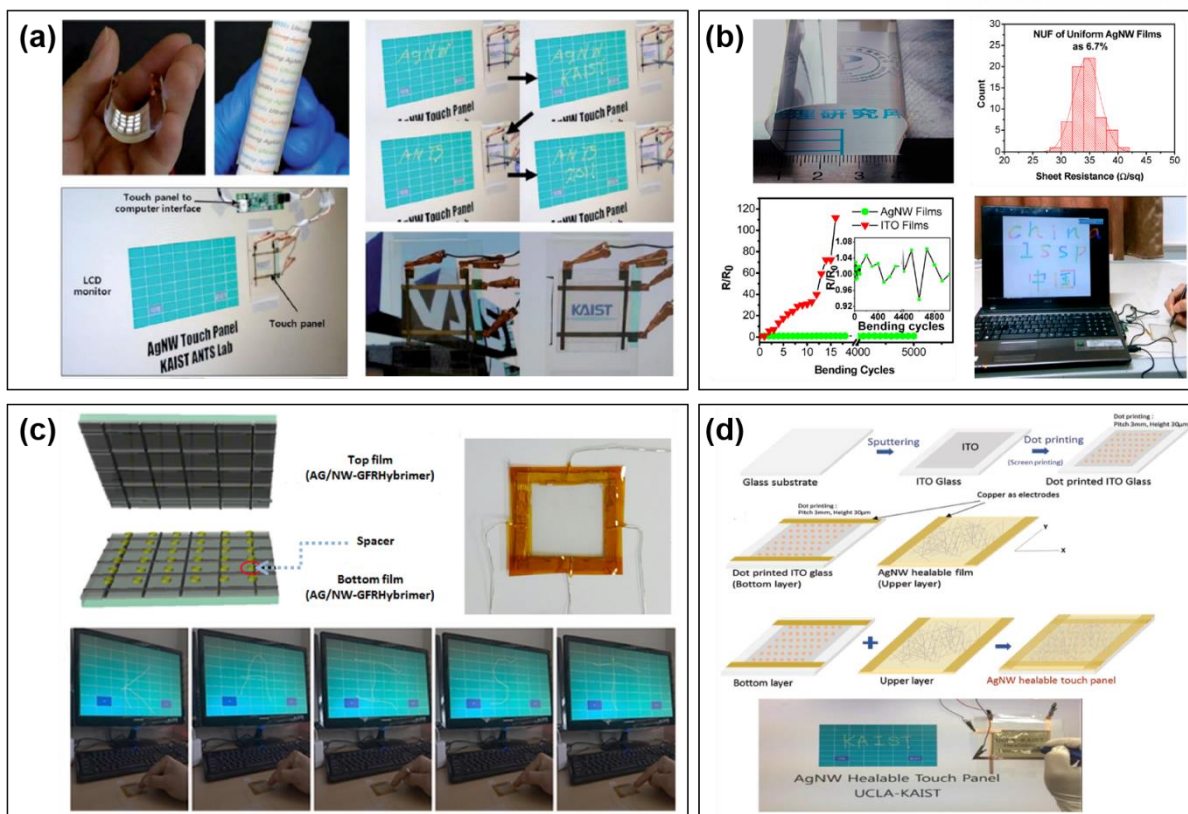


Figure 1.8. Resistive-type touch screen panel applications using the AgNW networks. (a) Demonstration of applying a very long AgNW transparent conductor for a touch screen panel (J. Lee et al. *Nanoscale* **2012**, *4*, 6408). (b) Demonstration for exact writing input using the uniform AgNW TCE-based flexible touch screen panel (Y. Jia et al. *ACS Appl. Mater. Interfaces* **2016**, *8*, 9865). (c) Demonstration of touch screen panel using the Ag/NW-GFRHybrimer films (J. Jang et al. *ACS Appl. Mater. Interfaces* **2016**, *8*, 27035). (d) Demonstration of healable touch screen panel using AgNW healable conductor on the LCD monitor (J.-S. Bae et al. *Adv. Mater. Technol.* **2018**, *3*, 1700364).

Compared to the resistive-type touch screen panels, a capacitive-type captures the pressure point by measuring the capacitance change. The capacitive-type touch screen panel is generally preferred over resistive because less pressure is required for the touch sensing via the human body's electrical current. Another advantage of capacitive-type touch screen panel is good stability compared to the resistive-type. Moreover, capacitive-type touch screen panel provides higher quality of visibility than resistive-type for the application in the smart displays. However, the fabrication process of capacitive-type touch screen panel is so complicated that requires the fine patterning of a TCEs for the high touch sensing accuracy. The first AgNW-based capacitive-type touch screen panel was reported using spray coated random AgNW electrodes (Figure 1.9a).⁶² The fabricated capacitive-type touch screen panel detects the capacitance change in four different positions without any response of the touch

during concave or convex flexions. For the fine patterning of AgNW networks, a laser ablation method is used for line patterning ranging from 5 to 50 μm for fabricating capacitive touch screen panels (Figure 1.9b).⁶³ The diamond shaped capacitive touch screen panel composed of 2×2 pixels successfully detects the capacitance change upon finger touching. For the wearable multifunctional sensors, capacitive-type touch screen sensor composed of screen-printed AgNW electrode and Ecoflex as a dielectric was demonstrated (Figure 1.9c).⁶⁴ This capacitive-type touch screen sensor can differentiate the two different kinds of touch modes such as proximity mode (no pressure) and pressing mode (with pressure) by measuring capacitance change upon finger movements. The stretchable capacitive-type AgNW-based touch screen panel was also demonstrated (Figure 1.9d).⁶⁵ Here, the AgNW networks adhere permanently to the surface of PDMS with the sigma-donating ability and hydrophilicity of silane modified surfaces, resulting in a fabrication of robust and stable device applications. To recover the surface damage, healable capacitive touch screen sensor based on transparent composite electrodes consisting of AgNW and healable Diels-Alder cycloaddition copolymer was fabricated (Figure 1.9e).⁶⁶ The healable touch screen sensor comprised of 8×8 pixels shows touch sensing performance before the cutting by a razor blade and after the healing processes at 80 $^{\circ}\text{C}$ for 30 s. Recently, stretchable and transparent touch screen sensors based on capacitive-type with 5×5 pixels was demonstrated with a simple structure of two AgNW/reduced GO (rGO) electrodes and polyurethane (PU) dielectric layer in between them (Figure 1.9f).⁶⁷ Thanks to the strain-insensitivity of patterned AgNWs/rGO lines embedded in PU dielectrics on PDMS, the fabricated touch screen sensor shows touch sensing ability in accordance with capacitance change. A variety of developed capacitive-type touch screen panels are applicable to future wearable and human-machine interface applications with conformability and good mechanical robustness.

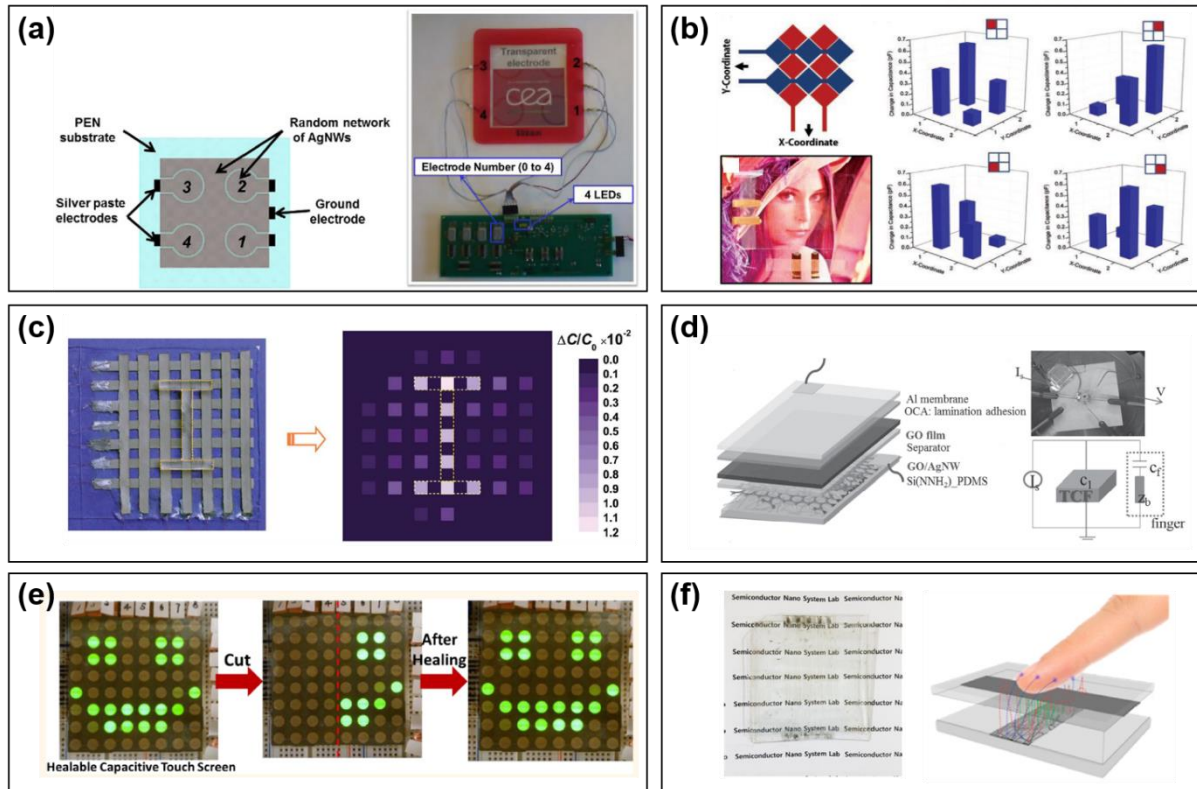


Figure 1.9. Capacitive-type touch screen panel applications using the AgNW networks. (a) Spray coated flexible AgNW electrode-based capacitive touch screen panel (C. Mayousse et al. *Nanotechnology* **2013**, *24*, 215501). (b) Capacitive touch screen panel with diamond patterns fabricated by selective laser ablation of AgNW percolation networks (S. Hong et al. *J. Nanosci. Nanotechnol.* **2015**, *15*, 2317). (c) Screen printed AgNW TCE-based capacitive touch screen panel (S. Yao & Y. Zhu *Nanoscale* **2014**, *6*, 2345). (d) Capacitive AgNW PDMS touch screen panel (H. Lee et al. *Adv. Funct. Mater.* **2014**, *24*, 3276). (e) Healable transparent capacitive touch screen panel based on healable AgNW-polymer composite electrodes (J. Li et al. *ACS Nano* **2014**, *8*, 12874). (f) Transparent and stretch-unresponsive capacitive touch screen panel with selectively patterned AgNW/rGO electrodes (T. Y. Choi et al. *ACS Appl. Mater. Interfaces* **2017**, *9*, 18022).

1.3.2 Flexible loudspeakers

With the recent advance of the fourth industrial revolution, the human-machine interfaces have attracted great attention with the rapid expansion of IoTs applications. Thus, the quality of acoustic environment performs important role in our daily lives. Accordingly, variety of researches on flexible and wearable acoustic devices have been actively conducted to replace conventional rigid, heavy, and low power efficient loudspeakers. However, due to the lack of operation stability and limitations in acoustic performance of flexible acoustic technologies, the devices are hard to be utilized in practical appliance. The material, structure, and sound-emission mechanism of devices should be designed carefully for the future wearable and skin-attachable acoustic devices. In this regard, the AgNW-based loudspeakers with different types of working mechanisms have been reported including piezoelectric⁶⁸ and thermoacoustic.^{69, 70}

Previously, piezoelectric thin film loudspeaker composed of poly(vinylidene fluoride) PVDF layer and graphene/AgNW hybrid TCEs was demonstrated (Figure 1.10a).⁶⁸ The audio frequency vibration of the PVDF thin film generates sound with the application of electric field to the TCEs. The fabricated acoustic device is highly transparent and flexible thanks to the excellent optoelectronic performance (R_s of $16 \Omega \text{ sq}^{-1}$ at T of 91.1%) and mechanical strength of graphene/AgNW hybrid TCEs. In addition to piezoelectric type, thermoacoustic sound-emitting devices have been introduced as a new type of speaker that generates sound via the Joule heating of conducting films and sequential temperature oscillation of the surrounding vibrating medium (Figure 1.10b,c). Compared to the typical speakers with complicated structure that need diaphragm for the mechanical vibration, thermoacoustic loudspeakers can be fabricated into very thin-film structure that produces sound without mechanical vibration. The conducting thin films based on the graphene and CNTs have been widely used for the thermoacoustic loudspeaker due to promising optoelectronic and mechanical properties of graphene and CNT-based TCEs, however, their electrical and optical performance are still not enough.^{71, 72} The thermoacoustic loudspeakers with highly transparent and conductive random AgNW networks were reported with low driven voltage.^{69, 70} The sound emission from the random AgNW networks show wide range of frequency responses between 15 and 45 kHz that matched well with theoretical results. Besides, AgNW-based thermoacoustic loudspeakers are easily fabricated into flexible and large-scale devices, enabling the integration with future soft acoustic-display electronic applications.

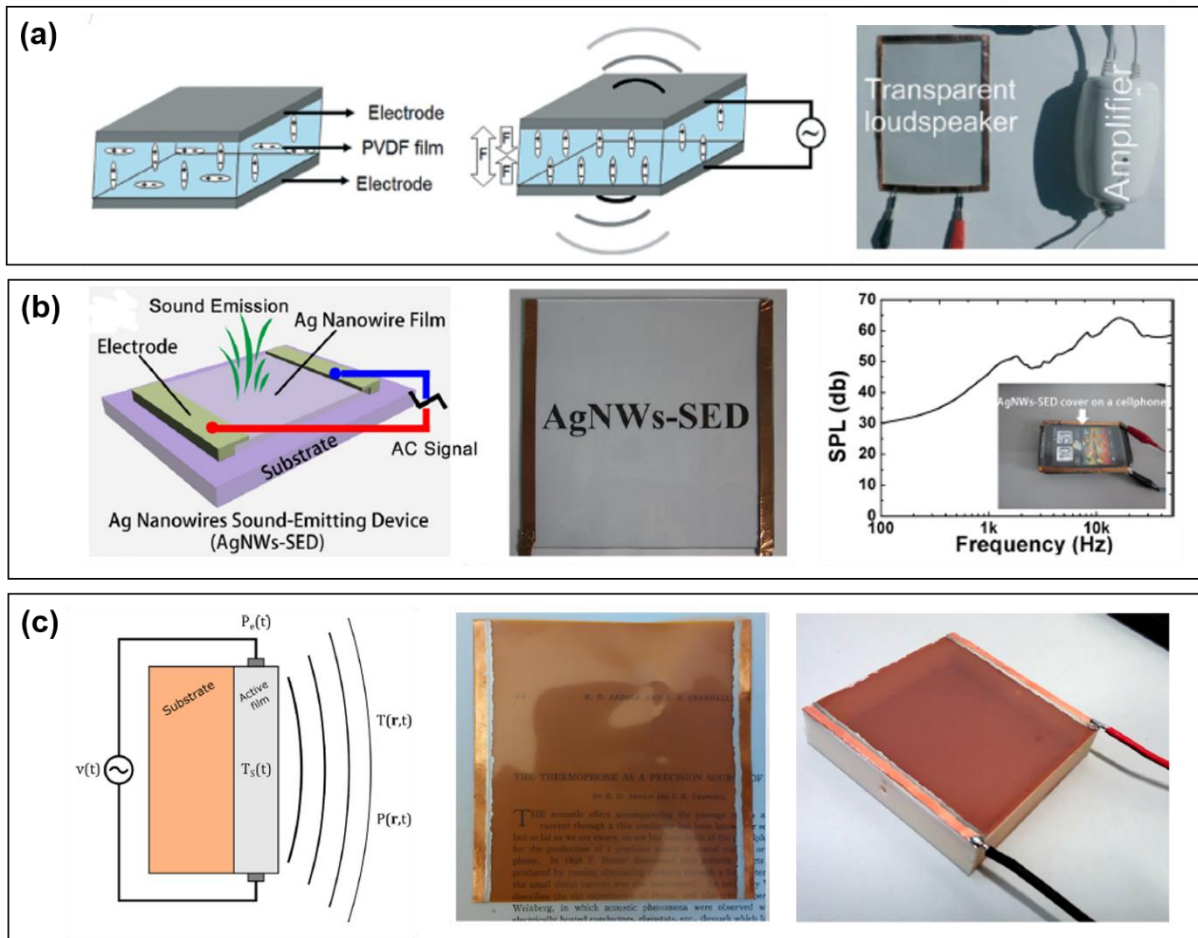


Figure 1.10. Various flexible loudspeakers using the AgNW networks. (a) The acoustic device consists of transparent graphene/AgNW TCEs and PVDF piezoelectric layer (S. Xu et al. *CrystEngComm* **2014**, *16*, 3532). (b) Flexible and transparent sound-emitting devices using AgNW electrodes (H. Tian et al. *Appl. Phys. Lett.* **2011**, *99*, 253507). (c) The thermoacoustic loudspeaker made of AgNW random networks on a polyimide substrate (P. L. Torraca et al. *J. Appl. Phys.* **2017**, *121*, 214502).

1.3.3 Acoustic sensors

Latest researches are mainly focused on the development of user-interactive devices related to the touch and vision which are the most important human sense enabling the future human-machine interface technologies. Furthermore, the use of acoustic sense is the most valuable and efficient bio-signal for communication and can provide more immediate and straightforward responses for connecting human beings and objects. In past years, the development of flexible and skin-attachable acoustic sensors or microphones that can precisely detect human voice has been intensively conducted in accordance with the growing interest in wearable telecommunication and human-machine interface devices with IoT applications such as electronic skins, intelligent mobile robots, smart hearing aids, remote control systems, and home automations. Recent researches have been based on the development of flexible and skin-attachable acoustic sensors that detect human voices by measuring the vibration of user's neck. The different types of working mechanisms for precise and accurate acoustic sensing have been utilized such as piezoelectric,⁷³ triboelectric,^{74, 75} piezoresistive,⁷ ferroelectric,⁷⁶ and piezocapacitive sensors.⁷⁷ For people who suffer from hearing loss by damage in the hair cells in the cochlea, biomimetic artificial cochlea was demonstrated using a $\text{Pb}[\text{Zr}_x\text{Ti}_{1-x}]\text{O}_3$ (PZT) inorganic piezoelectric material for acoustic nanosensor.⁷³ A laser lift-offed PZT film is transferred to the flexible plastic substrate and can detect vibration displacement of the silicone-based membrane with piezoelectric signals. As a result, nanosensor detects frequency in the range of 100 Hz to 1600 Hz with high sensitivity. Recently, triboelectric nanogenerator has attracted enormous attention for the application of self-powered devices. The self-powered acoustic sensors based on the triboelectricity were reported for artificial basilar membrane and robotic hearing aids.^{74, 75} With simple structure of triboelectric sensors carried out by triboelectrification from contact-induced electrification between two opposite layers, high sensitivity and broad-wide frequency response are achieved with the reduced power consumption. The intelligent artificial throat that detects sound stimulus was fabricated using laser induced graphene, enabling the integration of functions: generating and detecting sound in a single device.⁷ The fabricated acoustic transducer functions as sound source with thermoacoustic and sound detector with piezoresistive properties that can be used in a range of 100 Hz to 40 kHz. The ferroelectric-based thin film loudspeaker and microphone were also introduced for self-powered flexible electronic devices.⁷⁶ The acoustic transducer prepared by polypropylene film containing silicate particles with sputtered Ag film can generate and detect sound with a large range of frequency (10 Hz to 20 kHz) with high mechanical flexibility. For enhanced sensitivity of acoustic sensor, flexible and skin-attachable voice-recognition device having a hole-patterned diaphragm structure was demonstrated.⁷⁷ This piezocapacitive device shows outstanding sensitivity of 5.5 V Pa^{-1} and precise voice recognition over the voice frequency range due to the high skin conformity, facilitating the voice-security applications.

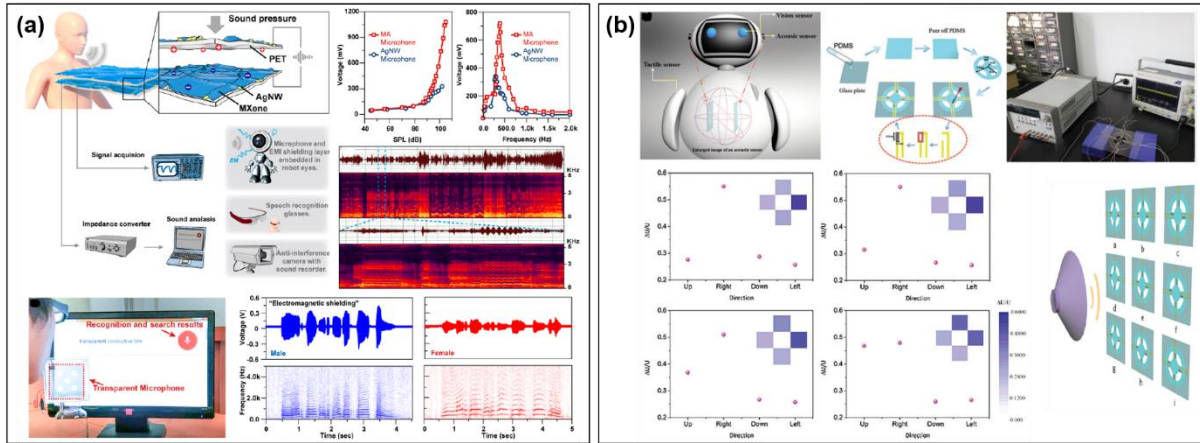


Figure 1.11. Acoustic sensors using the AgNW networks. (a) Self-powered microphone assembled with MXene/AgNW hybrid electrodes (W. Chen et al. *ACS Nano* **2020**, DOI: 10.1021/acsnano.0c01635). (b) Flexible acoustic sensor using AgNW/PDMS film with mass block-beam structure (Q. Zhang et al. *Soft Robot.* **2020**, DOI: 10.1089/soro.2020.0030).

The requirements of flexible next-generation acoustic sensors include high sensitivity, accuracy, skin-conformity, and mechanical robustness. Especially, wearable devices prefer more transparent feature that enables the watching of underneath surface of devices. Due to the strong mechanical strength as well as high electrical and optical properties, AgNW networks are applied to the highly transparent and flexible acoustic sensors with high sensitivity. Recently, transparent and flexible microphone using hybrid conducting film of transition metal carbide/carbonitride (MXene) and AgNW was demonstrated for electromagnetic interference shielding and sound pressure sensing (Figure 1.11a).⁷⁸ Here, the layer structured hybrid film of MXene-AgNW conducting film and PET substrate is constructed for triboelectric sensor to detect sound pressure. The fabricated microphone is successfully used for voice recognition that can differentiate the voice between male and female subjects when it is attached on the monitor without obstruction of vision information because of high transparency. In addition, flexible and localized acoustic sensor array using AgNWs coated on a thin PDMS film with mass block-beam structure was reported (Figure 1.11b).⁷⁹ The resistive dynamic response of AgNWs can detect the vibration of sound pressure with frequency, volume, speech recognition, and distance in the sound field. Furthermore, 2D and 3D sound source can be detected from the mass block-beam structure of the flexible acoustic sensor. The acoustic sensor can detect sound frequency in the range of 20 Hz to 2,000 Hz and a volume detection range of 83 dB to 108 dB. The development of flexible acoustic sensor using AgNW/PDMS electrodes provide a new platform for future soft acoustic sensing and voice recognition devices.

1.4 Stretchable and transparent AgNW electrodes and device applications

The evolution of technology has produced the remarkably enhanced flexible electronics that is far beyond the conventional, rigid, and bulky electronic devices. Accordingly, our daily life has become more convenient than before because of the development of various flexible electronic and optoelectronic devices including commercially available flexible smart appliances, wearable displays, bio-electronic devices, human-machine interfaces, and implantable medical devices, etc.

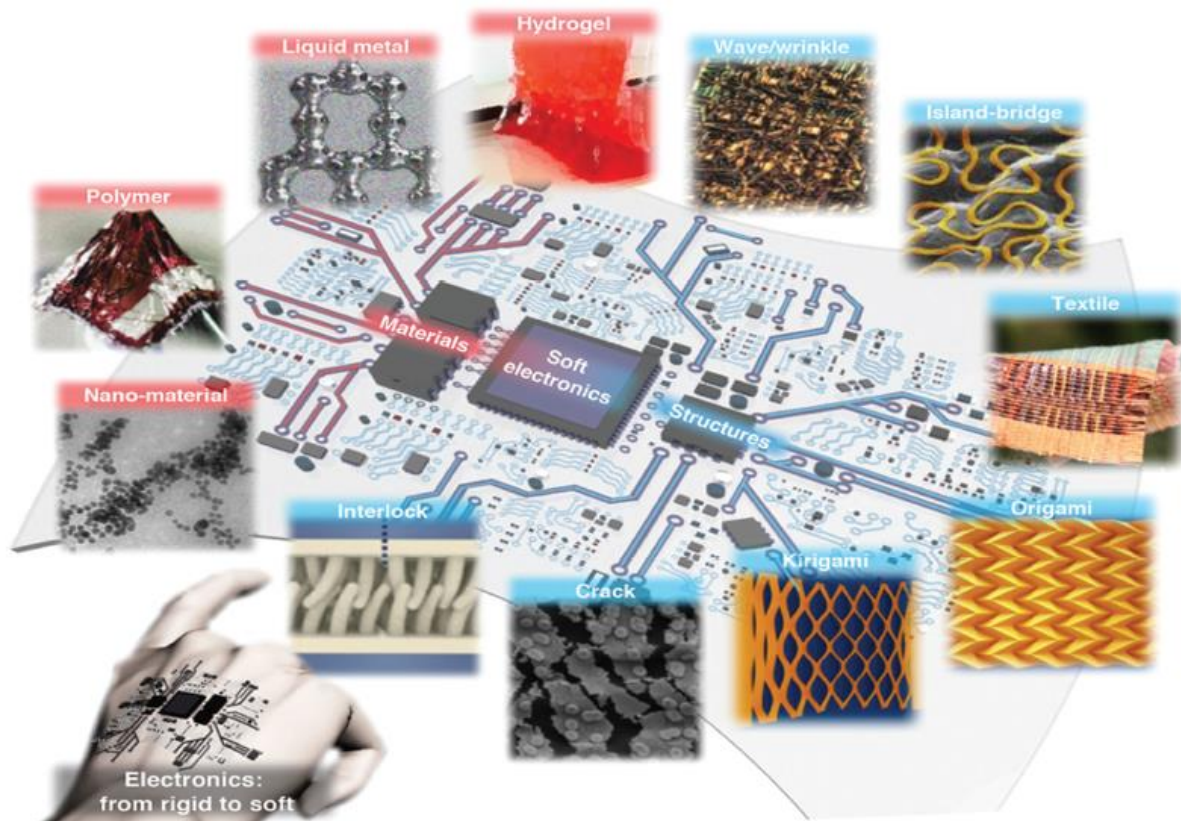


Figure 1.12. Two representative strategies can be applied to realize soft electronics. The materials innovation, by developing novel materials that are intrinsically stretchable; structural design, by making nonstretchable materials into specific structures that absorbs externally applied strain without fracturing (C. Wang et al. *Adv. Mater.* **2018**, *30*, 1801368). Hydrogel (H. Yuk et al. *Nat. Mater.* **2016**, *15*, 190). Liquid metal (C. Ladd et al. *Adv. Mater.* **2013**, *25*, 5081). Polymer (M. Kaltenbrunner et al. *Nat. Commun.* **2012**, *3*, 770). Nanomaterial (Y. Kim et al. *Nature* **2013**, *500*, 59.). Interlock (C. Pang et al. *Nat. Mater.* **2012**, *11*, 795). Crack (Z. Liu et al. *ACS Appl. Mater. Interfaces* **2014**, *6*, 13487). Kirigami (S. J. P. Callens and A. A. Zadpoor *Mater. Today* **2018**, *21*, 241). Origami (S. J. P. Callens and A. A. Zadpoor *Mater. Today* **2018**, *21*, 241). Textile (J. Chen et al. *Nat. Energy* **2016**, *1*, 16138). Serpentine (J. A. Fan et al. *Nat. Commun.* **2014**, *5*, 3266). Wave/wrinkle (D.-H. Kim et al. *Science* **2008**, *320*, 507).

However, the developed flexible technologies are not suitable for future soft electronic and optoelectronic device applications due to the lack of stretchability and conformability of flexible substrates, suffering from the imperfect integration between device and nonplanar surfaces such as cloth or human body. Therefore, stretchable electronics has been intensively researched with the recent developments in materials science and engineering to replace flexible electronics. Meanwhile, the high transparency of stretchable devices is also an important factor for invisible integration of devices into target devices. The transparent and stretchable electronic devices can be used in new applications such as transparent and stretchable transistors, displays, sensors, and medical devices where the high level of optical transparency and high stretchability are simultaneously required for the enhancement of device conformity on the human body or nonplanar surfaces with the maintenance of visibility. However, compared to the tremendous development of flexible and transparent electronics, the development of new soft electronics having high transparency and stretchability simultaneously is still significantly challenging.

To achieve the transparent and stretchable electronics, two major approaches have been researched: i) development of intrinsically transparent and stretchable materials; ii) structural engineering of transparent and stretchable substrates (Figure 1.12).⁸⁰ Nowadays, the former approach can be realized by developing intrinsically stretchable conducting building blocks, such as hydrogels, liquid metals, conducting polymers, and conducting nanomaterials for the material approach. Although these materials are highly stretchable, low optical transparency of liquid metal, instability and low conductivity of conducting polymer, and incompatibility of hydrogel materials with dry condition limit further applications in soft optoelectronic and electronic devices. Among them, conducting nanomaterials-based percolation networks including nanoparticles, nanowires, nanotubes, and nanosheets can successfully achieve transparent and stretchable electronics with high optical transparency, electrical conductivity, and stable compatibility with soft optoelectronic and electronic devices. By integrating conducting nanomaterials with elastomers, highly transparent and conducting stretchable electrodes can be fabricated. In the last decade, AgNW-based conducting percolation networks on the transparent elastic substrate are reported for the fabrication of highly stretchable and transparent electrodes (Figure 1.13). Hu and co-workers synthesized intrinsically stretchable and transparent electrodes based on AgNW networks embedded in the surface of a crosslinked polyacrylate composite matrix. The interpenetrating AgNW networks on the surface of in situ polymerized polyacrylate matrix provide high optoelectronic property ($50.1 \Omega \text{ sq}^{-1}$ at 92.4%), surface smoothness, and elasticity (Figure 1.13a).⁸¹ The sheet resistance of electrode increases by 2.3 times at 50% tensile strain with good repeatability over 600 cycles.

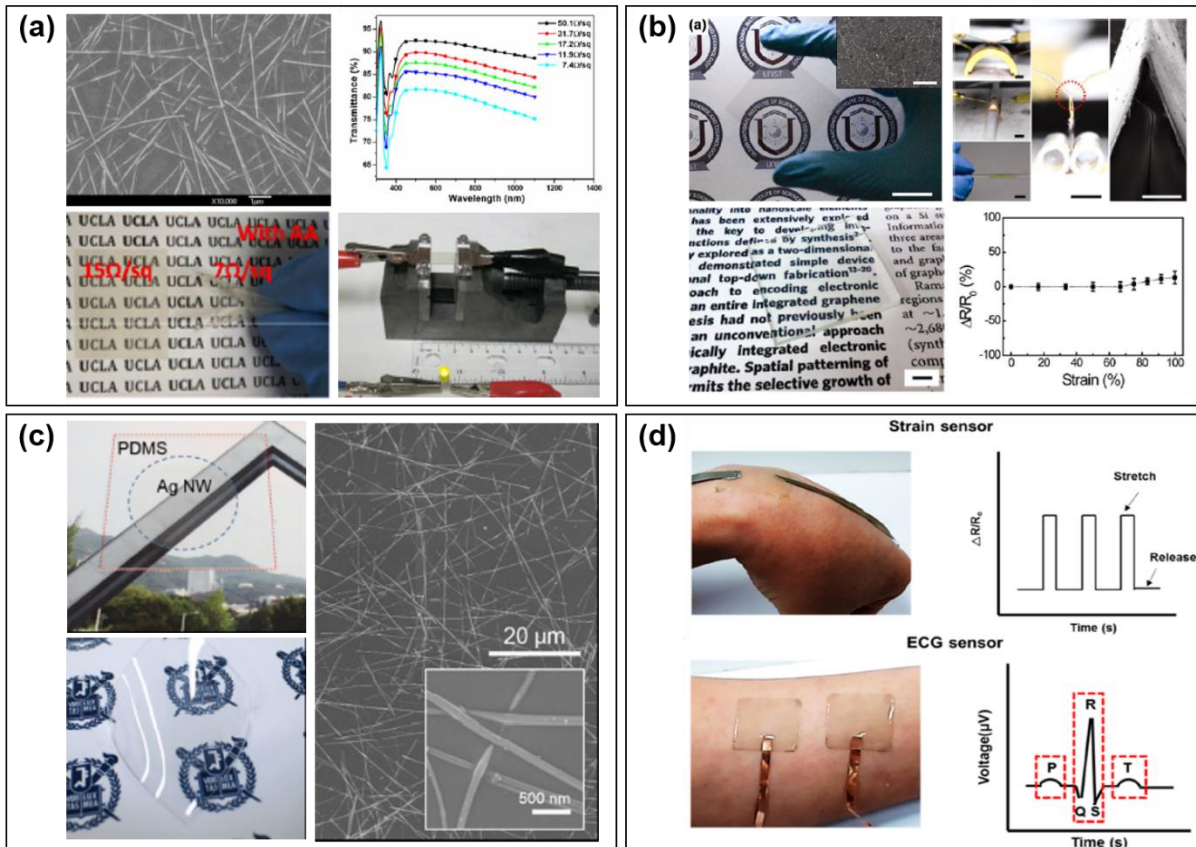


Figure 1.13. Transparent and stretchable electrodes using AgNW-based conducting networks. (a) Stretchable and transparent electrodes based on AgNW-crosslinked-polyacrylate composites (W. Hu et al. *Nanotechnology* **2012**, *23*, 344002). (b) Stretchable and transparent electrodes using graphene-AgNW hybrid structures (M.-S. Lee et al. *Nano Lett.* **2013**, *13*, 2814). (c) Stretchable and transparent AgNW/PDMS electrode (S. Hong et al. *Adv. Mater.* **2015**, *27*, 4744). (d) Stretchable, transparent, and adhesive AgNW electrodes (J.-H. Kim et al. *Nano Lett.* **2018**, *18*, 4531).

The stretchable and transparent electrodes based on graphene-AgNW hybrid structures on the PDMS have been also demonstrated (Figure 1.13b).⁸² With the addition of graphene in the AgNW percolation network, conducting percolation threshold can be improved by providing additional conductive pathways through defects of polycrystalline graphene in the hybrid networks. In addition, the AgNW/graphene hybrid structure improves the robustness of conducting networks. The hybrid electrode shows R_s of $\sim 33 \Omega \text{ sq}^{-1}$ at a transmittance of 94% with the thermal oxidation resistance property (85% in humidity, 85°C, 240 h) and high stretchability (tensile strain of 100%). The highly transparent and stretchable electrodes based on partially embedded AgNW percolation network on PDMS film was also demonstrated for the application of wearable transparent heaters (Figure 1.13c).⁸³

The vacuum filtration transfer method is applied for the fabrication of uniformly coated random AgNW networks on the PDMS substrate. The AgNW/PDMS electrode operates under strain over 60% with small resistance change. Besides, the AgNW/PDMS electrodes exhibits excellent optoelectronic performance ($T > 85\%$ at R_s of $30 \Omega \text{ sq}^{-1}$). Recently, highly conformable, transparent, and stretchable electrode based on AgNW networks embedded in the adhesive PDMS matrix was presented for the epidermal electronics application.⁸⁴ With the addition of nonionic surfactant Triton-X in the PDMS, adhesive PDMS matrix was fabricated by inhibiting the cross-linking reaction of PDMS. The adhesive electrodes have a loss in optical transparency due to the addition of Triton-X, however, mechanical properties and conformability of the electrodes significantly improved that can be utilized in various biosignal sensors.

The latter approach is based on the structural design by transforming flat substrate into specific structures that can relieve the applied stress from external strain. For structural engineering, wave/wrinkle, serpentine, textile, origami, kirigami, crack, and interlock structures have been demonstrated that absorbs strains under large mechanical deformation (Figure 1.12). However, some of structural engineering approaches have limitations in achieving high optical transparency with stretchability. The materials used in serpentine, textile, origami, kirigami, and interlock structures are not optically transparent. Besides, coverage of conducting materials in these structures is very low, restricting the actual area available for the deposition of active layer. Among them, wavy/wrinkle structures fabricated by pre-strain method have advantages over the other approaches due to the high efficiency with high surface coverage when it is applied to the optoelectronic and electronic devices. However, the wavy/wrinkled surface still suffer from the low optical transparency arose from the light scattering on the nonplanar surfaces. Therefore, the overcoming a trade-off between stretchability and optical transparency in transparent and stretchable electrodes has not yet been achieved.

1.4.1 Electroluminescence

Stretchable alternating-current electroluminescent (ACEL) devices are a new form of deformable electronics that are believed to be one of the most promising technologies for next-generation display and lighting applications. With the development of highly transparent and stretchable electrodes, the stretchable ACEL devices have been reported that can withstand large mechanical deformations such as bending, twisting, stretching, and folding. The stretchable ACEL devices also can be successfully applied to the soft and wearable electronics with excellent conformability on the arbitrary curvilinear surfaces. In accordance with recent progresses in the stretchable ACEL devices, the wide applications including bio-medical devices, photosensitive vision sensors, interactive displays, electronic skins, and robotics have been intensively researched. However, the degree of stretchability is still not enough to satisfy the high demand on mechanical requirements of stretchable ACEL devices. Thus, the development of transparent and stretchable electrodes having high stretchability and stability is still required.

Compared to the light-emitting diodes consist of *p*-type and *n*-type layer with the complex structure of *p-n* junction at the interface, the ACEL devices have simple structure with a single emissive layer composed of dielectric and phosphors sandwiched between top and bottom electrodes without the specific requirements for energy band matching that facilitates their easy application in cost effective, large-scale, flexible, and stretchable displays. Besides, capability of frequent overturning of the applied electric field results in an exclusion of the charge accumulation. The operation mechanism of ACEL devices are based on the field-induced impact excitation of electrons for light emission. The injected charge in the phosphor layers are accelerated under high applied electric field, resulting in the impact excitation of the luminescent centers by high-energy electrons (hot electrons) and radiative relaxation of the luminescent centers in the phosphors.

The most widely used phosphor materials for the ACEL device are ZnS doped with different impurities such as Cu, Al, and Mn for different color emissions. The integration of phosphors with elastomeric dielectric materials and stretchable AgNW electrodes facilitates the fabrication of deformable EL devices that can bring a plethora of new technologies of smart displays in a near future. However, the high operating voltage and low efficiency of the ACEL devices still limit the use of the ACEL device as the wearable and soft electronic devices. Recently, Wang and co-workers developed stretchable and self-deformable ACEL devices fabricated with simple all-solution processable method (Figure 1.14a).⁸⁵ The spray-coated AgNW/PDMS stretchable electrodes and ZnS:Cu microparticles are used for the fabrication of stretchable ACEL devices. The stretchable ACEL device shows good mechanical compliance with a sustained performance under tensile strain up to 100% due to the well-

maintained electrical conductivity from AgNW networks. In addition, fabricated ACEL device is used as self-deformable dielectric elastomer actuators (DEAs) showing the dynamic shape variable display. The soft ACEL device achieved area strain of 55% at the actuation voltage of 5 kV. After that, the stretchable ACEL devices with waterproof function was demonstrated (Figure 1.14b).⁸⁶ The ACEL devices consist of stretchable conductor that comprises AgNW on the PDMS substrate covered by polyurethane urea (PUU) film. Here, the strong hydrogen bonds between hydroxylated PDMS and PUU enable the water-resistance, mechanically stable, and stretchable device applications. The fabricated device can be elongated up to tensile strain of 150% and can work in the water over 30 min. Nowadays, high-*k* materials are introduced to improve the device efficiency by decreasing the working voltage of ACEL devices. The stretchable ACEL devices composed of top and bottom AgNW electrodes and the active layer with ZnS:Cu EL microparticles and barium titanate (BaTiO₃) high-*k* material are reported (Figure 1.14c).⁸⁷ The emissive matrix with high dielectric constant will focus the electric field to the phosphor microparticles, resulting in the enhanced light emission upon same applied voltages. The fabricated EL-BaTiO₃-PDMS device shows much higher luminance of ~121 cd m⁻² compared to the EL-PDMS device which shows luminance of ~16 cd m⁻² at the same driven voltage and frequency of 250 V and 2.2 kHz. Further, the stretchable and foldable seven-segment display was demonstrated that can be used under indoor lighting conditions. More recently, bright stretchable EL devices based on AgNW electrode and high-*k* thermoplastic elastomer were fabricated for enhancing working efficiency (Figure 1.14d).⁸⁸ Here, the EL device comprises the AgNW network embedded in high-*k* thermoplastic polyurethane (TPU) elastomer and phosphor EL layer with high-*k* dielectric matrix of e-poly-((vinylidene fluoride)-hexafluoropropylene) (e-PVDF-HFP). The dielectric constant of e-PVDF-HFP is above 10 over the wide range of frequencies. The ACEL device with e-PVDF-HFP shows 192 cd m⁻² with a drive voltage of 180 V and 2 kHz square wave. The development of AC-driven EL devices have provided the new perspectives for the realization of smart lighting and display technologies due to the simple structure and direct integration with AC power sources. Despite the remarkable progress in lowering the driving voltage and enhancing luminance, the stable and durable stretchable ACEL devices with extremely low power consumption should be researched for the future wearable and portable soft optoelectronic and electronic display applications.

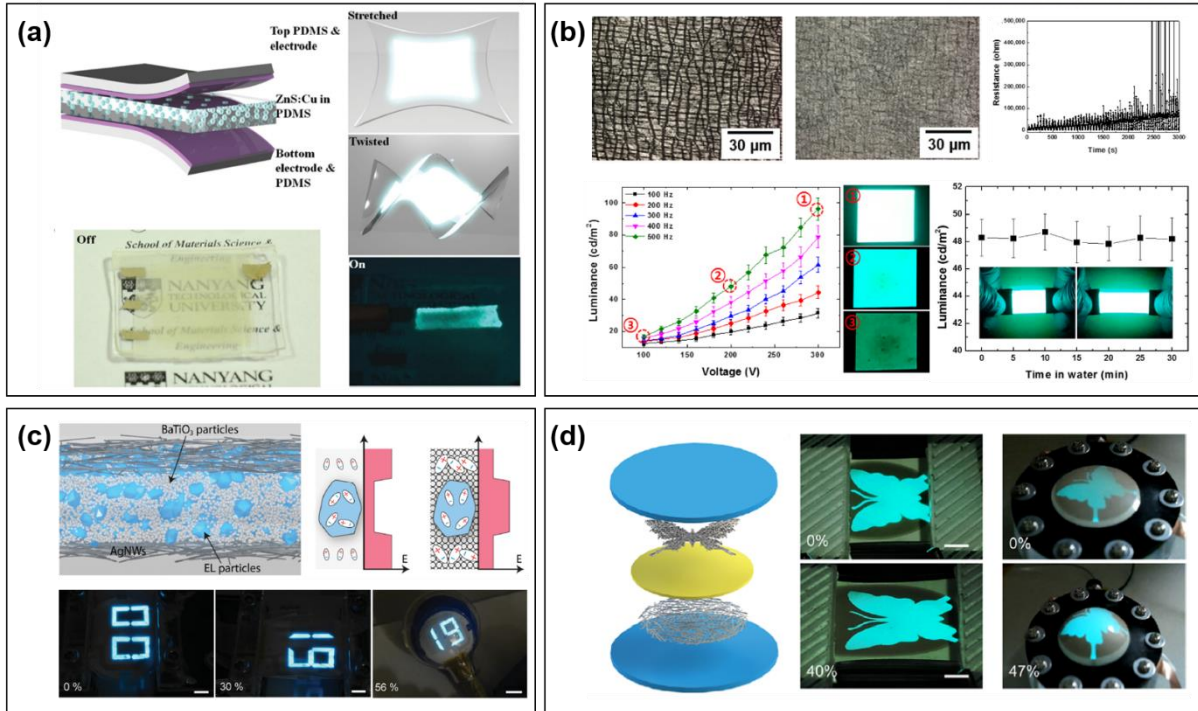


Figure 1.14. Stretchable ACEL devices based on AgNW electrodes. (a) Stretchable and self-deformable ACEL devices (J. Wang et al. *Adv. Mater.* **2015**, *27*, 2876). (b) Stretchable and waterproof EL devices (B. You et al. *ACS Appl. Mater. Interfaces* **2017**, *9*, 5486). (c) Bright stretchable ACEL devices based on high permittivity composites (F. Stauffer and K. Tybrandt *Adv. Mater.* **2016**, *28*, 7200). (d) Bright stretchable EL devices based on AgNW electrodes and high- k thermoplastic elastomers (Y. Zhou et al. *ACS Appl. Mater. Interfaces* **2018**, *10*, 44760).

1.5 Challenges of current flexible/stretchable transparent electrodes

In the introduction, we reviewed recent progress that has been made in recent years in the field of soft optoelectronic and electronic devices based on 1D conducting nanomaterials. Among the various next-generation conducting nanomaterials, the AgNWs are the most promising material for the fabrication of highly flexible/stretchable and transparent electrodes because of its superior optoelectronic properties and easy handling via solution-based coating methods. Despite the many advantages of the AgNWs, there are still limitations for the use of randomly oriented AgNW networks in the soft optoelectronic and electronic device applications, which are the high junction resistance, low uniformity, and low adhesion of random AgNW networks.

First, the conventional coating methods result in the random structure of AgNW networks and the large loss in the optical transparency and electrical conductivity of the random AgNW networks is inevitable because of the presence of many junction points between individual NWs surrounded by electrically insulating few nm-thick PVP capping layers.⁴⁶ Consequently, the large loss in trade-off relation between optical and electrical conductivity is expected in the formation of random AgNW networks. To overcome the junction resistance issue, diverse approaches including mechanical pressing,⁴⁸ plasmonic welding,⁴⁹ thermal annealing,⁵⁰ capillary-force-induced cold welding,⁵¹ and electrochemical Ostwald ripening⁵² have been suggested; however, these additional processes complicate the fabrication process and cannot solve the fundamental matter originated from the random structure of AgNW networks. In addition, most of conventional coating methods are hard to fabricate the large-area AgNW films with high uniformity due to the lack of scalability.

Second, the low adhesion of AgNW networks to the flexible/stretchable substrates is the critical problem that should be solved to develop stable and robust soft optoelectronic and electronic devices based on the transparent AgNW electrodes. There have been various approaches to enhance the adhesion of the AgNW networks on the surface of soft substrates including chemical^{89, 90} or physical approaches.^{91, 92} The chemical approaches that utilize the coating of the adhesion promoters on the surface of soft substrates can enhance the adhesion force between substrates and AgNWs with electrostatic force. Besides, the physical approaches, such as semi-embedding or perfect-embedding of NWs on the surface of substrate can significantly enhance the adhesion between substrates and AgNWs by burying the NWs on the surface of substrate. However, the chemical approaches are hard to provide enough adhesion force compared to the physical approaches. Whereas, physical approaches are cannot be applied to the large-scale fabrications due to the need of additional transfer processes.

Third, the development of wearable or skin-attachable optoelectronic and electronic devices is necessary with the growing demand for user-interactive, smart, and human-machine interface devices,

which can maximize the user experience. Accordingly, integration of diverse functions (e.g., speakers, sensors, actuators, and cameras) into the single device is important for the future technologies. Previously, most of researches already have been carried out to fabricate interactive displays with integrated with tactile sensors visualizing the physical stimulus,^{7, 10} by stimulating the human sense of vision to achieve their intuitive and instant perception. However, prior researches are mostly focused on the only visualization of mechanical stimulus for tactile display and human-machine interfaces, leaving the room for the development of visualization of acoustics underexplored. Some research groups have developed sound-in-display electronics that generates sound and vision information simultaneously; however, the lack of stretchability and low performance limit the use of devices in the wearable and skin-attachable electronic applications.^{93, 94}

To address these issues, this thesis reports the novel large-scale NW alignment technique using bar coating assembly for the fabrication of high-performance AgNW TCEs and their applications in various soft optoelectronic and functional electronic device applications. In addition, stretchable AgNW electrodes insensitive to tensile strain are demonstrated for the development of highly stretchable and wearable sound-in-display electronic devices. In chapter 2, we demonstrated the simple and facile NW alignment technique using the modified bar coating assembly for the fabrication of large-area ($>20 \times 20 \text{ cm}^2$) cross-aligned AgNW TCEs. With the careful manipulation of NW orientations, the efficient conductive percolation networks are constructed with superior optoelectronic performance of cross-aligned AgNW networks showing the sheet resistance of $21.0 \Omega \text{ sq}^{-1}$ at 95.0% of optical transmittance, which compares favorably with that of random AgNW networks (Sheet resistance of $21.0 \Omega \text{ sq}^{-1}$ at 90.4% of optical transmittance). The fabricated flexible, transparent, and force-sensitive touch screens using cross-aligned AgNW electrodes integrated with mechanochromic SP-PDMS composite film enable the precise monitoring of dynamic writings, tracing and drawing of underneath pictures, and perception of handwriting patterns with locally different writing forces. In chapter 3, we demonstrated ultrathin, transparent, and conductive hybrid NMs with nanoscale thickness, comprising of the orthogonal AgNW arrays embedded in the parylene polymer matrix. The ultrathin hybrid NMs greatly enhance the optoelectrical and mechanical performance with the reinforcement effect of orthogonal NW structure embedded in the parylene matrix, which can be intimately attached to the human skin. As a proof of concept demonstration, skin-attachable NM loudspeaker and microphone were fabricated with voice-based security system. In chapter 4, high-performance flexible ACEL device is demonstrated using high- k BTO:La nanodielectric and ZnS:Cu phosphor. The enhancement of dielectric constant of the ACEL device from 2.6 to 21 (at 1 kHz of frequency) enables the device operation at the lower operating voltage as well as higher luminance resulted from the e-field concentration on the phosphor emissive layers. Besides, the uniform brightness across the whole panel of ACEL device and excellent device

reliability are achieved by using the uniform networks of cross-aligned AgNW TCEs. In chapter 5, highly transparent, flexible, and self-healable TA loudspeakers are presented based on AgNW-PUHU TCEs. The self-healable AgNW/PUTU TCEs and TA loudspeakers exhibit outstanding self-healing performance for repairing the surface damages by the dynamic reconstruction of the reversible bulky urea bonds in PUHU. In chapter 6, the synchronized generation of sound and vision information is demonstrated for the highly stretchable sound-in-display electronics with the strain-insensitive AgNW electrodes and field-induced emissive EL layers. The presented soft sound-in-display electronics integrating light emission and acoustic sound waves in the single device can be further expanded to realize future IoT and human-machine interface applications. In this thesis, we suggest novel NW alignment technique and high-performance flexible/stretchable AgNW TCEs with the diverse optoelectronic and electronic applications. Through those studies, we believe that our researches pave the new way of realization of highly robust and reliable future soft devices and wearable optoelectronic and electronic applications.

Chapter 2. Large-scale AgNW alignment technique for flexible force-sensitive mechanochromic touch screens

2.1 Introduction

Flexible and transparent conductive electrodes (TCEs) have attracted great attention in a variety of flexible optoelectronic devices, such as touch screen panels,^{22, 26} organic solar cells,^{95, 96} and organic light emitting diodes.^{97, 98} High mechanical flexibility, optical transparency, and electrical conductivity are the critical properties that TCEs should possess for the realization of high-performance flexible optoelectronics. In addition, the development of scalable and cost-effective fabrication of large-area and uniform TCEs still remains a great challenge. In accordance with these demands, TCEs based on metallic nanowires (NWs) have attracted considerable attention as an essential component for a variety of next-generation optoelectronic applications due to their excellent conductivity, transmittance, and flexibility.^{13, 99, 100} Various solution-based processes, such as spin-coating,^{101, 102} spray-coating,^{101, 103} vacuum filtration,³⁹ and bar-coating^{104, 105} have been widely used for fabricating NW TCEs. In such conventional solution-making processes, NWs are assembled into random networks; this generates several drawbacks for optoelectronic applications, such as nonuniform networks, NW-NW junction resistance, entanglement between NWs, and surface roughness.^{9, 106-109} Manipulating percolating conductive networks to overcome the trade-off between electrical conductivity and optical transmittance has been a key hurdle for random NW network.^{33, 110-112} To address these issues, aligned NW networks have been proposed.³² While the alignment of various types of NWs has been carried out through various solution processes, such as Langmuir-Blodgett,⁵³ nanocombing,¹¹³ contact printing,¹¹⁴ capillary force,^{32, 115} and flow-enabled self-assembly,¹¹⁶⁻¹²⁰ these methods still have drawbacks such as the requirement of additional processes (substrate pre-patterning, post-transfer, pre-growing NWs), a slow evaporation rate, a slow coating speed, and incompatibility with large-scale development.^{32, 53, 113-120} To the best of our knowledge, a large-scale and high-throughput assembly of aligned NW networks with high uniformity has not yet been reported.

Here, we report a simple, fast, and large-scale NW assembly strategy for the fabrication of flexible TCEs based on cross-aligned silver nanowire (AgNW) networks. To achieve this, we adopt and modify a conventional bar-coating, or Meyer rod coating technique, that has been used extensively in large-scale solution-based coating applications. Numerous research groups have previously proposed various techniques for aligning AgNWs,^{54, 55, 121-125} but they had limitations in terms of scalability, controllability of NW density, degree of NW alignment, and large-scale uniformity needed for practical optoelectronic applications. Our NW alignment technique, however, can address all these limitations

and enables flexible TCEs to be produced with remarkable figures-of-merits (FoMs). As a proof of concept, we fabricate the large-area ($20 \times 20 \text{ cm}^2$), flexible, and transparent touch screen based on cross-aligned AgNW TCEs as the top and bottom transparent electrodes. In addition, force-sensitive response can be added to touch screens by integrating mechanochromic spiropyran-polydimethylsiloxane (SP-PDMS) composite film into the devices. Unlike conventional touch screens which can only perceive the location of writing, our touch screens enable the monitoring of handwriting patterns with locally different writing forces.

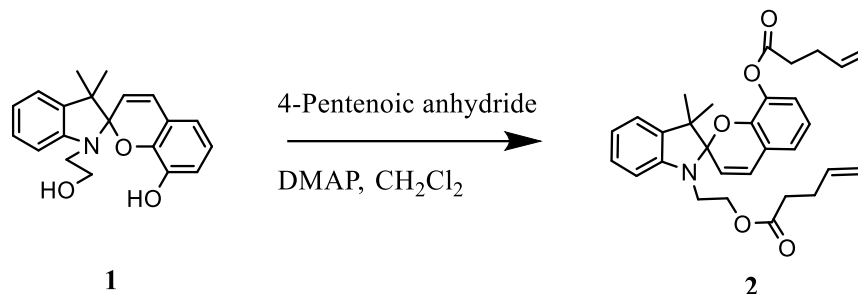
2.2 Experimental Details

Preparation of surface-modified substrates: Before surface modifications, all of the substrates were thoroughly cleaned by sonication for 10 min in the order of deionized (D.I.) water, acetone, and isopropyl alcohol (IPA). For generating –OH-terminated surfaces, cleaned substrates were treated with O₂ plasma for 10 min with a RF power of 18 W. Surface modification with –NH₂ group was prepared by spin-coating a 0.1% poly-L-lysine (PLL) solution in H₂O at 4,000 rpm for 60 s onto an O₂ plasma-treated substrate. The surface terminated with –CH₃ group was prepared by spin-coating hexamethyldisilazane (HMDS) at 4,000 rpm for 60 s.

Fabrication of large-area aligned AgNW arrays by bar-coating assembly: First, a Meyer rod (RD Specialties, Inc.) was mounted onto a bar coater, in which the coating speed and temperature can be precisely controlled. The target substrate was fixed onto the bar coater by using 3M scotch tapes on both edges. The thickness of scotch tape was used as a spacer between the Meyer rod and the substrate during the bar-coating assembly. AgNW ink (Nanopyxis Corporation) containing 0.15 wt.% AgNWs with an average length of 20 μm and diameter of 35 nm was injected into the empty space between the Meyer rod and the substrate, which resulted in the formation of meniscus by a capillary force. Subsequently, the meniscus dragging due to the moving of the Meyer rod at a constant speed resulted in the formation of highly uniform and aligned AgNW arrays along the coating direction. In order to fabricate cross-aligned AgNW arrays, right after complete drying of solvent, an additional bar-coating assembly was carried out on the aligned AgNW substrate in a direction that was perpendicular to that of the pre-aligned AgNWs. In the second bar-coating process, it is not necessary to repeat the chemical surface treatment by PLL on the first aligned AgNW substrate because AgNWs can be attached at the empty surface area between AgNWs. All of the fabricated AgNW TCEs were used in characterizations and applications without any post-treatments to increase the conductivity.

Fabrication of flexible and transparent touch screen: The transparent touch screen was operated by connecting a 4-wire resistive touch screen controller (ER-DBTP-USB04W-1, Eastrising Technology Co Ltd.) to a laptop computer. For the fabrication of the transparent touch screen based on a four-wire resistive-type touch sensor, cross-aligned AgNW TCEs were used as the top and bottom transparent electrodes of resistive touch sensor without any protective layers or dot spacers. The cross-aligned AgNW networks were fabricated by a bar-coating assembly on a 20 × 20 cm² PET substrate. In this bar-coating assembly, a #6 rod was used to align AgNWs at a coating speed of 10 mm s⁻¹ at room temperature. Then, two cross-aligned AgNW TCEs were assembled with AgNW-coated sides facing each other. Here, the top and bottom TCEs were separated by an air gap (thickness of ~1 mm) that had been developed by attaching 3M scotch tapes around the substrate edges. Finally, the prepared touch screen was connected to a laptop computer through a four-wire resistive controller board.

Synthesis of active spiropyran mechanophore: 1'-(2-hydroxyethyl)-3,3'-dimethyl-spiro[chromene-2,2'-indolin]-8-ol (1) and 3,3'-dimethyl-1'-(2-(pent-4-enoyloxy)ethyl)spiro[chromene-2,2'-indolin]-8-yl-pent-4-enoate (SP-2-H-bisPentenoate) (2).



In this study, SP-2-H-bisPentenoate was used as an active spiropyran mechanophore. For the synthesis of the SP-2-H-bisPentenoate, in a flame dried round bottom flask, dried under N₂, 1'-(2-hydroxyethyl)-3,3'-dimethyl-spiro[chromene-2,2'-indolin]-8-ol (12.7 g, 39.3 mmols, 1.0 equiv) and 4-dimethylaminopyridine (DMAP) (0.48 g, 3.93 mmols, 0.1 equiv) were added in 200 ml anhydrous CH₂Cl₂. Suspension was stirred at ambient for 10 min and 4-pentenoic anhydride (15 g, 82.5 mmols, 2.1 equiv) were added in 3 aliquots, 20 min apart. After the addition of first aliquot, solution became homogeneous, honey colored and a mild exotherm was detected. Stirring was continued for 1.5 h after last aliquot. Product solution was extracted with satd. NaHCO₃ (3x, 100 ml each), 1 M HCl (100 ml), D.I. water (2x, 100 ml each), dried over Na₂SO₄ and solvent removed to obtain 19 g (99 %) of pale honey colored oil.

The NMR spectra (¹H and ¹³C) were obtained on 600 MHz Bruker NMR Spectrometer (B600). Chemical shifts were recorded as parts per million (ppm) referenced to the residual ¹H or ¹³C peak at 5.32 ppm in CD₂Cl₂ or 53.84 in CD₂Cl₂, respectively. ¹H multiplicity was reported as: s (singlet), d (doublet), dd (doublet of doublets), dt (doublet of triplets), ddd (doublet of doublet of doublets), ddt (doublet of doublet of triplets), t (triplet), td (triplet of doublets), q (quartet), mp (multiplet), and b (broad). Coupling constants (J) were reported in Hertz. High-resolution mass spectrometry was performed on an Agilent LCMS-TOF-DART at Duke University's Mass Spectrometry Facility.

¹HNMR (600 MHz, CD₂Cl₂) δ 7.15-7.11 (dt, J = 7.6, 1.2 Hz, 1H), 7.09-7.05 (dd, J = 7.2, 0.9 Hz, 1H), 7.01-6.98 (dd, J = 7.5, 1.5 Hz, 1H), 6.94-6.91 (d, J = 10 Hz, 1H), 6.90-6.86 (dd, J = 7.9, 1.5 Hz, 1H), 6.85-6.75 (m, 2H), 6.65-6.62 (d, J = 7.6 Hz, 1H), 5.85-5.77 (m, 2H), 5.64-5.54 (m, 1H), 5.06-5.00 (qd, J = 16.9, 1.5 Hz, 1H), 4.99-4.95 (br qd, J = 10.2 Hz, 1H), 4.92-4.89 (br qd, J = 7.4 Hz, 1H), 4.89-4.87 (t, J = 1.5 Hz, 1H), 4.22-4.13 (m, 2H), 3.40-3.33 (m, 1H), 3.33-3.26 (m, 1H), 2.40-2.28 (m, 4H), 2.22-2.09 (m, 2H), 1.90-1.79 (m, 2H), 1.26 (s, 3H), 1.16 (s, 3H).

^{13}C NMR (150.9 MHz, CD_2Cl_2) δ 173.05, 171.28, 147.45, 145.36, 138.23, 137.27, 137.23, 136.78, 129.63, 127.78, 124.48, 123.05, 121.79, 120.35, 119.98, 119.79, 119.76, 115.48, 115.08, 107.04, 105.45, 63.01, 51.97, 42.74, 32.73, 33.35, 29.10, 28.85, 25.93, 19.52.

HRMS-ESI (m/z): $[\text{M} + \text{H}]^+$ calcd for $\text{C}_{30}\text{H}_{33}\text{NO}_5$, 488.2431; found, 488.2433.

Fabrication of force-sensitive mechanochromic touch screen: For the fabrication of mechanochromic composite films on top of the touch screen, spiropyran mechanophore was completely mixed with a PDMS base (Sylgard 184, Dow Corning) and PDMS curing agent (10:1 ratio for base to curing agent). The SP-PDMS composite was stored in a vacuum desiccator for 30 min to remove the bubbles. Then, the mechanochromic composite film was evenly deposited on top of the transparent touch screen by a bar-coating of the SP-PDMS composite solution using the #15 rod at a coating speed of 10 mm s^{-1} and thermal-curing at $60 \text{ }^\circ\text{C}$ for 6 h.

Characterizations: The chemical bonding and functional groups were investigated by the X-ray photoelectron spectrometry (XPS, K-alpha, Thermo Fisher, Waltham, MA, USA). The sheet resistances of the cross-aligned and random AgNW networks were measured using a four-point probe measurement device (Kiethley 2400 equipment). Optical transmittance and absorption spectra of unidirectional, cross-aligned, and random AgNW networks were measured by a UV-vis-NIR spectrophotometer (Jasco V-670). For the measurement of polarized absorption, a polarizer accessory (WP25M-UB, Thorlabs, Inc.) was equipped to the UV-vis-NIR spectrophotometer. The surface alignment structure of AgNW arrays was examined by an optical microscope (PSM-1000, Olympus). The mechanochromic colors were investigated by a spectroradiometer (PR-655, Photo Research, Inc.).

2.3 Results and Discussion

A Meyer rod is composed of a metal bar wrapped in wires, where the diameter of the wrapped wires determines the slit width (51–381 μm) and the amount of solution required to achieve the desired density of AgNWs (Figure 2.1). In this study, the alignment of AgNWs by bar-coating assembly is carried out by dragging a Meyer rod at a constant velocity and predefined rod-substrate gap distance over an AgNW solution on a surface-modified target substrate. Figure 2.2a shows a photograph of the bar-coating assembly process on a large polyethylene terephthalate (PET) substrate ($20 \times 20 \text{ cm}^2$). We pretreat the PET target substrate with poly-L-lysine (PLL) to enhance the AgNW adhesion to the substrate *via* an electrostatic force from amine-functional groups. By placing the AgNW solution into an empty space between the gap of the moving rod and the target substrate, thin uniform layer of AgNW solution film can be produced due to the confinement between the dense grooves of the Meyer rod and the target substrate. Dragging the trapped AgNW solution results in shear-induced hydrodynamic force on the trapped liquid film, which enables the alignment of AgNWs.

In the one-step bar-coating assembly, the interaction between shear-induced hydrodynamic and electrostatic forces enables the fabrication of highly aligned AgNW arrays (Figure 2.2b and 2.3). Unlike typical convective assembly processes, where NWs are aligned in an evaporation regime at a particularly slow coating speed ($10\text{--}100 \mu\text{m s}^{-1}$), the alignment of AgNW in the bar-coating assembly is dominated by the Landau-Levich regime which has a fast meniscus dragging speed ($> 1 \text{ mm s}^{-1}$), where the viscous forces caused by shearing of the meniscus are predominant.¹²⁶ During the alignment process, the hydrodynamic force can be calculated¹²⁷ as $F = \frac{4\pi\mu Ua}{\ln(2a/b)-0.72} = 3.26 \text{ nN}$, where μ is the viscosity of the fluid ($\sim 9.12 \times 10^{-3} \text{ Pa s}$, at 298.15 K for AgNW ink dispersed in ethanol), U is the velocity of capillary flow at the bottom of the moving bar (which is close to the moving speed of the bar, which is 10 mm s^{-1}), and a and b are the length ($\sim 20 \mu\text{m}$) and radius ($\sim 17.5 \text{ nm}$) of the NWs, respectively. This estimated drag force is comparable to the force ranges to align AgNWs by capillary forces³² and carbon nanotubes by hydrodynamic forces.¹²⁸ The AgNWs can be aligned during bar-coating assembly regardless of the solvent used, as long as the AgNW ink is viscous enough for generating the hydrodynamic force (Figure 2.4). The hydrodynamic drag force of the AgNW ink is estimated for various solvents, such as isopropyl alcohol (IPA) ($\mu = 9.37 \times 10^{-3} \text{ Pa s}$) and water ($\mu = 9.52 \times 10^{-3} \text{ Pa s}$), and the corresponding hydrodynamic force for the IPA and water are 3.35 nN and 3.4 nN, respectively.

The surface chemistry of the target substrate is a critical factor affecting the alignment of AgNWs capped with slightly negatively charged polyvinylpyrrolidone (PVP), which acts as a capping layer.^{129, 130} To investigate this effect, the target silicon (Si) substrates are pretreated with different functional groups, including amine ($-\text{NH}_2$), methyl ($-\text{CH}_3$), and hydroxyl groups ($-\text{OH}$) (Figure 2.5).

The amine group (-NH₂)-terminated PLL treatment provides the best aligned AgNW arrays because of the strong electrostatic interaction between the negatively charged PVP-capped AgNWs and the positively charged active amine groups of the PLL, which enhances the anchoring of the AgNWs onto the surface during the alignment process. To confirm the interaction between the AgNWs and the pretreated surfaces, X-ray photoelectron spectroscopy (XPS) is performed for AgNW-coated PLL/Si substrates and PLL/Si substrates (Figure 2.6). The high-resolution N 1s spectra of the pristine AgNW is composed of two fitted peaks at 400.1 and 399.5 eV, which can be attributed to pyrrolic N and N-C due to the N atom of the PVP on the AgNW surface.¹³¹ The N 1s spectra of the pristine PLL shows two deconvoluted peaks, with one arising from protonated amine (-NH₃⁺) at 401.3 eV and the other from N-C at 399.3 eV.¹³² After the deposition of the AgNW on the PLL-treated substrate, the high-resolution N 1s spectrum shows two fitted peaks at 400.2 and 399.3 eV, as is the case of pristine AgNW; however, the peak at 400.2 eV has broadened, which we believe is due to the involvement of pyrrolic N from PVP and -NH₃⁺ from PLL. The large downward shift of the binding energy (~ 1.1 eV) in the -NH₃⁺ peak of PLL is attributed to the charge transfer from the negatively charged PVP to the positively charged protonated amine groups in the PLL, which confirms the strong ionic interaction between the PLL and the AgNW (Figure 2.6a).⁸⁹

In contrast to PLL-modified surface, the surfaces modified using hexamethyldisilazane (HMDS) to produce the methyl group (-CH₃) and the surface modified by oxygen (O₂) plasma treatment to give the hydroxyl group (-OH) lead to a low density and poor alignment of the AgNWs (Figure 2.5b,c), which we attribute to the weak molecular interaction between the AgNWs and the methyl and hydroxyl groups, as shown by the XPS analysis. The XPS analysis of the high-resolution N 1s and C 1s spectra of the HMDS-treated and O₂ plasma-treated surfaces do not show any significant changes in the peak positions before and after the AgNW alignments (Figure 2.6a,b). Note that the high-resolution Ag spectra of none of the samples show any significant differences in the peak positions (Ag 3d_{3/2} and Ag 3d_{5/2} peaks at 374.3 and 368.3 eV in pristine AgNW), which suggests that Ag surface is intact to any kind of oxidation¹³³ and ionic interactions exist between the different functional groups (-NH₂, -CH₃, and -OH) and PVP rather than with the AgNW (Figure 2.6c).

Figure 2.2c shows a dark-field optical micrograph of a unidirectionally aligned AgNW array. The fast Fourier transform (FFT) image of the optical micrograph in the inset of the figure exhibits a clear line pattern, which indicates that the AgNW array has a highly aligned unidirectional structure. The advantage of our bar-coating assembly is that it allows for a multilayer AgNW arrays with precisely controllable interlayer orientations to be produced; this leads to cross-aligned AgNW arrays with user-defined internanowire angles (Figure 2.3). When a second bar-coating process is performed in a perpendicular direction on top of the pre-aligned AgNW array, cross-aligned AgNW arrays are observed

in the FFT image with a clear crossed-line pattern (Figure 2.2d), which indicates a 90° orientation between the first and second AgNW arrays. These cross-aligned AgNW networks, in contrast to the random AgNW networks, have several advantages for the fabrication of high-performance transparent electrodes, including highly uniform conductive networks, a lower percolation threshold, and excellent transparency at similar surface resistivity.¹³⁴

To quantitatively investigate the degree of alignment, radial summations of the pixel intensities of the FFT analysis are plotted as a function of the radial angle (0-360°) (Figure 2.7). The unidirectional AgNW array shows a clear and strong peak at 90°, which indicates a vertical alignment. The cross-aligned AgNW arrays show clear peaks at 0°, 90°, and 180° which indicate that the two aligned AgNW layers cross over at 90°. However, the random AgNW network does not provide any noticeable peaks, which is due to the lack of any particular orientation of the AgNWs, as indicated by the isotropic pattern of the FFT image in Figure 2.8. The AgNW alignment is also directly analyzed by measuring the distribution of the degree of alignment of 150 NWs from an aligned AgNW array in Figure 2.2c, which results in a full width at half maximum (FWHM) value of 21.4 (Figure 2.2e), confirming that most of the AgNWs are highly aligned along the direction of the coating.

One of the advantages of bar-coating assembly of the aligned AgNW networks is its scalability, as it can be used to produce films with large areas. Our bar-coating assembly can readily create uniformly aligned AgNW arrays on PET substrates over a 20 × 20 cm² area. The uniformity of the alignment over such an area is evaluated through an analysis of the distribution of FWHM values of aligned AgNW arrays in 16 local regions in a 20 × 20 cm² area (Figure 2.9). The FWHM values of AgNW arrays in all 16 local regions confirm the high uniformity and the scalability of the bar-coating assembly process (Figure 2.2f). Although the sample size is limited by the size of the equipment used in this study, we anticipate that the size of the aligned AgNW films can be further scaled up by using a longer Meyer rod or a roll-to-roll bar-coating process.

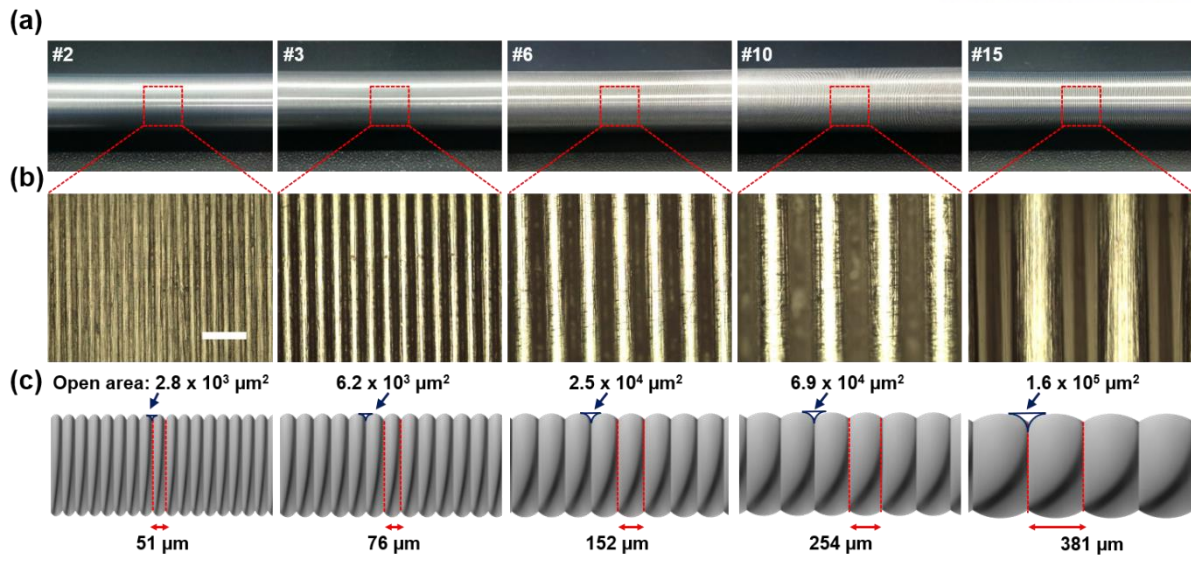


Figure 2.1 (a) Photographs of various kinds of Meyer rods (#2, #3, #6, #10, and #15) and (b) corresponding optical microscope images. The scale bar is 200 μm . (c) Schematic illustration of the specifications of various Meyer rods. The rod number determines the diameter of wrapped wires and the open area.

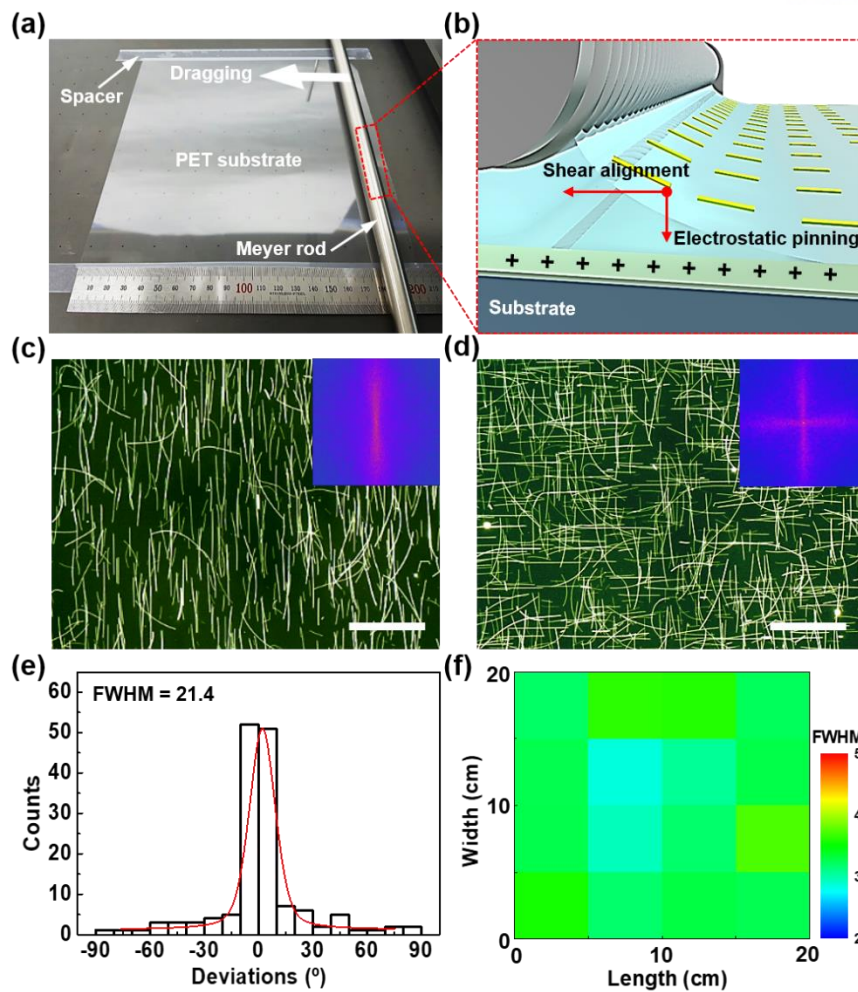


Figure 2.2 Large-scale bar-coating alignment of unidirectional and cross-aligned AgNW arrays. (a) A photograph of the solution-processed bar-coating alignment of the AgNWs on a $20 \times 20 \text{ cm}^2$ PET substrate and (b) a schematic showing the alignment process of AgNWs during the bar-coating assembly of the AgNW solution. The combined interaction between shear stress alignment and the electrostatic pinning produced highly aligned and uniform AgNW arrays during the dragging of a confined meniscus between the rod and substrate. (c) Dark-field optical microscope images of the unidirectionally aligned and (d) cross-aligned AgNW arrays. Insets are the fast Fourier transform (FFT) analyses of the optical micrographs indicating the direction and uniformity of the aligned AgNW structures. The scale bars are $40 \mu\text{m}$. (e) Distribution of the alignment degrees of 150 NWs in Fig. 1c with a full width at half maximum (FWHM) value of 21.4. (f) Mapping image showing the highly uniform distribution of FWHM values of each pixel in a 4×4 array over a large-area ($20 \times 20 \text{ cm}^2$) of aligned AgNWs. The FWHM values were calculated by fitting the radial summation of the pixel intensities of the FFT analysis.

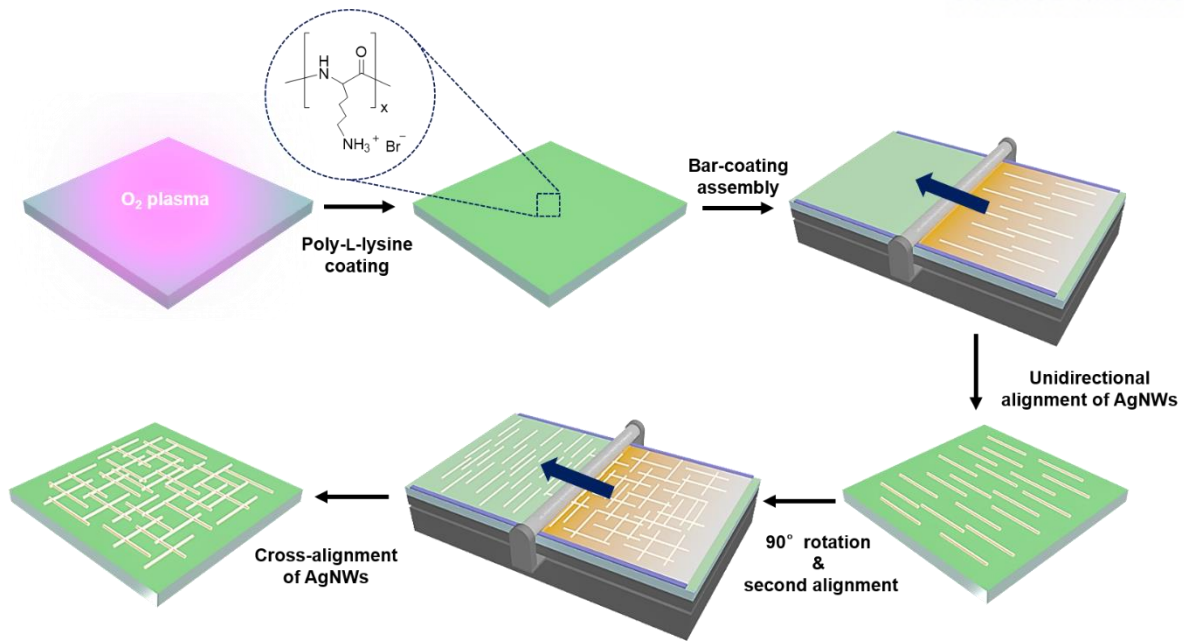


Figure 2.3 Schematic of an overall procedure for the solution-processed bar-coating assembly to fabricate unidirectionally and cross-aligned AgNW arrays. Before the bar-coating assembly, poly-L-lysine (PLL) solution is coated on O₂ plasma-treated target substrate to form amine groups on the surface. Consecutively, the meniscus dragging produces highly aligned AgNW arrays. The cross-aligned AgNW array is formed by repeating the bar-coating assembly in a perpendicular direction to that of the pre-aligned AgNW arrays.

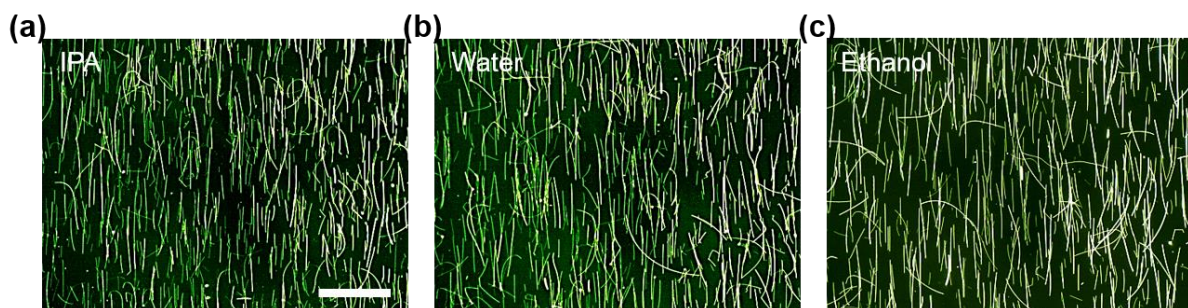


Figure 2.4 Dark-field optical micrographs of the unidirectionally aligned AgNWs coated with AgNW ink dispersed in different kinds of solvents; (a) isopropyl alcohol (IPA), (b) water, and (c) ethanol. During the bar-coating assembly, #2 bar, 3 μl of volume, and 10 mm s^{-1} of coating speed were used in all experiments. The scale bar is 40 μm .

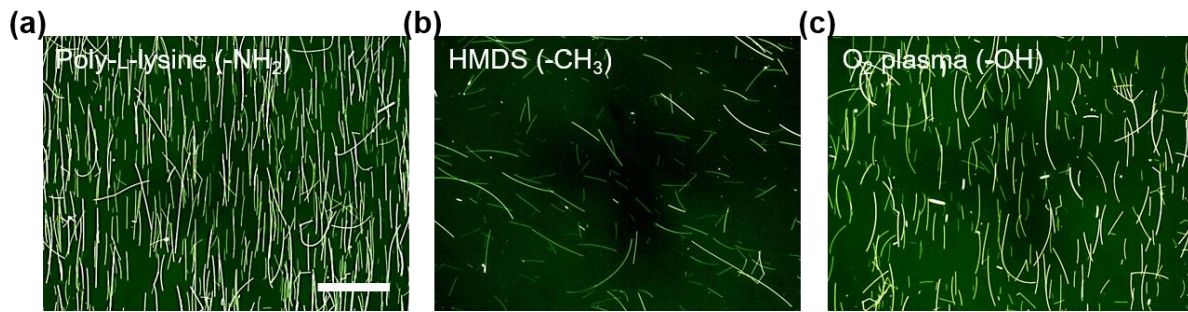


Figure 2.5 Dark-field optical micrographs of the aligned AgNW networks coated on substrates modified with different types of functional groups; (a) PLL (-NH₂), (b) hexamethyldisilazane (HMDS) (-CH₃), and (c) O₂ plasma (-OH). During the bar-coating assembly, #2 bar, 3 μl of volume, and 10 mm s⁻¹ of coating speed were used in all experiments. The scale bar is 40 μm.

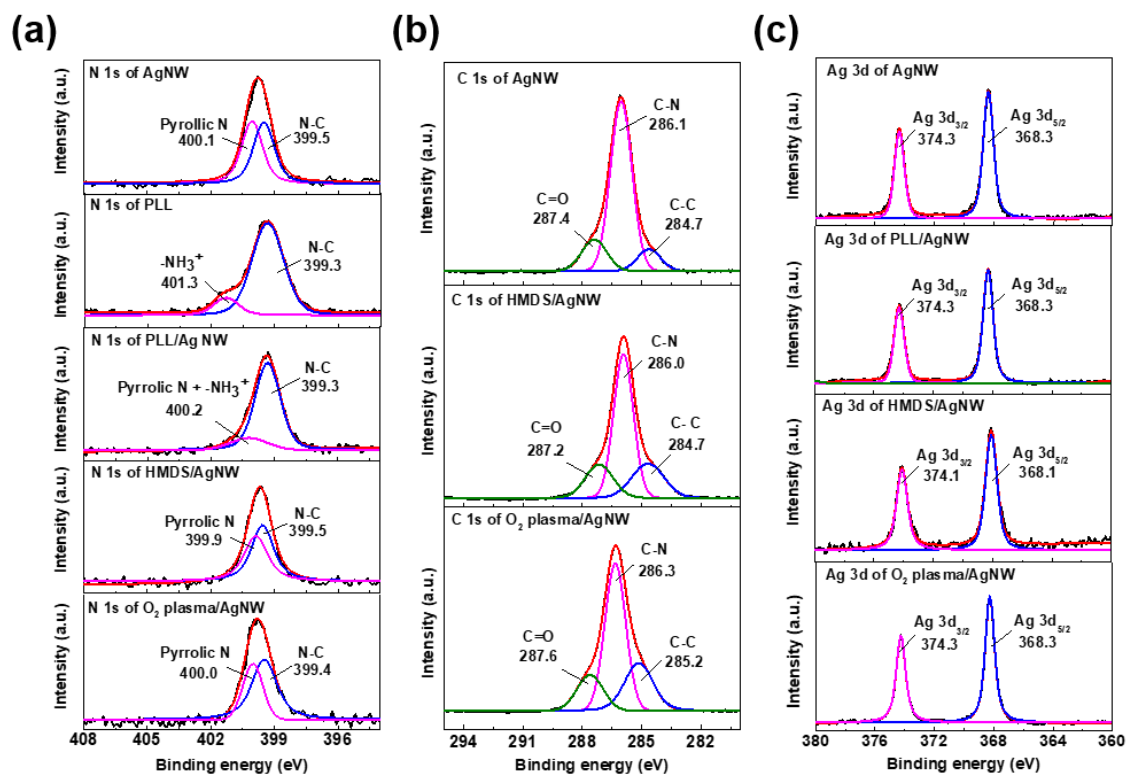


Figure 2.6 X-ray photoelectron spectroscopy (XPS) survey to investigate the interactions between AgNWs and the substrate surface pretreated with different functional groups with PLL, HMDS, and O₂ plasma. (a) High resolution N 1s spectra of the pristine AgNW, PLL, PLL/AgNW, HMDS/AgNW, and O₂ plasma/AgNW. (b) High resolution C 1s spectra of the pristine AgNW, HMDS/AgNW, and O₂ plasma/AgNW. (c) High resolution Ag 3d spectra of the pristine AgNW, PLL/AgNW, HMDS/AgNW, and O₂ plasma/AgNW.

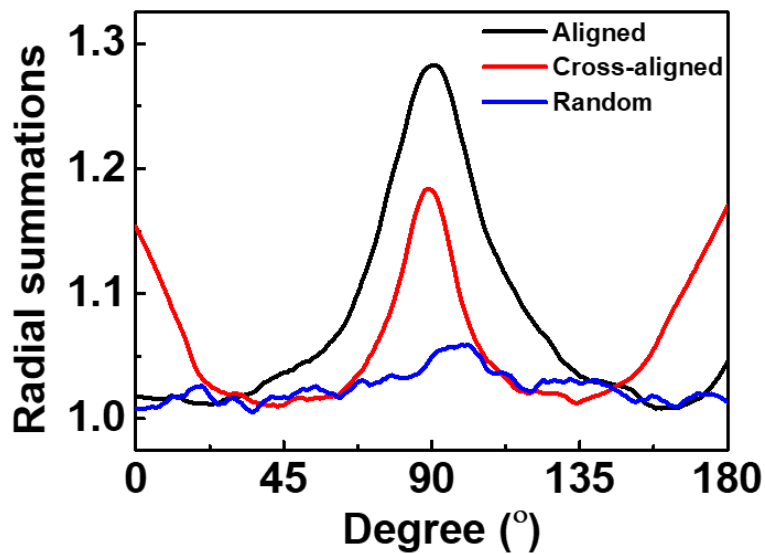


Figure 2.7 The radial summations of the pixel intensities of the fast Fourier transform (FFT) analysis data as a function of radial angle (0-180°) of the unidirectional AgNW array, cross-aligned AgNW arrays, and random AgNW network. Contrary to aligned and cross-aligned AgNWs networks which show clear Gaussian peaks, random AgNW network shows uncertain spectra of radial summations due to the lack of directionality.

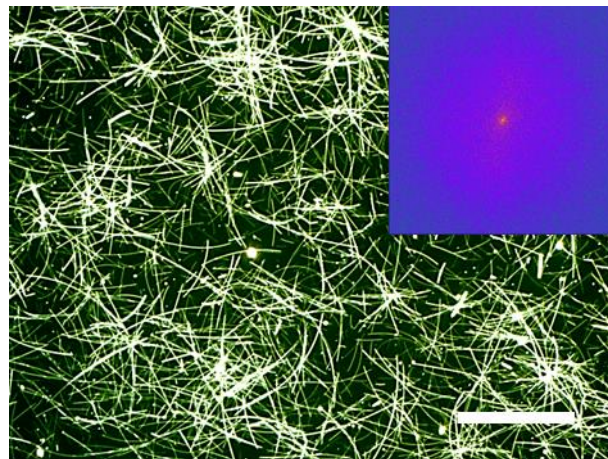


Figure 2.8 Dark-field optical micrograph of the random AgNW networks fabricated by conventional bar-coating process. Inset shows the corresponding FFT analysis data. The scale bar is 40 μm .

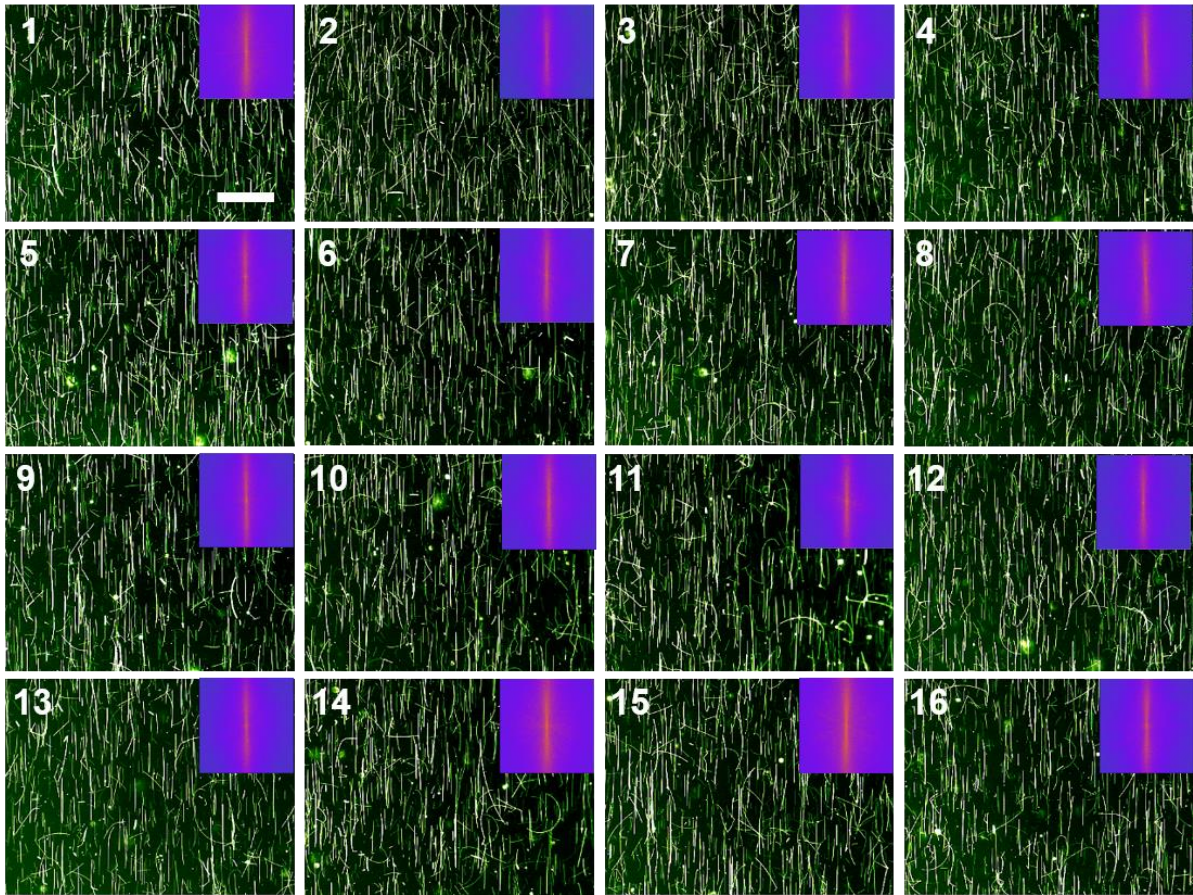


Figure 2.9 Large-area ($20 \times 20 \text{ cm}^2$) alignment of the AgNWs by bar-coating assembly. 16 dark-field optical micrographs of the aligned large-area AgNW arrays in a large-area PET film and the corresponding FFT analysis images in the insets. For the bar-coating assembly, #2 bar, $100 \mu\text{l}$ of volume, and 10 mm s^{-1} of coating speed were used in the experiment. The FWHM values of 16 AgNW arrays confirm the high uniformity and the scalability of the bar-coating assembly process as shown in Figure 1f. The scale bar is $40 \mu\text{m}$.

To further understand the mechanism behind the NW alignment, a number of parameters, including the amount of AgNW dispersion between the rod and substrate, the coating speed, and the substrate temperature, are investigated to monitor the alignment degree. We observed that the degree of alignment increases as the amount of AgNW dispersion, coating speed, and substrate temperature decrease (Figure 2.10a-c and Figure 2.11). As can be seen in Figure 2.10a, the FWHM value increases with the amount of AgNW dispersion, indicating that the degree of alignment of the NWs decreases. This behavior can be attributed to the increased meniscus thickness and contact area between the bar and the substrate, which increases the likelihood of misalignment of the AgNWs located far from the dragging bar (Figure 2.12). During the meniscus dragging, the shear force gradient is generated as a function of the height of the meniscus in a Couette flow.^{135, 136} Therefore, the AgNWs located far from the dragging bar have a high probability of misalignment due to a reduced shear force (Figure 2.13).^{55, 137} This relationship between the NW alignment and the meniscus thickness (or the shear force gradient) is also confirmed through the direct control of the gap distance between the Meyer rod and the substrate. Figure 2.14 shows that the degree of NW alignment decreases as the gap between the Meyer rod and the substrate increases, which indicates that the AgNWs located far from the dragging bar are likely to be misaligned due to the decreased shear force.

A decrease in the coating speed results in a decrease in the FWHM value, which indicates that the degree of NW alignment increases (Figure 2.10b). In our alignment system, the coating speed affects the shear force and the thickness of the confined meniscus film. The lowest coating speed used in our bar-coating assembly ($= 10 \text{ mm s}^{-1}$) is well above the minimum coating speed ($\approx 1 \text{ mm s}^{-1}$) required for a shear-stress-induced alignment of the AgNWs, which is still significantly faster than that of conventional evaporation-induced assembly ($\approx 10\text{-}100 \mu\text{m s}^{-1}$).¹³⁸ The lower coating speed decreases the thickness of the wet meniscus film,¹³⁹ which enhances the shear-induced hydrodynamic dragging force used to align the AgNWs. A higher coating speed, however, leads to a thicker meniscus film and hinders the formation of a uniform meniscus during the coating process. The degree of NW alignment is also affected by the substrate temperature. As the substrate temperature increases, the FWHM value increases (and the degree of NW alignment decreases) (Figure 2.10c). The reduced alignment of the AgNWs is attributed to decreased viscosity resulting from the increase in the substrate temperature,¹⁴⁰ which in turn results in a decreased shear force.

Our bar-coating process for NW alignment is different from conventional evaporation-induced assembly processes. In an evaporation-induced assembly process, NWs are aligned at the meniscus contact line due to the surface tension of the moving meniscus line during solvent evaporation;¹⁴¹ however, the surface tension of the moving meniscus line has minimal effects on NW alignment in our process. Before the solvent completely evaporates (which takes 0-7 s), most of the AgNWs are aligned

by the shear-induced hydrodynamic force. After complete drying of the solvent (7-9 s), the aligned AgNWs show negligible movement, which confirms the minimal effect of the surface tension of meniscus line on the prealigned NWs.

Highly aligned AgNW arrays produced by the bar-coating assembly exhibit the anisotropic optical properties. We investigate the polarized absorption spectra of the aligned AgNW arrays as a function of the polarization angle, θ , from 0 to 90°, where θ is the angle between the polarization direction of incident light and the alignment direction of the AgNW arrays (Figure 2.10d). Note that the absorption peak at 365 nm increases with θ , which is attributed to the greater effect of the transverse surface plasmon resonances of the AgNWs; meanwhile, the absorption peak at longer wavelength (> 500 nm) decreases, which is attributed to the longitudinal surface plasmon resonances of the AgNWs having less of an effect (Figure 2.10e).^{53, 55} Random AgNW networks without any anisotropic optical properties, however, do not show any noticeable change in their absorption peaks as the polarization angle increases (Figure 2.15). The strong anisotropic optical properties of the highly aligned AgNW array exhibit an optical dichroic characteristic; Figure 2.10f shows that the aligned AgNW arrays inside the “UNIST” letters become invisible or visible when the polarized light is parallel ($\theta = 0^\circ$) or perpendicular ($\theta = 90^\circ$) to the direction of the AgNW alignment, respectively; because the aligned AgNW arrays can act as a polarizing filter (Figure 2.16). These polarized absorption and dichroic properties clearly indicate the strong anisotropic optical properties of the aligned AgNW films.

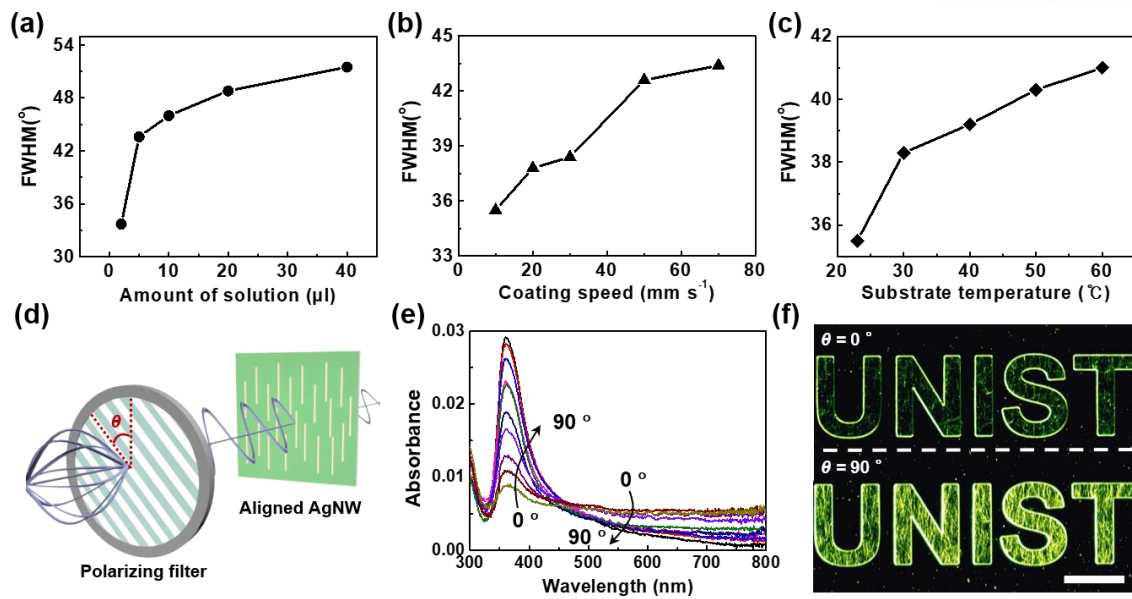
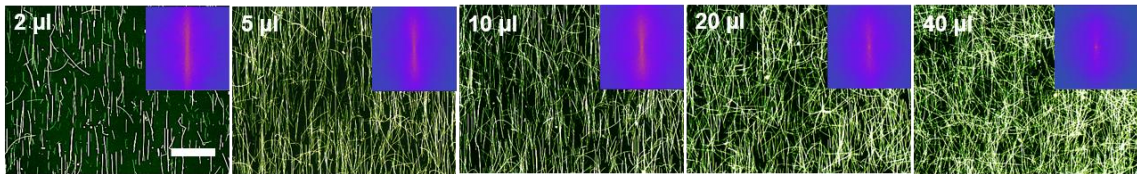
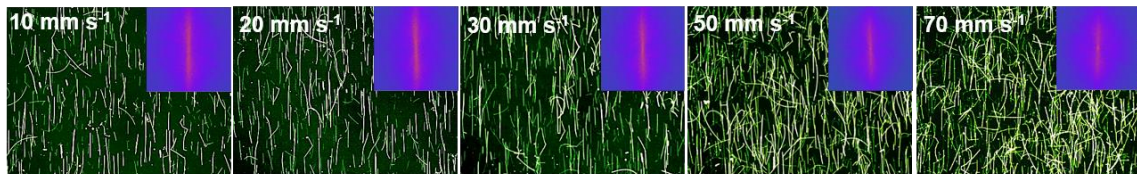
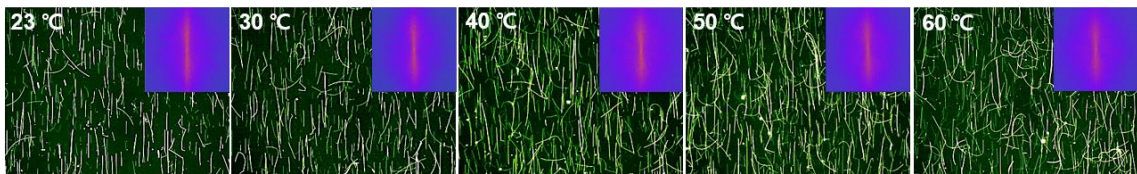


Figure 2.10 Unidirectional bar-coating alignment of the AgNW arrays and the anisotropic optical properties. (a-c) FWHM values according to the variation in the bar-coating parameters, including the amount of solution (2-40 μl), coating speed (10-70 mm s⁻¹), and substrate temperature (23-60 °C). (d-f) Anisotropic optical properties of the unidirectional AgNW arrays. (d) Schematic showing the polarized absorption test as a function of the angle θ between the direction of the polarized incident light and the NW alignment. (e) Polarized UV-vis absorption spectra of unidirectionally aligned AgNW arrays as a function of polarization angle (0-90°). (f) Optical dichroic property of unidirectionally aligned AgNW array. Polarized optical microscope images of "UNIST" patterns with different AgNW alignment directions exhibits invisible AgNW arrays when the light was polarized parallel to the direction of AgNW alignment ($\theta = 0^\circ$) and clearly visible AgNW array when the light was polarized perpendicular to the direction of AgNW alignment ($\theta = 90^\circ$). The scale bar is 100 μm.

(a) The amount of dispersion (μl)**(b) Coating speed (mm s^{-1})****(c) Substrate temperature ($^{\circ}\text{C}$)**

Decreased alignment degree \rightarrow

Figure 2.11 Dark-field optical micrographs of the aligned AgNW networks fabricated by the bar-coating assembly with different coating conditions; (a) volume of solution (2-40 μl), (b) coating speed (10-70 mm s^{-1}), and (c) substrate temperature (23-60 $^{\circ}\text{C}$). All insets show the corresponding FFT analysis images. The scale bar is 40 μm .

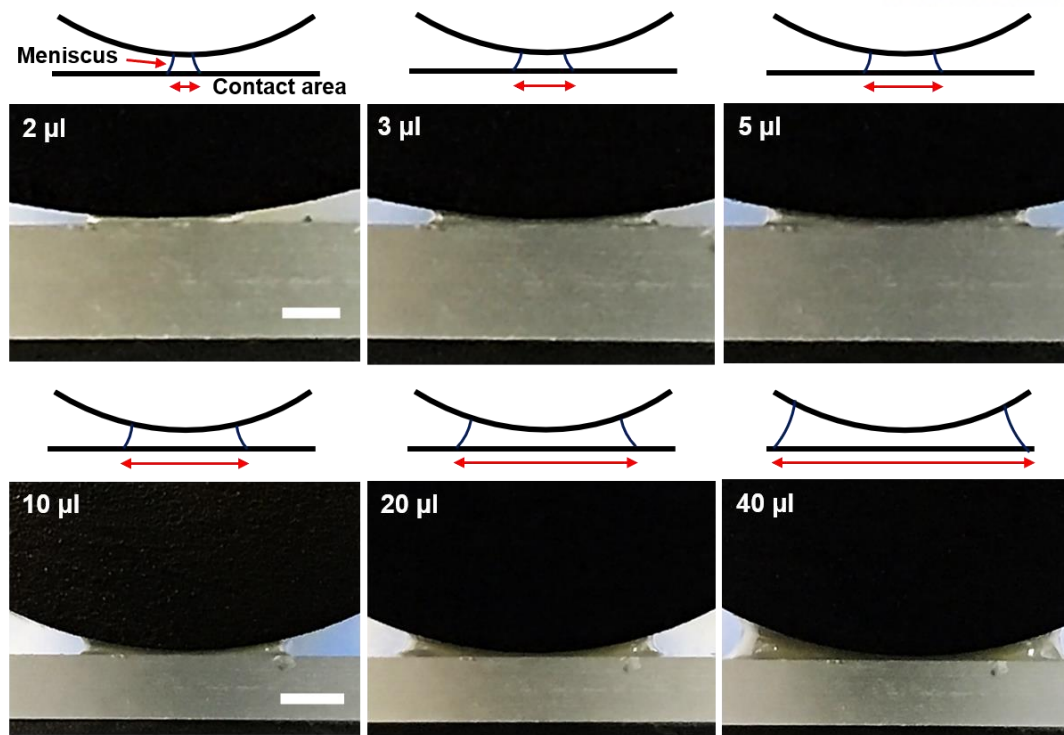


Figure 2.12 The effect of the amount of AgNW dispersion on the formation of contact area between the meniscus and the substrate. Schematics and close-up photographs show the meniscus between the rod and substrate with a different volume of dispersion (2-40 μl). As the volume of dispersion increases, the contact area becomes broader. The scale bars are 500 μm (top) and 1000 μm (bottom).

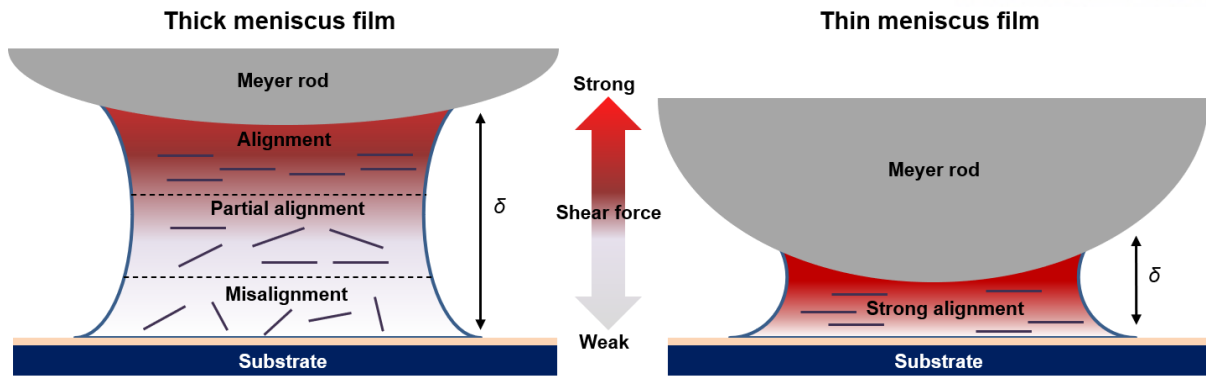


Figure 2.13 In the meniscus dragging process, the shear force gradient is generated as a function of the height of the meniscus in a Couette flow. Therefore, the AgNWs located far from the dragging bar have a high probability of misalignment due to a reduced shear force. In thick meniscus film, many of AgNWs are located far from the dragging bar and thus have a high probability of misalignment. In thin meniscus film, most of AgNWs are near the dragging bar, which results in the high probability of alignment.

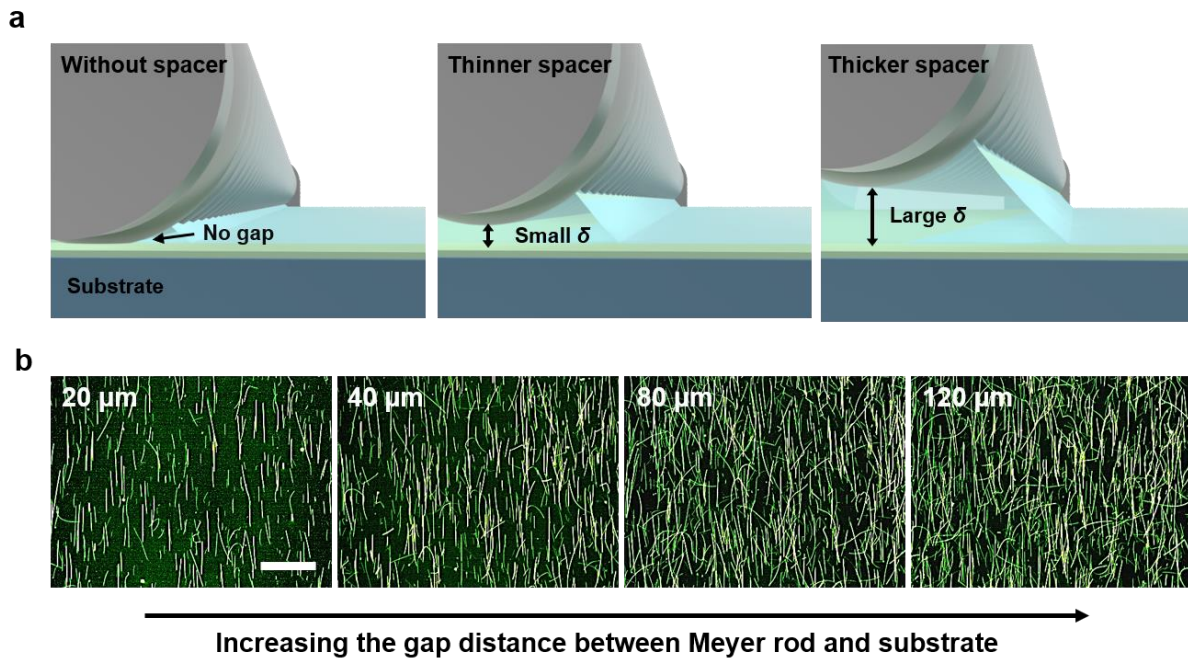


Figure 2.14 The effect of spacer thickness for the alignment of AgNWs. (a) Schematics showing the different height of the meniscus between the rod and the substrate depending on the thickness of spacer. As the thickness of spacer increases, the height of meniscus increases. (b) Dark-field optical micrographs showing the alignment of AgNWs depending on the variation of spacer thickness (20-120 μm). During the bar-coating assembly, #2 bar and 10 mm s^{-1} of coating speed were used in all experiments. The scale bar is $40 \mu\text{m}$.

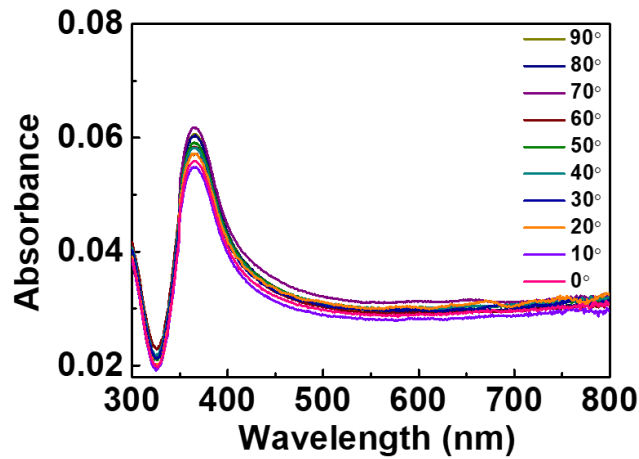


Figure 2.15 Polarized UV-Vis absorption spectra of the random AgNW networks as a function of polarization angle (θ) from 0 to 90°. As compared to aligned AgNW arrays, random AgNW networks without any anisotropic optical properties do not show any noticeable change in their absorption peaks as the polarization angle increases.

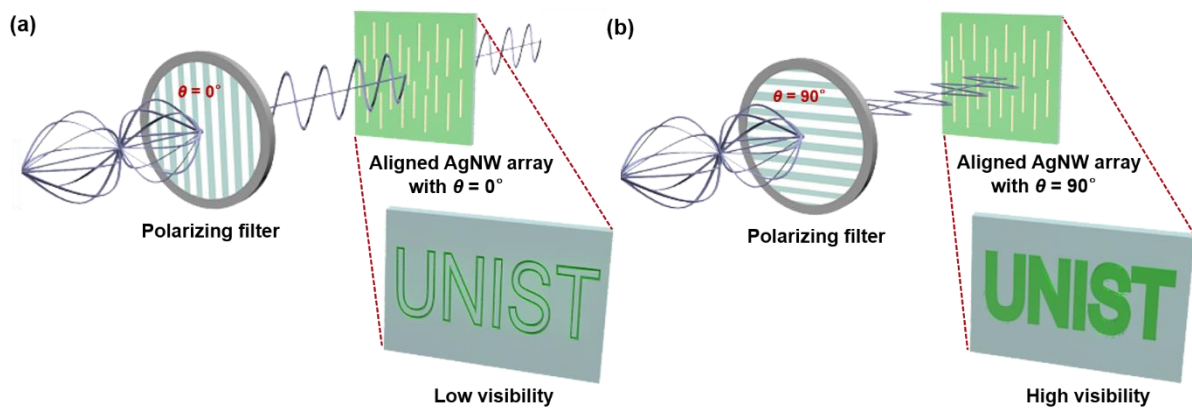


Figure 2.16 Schematics showing the polarized optical microscope modes according to the direction between the polarizing filter and the AgNW alignment direction; (a) $\theta = 0^\circ$, (b) $\theta = 90^\circ$. When the polarizing filter and the aligned AgNW array have the same vertical polarization direction ($\theta = 0^\circ$), vertically polarized light passes through the aligned AgNW film. However, when the polarizing filter and aligned AgNW array have the perpendicular polarization direction ($\theta = 90^\circ$), polarized light cannot penetrate the aligned AgNW film.

For TCE applications, aligned AgNW networks are more advantageous than random ones in terms of their higher network uniformity, lower percolation threshold, and better transparency.¹³⁴ We fabricated cross-aligned AgNW arrays with precisely controlled surface densities *via* a repeated multistep process, which provides highly uniform conductive networks (Figure 2.17). As seen in Figure 2.18a, cross-aligned AgNW arrays exhibit high optical transmittance (T of 87.6-97.2 % at 550 nm) and low sheet resistance (R_s of 10.4-69.7 Ω sq⁻¹) as a function of the number of cross-aligned coatings. Here, the increase in the number of coatings results in a dense and thick conducting film with lower optical transparency and higher electrical conductivity. To compare the tradeoff performance between R_s and T for the cross-aligned and random AgNW networks, a FoM for the electrical to optical conductivity ratio, defined as $T = \left[1 + \frac{1}{\Pi} \left\{ \left(\frac{Z_0}{R_s} \right) \right\}^{1/(n+1)} \right]^{-2}$, is used, where Z_0 is the impedance of free space ($Z_0 = 377 \Omega$), n is the percolation exponent describing the power law relationship between R_s and the film thickness, and Π is the percolative FoM.⁴⁵ A high FoM value indicates low and high value of R_s and T , respectively. In addition, a low n value is preferred to obtain a high value of Π , which means the reduced NW-NW junction resistances over the thin film. In Figure 2.18b, the Π and n values can be calculated by fitting R_s and T data for cross-aligned (T of 93.5-96.5 % at 550 nm with R_s of 18.8-42.3 Ω sq⁻¹) and random (T of 88.2-97.0 % at 550 nm with R_s of 15.9-88.62 Ω sq⁻¹) AgNW networks. The Π value of the cross-aligned AgNW arrays (FoM = 479) is much higher than that of random AgNW networks (FoM = 254), which confirms the superior optical and electrical properties of the cross-aligned AgNW arrays. Meanwhile, the lower n value of the cross-aligned AgNW arrays ($n = 0.12$) than that of random AgNW networks ($n = 0.14$) confirms the high uniformity and reduced interwire junction resistances of the cross-aligned AgNW arrays. The higher Π and lower n values of the cross-aligned AgNW arrays indicate that the cross-aligned AgNW TCE is better suited for overcoming the issue of the tradeoff between the electrical conductivity and optical transparency of conventional random AgNW networks.

Figure 2.18c compares the R_s to T performance of various AgNW based TCEs. The R_s - T performance of the cross-aligned AgNW arrays (18.8-42.3 Ω sq⁻¹ at 88.2-97.0 %) surpasses those of other random AgNW networks. The best R_s - T performance of the cross-aligned AgNW arrays ($R_s = 21.0 \Omega$ sq⁻¹, $T = 95.0$ %) is superior to that of the previously reported random AgNW networks, such as purified AgNWs (32.0-130 Ω sq⁻¹ at 95.1-99.1 %),¹⁴² spray-coated long AgNWs (20.0 Ω sq⁻¹ at 92.1 %),¹⁴³ graphene-AgNWs hybrids (33.0 Ω sq⁻¹ at 94.0 %),⁸² dry-transferred AgNWs (10.0 Ω sq⁻¹ at 85.0 %),¹⁴⁴ graphene oxide-soldered AgNWs (12.0-26.0 Ω sq⁻¹ at 86.0-92.1 %),¹⁴⁵ polymer-soldered AgNWs (25.0 Ω sq⁻¹ at 85.0 %),¹⁴⁶ multilength scaled AgNWs (28.0 Ω sq⁻¹ at 91.8 %),¹⁴⁷ very long AgNWs (9-69 Ω sq⁻¹ at 89-95 %),⁶ and hybrid of meso- and nanoscale metal NWs (0.36 Ω sq⁻¹ at 92 %).²⁷ In addition, our bar-coating assembly can produce large-area ($> 20 \times 20$ cm²) cross-aligned

AgNW arrays with a highly uniform spatial distribution of the AgNW networks without any additives, transferring or lithography processes, which cannot be achievable by most of the previously reported random AgNW networks.^{6, 27, 82, 142-144, 147} To verify the spatial uniformity over such a large area, we fabricate TCEs based on cross-aligned AgNW arrays on large-area ($20 \times 20 \text{ cm}^2$) flexible substrates (Figure 2.18d); the R_s and T values of each pixel in a 4×4 array are then investigated. Figure 2.18e,f show mapping images of the R_s distribution of cross-aligned and random AgNW networks with similar average R_s values. The cross-aligned AgNW arrays show a uniform distribution of R_s with a small standard deviation of 1.2, which compares favorably with that of the random networks having large standard deviation of 6.5 (Figure 2.18e,f). Likewise, the T distribution of the cross-aligned AgNW arrays show a better uniformity across the entire area, having a standard deviation of 0.3, which is small compared to that of the random AgNW network, which has a standard deviation of 0.8 (Figure 2.18g,h). These large-scale uniformities of cross-aligned AgNW arrays can be attributed to the ordered surface geometry of the conductive AgNW network as well as the uniform NW-NW junctions that didn't exist in randomly-entangled NWs. We also note that the cross-aligned sizable AgNW arrays exhibit a higher optical transparency (95.9 %) than that of the random AgNW arrays (91.9 %) for similar average R_s values. Besides, the cross-aligned AgNW networks possess an outstanding mechanical stability. Those films show a negligible variation in resistance under the bending radius as small as 1.5 mm (Figure 2.19a). In addition, there is no significant change in resistance even after repetitive bending of 1000 times at 1.5 mm of bending radius (Figure 2.19b). Furthermore, the cross-aligned AgNW arrays can be fabricated in several minutes, which is better than the previous slow and complicated processes requiring additional transfer process and post-treatment. All of these characteristics are critical factors for practical applications of AgNW based TCEs in large-area optoelectronic devices.

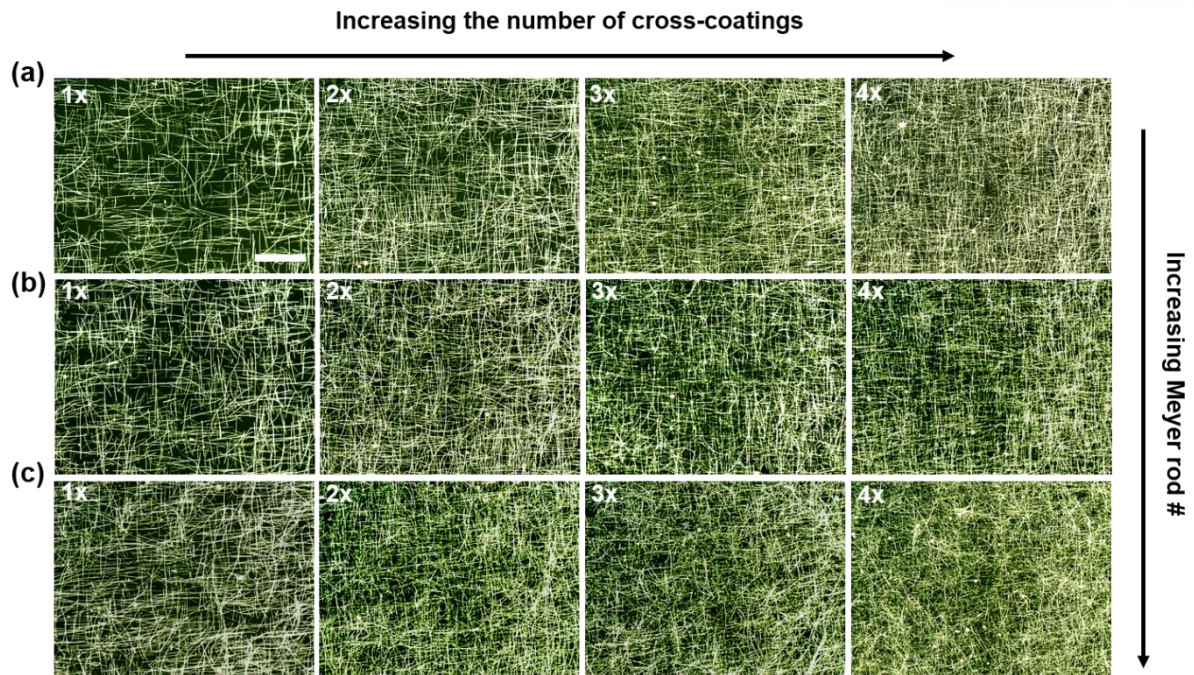


Figure 2.17 Dark-field optical micrographs of cross-aligned AgNW arrays by varying the number of cross-coatings for bar-coating conditions of (a) #2 bar and 3 μl , (b) #3 bar and 4 μl , and (c) #6 bar and 8 μl . All of the cross-aligned AgNW arrays were fabricated at the coating speed of 10 mm s^{-1} . The scale bar is 40 μm .

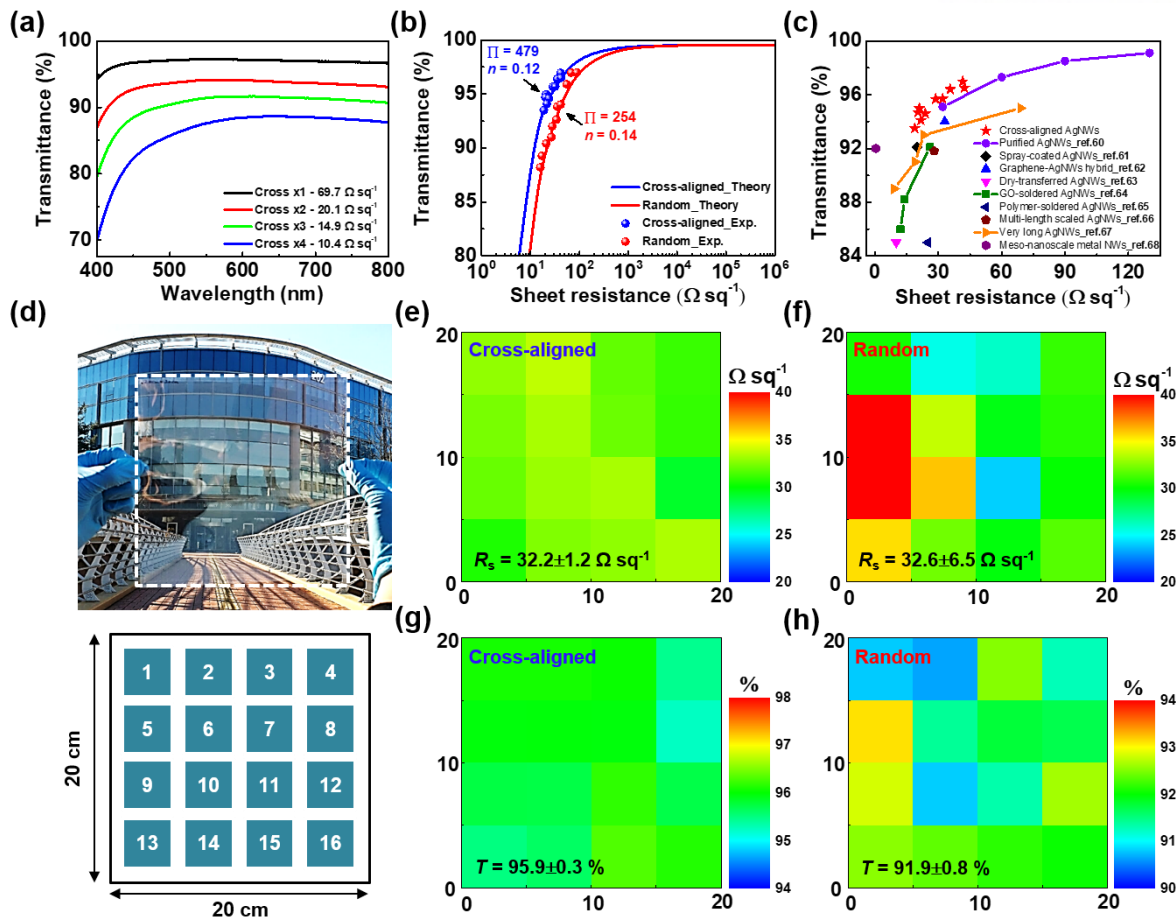


Figure 2.18 Optical and electrical performance of the large-area transparent conductive electrodes (TCEs) using the cross-aligned AgNW networks. (a) UV-vis spectra and corresponding sheet resistance, R_s , of cross-aligned AgNW arrays with different numbers of cross-coatings. The substrate was used as a reference in all UV-vis experiments. (b) R_s versus optical transmittance, T , at 550 nm for the cross-aligned and random AgNW networks fitted by percolative regime. (c) R_s versus T performance of various AgNW TCEs. (d) A photograph of large-scale ($20 \times 20 \text{ cm}^2$) TCE coated with uninform cross-aligned AgNW arrays (top), and schematic showing its 4×4 pixels for analysis (bottom). (e) 4×4 pixels mapping images showing the R_s distribution of cross-aligned and (f) random AgNW networks over a large substrate area ($20 \times 20 \text{ cm}^2$). The average R_s was set so as to be similar in both films. (g) 4×4 pixels mapping images showing the T distribution of cross-aligned and (h) random AgNW networks over a large substrate area ($20 \times 20 \text{ cm}^2$).

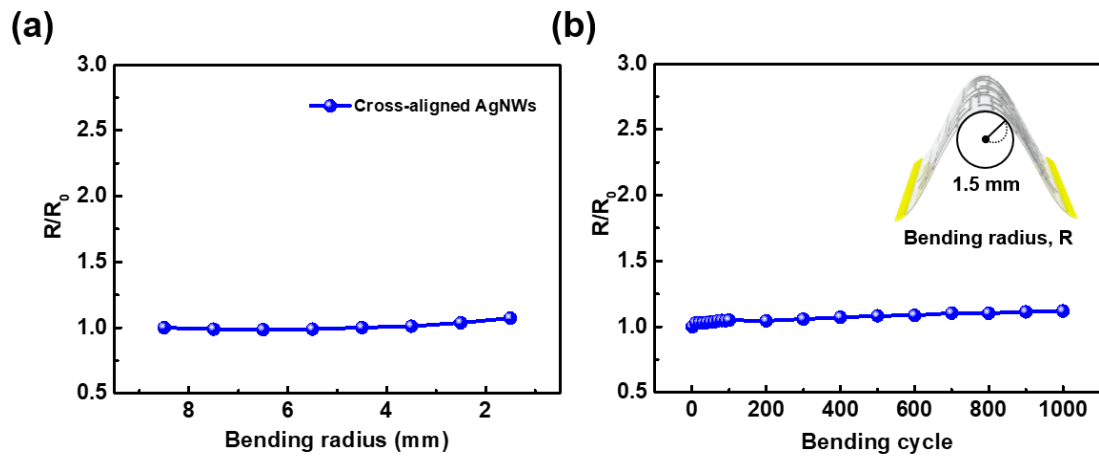


Figure 2.19. Mechanical stability of cross-aligned AgNW based TCEs on PET substrate. (a) Variation in resistance of cross-aligned AgNW TCEs as a function of bending radius. (b) Resistance change of cross-aligned AgNW TCEs during 1000 bending cycles at the bending radius of 1.5 mm.

For the proof of concept application of large-area TCEs, we demonstrated a large-area, flexible, and transparent touch screen based on a four-wire resistive-type touch sensor that uses cross-aligned AgNW TCEs as the top and bottom transparent electrodes without any protective layers or dot spacers (Figure 2.20a). Here, when the top electrode is depressed by an external force, the two resistive layers meet. When a voltage is applied across X or Y layers between X1-X2 or Y1-Y2 busbars, the other touching layer divides the applied voltage at the touch position and thus the controller circuit board captures the voltage change at the touch position along the X-Y coordinates. Figure 2.20b shows the flexible and transparent touch screen using a cross-aligned AgNW network that has an active area of $20 \times 20 \text{ cm}^2$. Figure 2.20c demonstrates the application of the large-scale touch screen for writing letters of the alphabet; we can write over the entire area of the touch screen without any disconnected lines or defects in the letters, which thereby demonstrates the outstanding touch sensitivity and uniformity of the device. Those writing performance can be attributed to the fine resolution of our touch screen. We investigate the resolution of touch screen by measuring the smallest distance between two adjacent touch lines that can be distinguished by our touch screen (Figure 2.21). The estimated resolution of touch screen is around $100 \mu\text{m}$ (Figure 2.21c), which is the smallest distance distinguishable by the touch controller board used in our study.

Note that the optical transparency of our touch screen allows for tracing and drawing underneath pictures. Figure 2.20d demonstrate the tracing of a picture of a butterfly below the transparent touch screen, where precise and continuous line drawing is possible without any defects. These results demonstrate the potential of our bar-coating assembly for fabricating cross-aligned AgNW arrays for large-area transparent electrodes that can be used in transparent and flexible touch screens. One advantage of our touch screen compared to previous ones is the optical transparency and flexibility, which enables the electronic tracing of underneath surface textures, graphics, and writings even on the curved surfaces, indicating bending-insensitive capability of our touch screens (Figure 2.22).

In addition to the tracing of touch location on the transparent touch screen, simultaneous detection of an applied force is beneficial in discriminating the pressure between gentle and hard touches on the screen during writing and tracing tasks. To create touch screens that recognize writing force as well as location, we incorporated a mechanochromic SP-PDMS composite film into the touch screen. The SP-PDMS film allows the visualization of applied force through a color change in response to the dynamic writing pressure. Spiropyran mechanophore (force-sensitive molecule) can be covalently coupled into PDMS network, so that local tension in the PDMS triggers a reversible color change in the spiropyran through a force-induced ring opening reaction,^{148, 149} that has been used previously for stress or strain sensing.¹⁵⁰⁻¹⁵² Figure 2.23a shows the schematic illustration of mechanochromic touch screens, which comprises cross-aligned AgNW TCE layers and over-coated mechanochromic SP-PDMS

composite film. The mechanochromic touch screen enables the detection of location of dynamic touch that is monitored by the resistive touch sensor; meanwhile, the intensity of force during the writing is detected by the change in color of mechanochromic force sensor, which is analyzed by the spectroradiometer (Figure 2.23b).

The applied writing force can be quantified by analyzing the intensity of visible color spectra as a function of dynamic writing force in horizontal lines that are drawn by a stylus (Figure 2.24). As can be seen in Figure 2.23c, the intensity of blue color obtained from the normalized luminance at 448 nm increases linearly with the writing force (luminance $\sim 0.37 \times F_{\text{write}}$). As seen in Figure 2.23d, the blue color intensity of the handwritten letters “FNL” gradually increases in response to increasing writing force (F_{write}) applied to a mechanochromic touch screen. This behavior can be attributed to the varying local deformation of the SP-PDMS film in response to different writing forces. Figure 2.23e shows the average intensities of blue color for handwritten letters “FNL”, which increases with the increase of dynamic writing force. Based on the linear calibration curve in Figure 2.23c, the applied forces can be determined to be from $F_1 = 4.3 \pm 0.2$ N to $F_5 = 14.9 \pm 3.4$ N. The degree of color change as a function of writing force can be further analyzed by standard colorimetric system called CIE 1931. Figure 2.23f shows the average color coordinates of letters “FNL” with different applied forces from 4.3 N to 14.9 N, where X-Y coordinates move to the deep blue region with increasing force. While the line width of writing letters in Figure 2.23d is ~ 1 mm, the resolution of dynamic writing on the SP-PDMS film can be further improved by decreasing the contact area of applied force. In our study, the line width of dynamic writing can be decreased down to ~ 79 μm by using a sharp stylus pen (Figure 2.25).

Combining the two detection mechanisms enables the simultaneous detection of location and intensity of force during the writing. When four different writing forces are applied for the handwritten letter “A”, the intensity of writing force can be discriminated by the different intensity of blue color on the mechanochromic touch screen (Figure 2.26a). At the same time, the corresponding location of writing signals of letter “A” can be precisely tracked on the monitor (Figure 2.26b). Moreover, writing touch signals and the color change can be clearly observed even under the bending state, indicating that the force-sensitive touch screen is insensitive to film bending. The real time visualization of writing force on the mechanochromic touch screen can be used to distinguish, for example, personal handwriting patterns with locally varying writing forces.¹⁵³ Figure 2.23g shows the spatial force mapping analysis (10×10 pixels array) of local writing force applied to the handwritten letter “A”. The locally different writing forces can be clearly observed along the letter “A”, indicating the potential application of mechanochromic touch screens for the enhanced security of personal identity based on the handwritten electronic signatures.

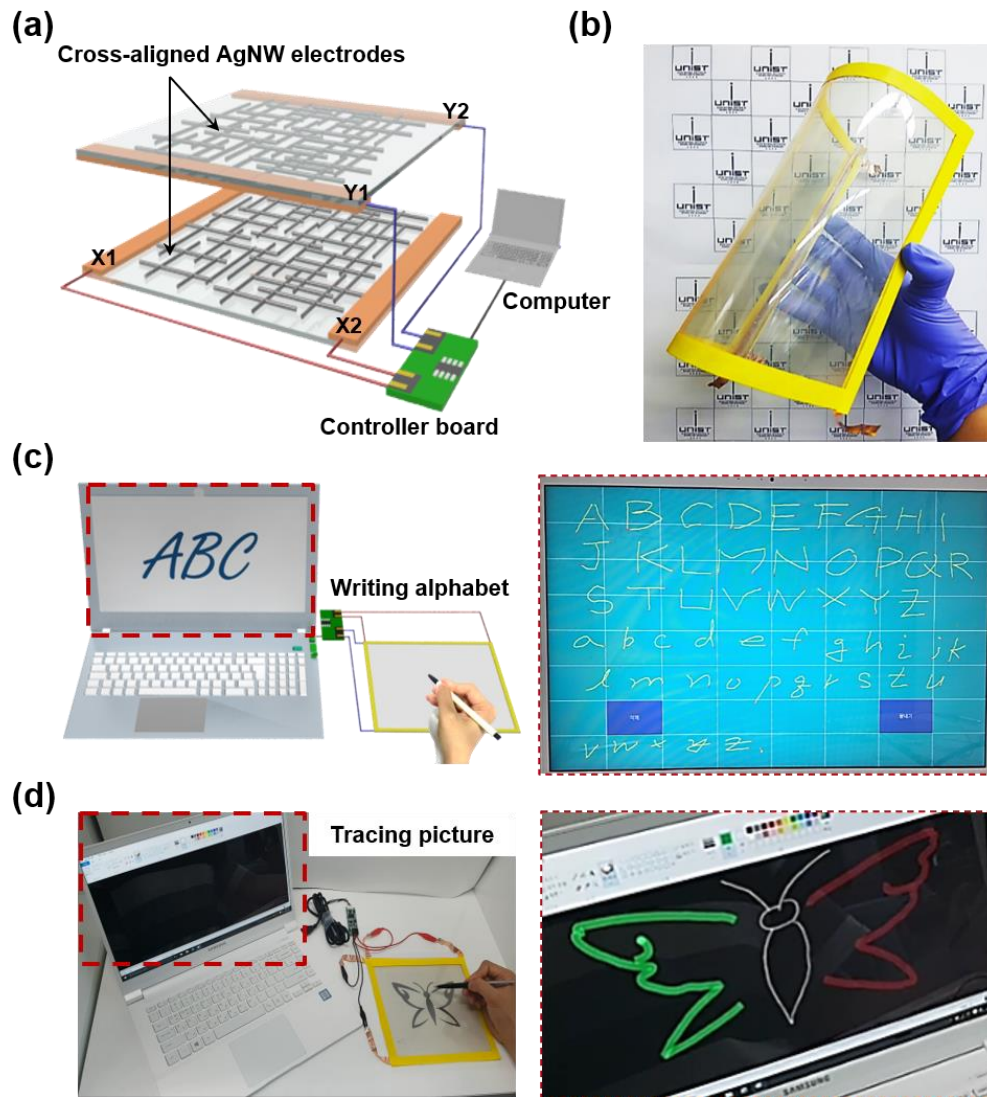


Figure 2.20 Large-scale, flexible, and transparent touch screens using cross-aligned AgNW TCEs. (a) Schematic showing the structure of the large-scale, flexible, and transparent touch screen using the cross-aligned AgNW arrays on a PET substrate connected to a laptop computer through a controller board. (b) A photograph of the large-scale, flexible, and transparent touch screen ($20 \times 20 \text{ cm}^2$) using cross-aligned AgNW TCEs. (c) Demonstration of writing alphabet letters on the transparent touch screen, which have been recorded on the computer monitor. (d) Demonstration of tracing a picture of a butterfly placed under the transparent touch screen.

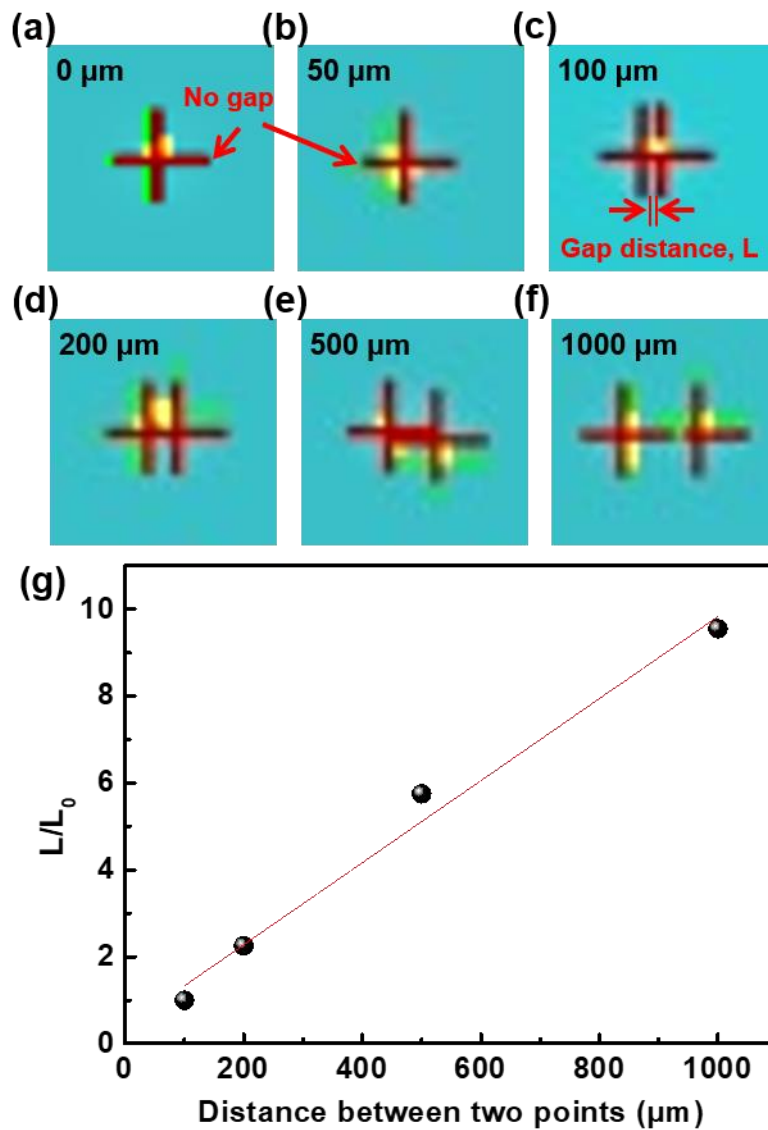


Figure 2.21 (a-f) Output images of touch signal and (g) normalized gap distance between adjacent touch signals, generated by two touch points pressed with different gap distance of (a) 0 μm , (b) 50 μm , (c) 100 μm , (d) 200 μm , (e) 500 μm , and (f) 1000 μm on touch screen based on cross-aligned AgNW TCEs. Our touch screen can detect touch location with the resolution of 100 μm , which corresponds to the resolution of touch controller board. L_0 is defined as minimum gap distance between two touch signals that can be distinguished by touch screen.

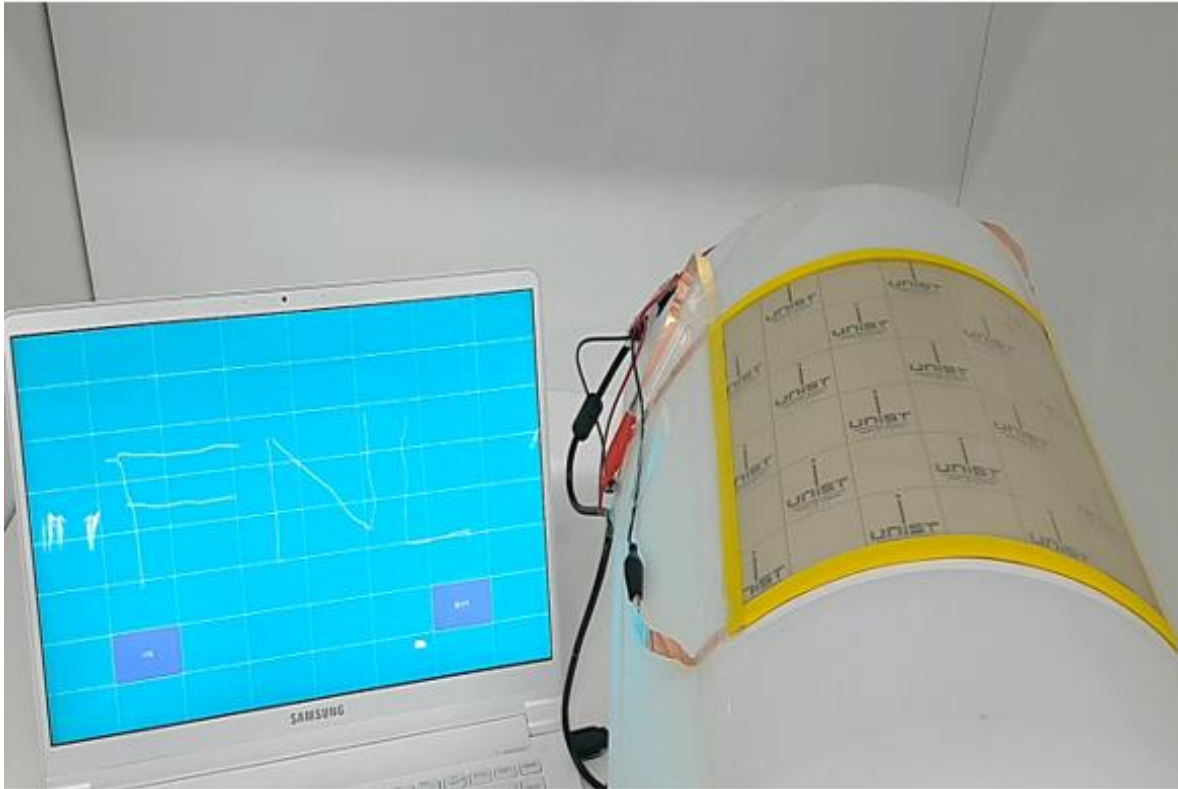


Figure 2.22 Demonstration of large scale, flexible touch screen fabricated by cross-aligned AgNW based TCEs. Handwritten letters “FNL” was precisely written on top of curved surface.

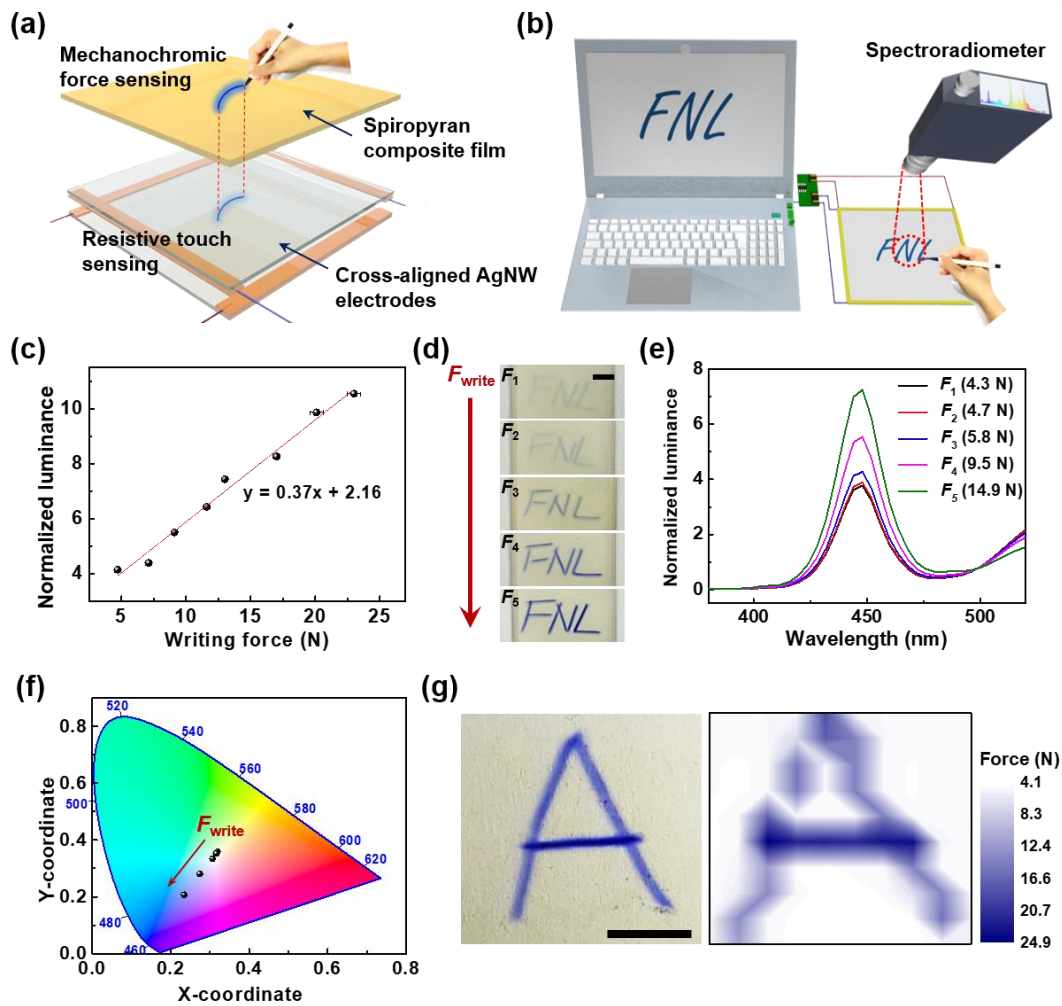


Figure 2.23 Flexible, transparent, and force-sensitive touch screens. (a) Schematic illustration of the device structure of a force-sensitive touch screen showing simultaneous force and touch sensing in response to dynamic writings. (b) Schematic illustration of the mechanochromic touch screen system with the color analysis using a spectroradiometer. (c) Normalized luminance at 448 nm wavelength as a function of the writing force. A fitted line shows a linear relationship between the normalized luminance and the writing force. (d) Photographs of mechanochromic color changes on the touch screen as a function of different dynamic writing force. The blue color intensity of the written letters “FNL” on the touch screen increases with the writing force. The scale bar is 1 cm. (e) Normalized luminance spectra of blue color letters “FNL” in visible range (380-520 nm). Based on the linear curve in Figure 5c, the applied forces can be determined to be from $F_1 = 4.3 \pm 0.2$ N to $F_5 = 14.9 \pm 3.4$ N. (f) Representation of the color coordinates on the CIE 1931 color space according to the different writing force. The X-Y coordinates move to the deep blue region with the increase of applied force. (g) A photograph of the written letter “A” on the mechanochromic touch screen (left) and its 10×10 pixels array of applied force mapping data showing the local force distribution (right). The scale bar is 1 cm.

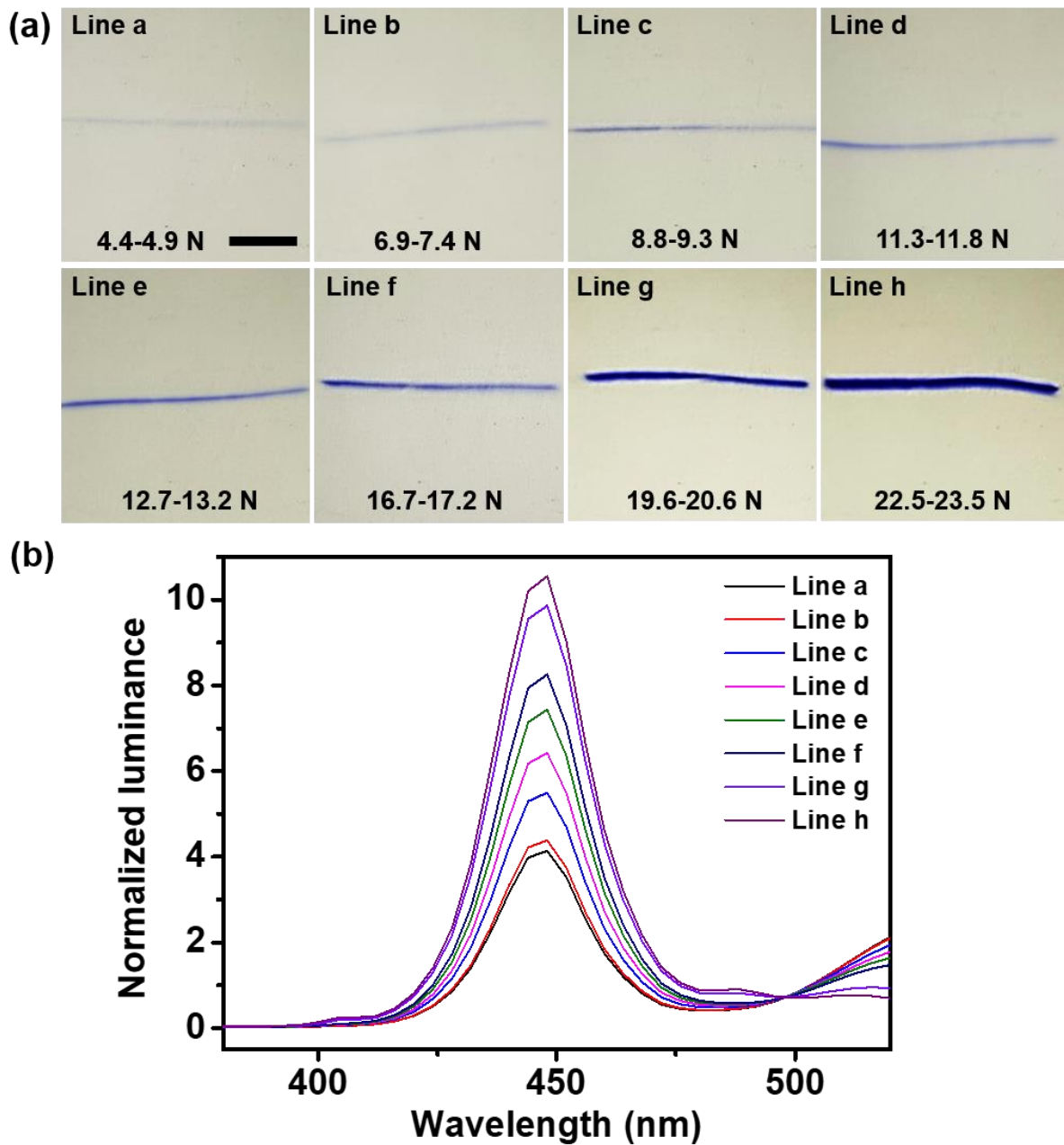


Figure 2.24 The investigation of the relationship between the color intensity and the applied writing force using a spectroradiometer. (a) The photographs of the different lines on the mechanochromic touch screen as a function of writing force and (b) its normalized luminance spectra in visible range (380-520 nm). The horizontal lines are drawn by a stylus as a function of dynamic writing force.

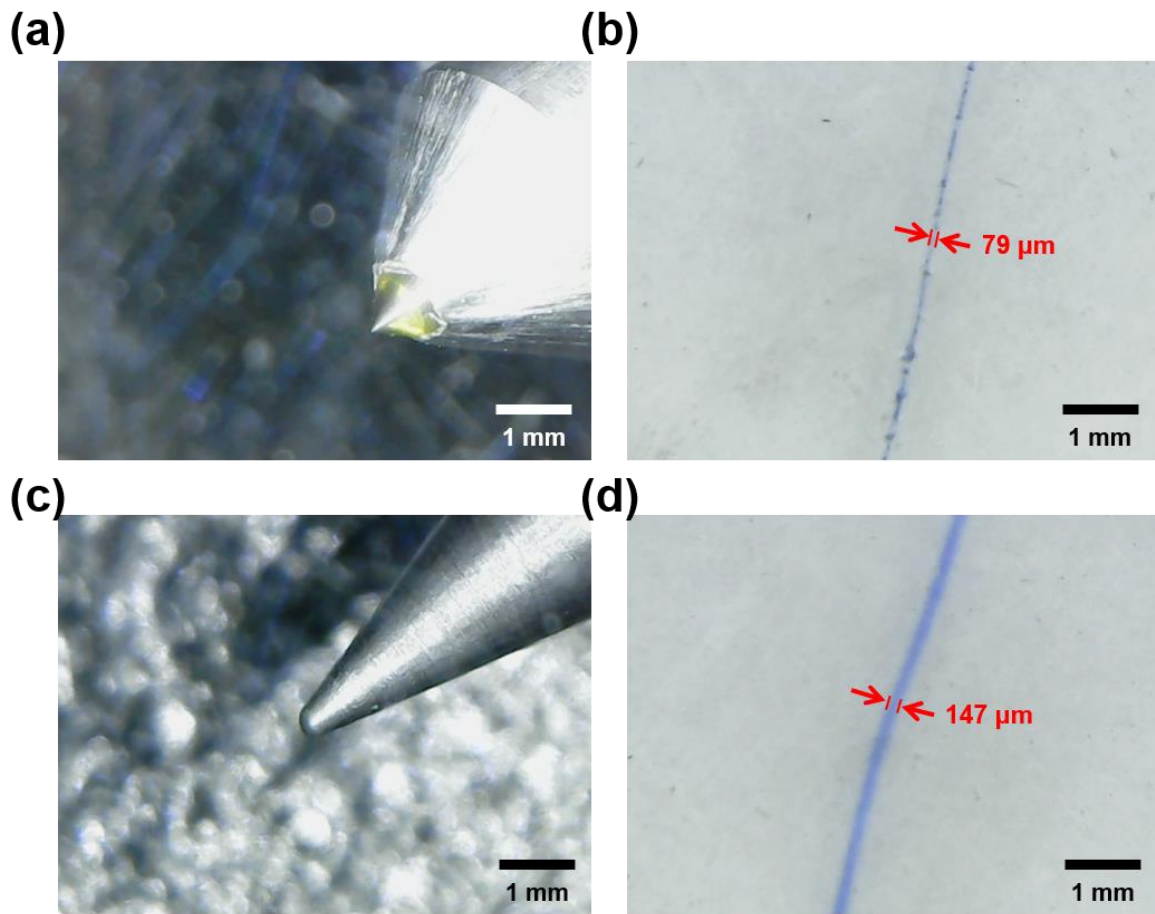


Figure 2.25 The resolution of line width drawn by using different tip size of stylus on mechanochromic SP-PDMS film. (a,b) The stylus with small size of tip can generate very thin blue line with the thickness of $\sim 79 \mu\text{m}$. (c,d) Stylus with large size of tip generates blue line with the thickness of $\sim 147 \mu\text{m}$.

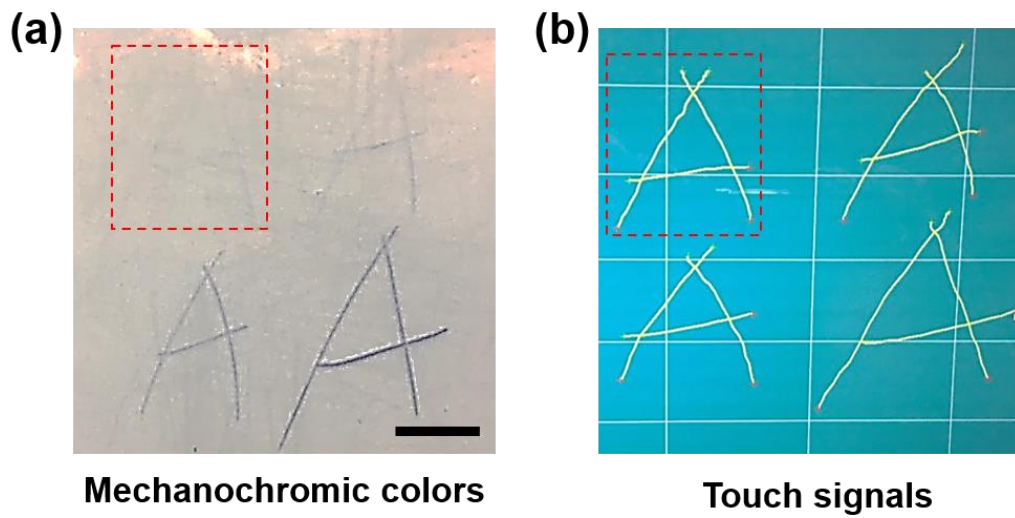


Figure 2.26 Real time monitoring images of mechanochromic colors on the touch screen (a) and its touch signals on the laptop monitor (b). The red dotted squares show the alphabet “A” written by the smallest force during the writing on the mechanochromic touch screen. The scale bar is 2 cm.

2.4 Conclusions

In conclusion, we developed a simple and efficient assembly strategy for the large-area, highly cross-aligned AgNW arrays for TCE applications through a modified bar-coating assembly. As opposed to conventional solvent-evaporation-induced assemblies, which are slow and produce nonuniform conductive networks, our modified bar-coating strategy enables fast, efficient, and uniform alignment of NWs in a large area by simply dragging the Meyer rod over AgNW solution on the target substrates. The cross-aligned AgNW arrays exhibited excellent electrical conductivity as well as optical transmittance over large area of film (R_s of $21.0 \Omega \text{ sq}^{-1}$ at 95.0 % of T over $20 \times 20 \text{ cm}^2$ area) with a FoM value of 479, which is much higher than that of the random AgNW networks (FoM = 254). For the potential applications of large-area cross-aligned AgNW transparent electrodes, we demonstrated large-scale, flexible, and transparent touch screens using resistive touch sensor based on cross-aligned AgNW electrodes, which exhibited highly uniform and precise touch sensing performance across the entire region. In addition, the combination of the force-sensitive touch screens and a mechanochromic SP-PDMS composite film has been developed to simultaneously detect human writing force and location. Our modified bar-coating assembly is not limited to AgNWs, but can be extended to align other types of metallic and semiconducting one-dimensional nanomaterials (copper, silicon, indium phosphide, *etc.*), as long as the NWs are formed in a solution state. Therefore, we anticipate that the suggested technique provides a robust and powerful platform for the controllable assembly of NWs beyond the scale of the conventional fabrication techniques, which can find diverse applications in multifunctional flexible electronic and optoelectronic devices.

Chapter 3. Orthogonal AgNW-embedded hybrid nanomembranes (NMs) for skin-attachable acoustic device applications

3.1 Introduction

Recently, various electronic devices have been developed to mimic the comprehensive capabilities of the human senses for a wide range of potential applications, such as electronic skin (E-skin) for tactile sensing,¹⁵⁴⁻¹⁵⁶ artificial basilar membranes for hearing,^{73, 74} and an artificial throat for speaking.⁷ The human voice has been an important bio-signal for realizing user interfaces with the rapid growth of the “Internet of Things (IoT)” interconnecting humans and machines. In addition, acoustic hearing and speaking devices have attracted great interest as essential technologies for many potential human-machine interactive applications, such as voice security, the control of drones and robots, communication with artificial intelligence (AI), and many kinds of voice recognition system.^{157, 158} For these applications, personal wearable acoustic devices require advanced flexible, portable, and miniaturized appliances capable of detecting or producing the human voice, as well as sounds.^{7, 76, 159-162} Previously, Fan et al. demonstrated an ultrathin, self-powered, and paper-like microphone for recording the human voice. This microphone generated a triboelectric voltage in response to sound pressure.¹⁶³ In addition, Tao et al.⁷ developed a graphene-based artificial throat, which can function as both loudspeaker and microphone. Despite the high-level of performance and functionality available from these flexible acoustic devices, they remain rigid, which prevents their intimate integration with the human skin or other electronic devices intended for a wearable device platform. Furthermore, wearable electronics are nowadays required to be ultrathin, lightweight, and transparent to offer better convenience and appearance,¹⁶⁴ which may yield emerging technologies, such as imperceptible electronics, skin-attachable E-skin, and conformal electronics.^{10, 165-171} Based on these concepts, highly conformal device/skin contact has become an essential feature because such devices can be directly attached to an uneven surface or even human skin, which can be characterized as a curvilinear and non-flat surface with a complex topology.¹⁷² To achieve conformal device/skin contact, various approaches have been suggested, including decreasing the substrate thickness, using bio-inspired structures, and adopting a micro-hair architecture, thus enabling the realization of a conformal interaction with the skin.¹⁷¹⁻¹⁷³

Free-standing nano-membranes (NMs) with a nanoscale thickness of less than a few hundred nanometers can provide a powerful platform for conformal electronics that offers many features such as lightness, excellent flexibility, optical transparency, and conformability,^{174, 175} which are not available with bulk materials. Graphene-based conformal devices formed on ultrathin polymer NM substrates

have been developed for skin-attachable devices.¹⁷¹ In addition, conformal tactile sensors fabricated by forming MoS₂ semiconductors on NM substrates have demonstrated good optical transparency and mechanical flexibility for high sensitivity E-skin applications.¹⁷⁰ Although such NM-based electronics are characterized by an extremely low bending stiffness, making them capable of achieving conformal contact with an uneven surface, the mechanical properties of such polymeric NMs are still limited by their low fracture toughness, which can result in mechanical failures, such as cracks or voids caused by the application of an externally applied strain.

Hybrid NMs differ from polymeric NMs, in that the electrical, optical, and mechanical properties of the NMs are determined by the type of the loading material, which can be metal nanoparticles (NPs), metal nanowires (NWs), carbon nanotubes (CNTs), or graphene.^{174, 176-178} In this respect, silver nanowire (AgNW)/polymer composite NMs are attractive candidates because they possess excellent mechanical and electrical/optical properties due to the large aspect ratio of the AgNWs used as reinforcement.^{176, 179} In addition, AgNW networks can be easily prepared by cost-effective and large-scale solution-based processes, such as spin-coating, drop-casting, rod-coating, and spray-coating.^{101-104, 110} A few studies have addressed the mechanical properties of free-standing AgNW/polymer composite NMs formed using a layer-by-layer (LbL) assembly technique.^{176, 180} Gunawidjaja et al. investigated the mechanical properties of unidirectionally oriented AgNW embedded in polymeric NMs, which results in a significant enhancement of the mechanical strength along the NW orientation.¹⁸⁰ However, the scalability and fabrication process are not suitable for commercial applications. Furthermore, to the best of our knowledge, there have been no attempts to exploit hybrid NMs with an AgNW network to fabricate NM-based wearable electronic devices.

Herein, we introduce ultrathin, conductive, and transparent hybrid NMs that can be applied to the fabrication of skin-attachable NM loudspeakers and microphones, which would be unobtrusive in appearance due to their excellent transparency and conformal contact capability. Our hybrid NMs consist of an orthogonal AgNW array embedded in a polymer matrix, which substantially enhances the electrical and mechanical properties of ultrathin polymer NMs without any significant loss in the optical transparency due to the orthogonal array structure.

3.2 Experimental Details

Sample preparation: Si substrates were cleaned with isopropyl alcohol and D. I. water using ultrasonication for 5 min, respectively. ZnO films were deposited on Si substrates by a RF sputtering process to act as a sacrificial layer. The ZnO layer was treated with O₂ plasma for 5 min to produce the surface wettability and hydrophilicity. Poly-L-lysine (PLL) with amine functional groups was applied to the ZnO films by spin-coating at 4000 rpm for 60 s. Orthogonal AgNW arrays were fabricated on the PLL-treated ZnO films by using a modified bar-coating technique, in which AgNW ink (Nanopyxis Corp.) containing 0.15 wt.% AgNWs in ethanol with an average length of 20 μm and a diameter of 35 nm was used. Parylene-C films were deposited by a CVD method using a parylene coater (Alpha plus Corp.) on the orthogonal AgNW array to fabricate the hybrid NMs. The as-fabricated hybrid NMs on the ZnO film/Si substrate were placed in an etchant solution (citric acid 10 wt.% dispersed in D. I. water) to remove the ZnO sacrificial layer, which enables the production of free-standing hybrid NMs. The hybrid NM loudspeaker was fabricated by connecting two Cu wires and pasting liquid metal (Eutectic Gallium-Indium) to the two edges of hybrid NM. For the fabrication of microstructure-patterned PDMS film, PDMS films were prepared by mixing silicone elastomer base (Sylgard 184, Dow Corning) and a curing agent in the ratio of 10:1. The well-mixed liquid PDMS prepolymer was stored in a vacuum desiccator for 30 min to eliminate air bubbles. Subsequently, the liquid PDMS prepolymer was poured onto Si micromolds with different micropatterns (i. e. line, pyramid, pillar, and dome) and thermally annealed at 90°C for 3 hours.

Characterization: The surface morphology of orthogonal AgNW array was examined by an optical microscope (PSM-1000, Olympus). The sheet resistance of the orthogonal AgNW array was measured using a four-point probe method (Keithley 2400). The optical transmittance in the visible range was determined using UV-vis spectroscopy (JASCO 620). The total thickness of the NMs was measured by using atomic force microscopy (DI-3100, Veeco). The applied AC voltage was generated by a function generator (AFG 3011C, Tektronix). The surface temperature of hybrid NM under the application of AC voltage was monitored by an IR camera (Therm-App TH, Therm-App). A dynamic signal analyzer (National Instruments Corp.), integrated with a commercial microphone (40PH, G.R.A.S.) was used to collect the sound emitted by the loudspeaker and analyze the SPL and frequency. The output voltage of the NM microphone was measured using an oscilloscope (DPO 2022B, Tektronix). The adhesion force of micropatterned PDMS films was measured by a texture analyzer (TXA, YEONJIN S-Tech). The voice-based security system was built by using LabVIEW software with the analysis of FFT.

3.3 Results and Discussion

Ultrathin, transparent, and conductive AgNW nano-membranes. Figure 3.1a is a schematic of the fabrication procedure for transparent and conductive hybrid NMs using orthogonal AgNW arrays as the nano-reinforcement, as well as a polymer matrix. Zinc oxide (ZnO) films (thickness: ~200 nm) deposited on silicon (Si) substrates are prepared as a sacrificial layer, such that the NMs can be released from the Si substrate after the fabrication process. Here, ZnO films were chosen to ensure the alignment of AgNW arrays, in which the sacrificial films should not be dissolved in both deionized (D. I.) water and ethanol solvent. The orthogonal AgNW arrays were fabricated onto the ZnO layer by using a solution-based bar-coating assembly technique. Subsequently, parylene-C films are deposited on the orthogonal AgNW arrays by a chemical vapor deposition (CVD) method to form a polymer matrix of nanometer thickness. This material was chosen because of its good bio-compatibility and chemical stability.¹⁸¹ The as-fabricated hybrid NMs on Si substrates were placed in an etchant solution (citric acid 10 wt.% dispersed in D. I. water) to dissolve the ZnO layer and release the hybrid NMs. Figure 3.1b shows a hybrid NM suspended on the surface of the etchant solution. Here, suspended hybrid NMs can be easily transferred without any damage by using anodic aluminum oxide (AAO) templates as a carrier, due to their low friction originated from the nanoporous surface structure (Figure 3.2). Figure 3.1c shows dark-field optical micrographs of an orthogonal AgNW array produced by the bar-coating process. The fast Fourier transform (FFT) image in the inset indicates that the geometry clearly exhibits a cross configuration. The orthogonal AgNW arrays are tightly embedded in the polymer matrix, giving a total thickness of 100 nm, as shown in both the cross-sectional scanning electron microscopy (SEM) and atomic force microscopy (Fig. 3.1d and 3.3).

The optical and electrical properties of the hybrid NMs are determined from the density of the orthogonal AgNW array produced via a multi-step assembly process, in which the density of orthogonal AgNW arrays was controlled by varying the number of coatings (Figure 3.4). For 3 times of multi-step coatings, the pure orthogonal AgNW array shows a high transmittance of 97.4% at the wavelength of 550 nm and a low sheet resistance of 47.4 Ω /sq (Figure 3.4). The pure polymer NM exhibits a high transmittance of 98.2% at the same wavelength. In particular, the hybrid NMs composed of orthogonal AgNW arrays embedded in polymer matrix exhibit an excellent transmittance of 93.1% at wavelength of 550 nm without any significant optical loss, which is comparable to those of other conventional transparent substrates such as polyethylene terephthalate (PET) (92.9%) and glass (93.5%) (Fig. 3.1e). Our hybrid NMs differ from other types of hybrid NMs integrated with nanomaterials, such as NPs, NWs, CNTs, and graphene,^{174, 176-178} in that the orthogonal AgNW arrays provide not only excellent electrical conductivity and optical transparency but also a significant improvement to the overall mechanical properties of the polymer matrix due to the effective interfacial interaction between the

AgNW and the polymer matrix, resulting in efficient load transfer within the polymer matrix.^{182, 183} Consequently, hybrid NMs suspended on the water surface maintain their original shape without any damage, such as cracking or fracturing when struck with a glass rod, or when lifted and lowered with a plastic pipette (Figure 3.1f). Furthermore, our transparent and free-standing hybrid NMs can be transferred on any three-dimensional (3D) surface with a curvilinear and complex morphology due to the low film thickness, which enables to be an imperceptible in appearance (Figure 3.1g-i). Note that hybrid NMs, placed on the back of a person's hand, maintain their electrical conductivity without breaking when subjected to a compression or stretching force.

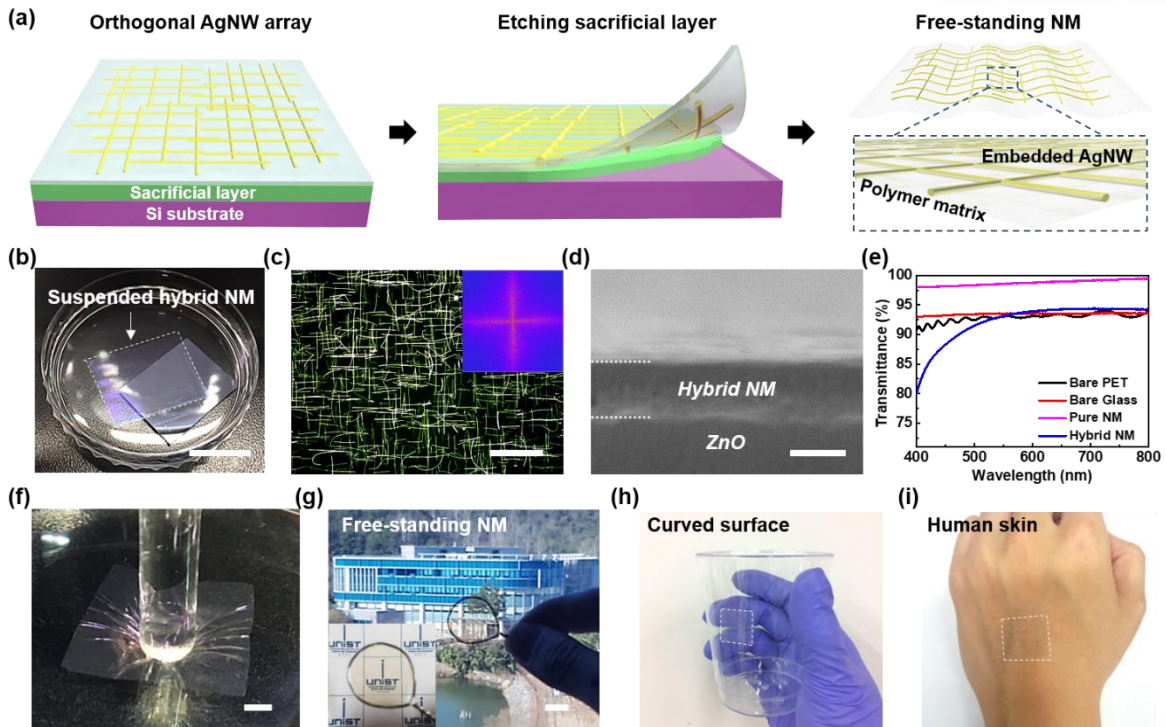


Figure 3.1 Fabrication of free-standing hybrid NMs with orthogonal AgNW array. (a) Schematic of fabrication procedure for free-standing hybrid NMs with orthogonal AgNW array embedded in polymer matrix. (b) Free-standing AgNW composite NMs floating on a surface of water. The scale bar indicates 1 cm. (c) Dark-field optical microscope image of orthogonal AgNW arrays. The inset shows a fast Fourier transform (FFT) image of the optical micrograph, corresponding to its surface geometric structure. The scale bar indicates 40 μm . (d) Cross-sectional SEM image of hybrid NM as-fabricated on a ZnO/Si substrate. The scale bar indicates 100 nm. (e) Optical transmittance of polymer NMs, hybrid NM, bare PET, and bare glass in visible range of 400-800 nm. The glass is used as a reference. (f) Photograph of hybrid NM on surface of water under compressive force applied by a glass rod. The scale bar indicates 3 mm. (g) Free-standing hybrid NM supported by a wire loop. Inset shows the high transparency of the hybrid NM. The scale bar indicates 1 cm. (h) Hybrid NMs transferred onto curvilinear surface and (i) onto human skin.

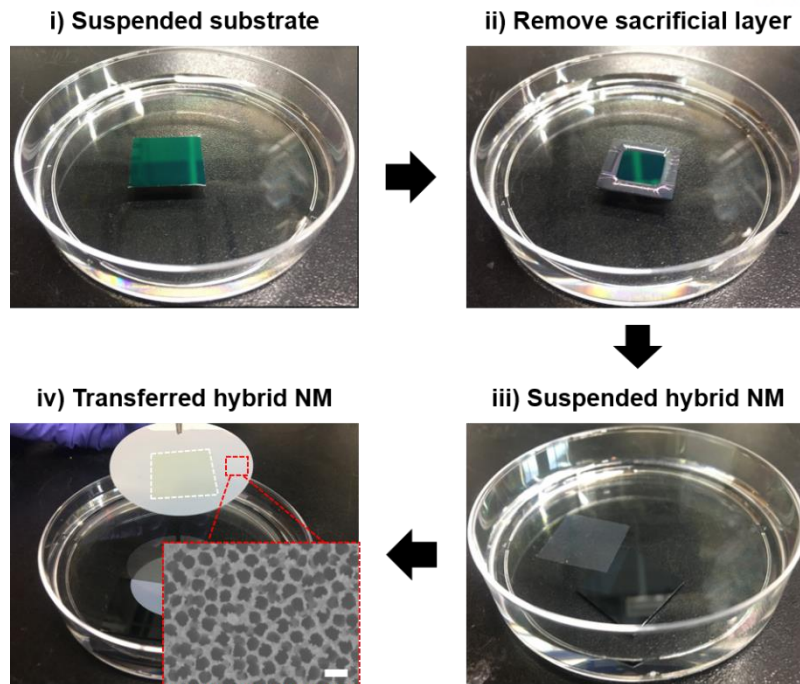


Figure 3.2 Fabrication of free-standing hybrid NM with orthogonal AgNW array by removing the sacrificial layer.

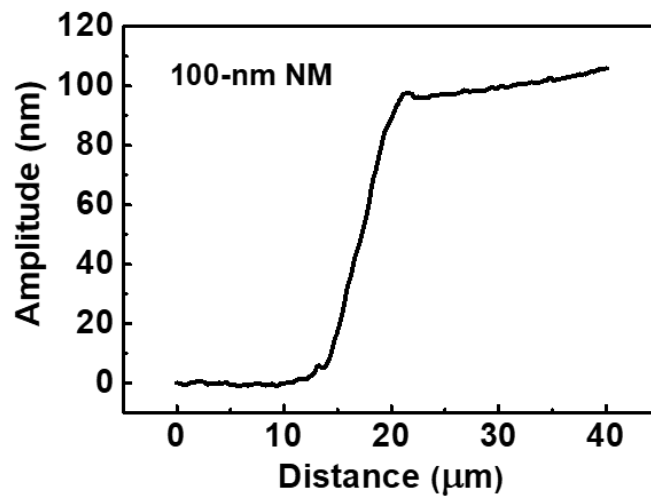


Figure 3.3 Total thickness of hybrid NMs measured by atomic force microscopy.

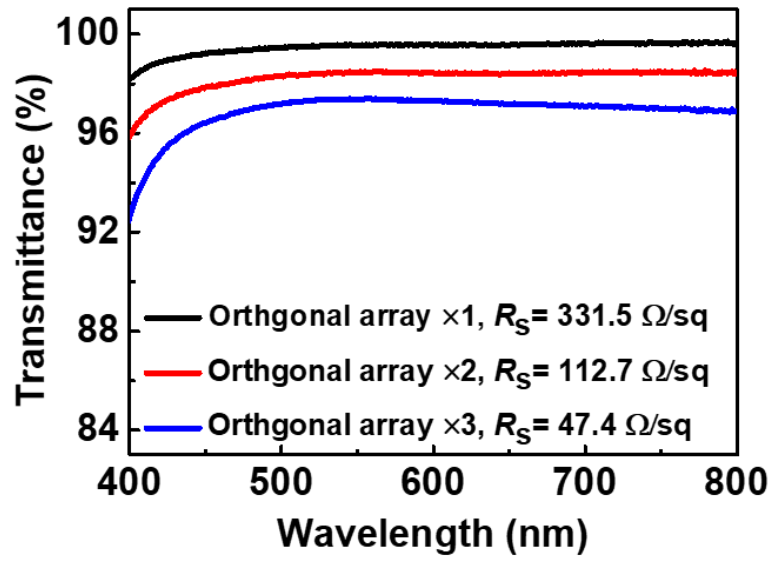


Figure 3.4 Transmittance in visible range of 400–800 nm and corresponding sheet resistance, R_S , of the orthogonal AgNW array with different numbers of orthogonal coatings.

Conformal contact capabilities of skin-attachable hybrid NMs. To quantitatively evaluate the conformal contact capabilities of hybrid NMs, we calculated the bending stiffness (EI) of hybrid NMs. For the calculation of bending stiffness of hybrid nanomembranes, a representative cross-sectional geometry of the thin film is illustrated in Figure 3.5. In this structure, there are n AgNWs with a radius of r and Young's modulus of 83 GPa, which were wrapped by a parylene film with the size of $b \times h$ and Young's modulus of 3.2 GPa. The distance between the neutral axis and bottom of the thin film is

$$y_0 = \frac{h}{2} * \frac{1 + \frac{2h' + 2r}{h} \left(\frac{E_{Ag}}{E_{Pa}} - 1 \right) n\pi r^2 / bh}{1 + \left(\frac{E_{Ag}}{E_{Pa}} - 1 \right) n\pi r^2 / bh} \quad (1)$$

where y_0 is the distance between the neutral axis and bottom of the thin film, h is the thickness of film, h' is the distance between bottom of AgNWs and thin film, r is the radius of AgNWs, b is the width of parylene film, and E_{Ag} and E_{Pa} are the Young's modulus of silver and parylene, respectively. From the value of y_0 , we can calculate the bending stiffness (EI) using the Eq (2) as below:

$$EI = E_{Pa}bh \left(\frac{1}{3}h^2 - hy_0 + y_0^2 \right) + (E_{Ag} - E_{Pa})n\pi r^2 \left[\frac{4}{3}r^2 + 2r(h' - y_0) + (h' - y_0)^2 \right] \quad (2)$$

As a result, hybrid NMs produced a bending stiffness of $5.51 \text{ GPa} \cdot \mu\text{m}^4$ which is comparable with previously reported values.^{169, 171, 184} Therefore, our hybrid NMs offer a high degree of bendability with a small bending radius of $\sim 2.2 \mu\text{m}$ due to their low bending stiffness caused by their nanoscale thickness, which facilitates the intimate contact even with 3D surfaces (Figure 3.6). Figure 3.7a is a schematic of the conformal contact property of a hybrid NM attached to human skin, the epidermis of which has a curvilinear and uneven surface with a complex topography. To prove the conformal contact capability of our NMs, we transferred hybrid NMs to the epidermis of human skin by using an AAO template as a carrier. Figure 3.7b shows a hybrid NM after being transferred to human finger, conformably contacting against fine ridges of the fingertip having a few hundred microns of surface roughness. To further investigate the conformal bendability, the hybrid NMs were transferred to polydimethylsiloxane (PDMS) that had been patterned with lines of widths of 20 and 120 μm . The transferred hybrid NMs were intimately adhered to the line-patterned PDMS surface and even along the edges of the line patterns, implying that the hybrid NMs have an excellent bendability (Figure 3.7c,d and 3.8). To show the conformal contact on the 3D surface, hybrid NMs with different film thicknesses

(40, 100, and 200 nm) were transferred on micropyramid-patterned PDMS substrates (diameter of ~ 10 μm and height of ~ 7 μm) (Figure 3.7e-g). As a result, 40 and 100 nm-thick hybrid NMs can form a conformal contact on the surface of micropyramid-patterned PDMS with the step surface coverage (ratio of film-covered height to the total height of 3D structure) of $\sim 92\%$ and $\sim 73\%$ while 200 nm-thick hybrid NMs cannot conformably cover the surface with the lowest step surface coverage of $\sim 15\%$ (Figure 3.9).

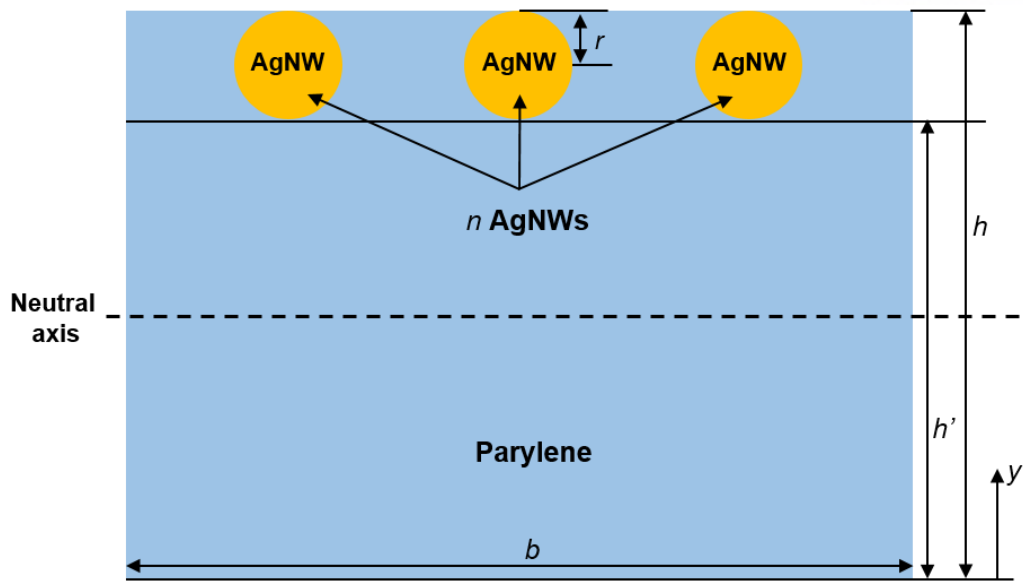


Figure 3.5 The structural design of the hybrid NM for the calculation of the bending stiffness with geometrical parameters illustrated.

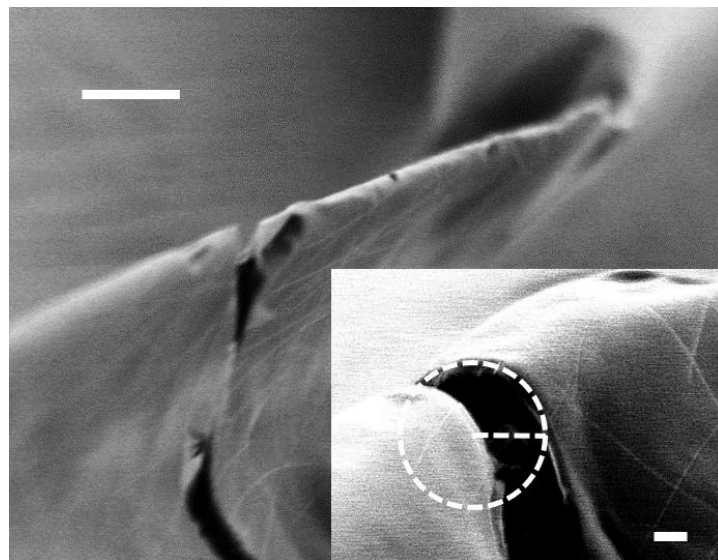


Figure 3.6 SEM images of the hybrid NM folded in half.

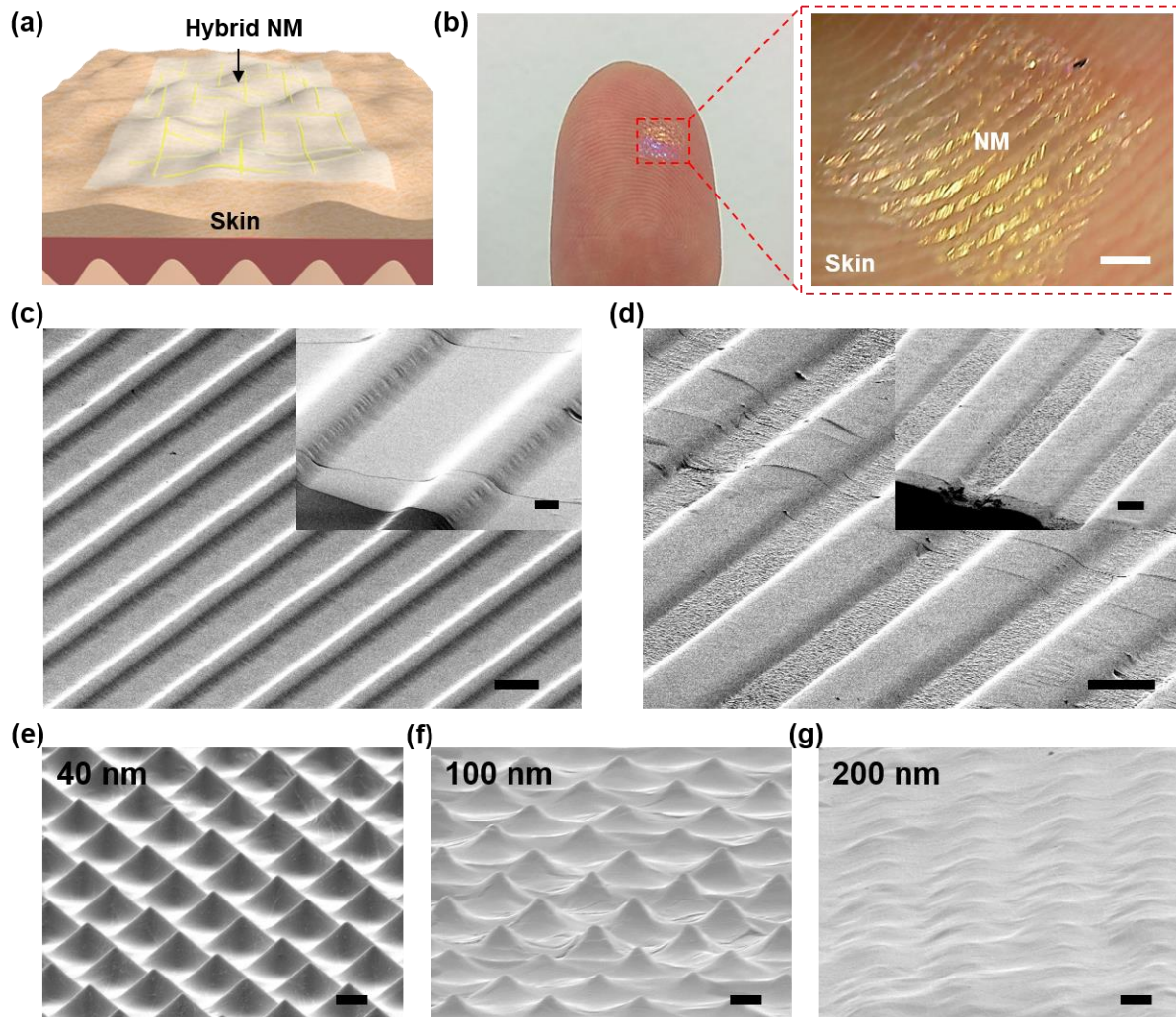


Figure 3.7 Conformal contact of AgNW composite hybrid NMs on 3D microstructures. (a) Schematic of conformal contact of NMs on the skin surface. (b) Hybrid NMs attached to a thumb. The inset shows a micrograph of a hybrid NM on the skin of a fingertip. The scale bar indicates 1 mm. (c) and (d) SEM images of the hybrid NMs transferred on line-patterned 3D PDMS microstructures with a line width of (c) 20 and (d) 120 μm . The scale bars indicate 10 and 20 μm , respectively. The insets show a magnification images with the scale bars indicating (c) 10 and (D) 50 μm . SEM images of the hybrid NMs with different thickness of (e) 40, (f) 100, and (g) 200 nm transferred on micropyramid-patterned 3D PDMS microstructures with diameter of 10 μm and height of 7 μm . All scale bars indicate 5 μm .

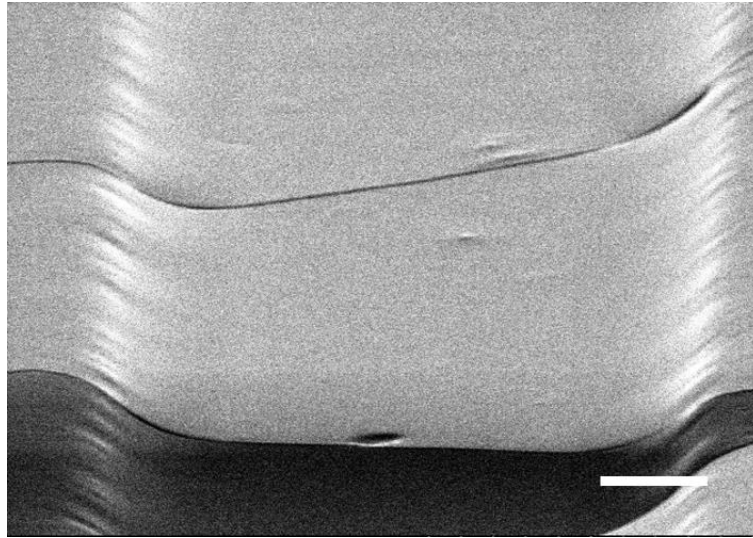


Figure 3.8 High magnitude SEM images of the hybrid NM transferred on the line-patterned PDMS with a line width of 20 μm .

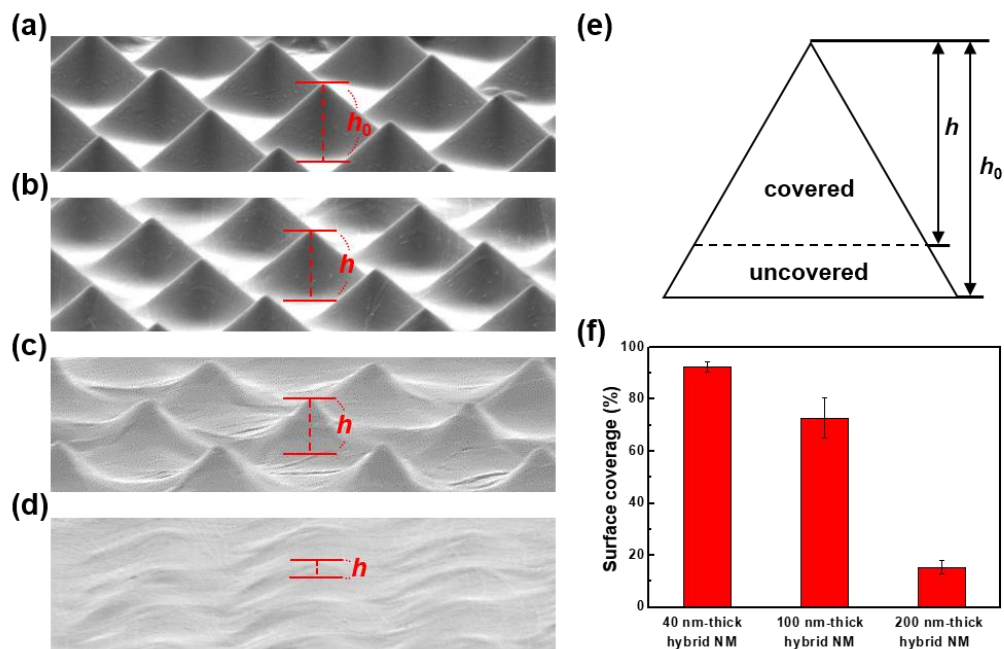


Figure 3.9 Estimated step surface coverage of the hybrid NMs with different thickness placed on a micropyramid-patterned PDMS substrate.

Mechanical properties of hybrid NMs. In general, conventional hybrid NMs containing nanomaterials exhibit enhanced mechanical properties relative to pure polymer NMs due to the reinforcing effect of fillers in the nanocomposite.¹⁷⁶ To evaluate the mechanical properties of hybrid NMs, we performed a mechanical test to measure the Young's modulus (E), as obtained from wrinkles formed by the capillary force generated by placing a droplet of water in the center of a floating NM, using an optical microscope (Figure 3.10a).¹⁸⁵ We observed that the number of wrinkles (N), as induced by the surface tension of the water droplet, decreased as the density of the orthogonal AgNW array increased (Figure 3.11). Hybrid NMs generate fewer wrinkles ($N < 39$) than pure polymer NMs ($N > 49$) without AgNWs. To further investigate the effect of an orthogonal AgNW array as a loading material on the Young's modulus, we plotted the number of wrinkles in the NM as a function of the combined dependence on the radius of the water droplet (a) and the thickness of the NM (h), captured by scaling $N \sim a^{1/2}h^{-3/4}$, as shown in Figure 3.12. Thus, the Young's modulus of the hybrid NMs was calculated using Eq.(3)¹⁸⁵;

$$N = C_N \left[\frac{12(1-A^2)\gamma}{E} \right]^{1/4} a^{1/2} h^{-3/4} \quad (3)$$

where C_N is the numerical constant, A is the Poisson ratio, and γ is the surface tension of the droplet. We obtained $C_N=3.2$ from the experimental results with the slope of the fit line shown in Figure 3.12. The Young's modulus of the hybrid NMs increases linearly with an increase in the density of the orthogonal AgNW arrays (Figure 3.10b). We also acquired the bending stiffness of hybrid NMs from the experimentally measured Young's modulus in Figure 3.10b. We compared the calculated and measured bending stiffness of hybrid NMs in Figure 3.10c. To investigate the measured bending stiffness of hybrid nanomembranes as a function of the density of orthogonal AgNW arrays, we assumed the hybrid NM as a single film and calculated the bending stiffness using the Eq (4);

$$EI = E_{Hybrid} bh \left(\frac{1}{3} h^2 - hy_0 + y_0^2 \right) \quad (4)$$

Here, E_{Hybrid} is the Young's modulus of hybrid NM with orthogonal AgNW arrays, which was experimentally obtained from the capillary wrinkling test. The measured bending stiffness (5.18 to 9.62 GPa· μm^4) increases with the density of orthogonal AgNW arrays, which is similar with the tendency of the calculated bending stiffness (5.33 to 6.88 GPa· μm^4). The slight difference in the calculated and measured values is attributed to the presence of random NW-NW junctions, which were not considered in the bending stiffness calculation in Figure 3.5.

We also performed an indentation test to measure the mechanical strength and ductility of the hybrid NMs while varying the density of the orthogonal AgNW array. In this test, free-standing hybrid NMs, placed over a hole in the supporting plate, were deformed by the application of a compressive force and then fractured when the force exceeded the maximum load that could be applied to the NMs (Figure 3.13). Figure 3.10d shows typical force vs indentation displacement (F - d) curves obtained by increasing the density of the orthogonal nanowire arrays. The F - d curves shown in Figure 3.10d clearly show the increase in the tensile strength of the parylene as the density of the stiff nanowire array increases. Generally, adding NPs increases the stiffness and strength of a composite film. On the other hand, however, this reduces the ductility of the composite film. Contrary to this behavior, our hybrid NM exhibits a progressive increase in the indentation displacement as the AgNW density increases due to the high ductility of nano-sized AgNWs with a large aspect ratio and stretchability of AgNW networks, which is advantageous for flexible device applications.

The complete loading and unloading curves for polymer NMs and hybrid NMs are shown in Figure 3.14. For the cyclic test, a predefined indentation load was repeatedly applied on the NMs at a loading/unloading rate of 0.1 mm/sec. For an indentation load of ~ 27 mN, F - d curves exhibit hysteresis behaviors for both hybrid and polymer NMs, indicating the inelastic deformation of AgNW networks and parylene polymer chains in the NMs during the indentation. The larger hysteresis of hybrid NMs than that of polymer NMs can be attributed to the larger inelastic deformation of hybrid NMs, in which the breakdown of interfacial bonding between AgNW and polymer matrix causes the larger energy dissipation than those by the polymer chain rearrangement. During the repeated loading-unloading cycles, the hysteresis gradually decreases. In particular, the hysteresis of hybrid NMs is greatly suppressed due to the permanent failure of AgNW and polymer interface. At a lower indentation load (~ 11 mN), both hybrid and polymer NMs exhibit weak hysteresis behaviors due to the elastic deformations. The maximum load and displacement that can be applied to the hybrid NMs until the failure gradually increases with the density of the orthogonal AgNW array (Figure 3.10e). The maximum load-displacement of the hybrid NMs with orthogonal AgNW arrays (load: 84.3 ± 3.03 mN, displacement: 2.85 ± 0.05 mm) is much higher compared with that of the pure polymer NMs (load: 44.8 ± 7.05 mN, displacement: 1.12 ± 0.06 mm). This could be attributed to the efficient load transfer between the orthogonal AgNW array and the polymer matrix in a nanocomposite system. These results suggest that the orthogonal AgNW array is an excellent loading material for enhancing the overall mechanical properties of a hybrid NM system.

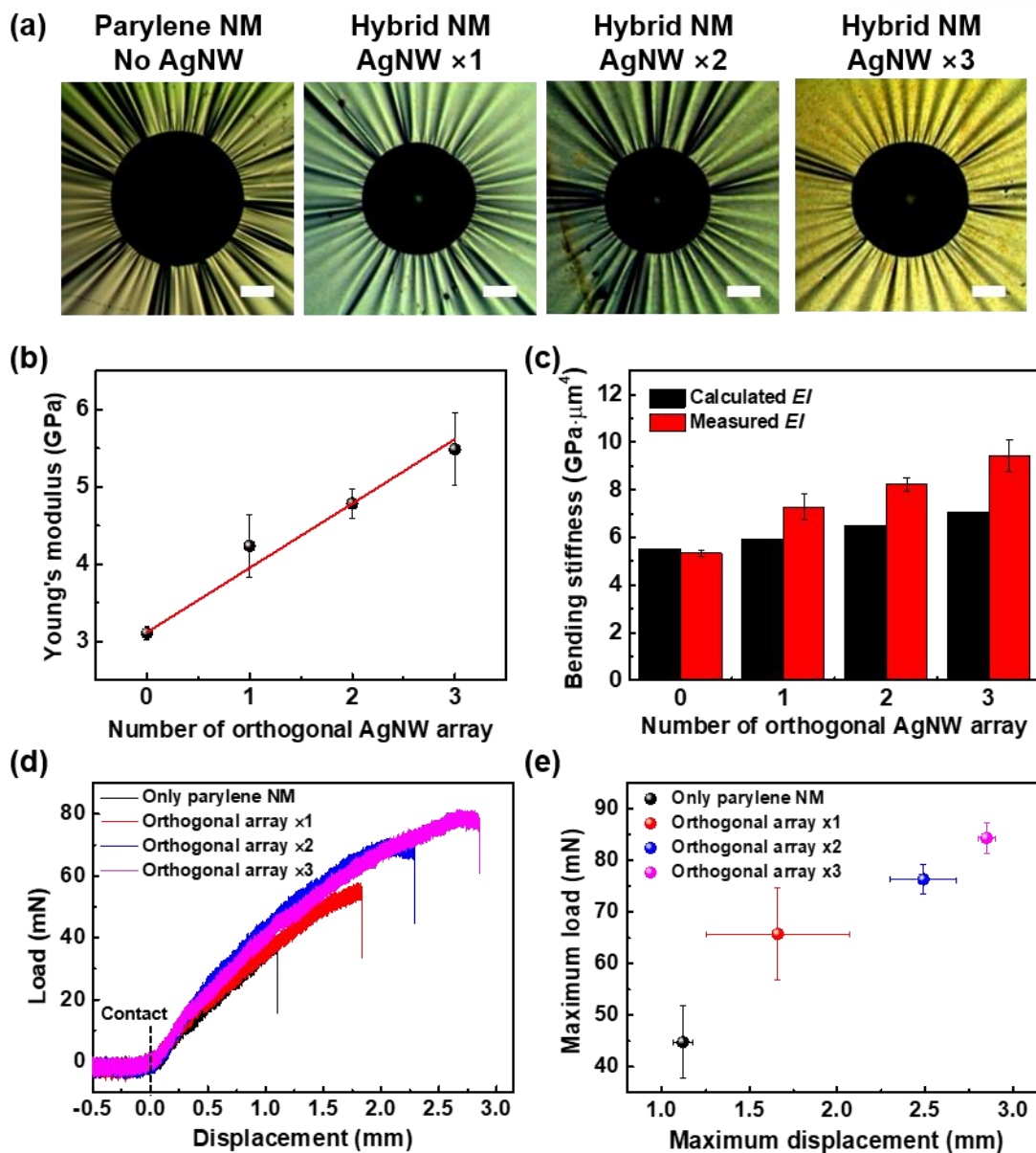


Figure 3.10 Mechanical properties of hybrid NMs with orthogonal AgNW array. (a) Free-standing hybrid NMs with different densities of orthogonal AgNW arrays floating on the water surface. NMs are wrinkled by a water droplet of radius $a \approx 0.3$ mm. The number of wrinkles decreases as the density of AgNWs increases. All scale bars indicate $200 \mu\text{m}$. (b) Young's modulus (E) of NMs as calculated from the wrinkle tests. (c) Comparison of calculated and experimental bending stiffness of hybrid NMs with different density of orthogonal AgNW arrays. Measured bending stiffness was calculated by using Young's modulus experimentally obtained from capillary wrinkling method. (d) Applied indentation load versus displacement of free-standing hybrid NMs as a function of density of orthogonal AgNW array. (e) Maximum indentation load versus displacement of hybrid NMs as a function of orthogonal AgNW arrays.

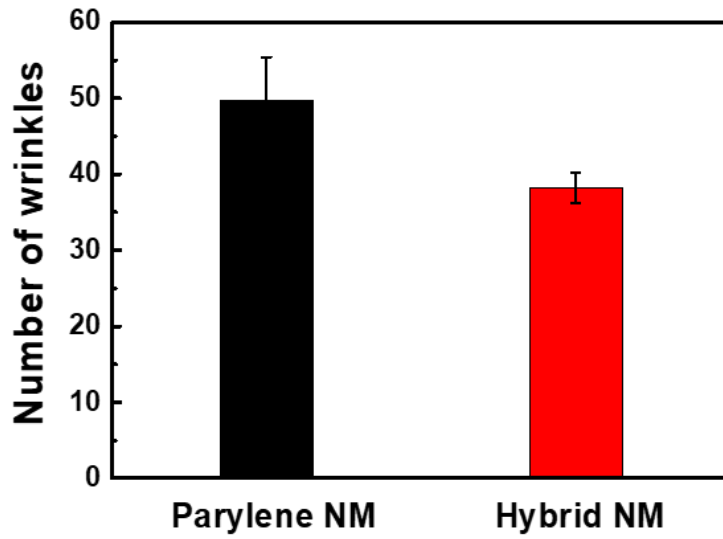


Figure 3.11 Number of wrinkles generated from a pure parylene NM and hybrid NMs.

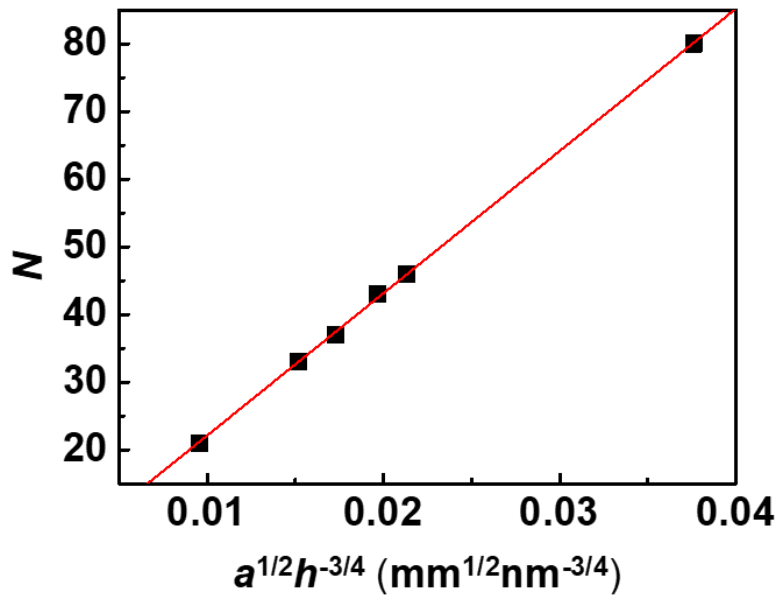


Figure 3.12 Variation in the number of wrinkles N as a function of $N \sim a^{1/2}h^{-3/4}$.

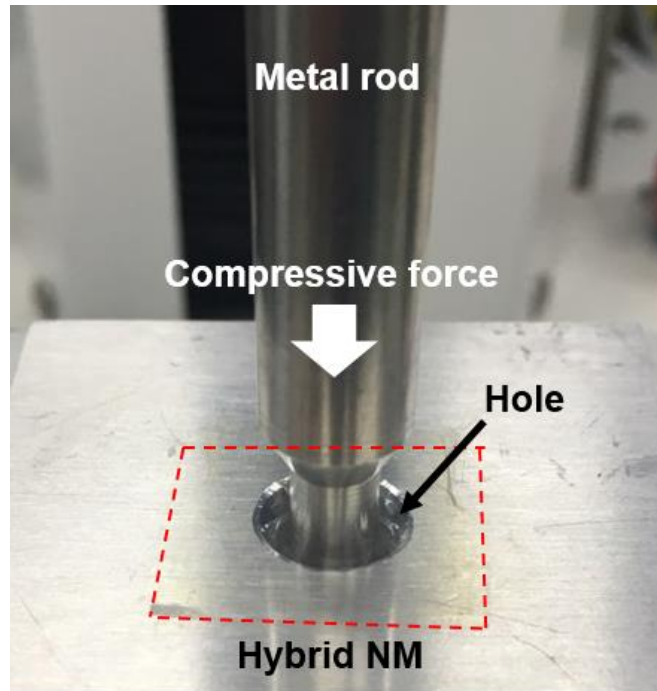


Figure 3.13 Indentation test for measuring the mechanical properties of NMs.

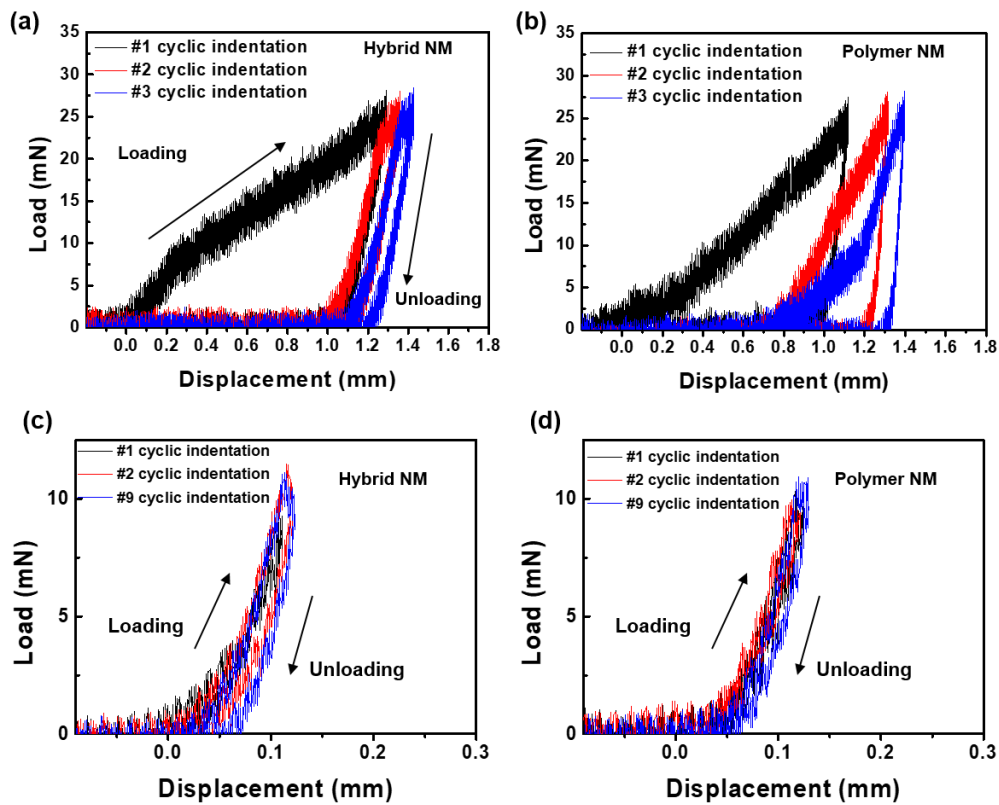


Figure 3.14 Loading-unloading indentation test.

Skin-attachable and transparent NM loudspeaker. For a proof-of-concept demonstration, we fabricated a skin-attachable loudspeaker using hybrid NMs. The speaker can emit thermoacoustic sound by the temperature-induced oscillation of the surrounding air. Here, the temperature oscillation is caused by Joule-heating of the orthogonal AgNW array upon the application of an AC voltage. Figure 3.15a is a schematic of the skin-attachable NM loudspeaker emitting thermoacoustic sound, where periodic Joule-heating generates a temperature oscillation, which then propagates into the surrounding medium, causing an air pressure oscillation (i.e., a sound wave). An infrared image of the loudspeaker with an orthogonal AgNW array reveals highly uniform Joule-heating performance with a slight increase in the surface temperature during a flow of AC 10 V at 10 kHz (Figure 3.16). Figure 3.15b shows the acoustic measurement system used to analyze the sound, as emitted from the NM loudspeaker upon the application of a voltage with a sinusoidal waveform, produced by a function generator. A commercial microphone was used to collect and record the sound produced by the loudspeaker. To characterize the sound generation of loudspeaker, we confirmed that sound pressure level (SPL) of the output sound increases linearly as the distance between the microphone and loudspeaker decreases (Figure 3.17).

Figure 3.15c shows the sound pressure for a hybrid NM-based loudspeaker and a thick PET film-based loudspeaker (with a PET thickness of around 220 μm) with an orthogonal AgNW array as a function of the input power at a frequency of 10 kHz and a fixed measurement distance of 3 cm. The output sound pressure from both loudspeakers increases linearly as the input power is increased. Notably, the loudspeaker based on a hybrid NM produces a much larger sound pressure than that using thick PET film with an orthogonal AgNW array at the same input power. Figure 3.15d shows the SPL spectrum as the sound frequency is varied over a range of 1–20 kHz. We confirmed that the SPL of both thick-film and the NM loudspeakers gradually increases with an increase of sound frequency. These results can be explained by the following theoretical formula:⁷²

$$P_{\text{rms}} = \frac{\sqrt{\alpha}\rho_0}{2\sqrt{\pi}T_0} \cdot \frac{1}{r} \cdot P_{\text{input}} \cdot \frac{\sqrt{f}}{C_s} \quad (5)$$

where, P_{rms} is the root-mean-square sound pressure, α is the thermal diffusivity of the ambient gas, ρ_0 is the density, T_0 is the temperature, r is the distance between the loudspeaker and the microphone, P_{input} is the input power, f is the sound frequency, and C_s is the heat capacity per unit area. Our experimental results are well matched with the theoretical prediction in equation (5), where the generated sound pressure increases as a function of input power and sound frequency. Notably, NM loudspeakers produce a massive enhancement in the SPL across the entire measured frequency range compared to

thick-film loudspeakers, attributed to a reduction in heat loss caused by substrates.^{71, 186} In general, a lower thermal effusivity of the substrate is preferred to facilitate the effective exchange of thermal energy with the surrounding air to efficiently generate sound.¹⁸⁶ The thermal effusivity (e) can be calculated using the equation $e = (\kappa \cdot \rho \cdot C_p)^{1/2}$ where κ is the thermal conductivity, ρ is the density, and C_p is the heat capacity. We obtained $e = 262 \text{ W} \cdot \text{s}^{1/2} / \text{m}^2 \cdot \text{K}$ for the parylene NMs using literature values of $\kappa = 0.08 \text{ W/mK}$, $\rho = 1230 \text{ kg/m}^3$, and $C_p = 700 \text{ J/kg} \cdot \text{K}$, which is a small value compared with other materials.⁷¹ In the NM loudspeakers, however, the low film thickness is a more crucial factor to minimize the heat dissipation for the enhanced sound pressure than the thermal effusivity.¹⁸⁶ To further validate the effect of heat loss for the low NM thickness, we calculated the theoretical SPL for both thick PET film and hybrid NM loudspeakers as a function of frequency using the Eq.(6),¹⁸⁶

$$\Delta P = \frac{3}{4\pi} \frac{P_{input} f}{v_{air}^2} \frac{e_{air}}{r \sqrt{2e_{air} + (d_{sub} \rho_{sub} C_{p,sub} + d_{film} \rho_{film} C_{p,film}) \sqrt{2\pi f}}} \quad (6)$$

where ΔP is the sound pressure, v_{air} is the speed of sound in the air, e_{air} is the thermal effusivity of air, ρ_{sub} and ρ_{film} are the density of substrate and film, $C_{p,sub}$ and $C_{p,film}$ are the heat capacity of substrate and film, and d_{sub} and d_{film} are the thickness of a substrate and film, respectively. We obtained SPL of both loudspeakers by converting the sound pressure to SPL. As a result, the change of theoretical SPL as a function of frequency for both loudspeakers exhibited a good agreement with our experimental results (Figure 3.15d). Note that the huge enhancement in SPL is not mainly attributed to the discrepancy in thermal effusivity between parylene NMs and PET films. From the theoretical calculation of SPL, the influence of thermal effusivity on the SPL is negligible for films with the nanoscale thickness while the low thermal effusivity enhances the SPL in the case of thick-film loudspeaker system (Figure 3.18). Therefore, the considerable enhancement in the SPL of the NM loudspeaker could be attributed to the efficient heat transfer to the surroundings resulting from the reduction in the heat loss to the very thin substrate.⁷¹ To demonstrate wearable and skin-attachable applications, the NM loudspeaker was mounted to the back of a subject's hand and connected by two copper-wire electrodes. This loudspeaker is unobtrusive in appearance due to the high transmittance and intimate contact with the human skin (Figure 3.15e). We were able to play and recognize Paganini's well-known "La Campanella" violin concerto when played through the NM loudspeaker attached to the skin.

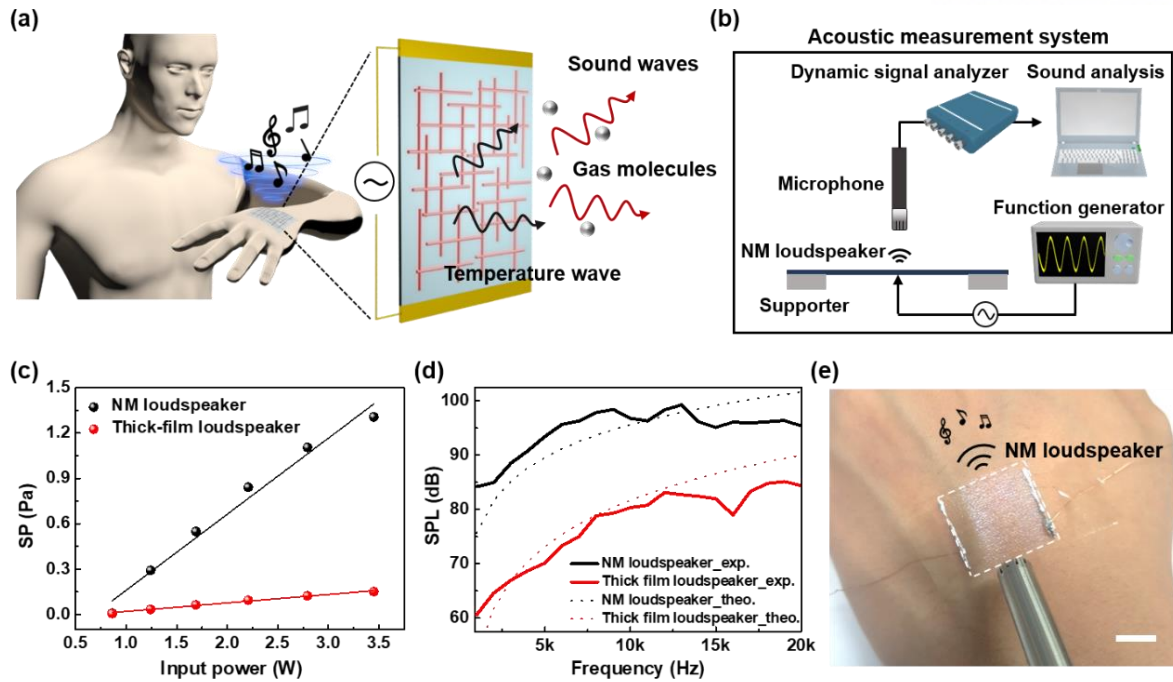


Figure 3.15 Skin-attachable NM loudspeaker. (a) Schematic of skin-attachable NM loudspeaker with orthogonal AgNW array. Sound is generated by temperature oscillation produced by applying an AC voltage. (b) Acoustic measurement system where sound emitted from NM loudspeaker is collected by a commercial microphone with a dynamic signal analyzer. (c) Variation in sound pressure (SP) generated from NM loudspeaker and thick film loudspeaker as a function of the input power at 10 kHz. (d) Experimental and theoretical values of sound pressure level (SPL) versus sound frequency for NM and thick PET film loudspeakers. (e) Skin-attachable NM loudspeaker mounted on the back of a hand. The scale bar indicates 1 cm.

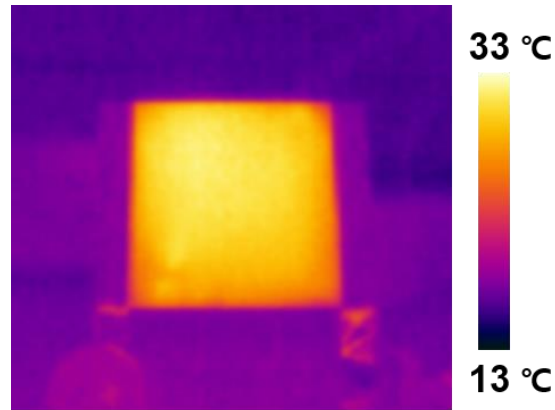


Figure 3.16 Infrared (IR) images of the orthogonal AgNW array with AC 10 V applied at a frequency of 10 kHz.

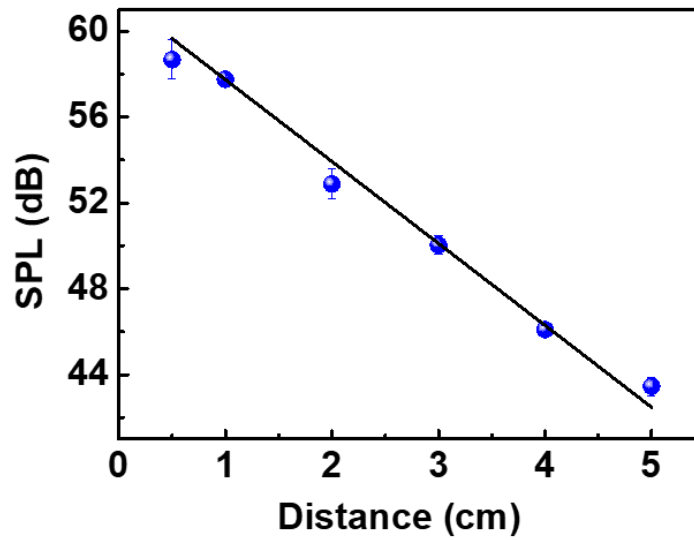


Figure 3.17 SPL versus distance between the commercial microphone and thermoacoustic loudspeaker using an orthogonal AgNW array on a PET substrate.

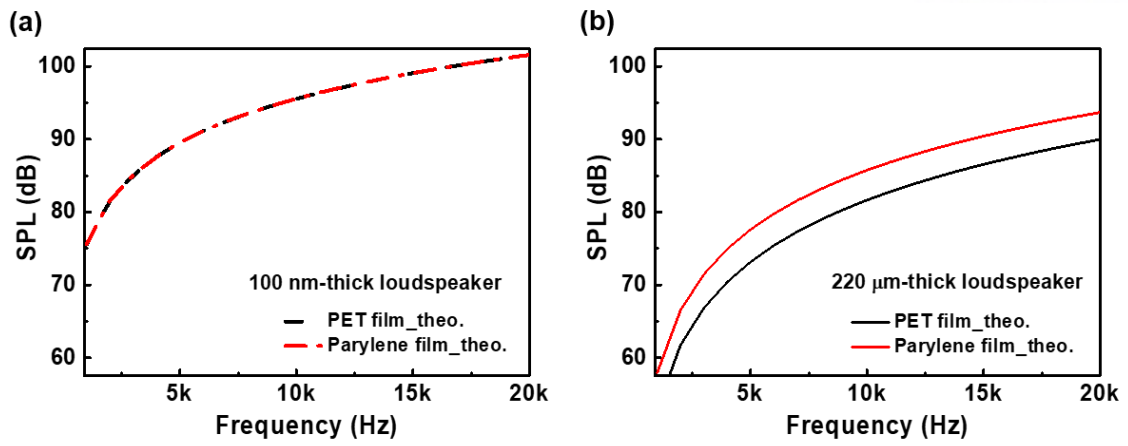


Figure 3.18 Theoretical values of SPL as a function of sound frequency for (a) 100 nm-thick and (b) 220 μm-thick loudspeakers with different substrates.

Wearable and transparent NM microphone. To further demonstrate the applicability of hybrid NMs, we designed a wearable and transparent microphone using hybrid NMs combined with micro-patterned PDMS (NM microphone). The resulting device was able to detect sound and recognize a human voice. Figure 3.19 illustrates the structure of the skin-attachable NM microphone, consisting of a hybrid NM mounted to a holey PDMS film and micropyramid-patterned PDMS film. This sandwich-like structure can precisely detect the sound as well as the vibration of the vocal cords by the generation of a triboelectric voltage resulting from the coupling effect of the contact electrification and electrostatic induction.¹⁸⁷ Figure 3.19b shows the NM microphone, which is highly transparent. The holey PDMS film was used to receive a sound wave and to support free-standing NMs. A micropyramid-patterned PDMS film is selected because it provides the smallest adhesive force with a hybrid NM, in comparison with those of the microdome or micropillar-patterned PDMS films, which can facilitate the contact-separation mode of the NMs (Figure 3.20). To evaluate the sensitivity of the NM microphone in response to sound emissions, we fabricated two different device structures, namely, a free-standing hybrid NM, integrated with a holey PDMS film (NM microphone), and another which was fully adhered to a planar PDMS film without a hole (the so-called “thin-film microphone”, Figure 3.21). In addition, we monitored the voltage waveforms emitted by both microphones in response to sound emitted from a speaker, as schematically illustrated in Figure 3.19c. Both microphones exhibit narrow and sharp output voltage peak across a frequency range of 100 Hz–10 kHz, with the maximum voltage being obtained at 400 Hz, after which it gradually decreases (Figure 3.19d). Notably, the NM microphone produces a much higher output voltage than the thin-film microphone across the overall frequency range. Furthermore, the variations in the output voltage of both microphones were monitored with a decreasing SPL at a frequency of 400 Hz to determine their minimum sound-detection capability (Figure 3.19e). For the same SPL, the output voltage of the NM microphone was higher than that of the thin-film microphone. These results can be attributed to the excellent vibrational sensitivity of the free-standing NM,¹⁷⁴ which enhance the coupling of triboelectric effect with an increase in the gap between the micropyramid-patterned PDMS and free-standing hybrid NM.¹⁸⁸ We monitored the time-dependent variation in the voltage waveforms produced by a human voice. A speech entitled “There’s plenty of room at the bottom” by R. Feynman was played to both the NM microphone and thin-film microphone to demonstrate their ability to monitor acoustic waveforms (Figure 3.19f). The time-dependent waveform of the output voltage and the corresponding spectrograms from the NM microphone (middle) are in good agreement with the original sound waveform and spectrograms (left) of the sentence. On the other hand, the thin-film microphone (right) cannot precisely detect a human voice in that there are some discrepancies in the acoustic waveforms and spectrograms. Moreover, our NM microphone exhibits an excellent acoustic sensing capability, which is comparable to the commercial microphone

(Figure 3.22). We also attempted to detect the vibrations produced by the vocal cords while speaking. We observed that a NM microphone attached to a person's neck can clearly detect the phonation of different words. This result indicates the applicability of the NM microphone to wearable or skin-attachable electronics, providing them outstanding acoustic sensing capabilities.

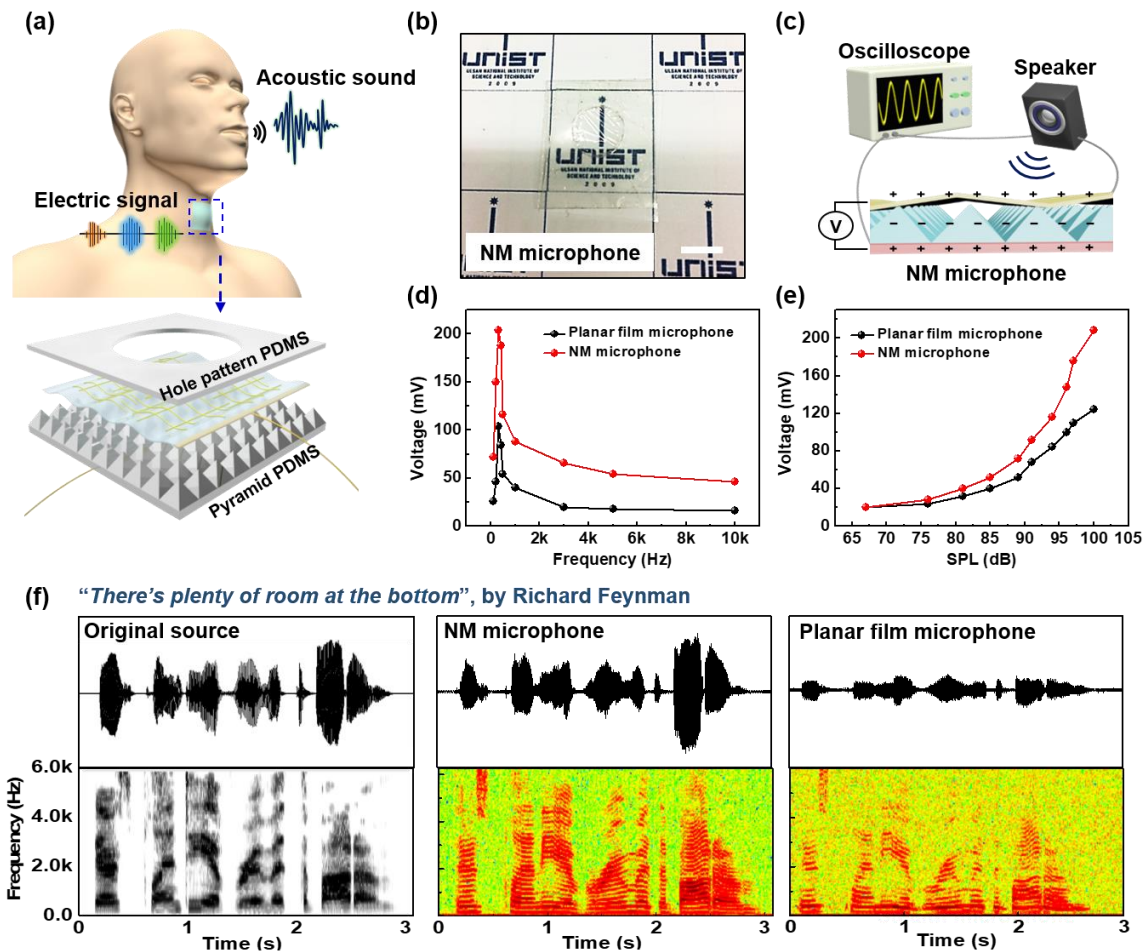


Figure 3.19 Wearable and transparent NM microphone. (a) Schematic of wearable NM microphone device. (b) Transparent NM microphone placed over "UNIST" logo, illustrating its transparent and unobtrusive appearance. The scale bar indicates 1 cm. (c) Sensing measurement system for NM microphone. Variation in the output voltages as a function of (d) sound frequency and (e) SPL for NM microphone and thin-film microphone. (f) Waveform and short-time Fourier transform (STFT) signals of original sound ("There's plenty of room at the bottom", left) extracted by the sound wave analyzer, the signal read from the NM-based microphone (middle), and thin-film microphone (right)

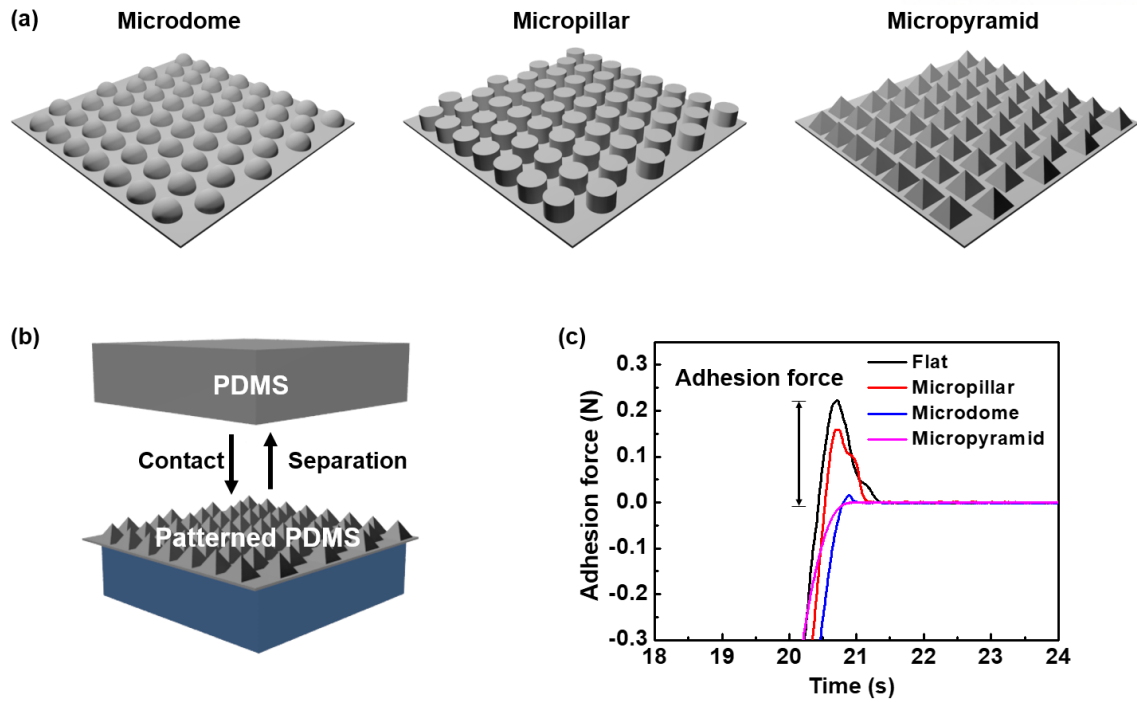


Figure 3.20 Comparison of adhesion force of various micro-patterned PDMS films.

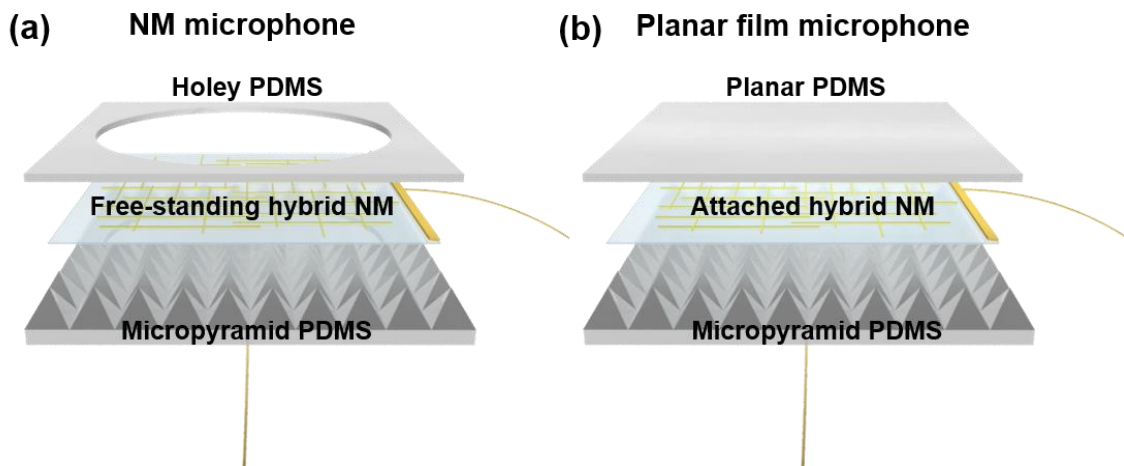


Figure 3.21 Schematic of (a) NM and (b) thin-film microphone devices. In the NM microphone, NMs are mounted to the “holey” PDMS film as a free-standing geometry. In the thin-film microphone, a hybrid NM mounted to a planar PDMS film without a hole is fully laminated with the surface of PDMS film, where NMs cannot be free-standing.

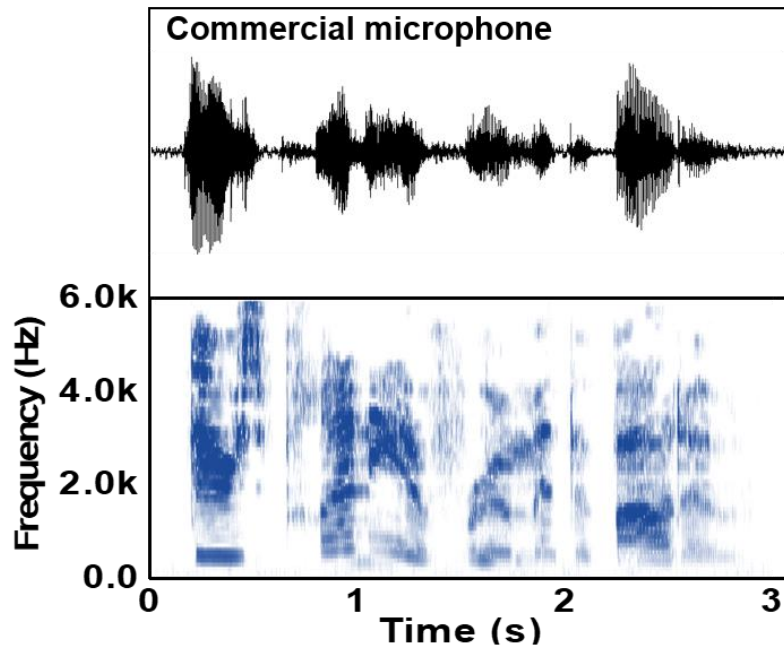


Figure 3.22 Waveform and short-time Fourier transform (STFT) signals of original sound (“There’s plenty of room at the bottom”) extracted by the sound wave analyzer, where the signal was read from a commercial microphone.

Personal voice security system. As personal information and security became more important, voice recognition has become essential to IoT sensors, voice security, and acoustic interaction with AI. To validate the acoustic sensing capability of the NM microphone and its applicability to human-machine interfaces, we designed a personal voice security system based on the NM microphone, which can recognize a registrant by perceiving the user's voiceprint. Figure 3.23a shows the voice-based security system with a free-standing NM microphone, which prevents unauthorized users from accessing the system by analyzing the user's voiceprint, as obtained from a recording of the user's voice. In the personal voice security system, we obtained user's voiceprint using LabVIEW software, where the sound waveform signal of user's voice was first recorded by a microphone and then the frequency-domain analysis was performed using FFT with noise filtering. From the FFT spectrum, the frequency of user's voiceprint is arranged according to the amplitude to quantitatively determine the probability of matching with the frequency ordering of authorized voiceprint by using a customized LabVIEW software (S.C.V Corp.). When the user says "hello" using the NM microphone, the computer analyzes the frequency pattern of the user's voiceprint based on the matching probability, relative to the registered voiceprint. If the matching probability is more than 98%, the computer authorizes the user to access the system, which issues a greeting.

Figure 3.23b shows the sound waveforms produced in response to the sound of the word "nano-membrane", recorded by a registrant, authorized user, and denied user using the NM microphone. The time-dependent acoustic information of the sound waveform of the authorized user corresponds closely to that of the registrant whereas that of the sound waveform of denied user is not matched. Figure 3.23c shows the voiceprints obtained for the original sound waveform produced by the registrant, authorized user, and denied user, all of which exhibit a frequency-dependent spectrum. The voiceprints of both the registrant and authorized user are well matched with a 99.3% matching probability in the frequency domain. In the analysis of FFTs, they also exhibit similar frequency patterns across the entire range with a higher pitch than that of a denied user (Figure 3.24). In addition, we could confirm that the overall frequency patterns of FFT obtained from the NM microphone are similar with those from a commercial microphone although there is a slight discrepancy of frequency domain in the same voice (Figure 3.25). To further certify whether the NM microphone could be applied to voice recognition, we compared the matching probabilities obtained using the NM and conventional microphones in response to the voice of a registrant for repeated test of 10 times, respectively (Figure 3.23d). It is worth noting that the matching probability using the NM microphone showed an average reliability of $98.6 \pm 0.8\%$ and a small error variance, which is comparable to that of a commercial microphone ($99.1 \pm 0.6\%$), implying that our NM microphone can accurately recognize registrant's voice with high accuracy and precision. To further validate the precision and selectivity of the NM microphone, we measured the

matching probability using the NM microphone in response to voice sounds generated by different persons including the registrant, a man, and two women (Figure 3.23e). As a result, our NM microphone can selectively recognize registrant's voices among different voices, in which all voices show different and reproducible frequency patterns (Figure 3.26).

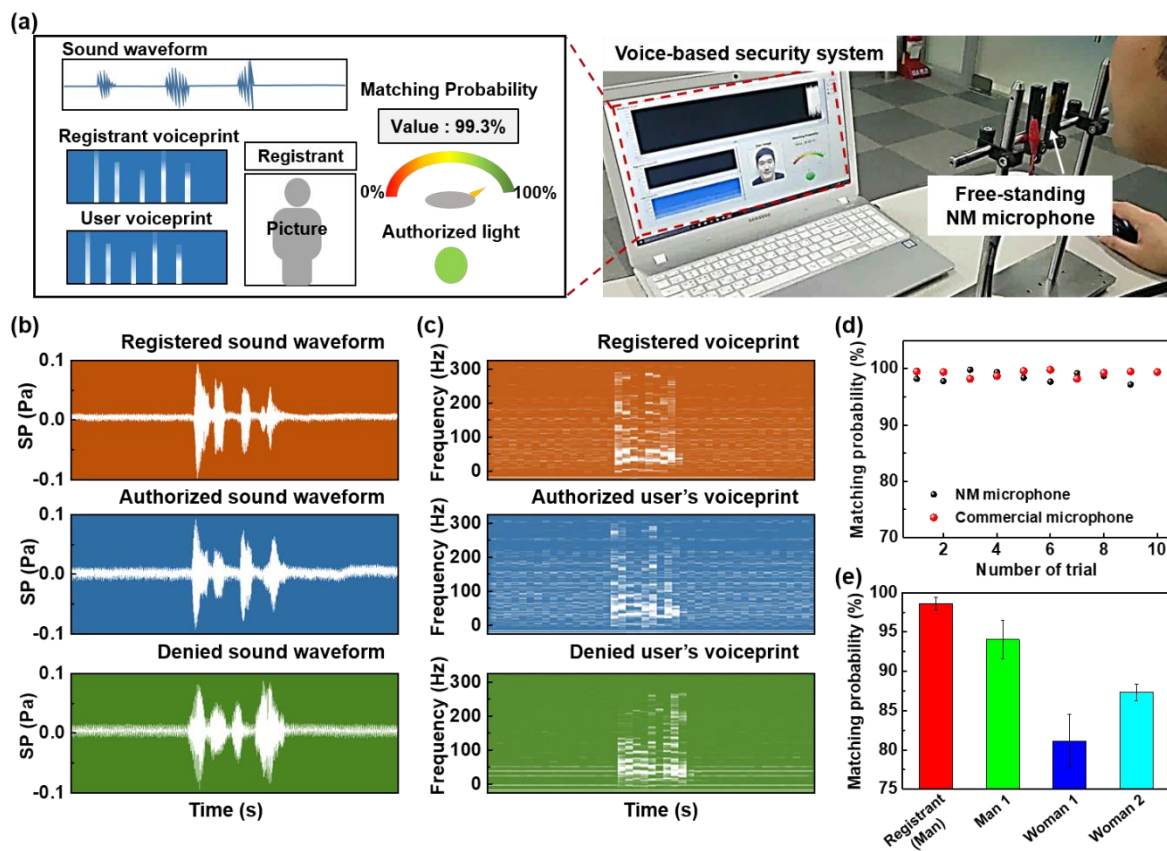


Figure 3.23 Personal voice-based security system. (a) Schematic of voice security system (left) and photograph of authorization process using free-standing NM microphone (right). (b) Sound waveforms and (c) voiceprints collected from registrant, authorized user, and denied user using NM microphone. (d) Matching probability of voiceprint for authorized user using NM microphone and commercial microphone. (e) Matching probability of voiceprints obtained from different users including registrant, man, and two women.

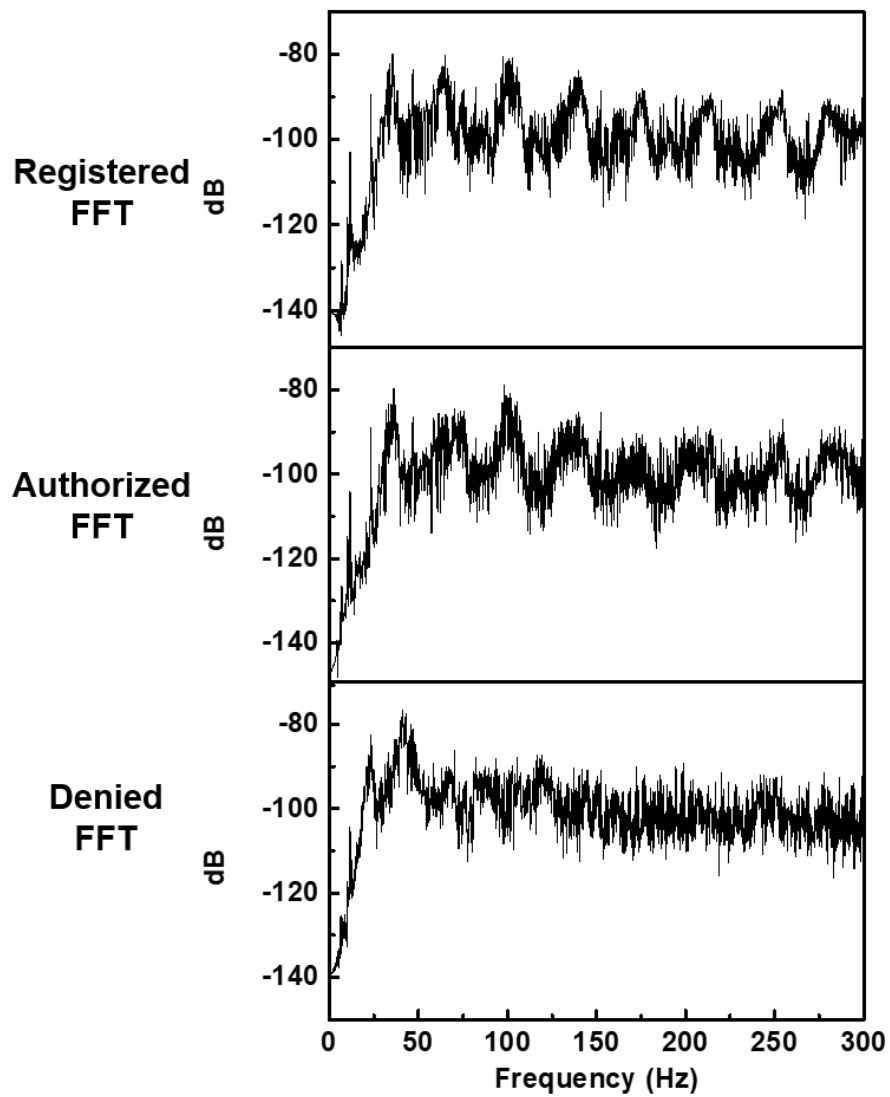


Figure 3.24 FFTs extracted from the sound wave of the word “Nanomembrane” obtained from voices of different subjects including the registrant, authorized user and denied users.

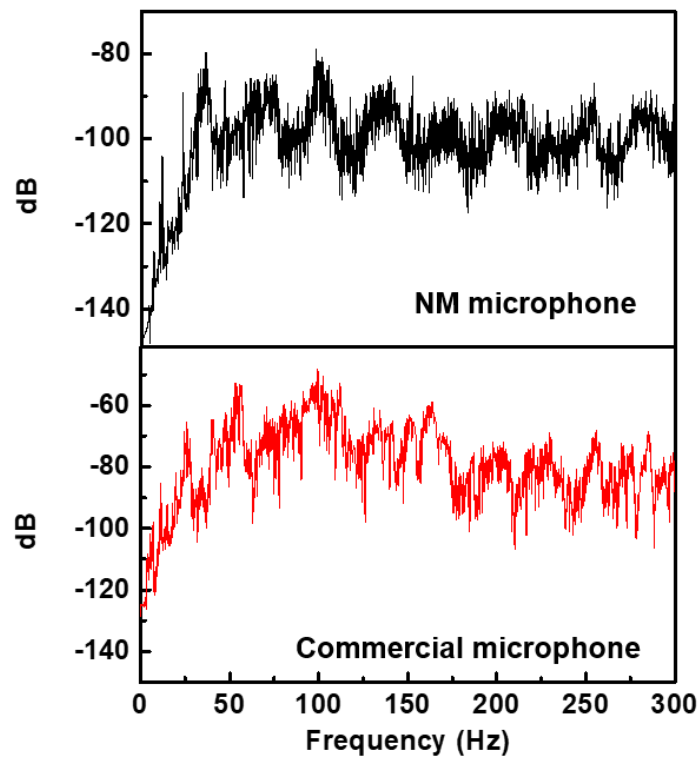


Figure 3.25 FFTs extracted from the sound wave, obtained from the voice of a registrant by using (upper) NM microphone and (bottom) commercial microphone (40PH, G.R.A.S.).

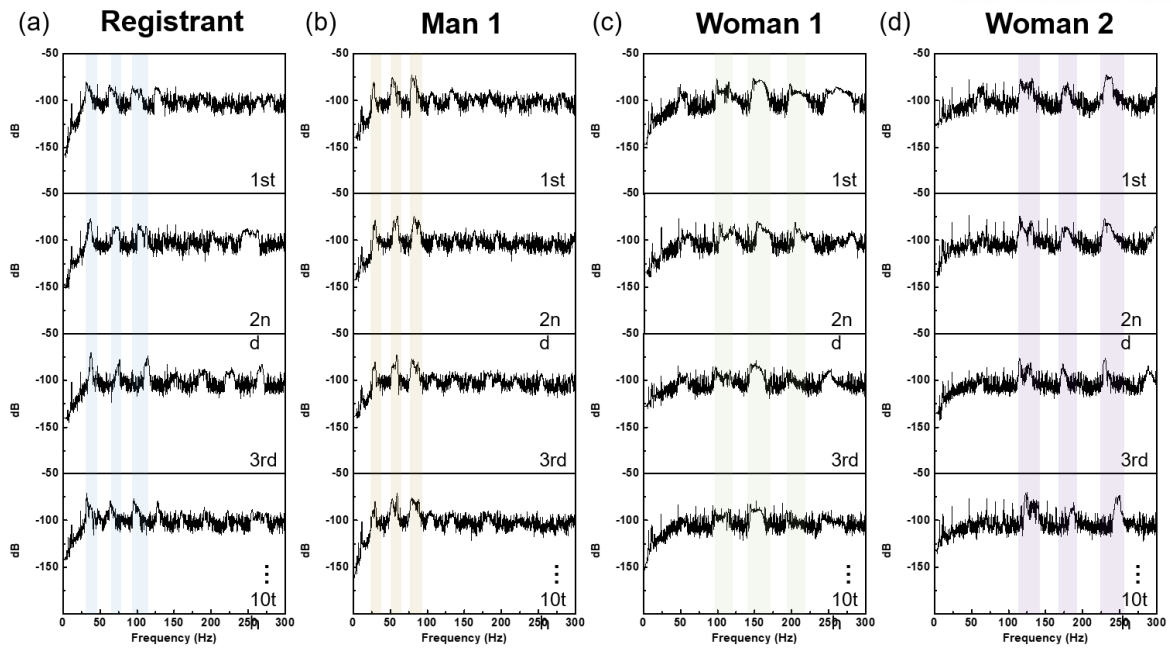


Figure 3.26 FFTs for repeated test of 10 times, extracted from the sound wave of the word “hello” obtained from various voices of different subjects including the registrant, a man, and two women.

3.4 Conclusions

In conclusion, we demonstrated a highly conductive and transparent hybrid NM, consisting of an orthogonal AgNW array embedded into a polymer matrix, which provides excellent electrical and mechanical properties compared to pure polymer NMs. Our hybrid NMs facilitate conformal contact with curvilinear and dynamic surfaces without any cracking or rupture. As a conformal/skin-attachable device application, a skin-attachable thermoacoustic NM loudspeaker is presented, enabling intimate contact with human skin, resulting in an imperceptible and transparent appearance. We have also presented a wearable and transparent NM microphone integrated with a micropyramid-patterned PDMS film for precisely detecting sounds as well as vocal vibrations produced by the triboelectric voltage signals corresponding to sounds. As a proof-of-concept demonstration, our NM microphone was applied to a personal voice security system requiring voice-based identification applications. The NM microphone was able to accurately recognize a user's voice and authorize access to the system by the registrant only. These NM-based acoustic devices can be further explored for various potential applications, such as wearable IoT sensors and conformal healthcare devices.

Chapter 4. High-performance flexible electroluminescent (EL) devices based on high- k nanodielectrics and cross-aligned AgNW electrodes

4.1 Introduction

Alternating-current electroluminescent (ACEL) devices are regarded as promising candidates for next generation displays due to their excellent robustness, simplified fabrication procedure, uniform light emission, low production cost, and stable performance under severe environmental conditions that are difficult to achieve in conventional displays.^{3, 85, 87, 189-191} However, their high operating bias leads to significant power consumption, which is a barrier to their wide adoption. One solution for this challenge would be to decrease the active layer thickness, which leads to a higher electric field strength and thus better device performance at a low operating bias.³ However, this approach is largely limited by the size of the phosphor materials and the device fabrication method.^{85, 192} Another approach is the use of high-quality dielectric layers to achieve high-performance ACEL devices.⁸⁷ A high- k dielectric layer induces the focusing of the electric field on the EL particles, leading to higher device brightness and a lower operating bias required to generate excitons.

Over the years, a number of inorganic high- k materials mixed with a polymer matrix have been utilized as dielectric layers such as barium titanate (BTO), alumina, boron nitride, and strontium titanate nanoparticles (NPs).^{87, 193-199} For example, when high- k BTO NPs were added into an electroluminescent (EL) composite layer, the resulting ACEL devices showed enhanced brightness compared to the devices without BTO NPs (i.e., ~ 30 cd/m² vs ~ 9 cd/m² at 200 V, 400 Hz).⁸⁷ However, the dielectric constant of the BTO composite was still low (~ 10 at 1 kHz), which suggested that there was room for the improvement of the dielectric constant of BTO composites to further enhance the brightness of ACEL devices. La ion doping is an efficient way to increase the dielectric constant of BTO.²⁰⁰ Previously, La-doped BTO (BTO:La) was used as a high energy density material in capacitor applications due to its excellent dielectric properties.²⁰¹⁻²⁰⁴ Since the energy stored in a capacitor is proportional to the dielectric constant, materials with a high dielectric constant are required. Despite such high dielectric values, BTO:La has not yet been explored for use in EL devices.

In addition to high- k dielectric layers, highly transparent and conductive electrodes are required for high brightness ACEL devices. Various transparent and conductive materials have been explored for the flexible and transparent electrodes of flexible ACEL devices, such as single-walled carbon nanotubes,²⁰⁵ graphene,²⁰⁶ ionic conductors,¹⁸⁹ and silver nanowires (AgNW).^{85, 87} In particular, random AgNW networks have been intensively used for the transparent electrodes of ACEL devices due to their excellent conductivity, transparency, solution processability, and flexibility.^{85, 87, 207, 208} While

regularly aligned AgNW networks exhibited great potential as transparent and conductive electrodes with excellent optical and electrical properties, low surface roughness, and uniform sheet resistance (R_{sh}),^{209, 210} there have been no reports on the effect of regular AgNW networks on the brightness and performance of flexible ACEL devices.

Herein, we present a rational method to synthesize high- k BTO:La nanocuboids (NCs) and the fabrication of efficient flexible ACEL devices via a simple solution-processing method.^{86, 211, 212} We synthesized BTO:La NCs with a larger permittivity than the pure BTO *via* the local disorder induced by an aliovalent substitution between barium ions (Ba^{2+}) and La^{3+} .²⁰⁴ The ACEL devices with the high- k BTO:La NCs displayed significantly enhanced brightness (4–6 times at 60–320 V, 1 kHz) compared to the pristine BTO-based ACEL devices. Furthermore, we fabricated cross-aligned AgNW electrodes with excellent optical and electrical properties, low surface roughness, and uniform R_{sh} over a large area, which can further enhance the brightness compared to random AgNW electrodes and circumvent the brightness gradient issue in ACEL devices. To the best of our knowledge, this is the first demonstration of flexible ACEL devices using a solution-processed high- k BTO:La nanodielectric and cross-aligned AgNW electrodes, resulting in high luminance at low operating voltage along with a minimal brightness gradient over a large device area.

4.2 Experimental Details

Bar-coating of cross-aligned AgNW flexible electrodes: For the aligned AgNWs arrays, the AgNW ink (Nanopyxis Corporation) was coated onto PET substrates treated with poly-L-lysine (PLL) adhesion layers by a Meyer-rod coating method, as reported in our previous study.⁴² In this process, the AgNW ink containing 0.15 wt% of AgNWs with an average length of 20 μm and diameter of 35 nm was injected into the empty space between the Meyer rod and the substrate, which resulted in the formation of a meniscus due to the capillary force. Subsequently, the meniscus dragging by the Meyer rod at a constant speed resulted in the formation of highly uniform and aligned AgNWs arrays along the coating direction. To fabricate cross-aligned AgNWs arrays, an additional bar-coating process was carried out on the aligned AgNW array in the perpendicular direction to the pre-aligned AgNW array.

Hydrothermal synthesis of La-doped BTO nanocuboids: BTO:La NCs (xLa: BaTiO₃, x = 0, 0.5, and 1.0) were synthesized using a modified hydrothermal method previously reported in the literature.^{213, 214} The precursors used for the hydrothermal reaction include Ba hydroxide monohydrate [Ba₂•(H₂O), Sigma-Aldrich, 98%], Ti butoxide [Ti(O(CH₂CH₃)₂)₄, Sigma-Aldrich, 97%], La nitrate hexahydrate [La(NO₃)₃•6H₂O, Sigma Aldrich], and diethanolamine [NH(CH₂CH₂OH)₂, DEA, Sigma-Aldrich]. First, 25 mmol of Ti butoxide was added to 10 mL of ethanol followed by the addition of 3.5 mL of ammonia at room temperature, resulting in the formation of TiO₂•yH₂O (Solution A). Another pre-solution (Solution B) was prepared by dissolving 37.5 mmol of Ba hydroxide and an appropriate amount of La(NO₃)₃•6H₂O in 12.5 mL of DI water at 90 °C. Solution A was then mixed with Solution B to form a suspension. The DEA (2.5 mL) was then added to the solution to control the size and polydispersity of the nanoparticles. The final solution was transferred to a Teflon-lined stainless-steel autoclave and kept in an oven at 200 °C for 48 h for the hydrothermal reaction. Then, the autoclave was cooled down to room temperature and the particles were washed several times using ethanol and DI water. The final product was dried at 80 °C for 48 h.

Preparation of nanodielectrics ink: The dielectric ink was prepared by first mixing PDMS (base only) and BTO:La NCs followed by magnetic stirring for 30 min. The mixture was then subjected to successive bath sonication (4 h) and probe sonication (15 W, 5 min) to break down the large aggregates of BTO NCs. BTO/PDMS dispersions were prepared with a BTO content of up to 46%. Later, the concentration was fixed at 26% due to the agglomeration observed at higher concentrations. The dispersions with BTO were spin-coated on silicon or glass to fabricate parallel capacitors, which were used to characterize the dielectric constant of the BTO/PDMS films. The electroluminescent layer was prepared by mixing ZnS:Cu particles with PDMS (3:1 ratio) with a viscosity of ~10 Pa·s (Figure 4.1), which is suitable for the screen-printing process.²¹⁵

Fabrication of flexible ACEL devices: For the fabrication of flexible ACEL devices, AgNWs were first Meyer-coated onto PET substrates, forming the bottom electrodes, followed by screen-printing of the mixture of BTO:La nanodielectrics/PDMS as the high- k dielectric layer onto the bottom electrodes. Subsequently, ZnS:Cu particles (SEM, PL, and XRD analysis data in Figure 4.2) mixed with liquid PDMS (ratio 3:1) prepolymer and BTO:La nanoparticles were then screen-printed on top of the high- k dielectric material layer. Finally, another layer of AgNWs on PET substrates was used to form the top electrodes. Thereafter, flexible ACEL devices were dried and encapsulated with thin PDMS layers to protect the devices.

Characterization: The R_{sh} values of the AgNW electrodes were measured using a four-point probe method (Keithley, 2400). Optical transmittance and absorption spectra of AgNW networks were measured by a UV–vis–NIR spectrophotometer (Jasco, V-670). The surface alignment structure of the AgNW arrays was examined using an optical microscope (PSM-1000, Olympus). The purity and crystalline phases of the BTO nanodielectrics were analyzed by powder XRD data, which were collected using a Bruker D8 Advanced diffractometer equipped with Cu $K\alpha$ radiation source and a diffractometer monochromator that was operated at 40 kV and 40 mA. The surface morphology of the BTO powder was examined using a field-emission SEM (FE-SEM, Hitachi S4800) at an operating voltage of 10 kV. The specimens used for TEM (JEM 2100, JEOL) analysis were obtained by drying droplets of the as-prepared samples in an ethanol dispersion onto a carbon-coated copper grid. The chemical bonding and functional groups of the BTO powders were investigated using an X-ray photoelectron spectrometer (K-alpha, Thermo Fisher). The rheological properties of the BTO nanodielectric slurries were studied with a rheometer (Haake MARS3, Thermo Fisher). The dielectric data of the nanodielectrics were obtained using an impedance analyzer (BioLogic) equipped with a frequency response analyzer (FRA2 module), which has a current range from 10 nA to 10 mA with a resolution of 0.0003% and a potential resolution of 3 μ V. The dielectric data was measured by supplying an unbiased voltage signal with a peak voltage of 0.5 V and a frequency range of 10^{-2} to 10^5 Hz with a resolution of 0.0003%. A function generator connected with a power amplifier was used to apply an alternating operation voltage to the flexible ACEL devices. Luminescence spectra of the flexible ACEL devices were recorded by a spectroradiometer (PR-655, Photo Research, Inc.).

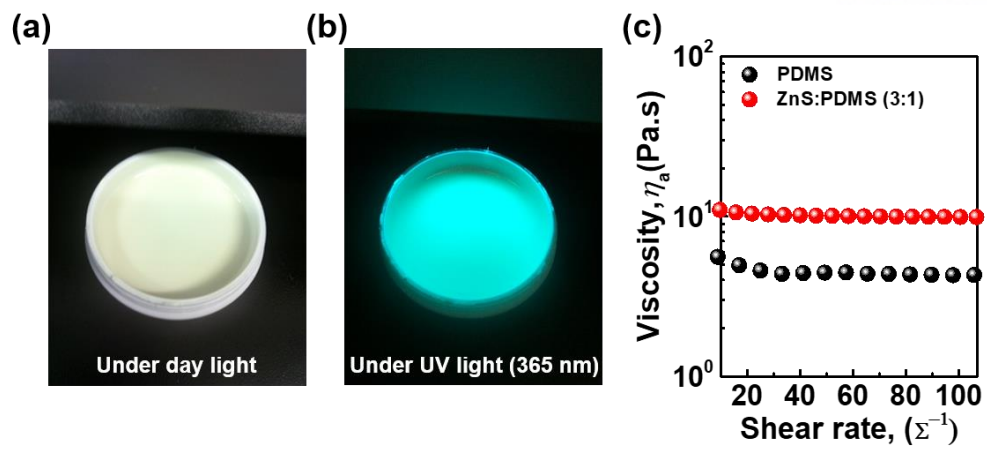


Figure 4.1 (a) A photograph of ZnS:Cu/PDMS slurry in ambient light and (b) under a UV lamp. (c) Rheological behavior of slurry prepared with varying shear rate sweeps.

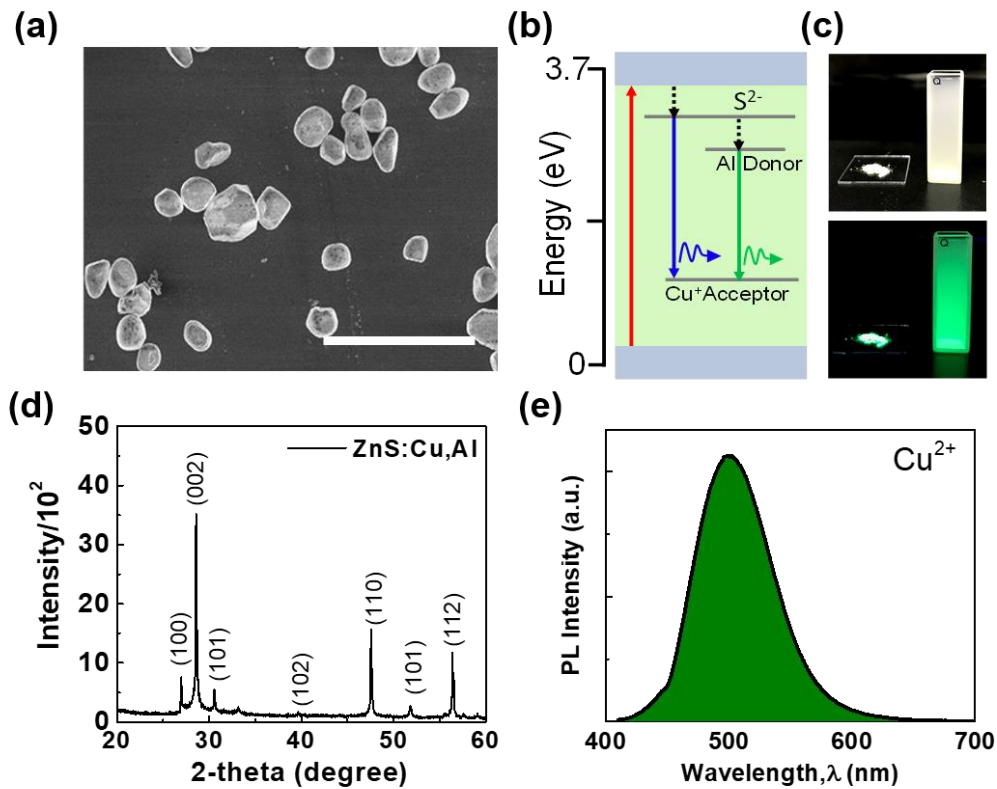


Figure 4.2 (a) SEM micrograph of ZnS:Cu particles with a mean particle size of $\mu = 26 \mu\text{m}$ and standard deviation of $\sigma = 5.5 \mu\text{m}$. The scale bar is $100 \mu\text{m}$. (b) Photoluminescence mechanism in ZnS doped with Cu impurity. (c) A photograph of ZnS:Cu particles placed on a glass plate and in a glass vial (dispersed in methanol). (d) X-ray diffraction pattern of hexagonal ZnS matched with standard JCPDS card (JCPDS card no.: 79-2204). (e) Photoluminescence spectra of ZnS:Cu recorded at room temperature with an excitation wavelength of 400 nm, which resulted in a green emission spectrum with peak emission wavelength at 500 nm.

4.3 Results and Discussion

The flexible ACEL devices were fabricated using a simple screen-printing method (Figure 4.3).^{216, 217} The structure of the flexible ACEL device is schematically illustrated in Figure 4.4a. The flexible ACEL device consists of BTO:La/polydimethylsiloxane (PDMS) as high- k dielectric layer and a polycrystalline ZnS:Cu/PDMS active EL layer that are sandwiched between a pair of cross-aligned AgNW transparent electrodes. The fabrication process of the flexible ACEL display is outlined in Figure 4.3. First, cross-aligned AgNW networks were fabricated on a polyethylene terephthalate (PET) film to form the bottom electrode by using a bar-coating technique.⁴² Second, screen-printing was utilized for the sequential multilayer formation of a high- k BTO:La/PDMS layer and a ZnS:Cu/PDMS EL layer (layer thickness $\sim 50\text{--}60\ \mu\text{m}$). Finally, another cross-aligned AgNWs/PET electrode was used as a top electrode. By employing cross-aligned AgNW electrodes with a low resistance and uniform distribution of R_{sh} , we demonstrated high performance flexible ACEL devices with uniform brightness over a large area ($12 \times 2\ \text{cm}^2$) (Figure 4.4b,c). Figure 4.4d exhibits a cross-sectional scanning electron microscopy (SEM) image of a typical multilayer-structured flexible ACEL device, consisting of top and bottom AgNW electrodes (Figure 4.4e), a BTO:La/PDMS high- k layer (Figure 4.4f), and a ZnS:Cu/PDMS EL layer. It is evident that ZnS:Cu particles were well dispersed in the PDMS matrix without aggregation or voids that can reduce the dielectric constant of composites. The working principle of the ACEL device is illustrated in Figure 4.5. Under a high electric field, injected hot carriers in the phosphor are accelerated to high energy and trigger impact ionization, followed by radiative relaxation of the luminescent center, resulting in green light emission.²¹⁸

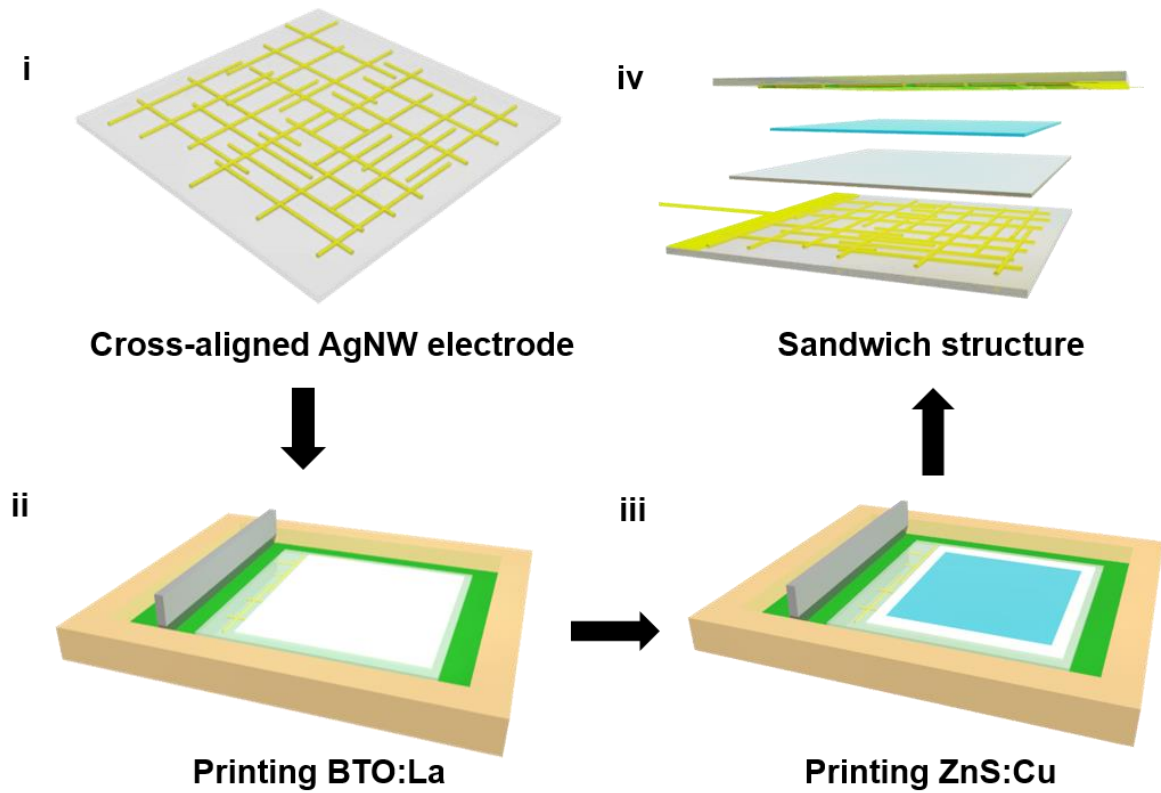


Figure 4.3 Schematic representation of the overall procedure used to fabricate flexible ACEL devices using screen printing. i) The orthogonal AgNWs are formed by repeating the barcoating assembly in a perpendicular direction to that of the pre-aligned AgNW arrays. ii) Afterward, a BTO:La dielectric layer is screen printed on top of the AgNWs. iii) This is followed by a ZnS/PDMS layer. iv) Finally, the top electrode of AgNWs was deposited to obtain sandwich-like flexible ACEL device structure.

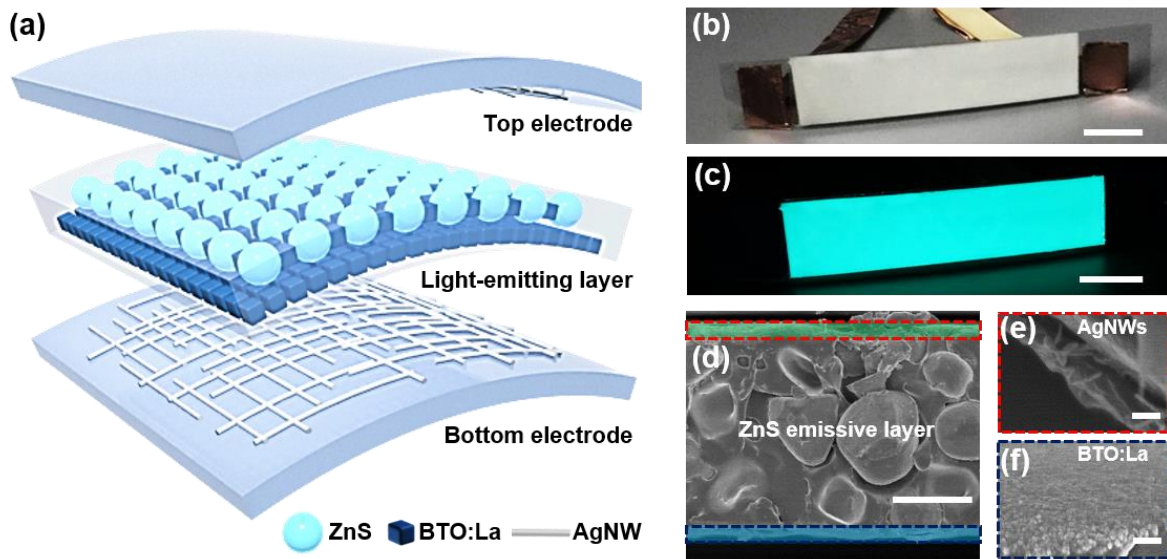


Figure 4.4 Flexible alternating-current electroluminescent (ACEL) devices. (a) Schematic representation of flexible ACEL device consisting of top and bottom crossaligned AgNW electrodes, ZnS emissive material, and high- k BTO:La nanodielectrics. (b) Photographs of the flexible ACEL device before and (c) after lighting up under applied bias. The scale bars are 2 cm. (d) A cross-sectional SEM image of flexible ACEL devices showing the homogeneous distribution of ZnS particles in the PDMS matrix. The scale bar is 100 μm . (e) Partially enlarged cross-section view of top AgNWs. The scale bar is 20 μm . (f) Partially enlarged tilted view of nanodielectrics. The scale bar is 5 μm .

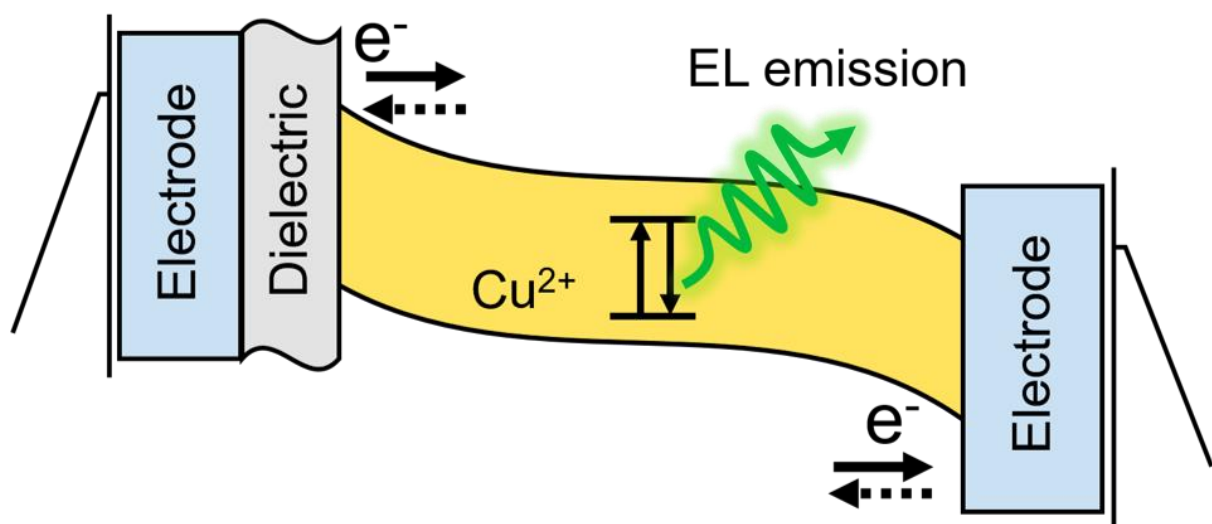


Figure 4.5 Band structure diagram showing EL mechanism for flexible ACEL devices caused by impact-excitation of Cu^{2+} in ZnS EL particles.

BTO:La nanodielectrics were synthesized by a wet chemical hydrothermal process (see the Experimental Section for details of the synthesis process). The as-obtained BTO:La NCs exhibited a morphology of uniform tetragonal-shaped nanoparticles (Figure 4.6) and a size distribution centered around ~150 nm (see the inset histogram). Such a small particle size is required to improve the performance of ACEL displays as it can induce a higher packing density and yield a smooth surface coating. The field-emission transmission electron microscopy (FETEM) image of BTO:La NCs shows a rectangular-like structure and single phase (Figure 4.6b, inset electron diffraction pattern) and a lattice fringe spacing of 4.02 Å (Figure 4.7). A common problem during the synthesis of BTO:La NCs is the creation of a Ba carbonate impurity phase, which affects the dielectric properties of the samples.²¹⁹ The X-ray diffraction (XRD) pattern of the BTO:La NCs reveals a highly crystalline phase of BTO:La without any Ba carbonate impurity phase, even at high doping concentrations (Figure 4.6c). The formation of this pure crystalline phase after the La doping indicates that La ions preferentially substitute for Ba ions in the BTO lattice because of the similarity of their ionic radii. The influence of La incorporation on the crystalline structure of BTO:La can be evaluated by examining the XRD pattern in the region near the (200) reflection ($2\theta \approx 42\text{--}46^\circ$), as shown in the inset of Figure 4.6c. With the doping of 1% La, the specific (002) and (200) peaks of the tetragonal structure merge into a single (200) peak (Figure 4.8), suggesting a transformation from the tetragonal to the cubic phase.²²⁰ The XRD pattern of BTO with 1% La doping indicates that the cubic phase is dominant. The evolution of the tetragonal unit cell parameters (a , c) with La concentration is shown in Figure 4.8c (Supporting Information), where c decreases while a increases with increasing La doping concentration. The c/a ratio, which is directly related to the tetragonality, shows that a higher La concentration tends to change the unit cell symmetry from tetragonal to cubic (Figure 4.8d). It was also found that La doping affects the average NC size (Figure 4.9). The NC size became smaller with increasing doping concentration. When doped with 1% La, the NC size decreased to 140 ± 40 nm compared to undoped BTO (165 ± 60 nm) due to the reduction in the c/a ratio (Figure 4.9a).

Figure 4.6d and Figure 4.10 (a–d) show the X-ray photoelectron spectroscopy (XPS) analysis of BTO:La NCs. Figure 4.10a shows the XPS survey spectrum of BTO:La, which displays the presence of Ba, Ti, and O elements. The XPS spectrum of Ba contains two peaks at 778 eV and 793 eV due to the splitting of Ba 3d_{5/2} and Ba 3d_{3/2} spin states (Figure 4.10b). It also indicates that the oxidation state of Ba is +2. The XPS spectrum of Ti contains two peaks at 458.1 eV and 463.7 eV, which are associated with Ti 2p_{3/2} and Ti 2p_{1/2} due to the Ti⁴⁺ oxidation state (Figure 4.10c). The XPS spectrum of O shows two deconvoluted peaks at 530.9 and 532.1 eV, which are ascribed to the O in BTO and chemisorbed species (such as OH) or other O vacancies (Figure 4.10d). In the high-resolution spectrum of La 3d (Figure 4.6d), two peaks at 834 and 851 eV are attributed to La 3d_{5/2} and La 3d_{3/2}. The binding energy

peak of La 3d splits into two peaks due to the spin-orbit interaction that separates La 3d_{5/2} and La 3d_{3/2} electrons.²²¹ This split is caused by the transfer of an electron from O to the f orbital of La, indicating La insertion into the BTO crystal structure, which confirms the presence of La (Figure 4.6d). These results indicate that highly crystalline and pure phase BTO:La NCs are successfully synthesized.

The properties of the transparent electrode critically affect the performance of flexible ACEL devices. The use of cross-aligned AgNW transparent electrodes is advantageous for achieving low resistance, high transparency, and a uniform resistance distribution over a large area, resulting in high brightness at a low operating voltage and flexible ACEL devices with uniform brightness. In our previous work, transparent electrodes based on cross-aligned AgNW networks exhibited a higher electrical to optical conductivity ratio, a smoother surface, and more uniform resistance distribution compared to random AgNW networks.⁴² Figure 4.11a shows the dark-field optical micrograph of a cross-aligned AgNW network on a PET substrate. The corresponding fast Fourier transform (FFT) image in the inset clearly shows the cross-line pattern, indicating the cross-aligned structure of the AgNW networks. Our cross-aligned AgNW electrodes also exhibited a high optical transmittance, which is needed to minimize the absorption of generated EL (Figure 4.11b). Figure 4.11b shows the optical transmission *versus* sheet resistance (R_{sh}) of cross-aligned AgNW electrodes. Fitting this curve based on a mathematical equation for the percolative figure-of-merit (FoM):

$$T = \left[1 + \frac{1}{\Pi} \left\{ \left(\frac{Z_0}{R_{sh}} \right) \right\}^{1/(n+1)} \right]^{-2} \quad (1)$$

Equation 1 is the mathematical expression for the electrical to optical conductivity ratio, where Z_0 is the impedance of free space ($Z_0 = 377 \Omega$), n is the percolation exponent describing the power law relationship between R_s and the thin film thickness, and Π is the percolative FoM. A high value of Π means a low value of R_s and a high value of T . The device shows $\Pi = 468$ and $n = 0.13$, where Π is the FoM value and n is the percolation exponent. The extremely high value of Π and low value of n can be attributed to the efficient formation of a conductive nanowire network and reduced inter-nanowire junction resistances, resulting in a high transparency of the electrode, which is favorable for high-brightness light emission devices. Consequently, the flexible ACEL device with cross-aligned AgNW electrodes shows enhanced brightness compared to random AgNW electrode-based flexible ACEL devices (Figure 4.12).

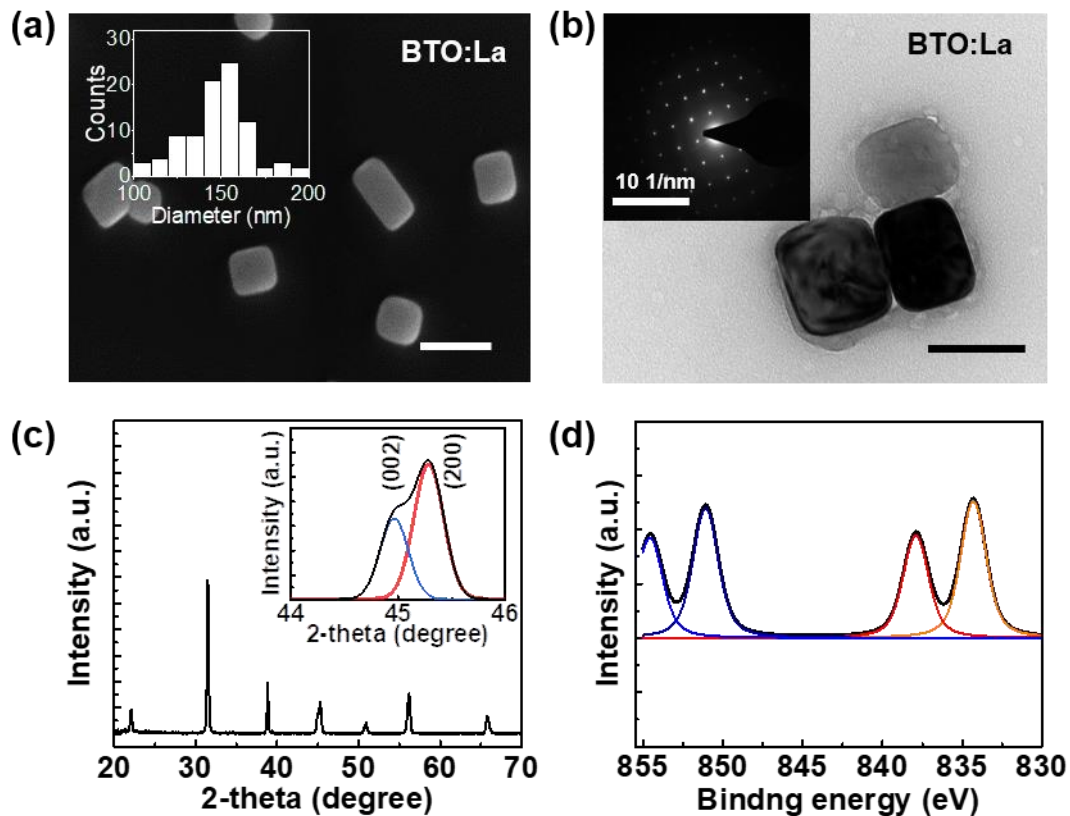


Figure 4.6 Synthesis and structural characterization of hydrothermally prepared bare and La-doped BTO nanodielectrics. (a) SEM images of tetragonal BTO:La nanodielectrics. The scale bar is 200 nm. The inset shows the particle size distribution histogram. (b) FETEM image of BTO:La nanodielectrics showing distinct tetragonal shape and the inset shows the selected area electron diffraction (SAED) pattern showing bright diffraction spots. The scale bar is 100 nm. (c) Room temperature X-ray diffraction patterns for the La-doped BTO. Inset shows a magnified view of the region corresponding to the diffraction angles $2\theta = 44^{\circ}$ – 46° and (200) planes showing the peak splitting indicative of a tetragonal phase. (d) High resolution XPS spectra for La 3d showing two peaks at 834 and 851 eV, indicating La insertion into the BTO crystal structure.

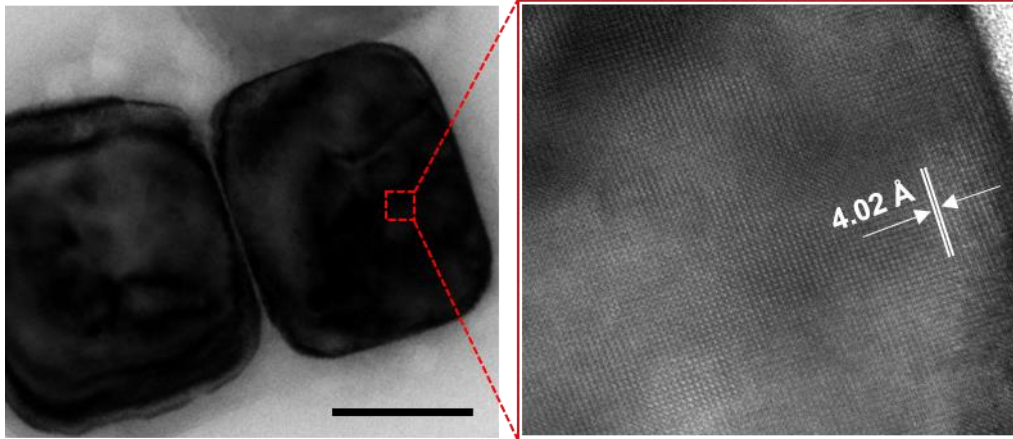


Figure 4.7 FETEM image of La doped BTO nanocuboids and magnified FETEM image showing inter-planer spacing. The scale bar is 50 nm.

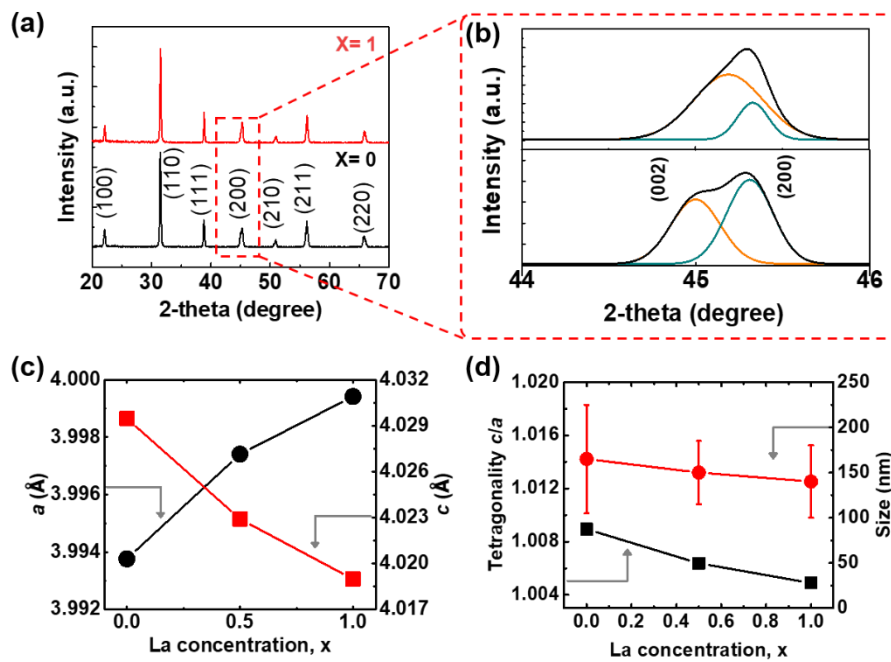


Figure 4.8 Structural characterization of hydrothermally prepared bare and La-doped BTO nanodielectrics. (a) Room temperature X-ray diffraction patterns for the La-doped BTO. (b) Magnified view (dashed rectangle of a) of the region corresponding to the diffraction angles $2\theta = 44\text{--}46^\circ$ and (200) planes showing peak splitting indicative of the tetragonal phase. (c) Evolution of lattice parameters vs. La content. (d) Dependence of tetragonality on La content and effect of La content on BTO nanoparticle size.

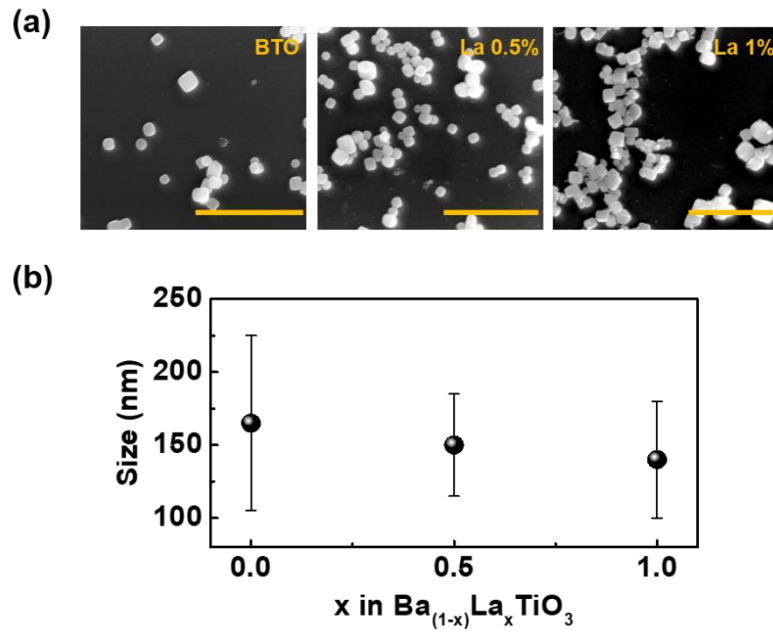


Figure 4.9 (a) FESEM images of undoped and La-doped BTO nanocuboids with different La concentrations. All scale bars are 1 μm. (b) Effect of La doping on BTO nanoparticle size variations.

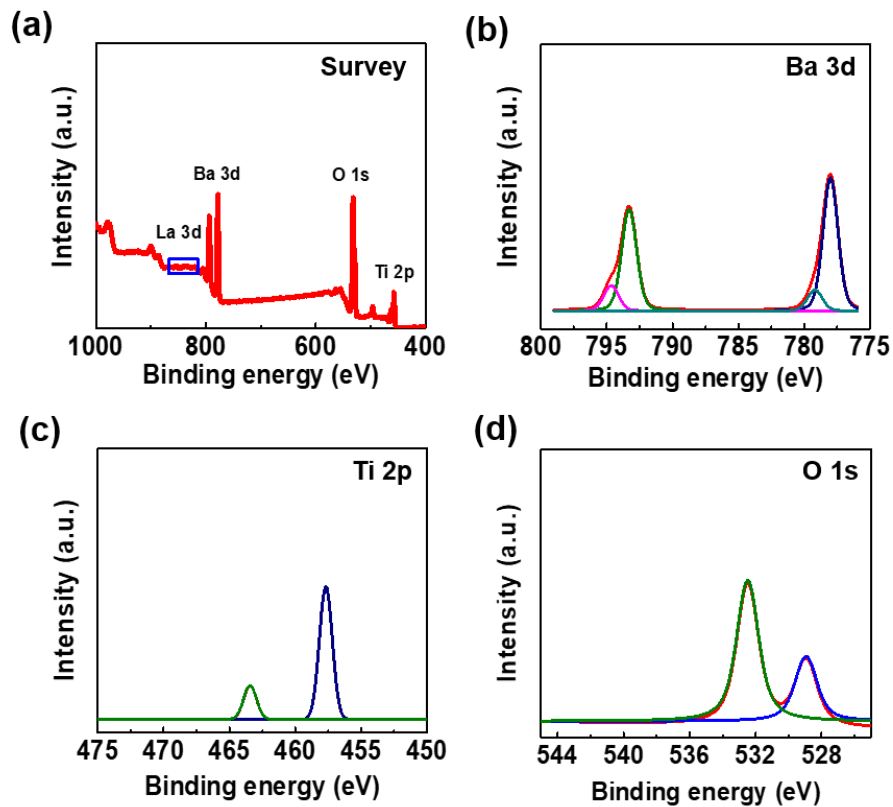


Figure 4.10 XPS spectra showing Ba 3d, Ti 2p, O 1s and La 3d peaks of xLa: BTO samples.

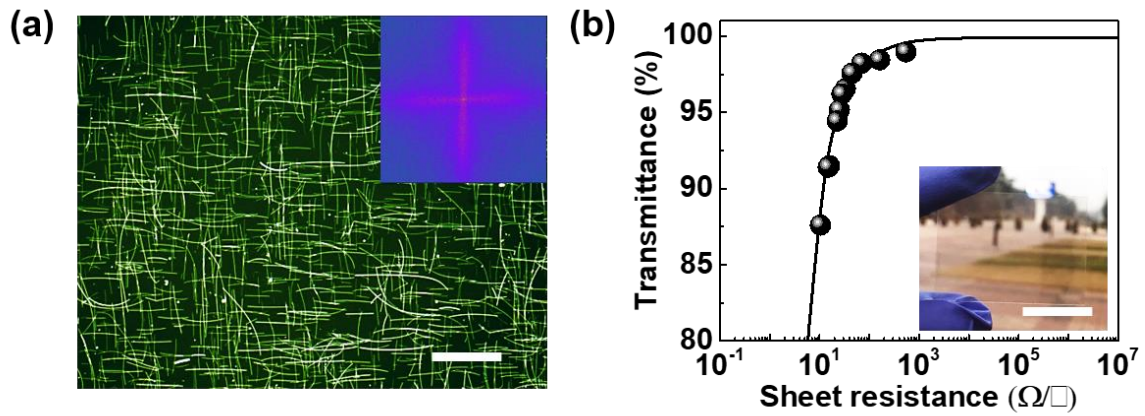


Figure 4.11 (a) Dark field optical microscopy image of orthogonally aligned AgNW network and corresponding FFT images showing orthogonal alignment of nanowires. The scale bar is 20 μm. (b) Optoelectrical properties of AgNW films. Transmittance (at 550 nm) is plotted as a function of sheet resistance. Photograph of a thin AgNW network with $T = 95\%$. The scale bar in the inset photo is 2.5 cm.

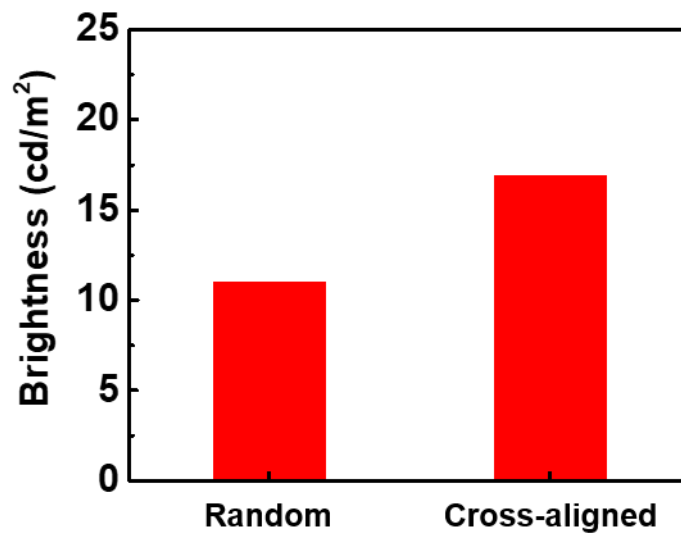


Figure 4.12 Comparison of brightness between flexible ACEL devices with random AgNW electrodes and with cross-aligned AgNW electrodes.

Dielectric permittivity and EL spectroscopic studies of flexible ACEL devices. We prepared high- k BTO:La/PDMS nanodielectrics by mixing BTO:La NCs with PDMS polymer (details in experimental section). The dielectric constant of the BTO:La/PDMS composites as a function of BTO:La volume fraction is shown in Figure 4.13, which can be fitted using Lichtenecker's empirical mixing rule, as shown in equation 2: The obtained dielectric data can be well fitted with the Lichtenecker model:

$$\varepsilon'_{\text{total}} = \varepsilon'_{\text{matrix}} (\varepsilon'_{\text{BTO}} / \varepsilon'_{\text{matrix}})^{\phi_{\text{BTO}}} \quad (2)$$

where $\varepsilon'_{\text{matrix}}$ and $\varepsilon'_{\text{BTO}}$ are the dielectric constants of the matrix polymer and BTO, respectively, and ϕ is the volume concentration of BTO. The fitting parameters result in the apparent dielectric constants of $\varepsilon'_{\text{BTO}} \sim 300$ and $\varepsilon'_{\text{matrix}} \sim 2.6$. Although the dielectric constant increased with increasing filler concentration, high filler loadings over 26% led to the agglomeration and phase separation of the NCs (Figure 4.14). To characterize the dielectric properties of flexible ACEL devices, the nanodielectric layers were sandwiched between the ZnS:Cu EL layer and the AgNW electrodes. Figure 4.15a displays the frequency-dependent dielectric constants of different ACEL devices including a pure PDMS matrix, PDMS with ZnS:Cu and BTO NCs (PDMS/ZnS:Cu/BTO), and PDMS with ZnS:Cu and BTO:La NCs with different La concentrations of 0.5 % and 1.0 % (PDMS/ZnS:Cu/BTO:La). The dielectric constant of the PDMS matrix increased from 2.4 to 10.4 at a frequency of 1 kHz when tetragonal BTO NCs were introduced into the PDMS matrix. Furthermore, the addition of BTO:La NCs (0.5 %) increased the dielectric constant to 21.1 compared to the addition of pristine BTO NCs (~ 10.4). The La substitution in the BTO lattice generates Ti vacancies to compensate for the induced charge imbalance, which leads to the distortion of Ti-O bonding and the generation of local polarization that enhances the permittivity.^{222, 223} The flexible ACEL device fabricated with 0.5 % BTO:La exhibited a dielectric constant of 21.1 at 1 kHz, whereas the dielectric constant of the flexible ACEL device with 1 % BTO:La decreased to 18.1 at 1 kHz. This decrease in the dielectric constant can be attributed to the structural changes at elevated La concentration, which promotes the structural transition from tetragonal to cubic.^{224, 225} Instead, excess La is segregated on the NP surfaces either by interstitials or nearby substitutional sites as secondary phase, indicating the solubility limit of La, which modified the dielectric behavior.^{222, 226}

The increase in the dielectric constant of the surroundings induces the focusing of the applied electric field on the ZnS:Cu particles, which increases the charge separation within ZnS, resulting in a higher light emission.⁸⁷ The EL characteristics of the flexible ACEL device were investigated using a spectroradiometer while controlling the applied AC voltage by a function generator and an amplifier (Figure 4.16). Figure 4.16b shows a representative photograph of a fabricated flexible ACEL device

when operated with a sinusoidal pulse function (pulse voltage of ± 200 V, 1 kHz). While the EL spectra of flexible ACEL devices with two different dielectric layers (BTO and BTO:La) exhibit emission peaks centered at 500 nm due to the same EL ZnS:Cu material, the flexible ACEL device with the BTO:La nanodielectric layer showed a higher luminescence intensity under the same voltage and frequency due to the increased field strength as a result of the higher dielectric constant of the BTO:La matrix (Figure 4.15b). In flexible ACEL devices, the high- k nanodielectric layer can be simply considered as capacitors in series with the emitting layer of ZnS:Cu (Figure 4.17).²²⁷ A larger dielectric constant or insulator capacitance of the BTO:La nanodielectric layer means that a larger fraction of the applied voltage is concentrated on the emitting layer of ZnS:Cu, which results in a decrease in the threshold voltage (Figure 4.17). Therefore, a larger dielectric constant drives the acceleration of a larger number of charge carriers at a given voltage, thus leading to an increase in the luminance as well as a decrease in the operating voltage.²²⁸

We further examined the distribution of the field strength and charge density in the flexible ACEL devices with finite element simulations. Numerical simulations were performed using COMSOL Multiphysics software in the AC/DC electrostatics module. We calculated the electric potential V by solving Laplace's equation with a dielectric $\nabla \cdot (\epsilon \nabla V) = 0$. This is solved using the finite element method with quadratic Lagrange elements interpolating the potential V . The electric field is $E = -\nabla V$. The potential was set to zero and 500 V on the lower and upper electrodes, respectively. The four long sides of the domain have periodic boundary conditions. The two remaining boundaries have the natural boundary condition for the Laplace equation, or $\hat{n} \cdot D = 0$. This field strength of the BTO:La ACEL device was further verified by simulating the distribution of electric field with the help of finite element methods, as illustrated in Figure 4.18. The model was established using the realistic geometry of the ACEL device, determined from SEM micrographs. The AgNWs form the top layer in the device. The next layer is the ZnS:Cu light-emitting layer with a thickness of 60 μm . The violet layer is the 1- μm -thick dielectric layer, and the bottom layer is again the back AgNWs electrode. A typical electrical potential distribution is shown in Figure 4.18b. Figure 4.18c,e show that upon increasing the dielectric constant of the material from ~ 11 (for undoped BTO) to ~ 21 (for BTO:La), the field strength was found to decrease slightly from 1.98×10^7 V/m to 1.71×10^7 V/m, which is attributed to the more strong dielectric nature of BTO:La. Higher dielectric constant materials provide higher degree of polarization, resulting in the decreased effective electric field.²²⁹ On the other hand, the maximum charge density of the BTO:La device (0.13 C/m², Figure 4.18f) was 62% higher than that of the undoped BTO device (0.08 C/m², Figure 4.18d). These results clearly indicate that a greater fraction of the applied voltage is locally concentrated on the ZnS:Cu layer due to the BTO:La high- k nanodielectrics, which increases

the charge density and results in an increase in the luminance.²²⁸ The local field strength depending on the matrix dielectric constant can be approximated analytically by Equation 3 as follows:^{230, 231}

$$E_{\text{ZnS}} = E_{\text{matrix}} \left[\frac{3\epsilon_{\text{ZnS}}}{2\epsilon_{\text{ZnS}} + \epsilon_{\text{matrix}} - \phi(\epsilon_{\text{matrix}} - \epsilon_{\text{ZnS}})} \right] \quad (3)$$

Figure 4.19 shows that the local field strength increases as the dielectric constant of the matrix increases. For the flexible ACEL device with an active layer thickness of $\sim 60 \mu\text{m}$, the calculated electric field strength based on Equation 1 is on the order of 10^7 V/m for an applied voltage of 100 V and ZnS dielectric constant of ~ 8.5 .²³²

Figure 4.15c shows the voltage dependent brightness of flexible ACEL devices with different nanodielectrics (BTO and BTO:La), indicating a strong dependence of the device brightness on the applied voltage. The brightness of the flexible ACEL devices increased linearly as the applied AC voltage was increased and saturated at a voltage over 240 V. This behavior is due to the electric field clamping effect, where the dielectric field strength of the device is saturated by the Joule heating induced at a higher operating bias. The flexible ACEL devices with the BTO:La nanodielectric layer exhibited a brightness of $\sim 57.5 \text{ cd/m}^2$ at $\pm 240 \text{ V}$ and 1 kHz, which is over 4 times higher than that of the undoped BTO devices ($\sim 14.3 \text{ cd/m}^2$). At a lower operating voltage of 80 V, the BTO:La flexible ACEL device showed a ~ 6 -fold increase in brightness of 5.7 cd/m^2 compared to undoped devices ($>1 \text{ cd/m}^2$). This voltage-dependent brightness behavior can be modelled with the Lehmann model using Equation 4 (Figure 4.20).²³³

$$L = aV^n \exp \left[\left(-\frac{b}{V^{0.5}} \right) \right] \quad (4)$$

where L is the luminescence, V is the applied voltage, and a and b are arbitrary parameters characterized by large values of a and small values of b . The exponent n ranges from -11 to 0.67 (Figure 4.20 inset). The slight deviation in modelling is due to the particle size distribution of ZnS:Cu.

The brightness of a flexible ACEL device also depends on the applied frequency (Figure 4.15d). The device brightness increased monotonically with the frequency for both BTO and BTO:La ACEL devices. Notably, the emission color can be easily tuned by changing the frequency of the applied voltage. For example, for a frequency of 5 kHz and AC voltage of 200 V, the EL spectrum is centered at 456 nm, which can be deconvoluted into two peaks (Figure 4.15e). When the frequency is decreased from 5 kHz to 1 kHz, the EL emission peak maximum shifts from 456 nm (blue color) to 500 nm (green color) (inset in Figure 4.15e). This frequency dependent color change can be clearly observed in a CIE

1931 chromaticity diagram (Figure 4.15f). Upon increasing the frequency from 100 Hz to 20 kHz, the chromaticity coordinates gradually vary from green to bluish green in the color space. The inset photographs in Figure 4.15f show that the emission color of a flexible ACEL device shifts from green to bluish green for a frequency change from 100 Hz to 20 kHz. The frequency dependent color change is attributed to the presence of two different types of shallow and deep traps, where deeper traps have a longer lifetime than the shallower ones.²³⁴ For the lower frequency with weak electron/hole injection, mainly shallow traps are occupied, leading to the green emission. Upon increasing the electron/hole injection further by increasing the frequency, the deeper traps responsible for the blue emission become filled and begin to saturate, while the shallower trap states become depopulated, leading to the high-energy blue emission.

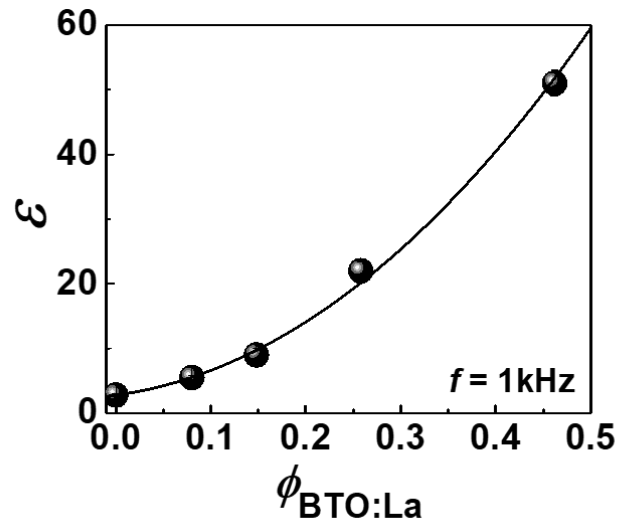


Figure 4.13 Dielectric constant of BTO:La/PDMS nanocomposite. The plot is fitted with theoretical Lichteneker's mixing rule, which is shown with a solid line.

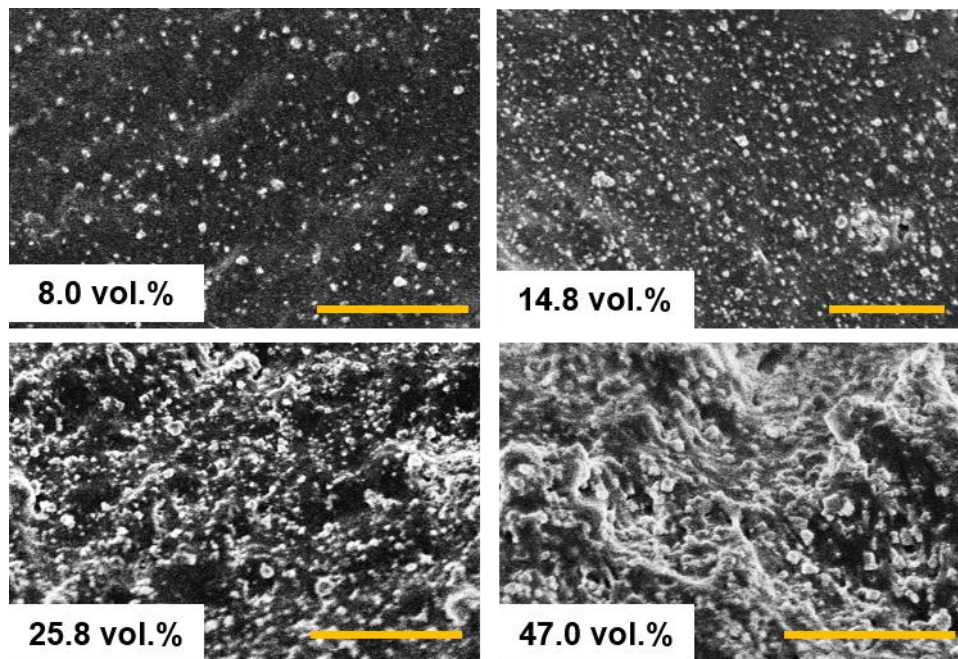


Figure 4.14 SEM images showing the fractured cross-sections of two types of composites containing $\phi_{\text{BTO:La}} = 8.0, 14.8, 25.8,$ and 47.0 vol.%. More agglomeration of the filler was observed at higher La concentration (47.0 vol. %) BTO:La. All scale bars are $5 \mu\text{m}$.

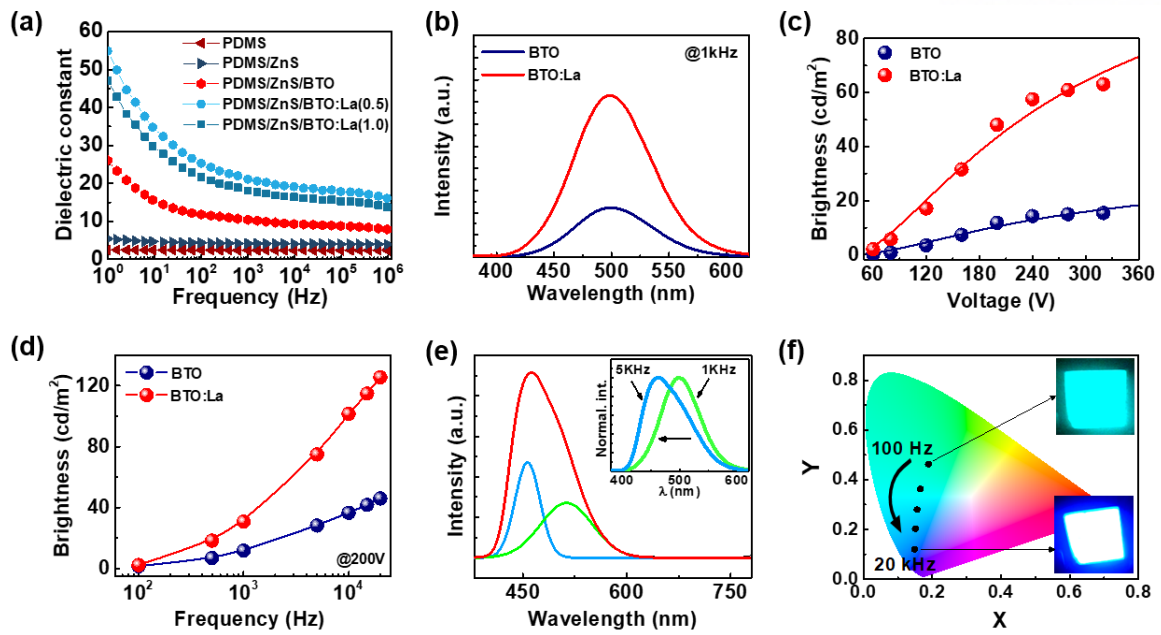


Figure 4.15 Dielectric permittivity and EL spectroscopic studies of flexible ACEL devices. (a) Frequency dependence of dielectric constant of PDMS, PDMS/ ZnS, PDMS/ZnS/BTO, PDMS/ZnS/BTO:La (0.5), and PDMS/ZnS/BTO:La (1.0). (b) EL intensity comparison spectra of flexible ACEL devices with and without BTO:La nanodielectrics, showing that La doping enhances the device brightness when driven at an AC bias of 200 V and 1 kHz. (c) Brightness comparison of the devices under various applied voltages and under an applied fixed frequency of 1 kHz. (d) Brightness of flexible ACEL devices under varying frequencies and fixed applied AC voltage. (e) EL spectrum of La-doped flexible ACEL device driven at a high frequency of 5 kHz frequency exhibiting emission color tuning as the peak position is shifted from green to blue emission wavelength. The right inset shows a comparison of EL spectra at low and high frequencies. (f) CIE 1931 color space chromaticity diagram showing CIE coordinates (x , y) of light emission calculated from the EL spectra obtained by varying the applied frequency.

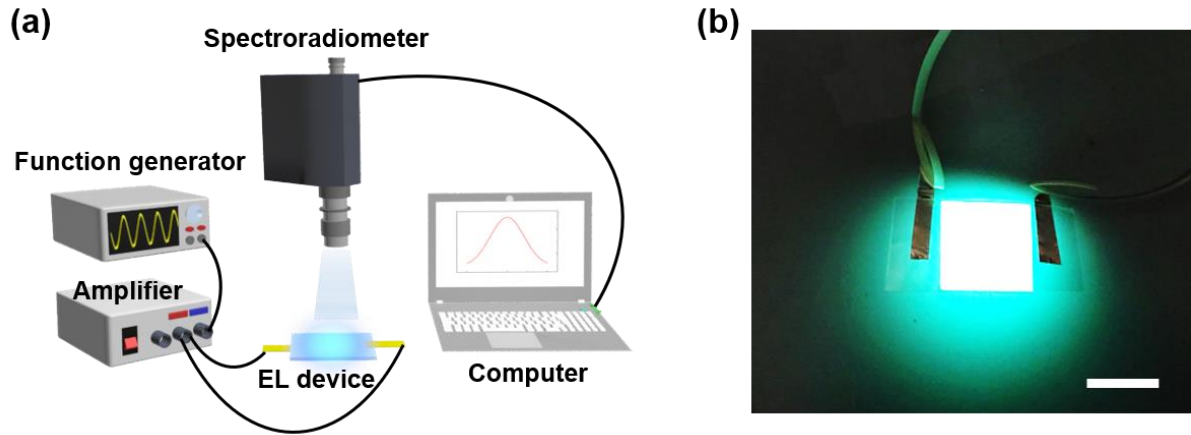


Figure 4.16 (a) Schematic illustration of setup used to characterize flexible ACEL devices. (b) Optical photograph of flexible ACEL device driven with 200 V and 1 kHz of AC bias. The scale bar is 3 cm.

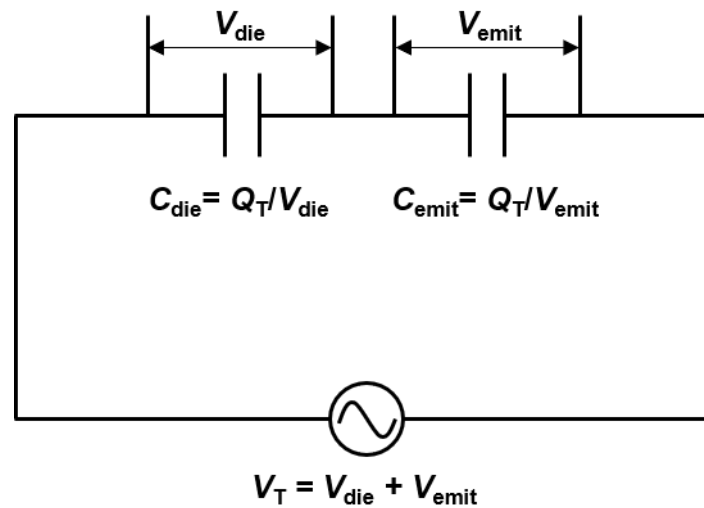


Figure 4.17 Schematic illustration of the ACEL device with the corresponding simplified equivalent circuit model, where V_T and Q_T are the total voltage and charge, C_{die} and V_{die} are capacitance and voltage of the BTO:La high- k nanodielectric layer, and C_{emit} and V_{emit} are capacitance and voltage of emitting layer, respectively. When an external voltage of V_T is applied to the circuit, V_T is dropped into V_{die} and V_{emit} , that are in inverse proportion to the capacitance values. Now that Q_T is same for both components in this series circuit, a higher dielectric constant or C_{die} means a lower V_{die} , resulting in the increase of V_{emit} .

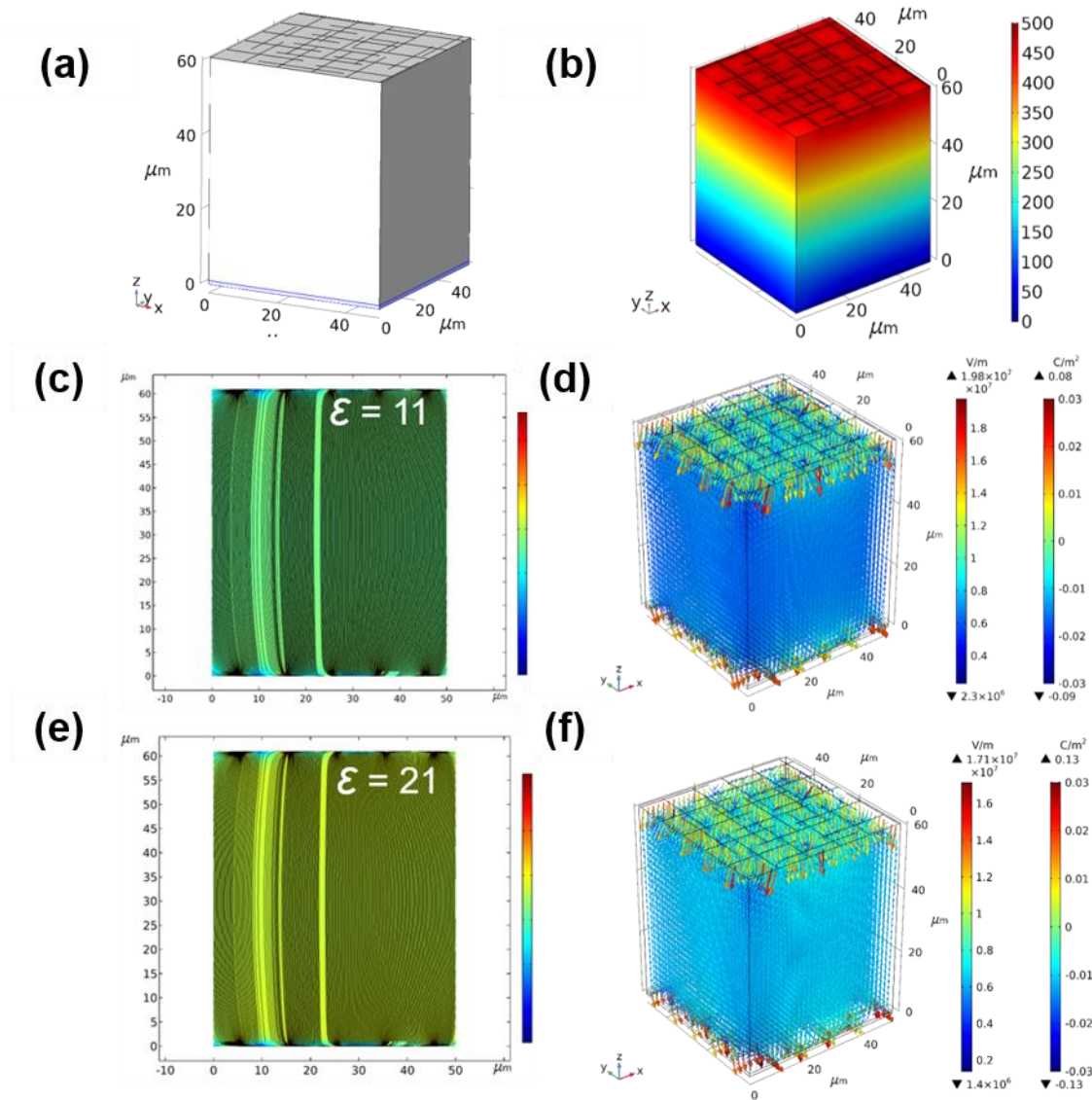


Figure 4.18 (a) Schematic of the model showing the mesh structure of a flexible ACEL device consisting of top and bottom electrodes, ZnS layer, and high- k dielectric layer. (b) Electrical potential distribution in a flexible ACEL device. The finite element models show 2D maps of the electric field (c and e) and charge density distribution (d and f) in flexible ACEL devices with different dielectric strengths. The materials used were undoped BTO and BTO:La. The dielectric constants of undoped and BTO:La were taken as 11 and 21, respectively.

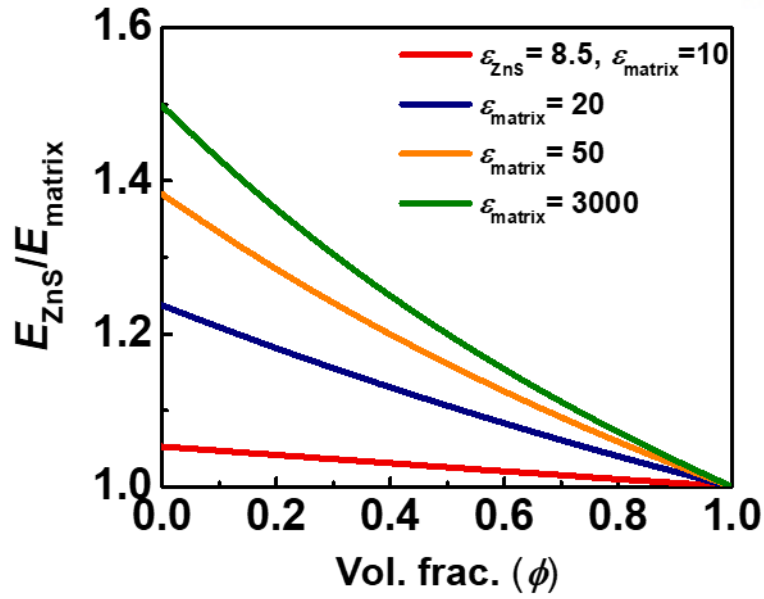


Figure 4.19 Local field strength variation with high dielectric matrix.

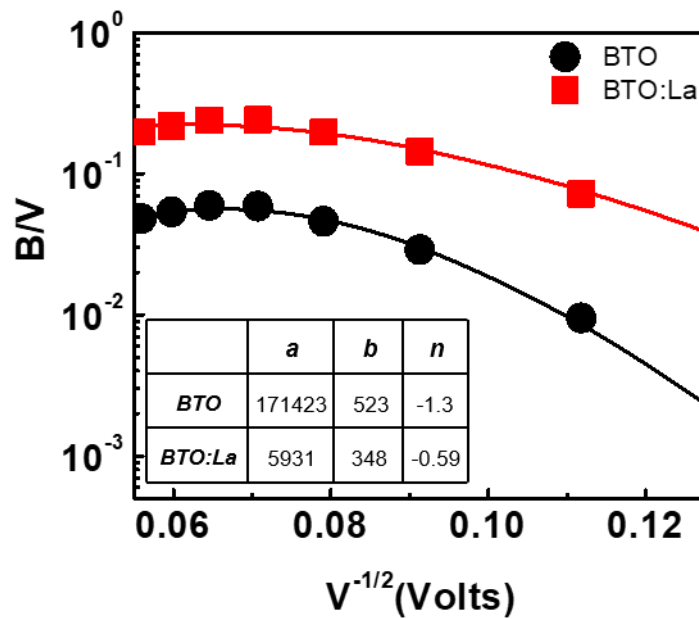


Figure 4.20 Relationship between voltage and device brightness fitted with Lehmann model (red squares and black circles are experimental data points and solid lines are fits to the Lehmann model).

The performance of a flexible ACEL device is strongly affected by the flexible transparent electrodes, which typically lead to a high operating voltage and a brightness gradient across the flexible ACEL devices.^{214, 235} By employing cross-aligned AgNW electrodes with a low resistance and uniform distribution of R_{sh} , we demonstrated high-performance flexible ACEL devices with uniform brightness over a large area ($12 \times 2 \text{ cm}^2$) (Figure 4.4c). For the quantitative analysis of EL uniformity, the normalized brightness of the flexible ACEL device collected at different spots along the whole device was measured, where the brightness was normalized to the first data point measured close to the electrode contact point (Figure 4.21a). For comparison, the normalized brightness values for different electrodes have been incorporated from previously published studies. Flexible ACEL devices with cross-aligned AgNW electrodes exhibited a uniform brightness over the whole device area due to the negligible voltage drop across the flexible ACEL device. On the other hand, devices with single-layer graphene and poly(3,4-ethylenedioxythiophene)-poly(styrenesulfonate) electrodes showed a significant drop in the device brightness.^{214, 235} FeCl_3 -intercalated few-layer graphene electrodes did not exhibit a voltage drop but did show a relatively non-uniform brightness compared to cross-aligned AgNW electrodes (Figure 4.21a). These results indicate that the device brightness strongly depends on the properties of the electrodes. Our flexible ACEL devices based on cross-aligned AgNW electrodes did not exhibit a brightness gradient due to the low sheet-resistance over the whole uniform cross-aligned AgNW networks. To investigate the uniformity of the cross-aligned AgNW electrodes, we monitored the temperature distribution in the Joule-heated electrodes using a noncontact IR thermal camera (Figure 4.22). Our cross-aligned AgNW electrodes showed a highly uniform temperature distribution of $70 \text{ }^\circ\text{C}$ at an applied voltage of 7 V (Figure 4.22b), indicating the uniformity of R_{sh} .

Our flexible ACEL devices exhibited excellent mechanical flexibility and stability under repeated bending tests. Figure 4.21b displays sequential optical micrographs showing the reliable device operation at a bending radius of curvature as high as 15 mm . The flexible ACEL devices exhibited a small (5 %) increase in device brightness as the radius of curvature was increased (Figure 4.21c), which can be attributed to the decreased thickness of the active layer during the bending, resulting in a reduction in the inter-electrode distance. Figure 4.21d shows that the brightness of the flexible ACEL device remained stable for up to 500 bending cycles. Table 4.1 shows the performance of our flexible ACEL device compared to EL devices reported in the literature in terms of operating voltage and frequency, electrode materials, and their luminance. Compared to previous EL devices, our BTO:La-based flexible ACEL device showed a higher luminance of $\sim 18 \text{ cd/m}^2$ at a similar voltage ($\sim 120 \text{ V}$) and frequency (1 kHz).

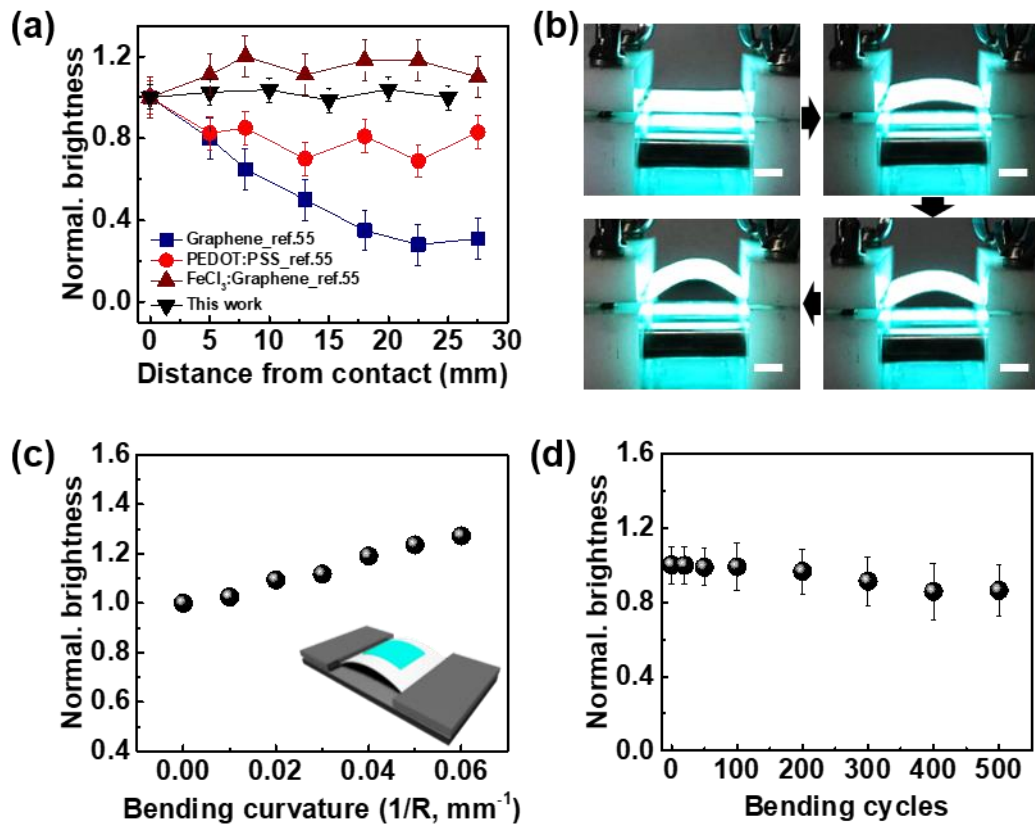


Figure 4.21 Device uniformity and flexibility. (a) Normalized brightness as a function of distance from the contact for high-aspect-ratio flexible ACEL devices, as shown in Figure 4.4c. (b) Sequential optical photographs of a flexible ACEL device undergoing increasing bending. The flexible ACEL device was bent into a convex shape, demonstrating excellent mechanical stability in terms of flexibility and bendability of the device. All scale bars are 1 cm. (c) Device operation under different bending radii. (d) Normalized EL intensity under cyclic bending tests showing excellent brightness retention.

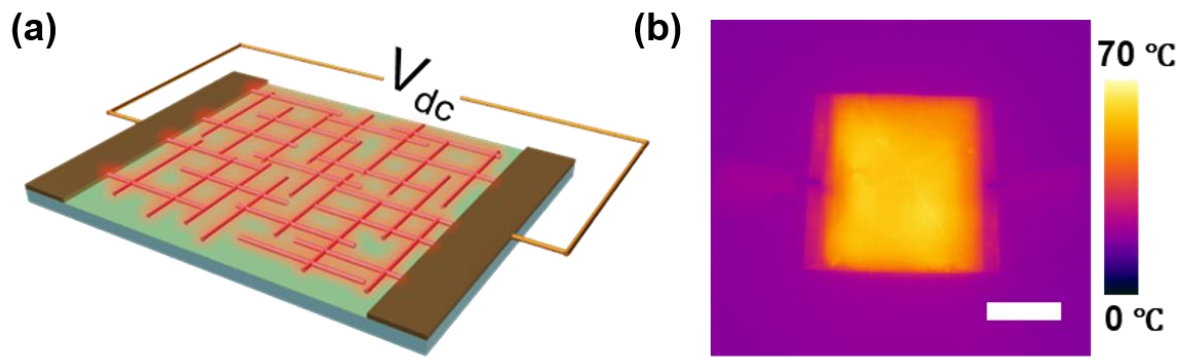


Figure 4.22 (a) Schematic of Joule heating test using an orthogonal AgNW network as a transparent electrode. (b) IR camera images of orthogonal AgNW networks at an applied voltage of 7 V. The scale bar is 2 cm.

Electrode	Luminance	Voltage	Frequency	Reference
AgNWs	> 5 cd/m ²	120 V	400 Hz (Square)	<i>Adv. Mater.</i> , 2016, 28, 7200
AgNWs	> 12 cd/m ²	120 V	1 kHz	<i>Adv. Mater.</i> , 2015, 27, 2876
AgNWs	~ 1 cd/m ²	120 V	1 kHz	<i>RSC Adv.</i> , 2017, 7, 8816
AgNWs	> 15 cd/m ²	120 V	1 kHz	<i>Appl. Surf. Sci.</i> , 2018, 429, 144
ITO	> 5 cd/m ²	120 V	1 kHz	<i>Opt. Express</i> , 2016, 24, 23419
Graphene	> 10 cd/m ²	120 V	16 kHz	<i>ACS Nano</i> , 2011, 5, 7149
PEDOT:PSS	> 5 cd/m ²	120 V	1 kHz	<i>Adv. Mater.</i> , 2011, 21, 305
PEDOT:PSS	4 cd/m ²	120 V	1 kHz	<i>RSC Adv.</i> , 2017, 7, 16885
Polar liquids	~ 40 cd/m ²	120 V	1 kHz	<i>Adv. Mater.</i> , 2017, 1703552
rGO	~ 10 cd/m ²	120 V	1 kHz	<i>RSC Adv.</i> , 2014, 4, 55671
AgNWs	~ 18 cd/m ²	120 V	1 kHz	This work*

Table 4.1 Comparison of results achieved in this study with performance of previously reported ACEL devices.

4.4 Conclusions

In summary, we have demonstrated low-voltage and high-brightness flexible ACEL devices based on screen-printed BTO:La high- k nanodielectrics and cross-aligned AgNW flexible electrodes. The La doping alters the crystallographic structure of BTO, leading to an increase in the dielectric constant at the appropriate doping concentration. The electric fields induced by the high- k BTO:La nanodielectrics significantly increased the device brightness. The flexible ACEL devices fabricated with high- k nanodielectrics exhibited low operating voltages below 120 V, a negligible brightness gradient, and enhanced brightness. In addition, we showed flexible ACEL devices with a low operating voltage and negligible brightness gradient by virtue of the low resistivity and low surface roughness of the cross-aligned AgNW electrodes. This study provides a robust platform for the development of efficient high- k dielectric materials based on aliovalent doping of ferroelectric nanoparticles for high-performance flexible EL devices.

Chapter 5. Self-healable and flexible thermoacoustic loudspeakers with AgNW/poly(urethane-hindered urea) PUHU electrodes

5.1 Introduction

Recently, thermoacoustic (TA) loudspeakers have attracted significant attention as a new type of speaker that does not rely on the vibration of the diaphragm; rather, these speakers depend on the temperature oscillation of the surrounding vibrating air to generate sound.^{70-72, 236-246} Typical speakers require space for the vibration of the diaphragm, which necessitates a complicated fabrication process and a large volumetric speaker size. However, the TA loudspeaker can be easily fabricated into a thin film-type speaker with a conductive film, thereby producing sounds without mechanical vibration. Generating sound with the simple thin film-type speaker is a great advantage of TA loudspeaker. It provides several advantages over typical speakers such as simple fabrication process, device-miniaturization, and flexibility for wearable applications. TA loudspeaker generates thermoacoustic sounds under an alternating current (AC) voltage, where periodic Joule heating of a conductive film by AC voltage induces the temperature oscillation that vibrates the surrounding air and generates sounds.^{71, 72} The first TA loudspeaker was manufactured using a platinum strip clamped to lead electrodes with extremely high heat capacities.²³⁶ Conducting nanomaterials reduce the effective heat capacity per unit area (HCPUA) of the TA loudspeaker owing to the lower matter content compared to bulk materials, thereby enhancing heat release into the surrounding air and the sound pressure by air vibration.⁷² Recently, there have been significant interests regarding the use of various conducting materials such as carbon nanotubes (CNTs),^{72, 237} graphene,^{71, 238, 239} graphene oxide aerogel,²⁴⁰ gold,²⁴¹ copper nanowires (CuNWs),²⁴² polystyrene sulfonate (PEDOT:PSS),²⁴³ MXenes,²⁴⁴ and silver nanowires (AgNWs)^{70, 245} for the fabrication of low heat-capacity films in TA loudspeakers. Although the TA loudspeaker that uses nanomaterials as conductive fillers has significant advantages on sound performance, previously researched TA loudspeakers are vulnerable to external damage, which leads to a disconnection of the conductive network and a reduction in their mechanical durability and flexibility when they are used in wearable electronic devices.^{71, 72, 245, 246} In addition, transparent TA loudspeakers can offer better appearance and good aesthetic impression in wearable electronic devices.²⁴⁷ Fabricated transparent TA loudspeakers can be applied to smart watches, surfaces of windows, posters, and computer screens without damaging the aesthetic appearance of applied surface.²⁴⁸ To apply the TA loudspeaker in wearable devices, the device should endure harsh outside environments to avoid device failure. Thus, developing TA loudspeakers that exhibit transparency, flexibility, long-term stability, outstanding durability, and self-healability is essential.

Through the application of self-healing polymers, the TA loudspeaker can become fault-tolerant, durable, recyclable, and shape-persistent. Previously, several types of self-healing polymers based on different mechanisms such as covalent bonds (e.g., Diels-Alder reaction and disulfide bonds) and non-covalent bonds (e.g., hydrogen bonds, ionic bonds, π - π interaction, and host-guest interactions) have been demonstrated.^{249, 250} Recent development of self-healing polymers such as Diels-Alder polymer,⁶⁶ hydrogen-bonding-based PDMS,^{251, 252} metal-ligand-based polymers,²⁵³ hydrogels,²⁵⁴⁻²⁵⁶ thiol-based polymer,²⁵⁷ and poly(urethane-hindered urea) (PUHU)^{258, 259} have enabled further applications to self-healable flexible devices such as capacitive touch sensors, electronic skins, or triboelectric nanogenerators, which maintain their functionality *via* self-healing processes. Moreover, each self-healing material exhibits pros and cons depending on its chain dynamics and modulus. Self-healing polymers with high modulus such as Diels-Alder polymers and PUHU require high temperature for self-healing. However, they have a solid polymer network and stronger covalent bond such as a C–C bond in Diels-Alder polymer and a C–N bond in hindered urea bond. Li *et al.*⁶⁶ demonstrated a healable capacitive touch screen based on Diels-Alder polymers, where re-establishment of Diels-Alder bonds enables strong bond reconstruction after the healing process. Hydrogels and thiol-based self-healing polymers with low modulus can be healed at a low temperature because of the great chain dynamics of low modulus polymers.^{260, 261} Self-healing polymers with low modulus is difficult to maintain its original performance. Due to their vulnerability to damages, low modulus limits their usage. In addition, hydrogels are inapplicable under dry conditions and thiol-based polymers exhibit a yellowish color owing to the presence of sulfur, limiting their use in transparent devices under ambient conditions.

Therefore, in this study, we propose polyurethane bearing bulky urea bonds to address the drawbacks of the previous self-healing polymers because of their transparency in a film state, strong covalent bonding, and fast reaction kinetics between free isocyanate and bulky amine groups that resulted in the rapid healing of surface damages. Transparent and conductive AgNW networks are fabricated on the PUHU film by a simple solution-based process as a highly transparent and self-healing material. The dynamic bonds in PUHU can successfully heal the damages and the AgNW networks covering the PUHU substrate is reconnected under the conditions of 95 °C and 80% relative humidity (RH) within 5 min. The AgNW networks that are completely disconnected are reconnected by reconstructing their conducting pathways after carrying out the self-healing process for 5 min. Additionally, the AgNW networks on the PUHU can be repetitively healed and their resistance is maintained after 1,000 taping tests and 10,000 bending cycles at a bending radius of less than 1.5 mm. To prove this concept, a transparent, flexible, and self-healable TA loudspeaker has been proposed, which is based on the AgNW/PUHU self-healable electrodes exhibiting an excellent sound generation

that is consistent with its initial sound pressure level (SPL). Our self-healable TA loudspeakers can be diversely applied in multifunctional, flexible, and smart electronic devices with improved convenience, appearance, and reusability owing to the excellent transparency, flexibility, and fault tolerance of AgNW/PUHU self-healable electrodes.

5.2 Experimental Details

Synthesis of Poly(carbonate diol) (PCD) Containing Hindered Urea Group: First, N,N'-di-tert-butyl ethylene diamine (3.00 g, 17.4 mmol) solution in 2-butanone (20 mL) was slowly added into IPDI (7.74 g, 34.8 mmol) solution in 2-butanone (10 mL) dropwise using a dropping funnel while stirring for 2 h at 35 °C. Second, the obtained HU-IPDI solution was poured into PCD-diol solution (Asahi Kasei, Duranol™, T5650J, $M_n = 800$ g/mol) in 2-butanone (27.8 g PCD-diol and a catalytic amount of dibutyltin dilaurate (DBTDL) in 50 ml of 2-butanone) while stirring at 70 °C for 1 h and 150 °C for 30 min. Third, the reaction mixture was concentrated using a rotary evaporator under low pressure after the urethane reaction was complete. Finally, PUHU was obtained as a colorless viscous liquid with quantitative yield.

Synthesis of Control Sample - Poly(carbonate diol) (PCD) Containing Ethylenediamine Groups: “A control sample, poly(carbonate urethane urea) (PUU), was prepared following the same synthesis procedure with the PUHU except using ethylenediamine instead of 1,2-bis(tert-butylamine)ethane.”

Fabrication of the Flexible and Self-Healable Substrates Using PUHU Polymer: First, to mix the reagents with the predetermined equivalence ratio of 1:1.5, 1.1 μmol of the synthesized PCD solution is mixed with 24.9 μmol of hexamethylene diisocyanate (HDI) (Sigma-Aldrich, 52649, $M_n = 168.19$ g/mol). Second, the PUHU mixture is poured on a prepared PEN substrate (2.5×2.5 cm²). The poured sample is manually spread out and stored at 25 °C for 20 min. Thereafter, the sample is put in an oven at 50 °C for 20 min. Finally, the temperature of the oven is subsequently raised to 70, 100, and 150 °C, with 40 min for each step, where 20 min is for increasing the temperature and the remainder 20 min is for annealing the sample on the temperature of each step.

Fabrication of the Flexible and Self-Healable Substrates Using Control Sample Ethylenediamine Polymer: First, to mix the reagents with the predetermined equivalence ratio of 1:1.5, 1.1 μmol of the synthesized PCD solution is mixed with 37.4 μmol of hexamethylene diisocyanate (HDI) (Sigma-Aldrich, 52649, $M_n = 168.19$ g/mol). Second, the PUHU mixture is poured on a prepared PEN substrate (2.5×2.5 cm²). The poured sample is manually spread out and stored at 25 °C for 20 min. Thereafter, the sample is put in an oven at 50 °C for 20 min. Finally, the temperature of the oven is subsequently raised to 70, 100, and 150 °C, with 40 min for each step, where 20 min is for increasing the temperature and the remainder 20 min is for annealing the sample on the temperature of each step.

Fabrication of the free-standing film for tensile test: Pouring mixed reagents at Polytetrafluoroethylene mold (2.5×5.0 cm²). The poured sample is manually spread out and stored at 25 °C for 20 min. Thereafter, the sample is put in an oven at 50 °C for 20 min. Finally, the temperature

of the oven is subsequently raised to 70, 100, and 150 °C, with 40 min for each step, where 20 min is for increasing the temperature and the remainder 20 min is for annealing the sample on the temperature of each step.

Fabrication of the Self-Healable AgNW/PUHU Electrodes: First, the surface of the substrate is pretreated with O₂ plasma at a radio frequency (RF) power of 18 W for 10 min before coating the AgNW solution on the self-healable PUHU substrate. This step generates a -OH terminated hydrophilic surface and cleans the surface of the substrate. The AgNW solution (Flexio Co., ltd.) containing 0.5 wt.% AgNWs with an average length of 23 μm and diameter of 23 nm is spin-coated on the surface.

Self-Healing Test of PUHU Polymer Samples: The scratched self-healable polymer sample was placed in the thermo-hygrostat (MG Indus, MG-TH series) tuned at 95 °C and a RH of 80%. Thereafter, a stabilization step was performed for 1 min before the 5 min self-healing process to re-balance the lost temperature/humidity conditions.

Fabrication of the Self-Healable TA Loudspeaker: First, the self-healable PUHU substrate was pretreated with O₂ plasma for 10 min and the AgNW solution was spin-coated on the 1.5 × 2.5 cm² area. Finally, Cu electrodes were attached at each end of the AgNW networks.

SPL Test of Self-Healable TA Loudspeaker: 1 V DC voltage and 7 V AC voltage is applied to fabricated TA loudspeaker and the distance between TA loudspeaker and commercial microphone was 2 cm.

Characterization: The surface morphology of the self-healable electrodes was examined using an OM (PSM-1000, Olympus) and a field emission SEM (FE-SEM, Hitachi S4800) at an operating voltage of 10 kV. The glass transition temperature of PUHU polymer was determined by DSC (Q200, TA instruments); Tensile test of PUHU and control sample synthesized by ethylenediamine (TXA, YEONJIN Co., Korea); Self-healing efficiency test result with scratch depth profile (OLS3100, Olympus); The optical transmittance in the visible range was determined using ultraviolet-visible spectroscopy (Cary 5000, Agilent). The resistance of the self-healable electrodes was measured using a digital multimeter (3201, Müller). The surface profile of self-healable electrodes was examined using an AFM (DI-3100, Veeco). The characterization of AgNW/PUHU electrode after repetitive self-healing processes is measured by FTIR spectrometer (670/620, Varian); The applied AC voltage was generated by a function generator (AFG 3011C, Tektronix). To capture the sound emitted by the loudspeaker and analyze the SPL and frequency, a dynamic signal analyzer (National Instruments Corp.) integrated with a commercial microphone (40PH, GRAS) was used. All the SPL tests of the TA loudspeaker were performed in an anechoic chamber with a cut-off frequency of 500 Hz and a sound transmission class > 30 dB (SMB-80, IDS technology).

5.3 Results and Discussion

The hindered urea-based isophorone diisocyanate (HU-IPDI) is first synthesized as a self-healing agent; this is aimed at preparing the self-healable PUHU polymer (Figure 5.1a), wherein the functional groups including hindered urea and isocyanate groups are confirmed *via* Fourier-Transform Infrared Spectroscopy (FT-IR) analysis (Figure 5.2). The IPDI and HU-IPDI peaks appear at approximately 2,250–2,270 cm^{-1} from the isocyanate (-NCO) group and at 1,630 cm^{-1} from the C=O bond of urea linkage. Thereafter, the self-healable prepolymer is prepared by reacting the synthesized HU-IPDI and polycarbonate diol (PCD), resulting in the formation of both urethane and urea functional groups in the prepolymer chain. As illustrated in Figure 5.2, while the peak from the -NCO group disappears in the PUHU indicating complete reaction without residual reagents, new peaks appear at 1,745 cm^{-1} and at approximately 3,200–3,700 cm^{-1} , which corresponds to the C=O bond from the ester group of the PCD and hydroxyl group from the end of PCD, respectively. The self-healable matrix is prepared by reacting PUHU prepolymer with the reagent hexamethylene diamine (HDI). To slowly evaporate the methyl-ethyl-ketone solvent in a prepolymer solution to form a PUHU film without bubbles, the PUHU polymer on the polyethylene-naphthalate (PEN) substrate was cured in an oven under the stepwise increase of temperature (50, 70, 100, and 150 °C for 40 min at each step). As observed in the optical microscopy (OM) and the scanning electron microscopy (SEM) images showing the surface morphology of PUHU films after the scratching and healing processes, the fabricated PUHU polymer film exhibits excellent self-healing behavior (Figure 5.3). The images show the surface-damaged PUHU film was reconstructed after the self-healing process. Figure 5.1b illustrates the self-healing mechanism of the PUHU polymer *via* the dynamic hindered urea bonding. The self-healable matrix occurred when the dynamic covalent hindered urea bonds with bulky substituent reversibly dissociate into isocyanate and amine groups under a catalyst-free condition.^{258, 262} To confirm the effect of hindered urea bond to healing efficiency, self-healing test was conducted to the PUHU and control sample synthesized by ethylenediamine coated on the PEN substrate. The mechanical property of each polymer is characterized in Figure 5.4. The self-healing test result measured by confocal OM showed distinct effect of hindered urea bond (Figure 5.5). Moreover, suitable humidity conditions due to more hydrogen bonding between the amine formed by the free isocyanates and surrounding water can improve the self-healing performance.²⁵⁹ Figure 5.6 shows the OM images of PUHU polymer after self-healing processes with and without humid environment. When PUHU polymer is exposed to humid condition at the self-healing process, the scratch on the PUHU film healed rapidly with higher healing efficiency. To prepare the highly transparent and self-healable AgNW electrodes (Figure 5.1c), the reacted PUHU is first coated on the PEN substrate; thereafter, the AgNW solution is coated on the PUHU film *via* a spin-coating method (Figure 5.7). Figure 5.1d illustrates the SEM image of the

conductive AgNW networks on the PUHU film. The AgNWs form a dense conductive network without aggregation. As observed in Figure 5.1e, the fabricated 2.5 cm × 2.5 cm sized self-healable AgNW electrodes exhibit transmittance of 70.1–80.2% at a wavelength of 550 nm with a resistance range of 33–238 Ω by varying the number of coatings. The dense and thick conducting AgNW films with lower optical transparency and higher electrical conductivity are formed as the number of coatings increase.

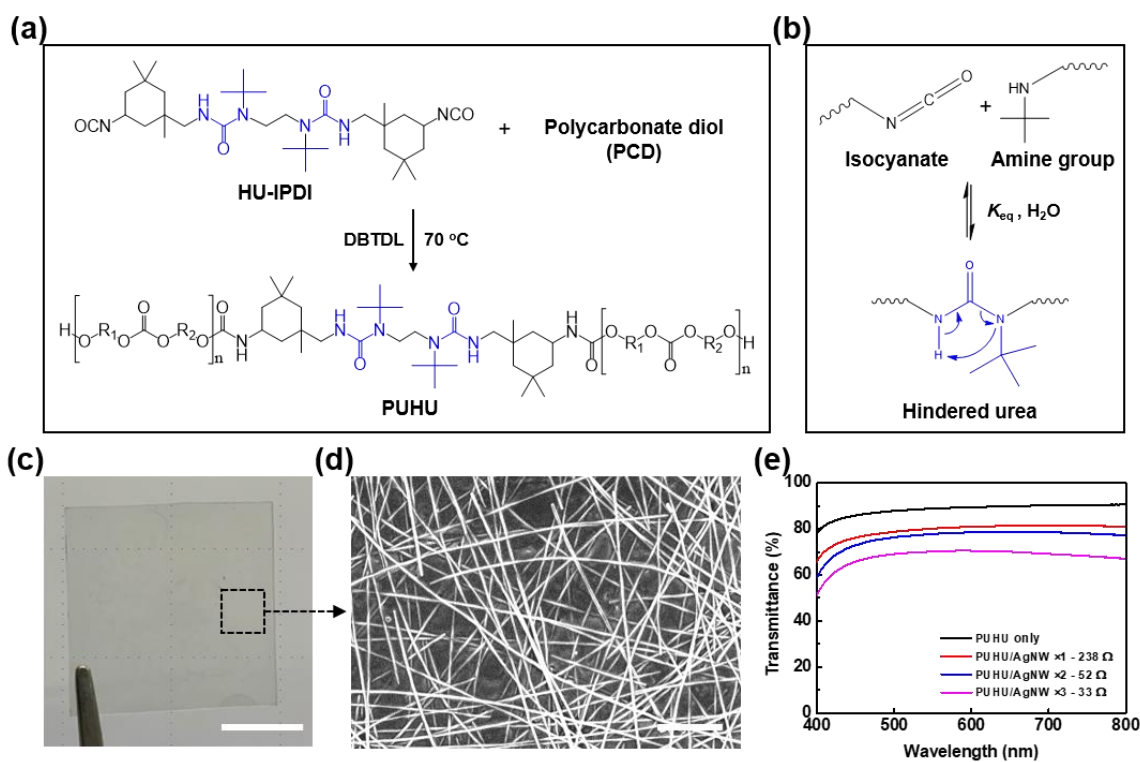


Figure 5.1 Self-healable and transparent AgNW/PUHU electrodes. (a) Synthetic scheme and chemical structure of the self-healable PUHU polymer (Hindered urea bond is indicated in blue lines). (b) Mechanism of the self-healing process of the PUHU polymer. (c) Photograph of the fabricated self-healable AgNW electrode. The scale bar is 1 cm. (d) SEM image of self-healable AgNW/PUHU electrodes. The scale bar is 1 μm. (e) Optical transmittance of AgNW-coated self-healable electrodes in the visible range of 400 to 800 nm. The air was used as standard reference.

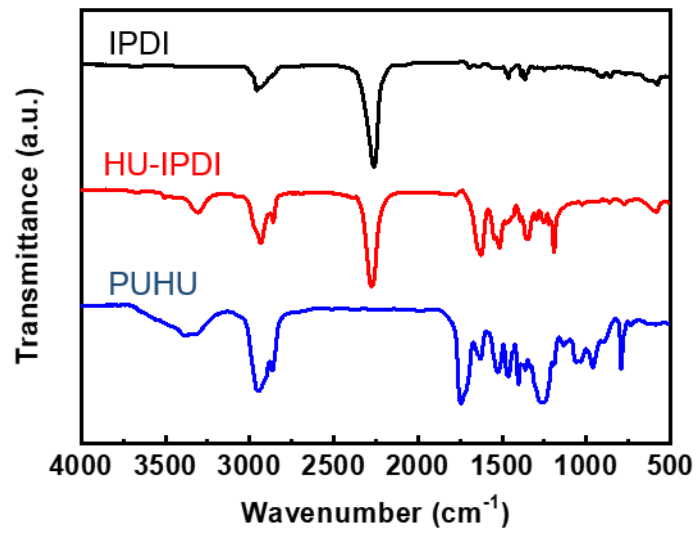


Figure 5.2 FT-IR spectra of IPDI, HU-IPDI, and PUHU. Isocyanate peak disappeared in PUHU (at $\nu = 2,250 \text{ cm}^{-1}$).

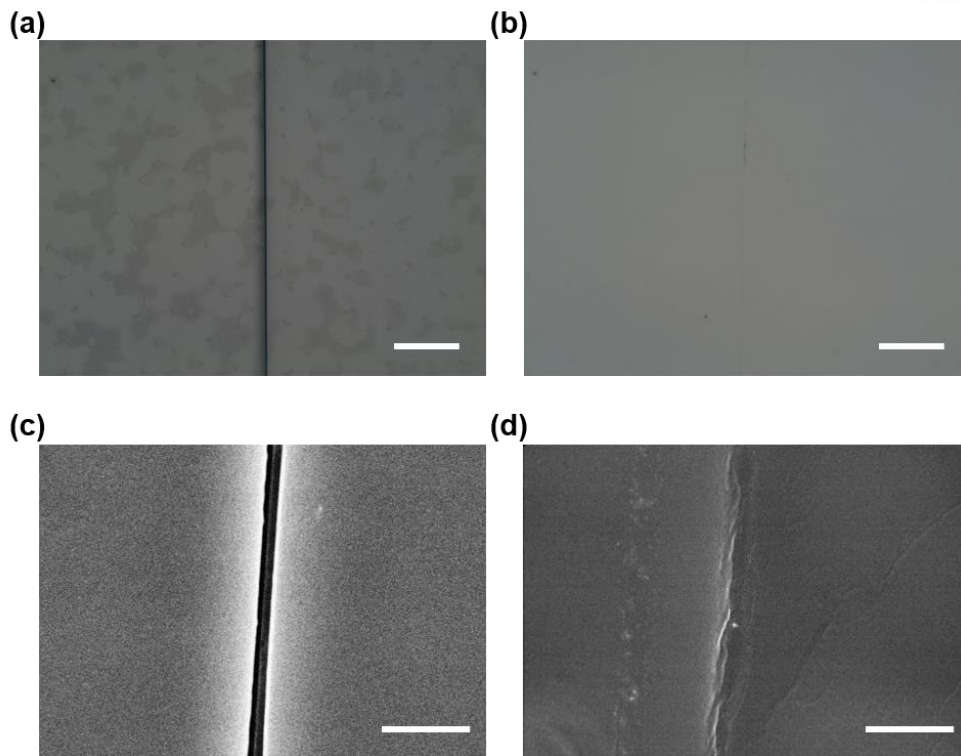


Figure 5.3 Surface morphology of the bare PUHU film. (a) OM image of the PUHU film after scratching and (b) after the healing process; the scale bars are 30 μm . (c) SEM image of the PUHU film after scratching and (d) after the healing process; the scale bars are 5 μm and 2.5 μm , respectively.

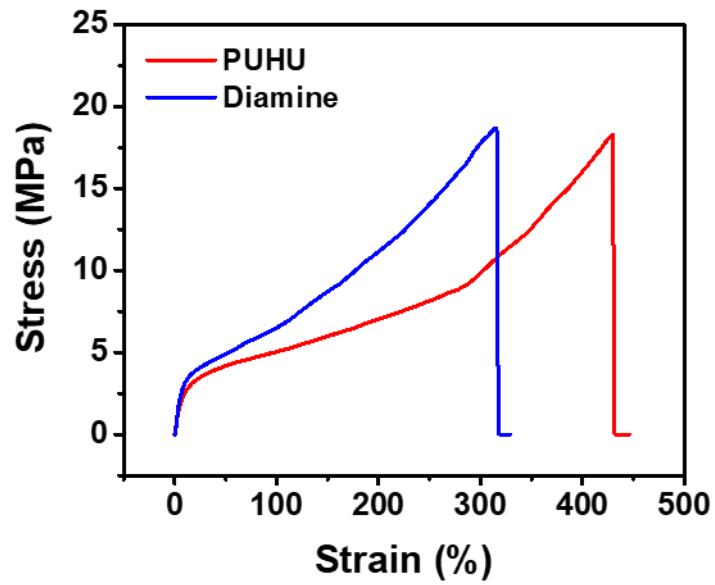


Figure 5.4 Tensile test result of PUHU and control sample synthesized by ethylenediamine. The modulus was 59 MPa for PUHU and 63 MPa for the control sample, respectively.

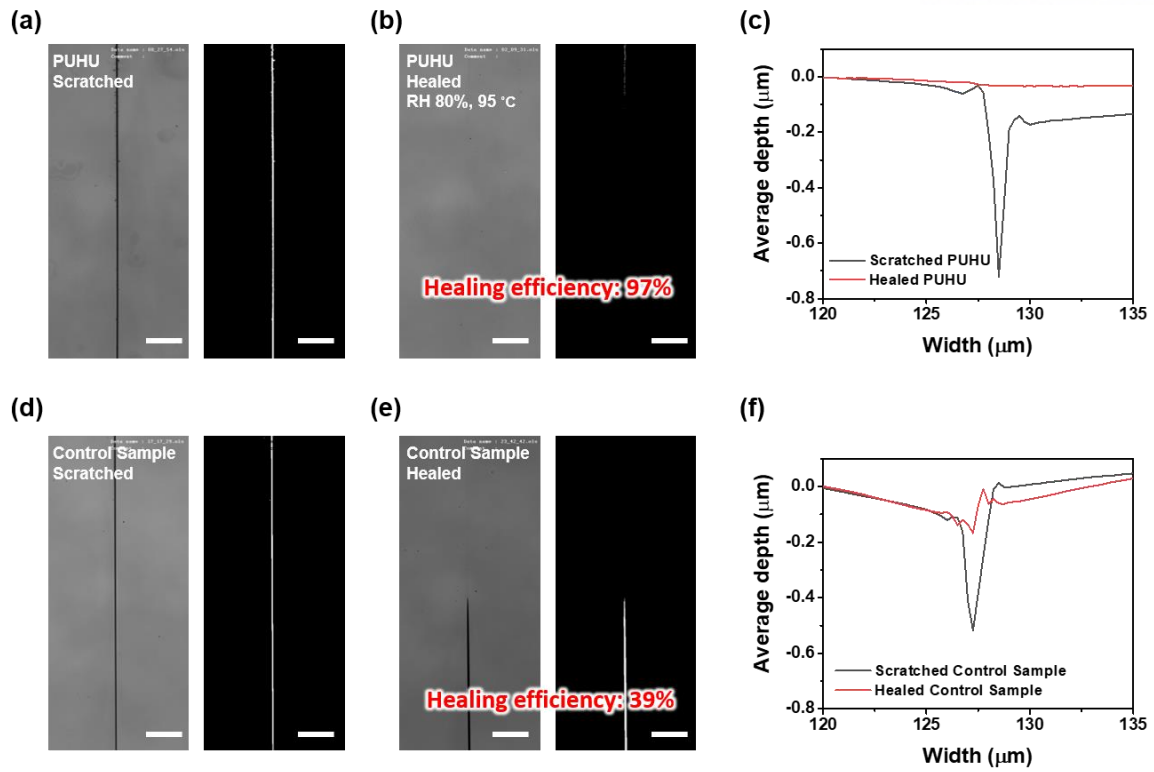


Figure 5.5 Confocal OM images of a PUHU film on a PEN substrate (a) before healing, (b) after healing, and (c) depth profile of a and b. Confocal OM images of a control sample synthesized with ethylenediamine on a PEN substrate. (d) before healing, (e) after healing, and (f) depth profile of d and e. All scale bars are 30 μm.

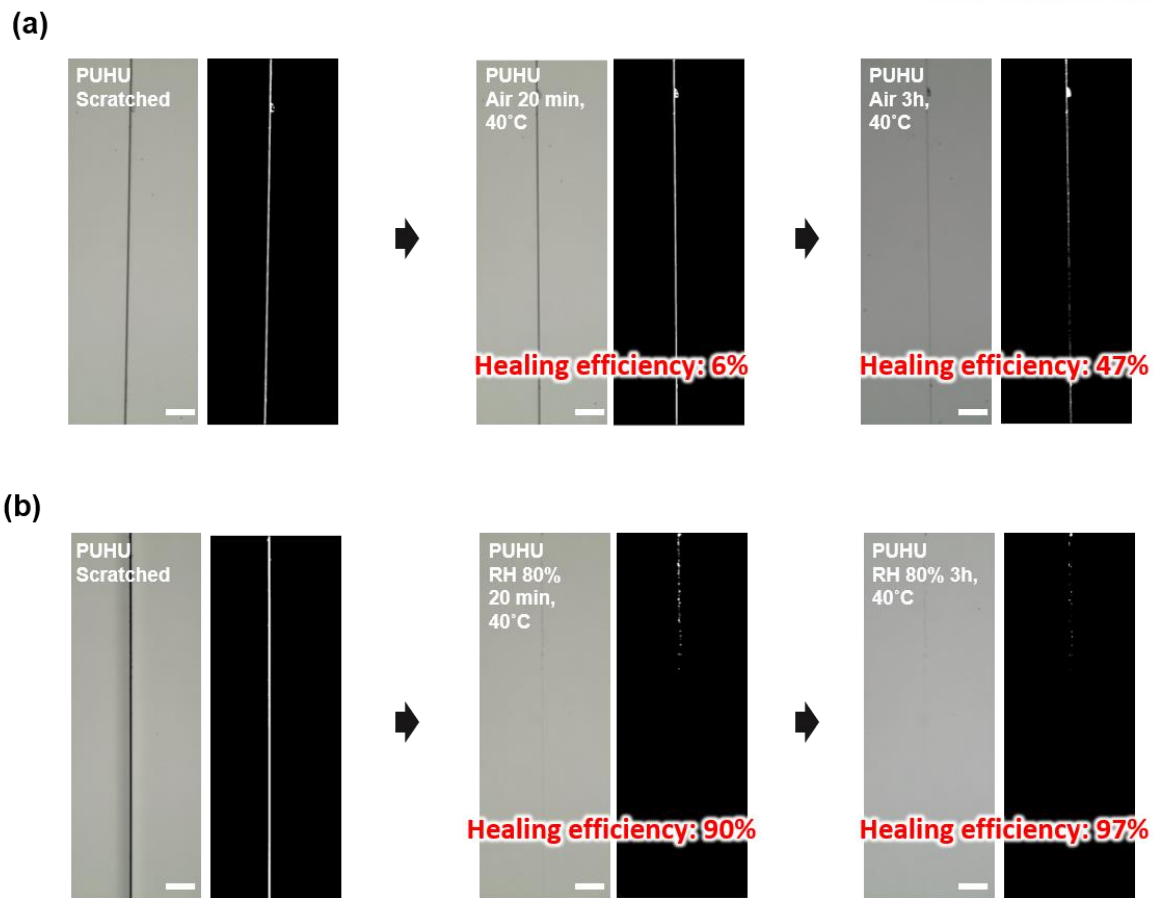


Figure 5.6 OM images of self-healing processes of PUHU polymers at (a) ambient air condition and 40°C and (b) RH 80% and 40°C. All scale bars are 30 μm.

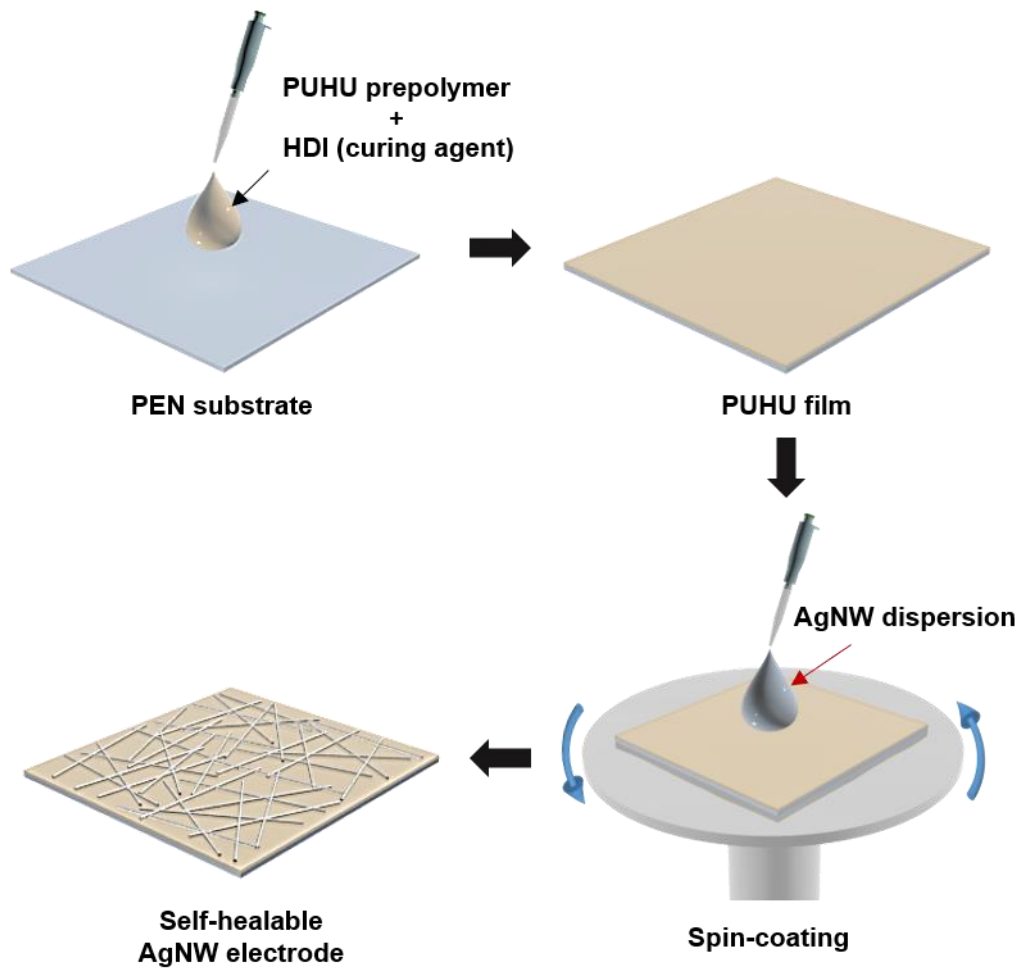


Figure 5.7 Fabrication process of self-healable AgNW/PUHU electrode.

The AgNW/PUHU self-healable electrode exhibits a substantial degree of self-healing property against the surface damage. The detailed scheme of the self-healing process of AgNW/PUHU electrodes is illustrated in Figure 5.8a. To test the self-healing of AgNW/PUHU electrodes, the electrode surface is scratched using a razor blade (ST-300, DORCO) with a force of 100 mN to completely disconnect the conducting AgNW network on the surface of the PUHU film, resulting in complete disconnection of conductive AgNW networks at the scratched area. The scratched AgNW/PUHU electrode undergoes the self-healing process at 95 °C and 80% RH. However, the hindered urea bond has a stability issue at humid condition. When the bulky urea bonds are exposed in a humid condition for a long time, the bulky urea bonds can be dissociated to carbamic acid and amine group and form random irreversible urea bonds.²⁶³ To check the stability of the PUHU polymer at high temperature and humid condition, the DSC analysis was performed for PUHU polymers at different humid-heat treatment conditions (Figure 5.9). The DSC curves of PUHU polymers with different time of heat and humid treatments were not perfectly matched with one another. The glass transition temperatures were similarly appeared at around -19.5 °C, but the slight shift may come from the hydrolysis of the PUHU polymer, which still did not affect the self-healing behavior of our device. As illustrated by Figure 5.8a, the rearrangement of polymer chains (containing amine groups with a bulky substituent) and free isocyanates of other adjacent bulky urea groups is observed to flatten the electrode surface configuration, resulting in reconstruction of the conductive AgNW networks. The detailed analysis of the surface morphology of the AgNW/PUHU electrode before and after the healing process at 95 °C and 80% RH for 5 min was exhibited by the atomic force microscopy (AFM) analysis (Figure 5.8b,c). Figure 5.8b shows the surface scratch of ~0.75 μm width that was completely self-healed because of the reaction between the residual isocyanate groups and amine groups having a bulky substituent on the PUHU film. To verify the healing success of the conducting networks, the surface roughness (R_q) is increased steeply for the scratched AgNW/PUHU film and restored after the healing process. The surface-height profiles from the AFM results confirm the successful reconstruction of the disconnected AgNW network after the self-healing process (Figure 5.8c). Figure 5.10 shows OM and SEM images of the AgNW/PUHU electrode before and after the self-healing process at 95 °C and 80% RH for 5 min. Figure 5.11 shows the SEM and corresponding energy dispersive X-ray spectroscopy (EDS) images of the AgNW/PUHU electrode before and after the self-healing process. The EDS elemental mapping images show that Ag is absent on the scratched area (Figure 5.11a); and it appears after the self-healing process (Figure 5.11b), verifying the successful reconstruction of the AgNW networks. Further, the resistance of the AgNW/PUHU electrode was measured by increasing the self-healing time from 1 to 5 min to investigate the effect of healing time on the recovery of the conductive networks. Subsequently, the relative resistance value ($R_{\text{heal}}/R_{\text{initial}}$) of electrodes is ~1 after 5 min,

indicating the complete recovery of the initial resistance of the AgNW/PUHU electrode (Figure 5.8d). Notably, the self-healing AgNW/PUHU electrodes can be healed continually even with the repetitive formation of scratches at the same location (Figure 5.8e). Therefore, the resistance of the self-healing AgNW/PUHU electrodes perfectly disconnected after surface scratching process. The resistance value of the self-healing AgNW/PUHU electrodes during both the repeated healing and scratching processes recovered from 17 to 39, 54, 430, 880, and 1,500 Ω after each cycle of the scratching and healing process. However, the humid environment is unstable for isocyanate group during self-healing process. To analyze the bonding after the repetitive self-healing processes, FT-IR of repetitively healed AgNW/PUHU electrode was measured (Figure 5.12). After 5 times of healing process, the AgNW/PUHU electrode shows the same trend of spectra which proves the electrode can endure the humid condition. Figure 5.13 shows the OM images of the surface of AgNW/PUHU electrode that was repetitively healed. The red box of OM images confirmed that the newly and previously healed surfaces coexist while intersecting each other. In addition, the resistance recovery of the AgNW/PUHU film after the self-healing process is shown *via* its utilization in an electrode for a LED lamp (Figure 5.14). The LED lamp turns off when the electrode is scratched and turns on after the self-healing process. This indicates the successful reconstruction of the conductive AgNW networks.

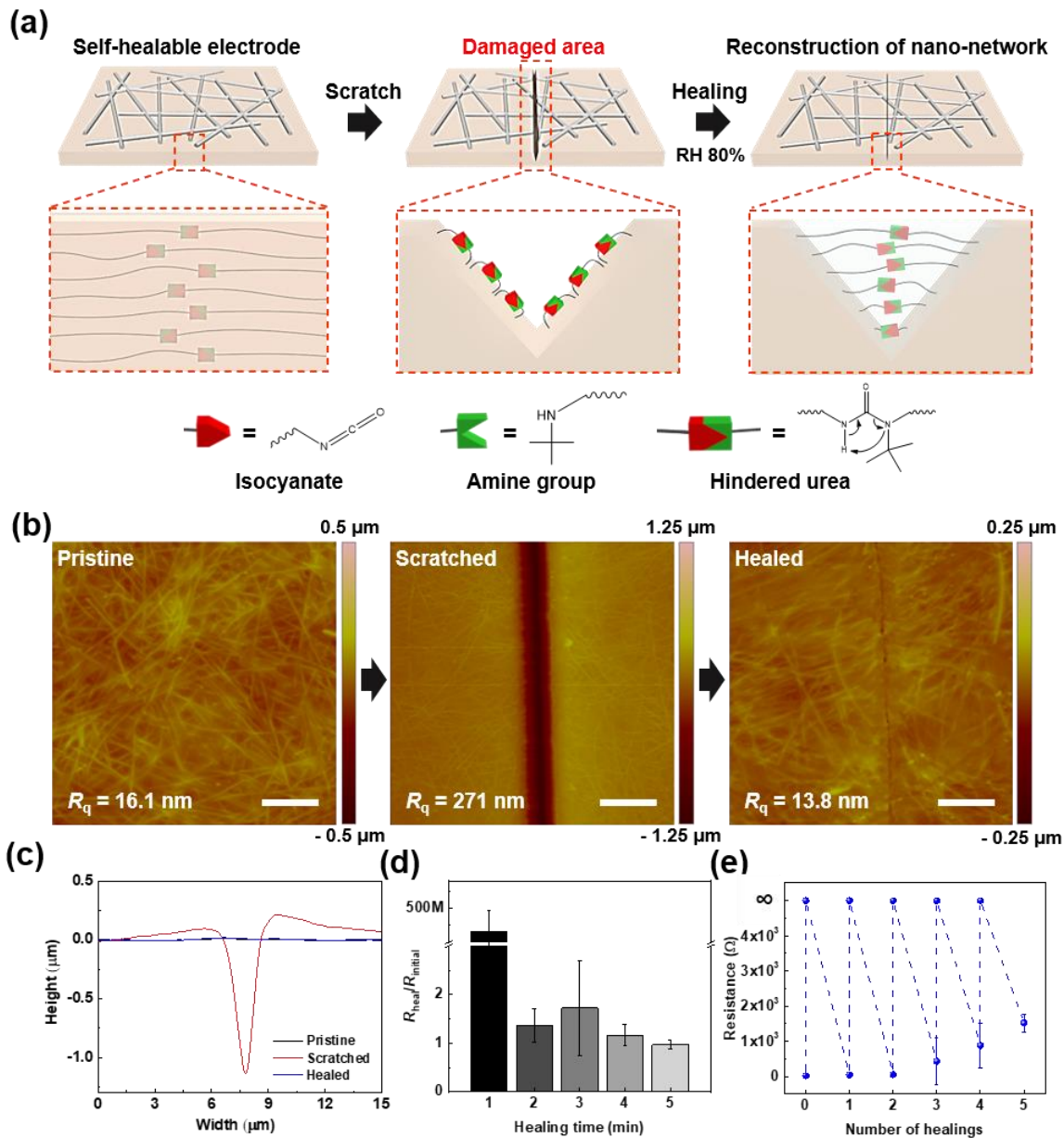


Figure 5.8 Self-healing behavior of the AgNW/PUHU electrodes. (a) Schematic illustration of the self-healing process of the presence of the healable AgNW/PUHU electrode. (b) AFM images of the self-healable AgNW/PUHU electrode before scratching (pristine), after scratching, and after the self-healing process. All scale bars are 3 μm . (c) Surface height profiling of the self-healable AgNW/PUHU electrode before scratching (pristine), after scratching, and after the self-healing process. (d) Plot of resistance after repetitive scratching and self-healing processes. (e) Plot of resistance after repetitive scratching and self-healing processes.

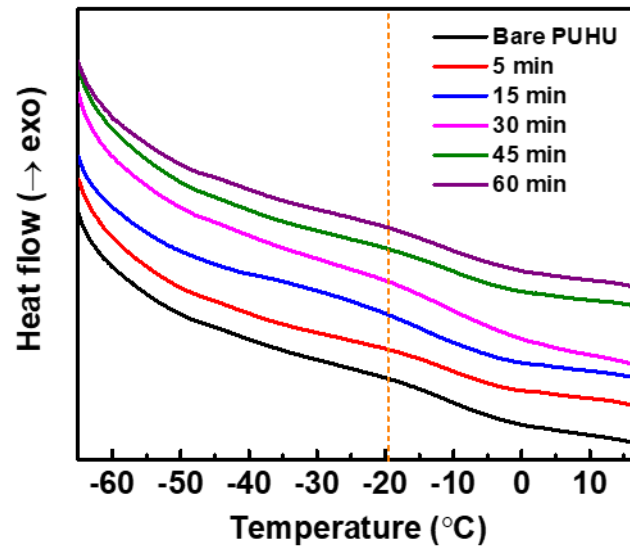


Figure 5.9 DSC curves of PUHU polymers after humid treatment at 95 °C and RH 80%. The glass transition temperature appeared near -19.5 °C.

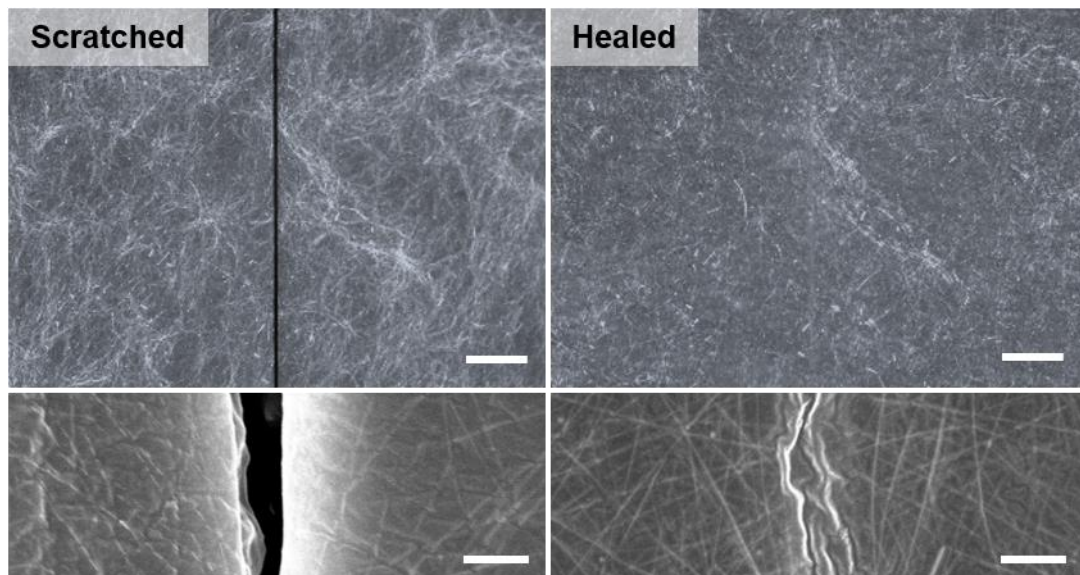


Figure 5.10 OM and SEM images of the AgNW/PUHU electrode after scratching (left) and the healing process (right). The scale bars are $2\ \mu\text{m}$ for (OM) and $1\ \mu\text{m}$ for (SEM).

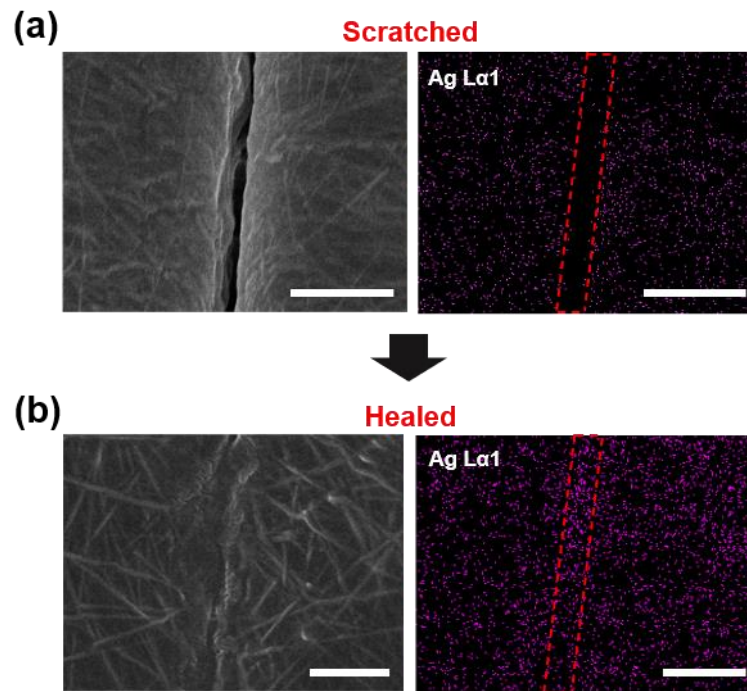


Figure 5.11 SEM and EDS images of self-healable AgNW/PUHU electrodes (a) after scratching and (b) after the healing process. The scale bars are 2.5 μm for (a) and 1 μm for (b).

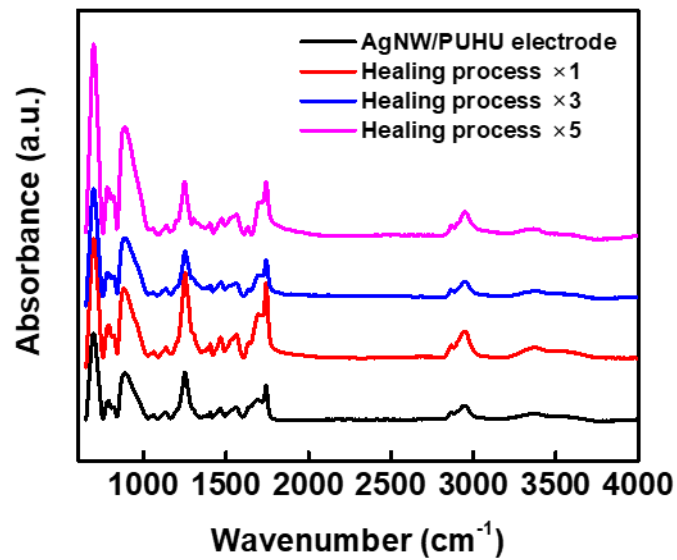


Figure 5.12 FT-IR spectra of AgNW/PUHU electrode after repetitive healing processes at 95 $^{\circ}\text{C}$ and RH 80%.

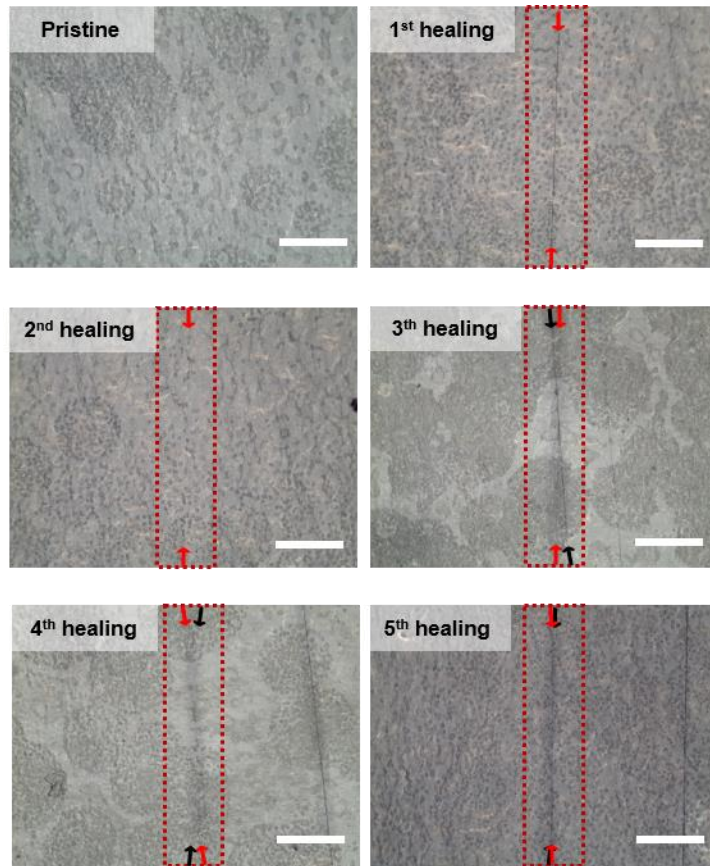


Figure 5.13 OM images showing the repeatedly healed AgNW/PUHU electrode surface.

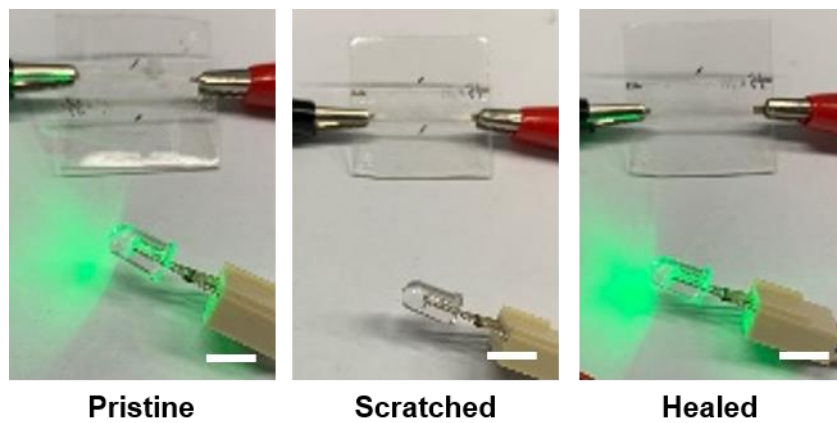


Figure 5.14 Photograph of the self-healable AgNW/PUHU electrode connected to the LED lamp during scratching and self-healing processes. All scale bars are 1 cm.

The mechanical and electrical stability of self-healable electrodes is significantly affected by the adhesion between the AgNW network and PUHU film. In that point, our self-healable electrodes show an excellent adhesion of AgNW networks on the PUHU substrate even without any adhesive enhancement additive, which is attributed to the semi-embedded AgNW network on the PUHU polymer during the coating process of the AgNW solution (Figure 5.15). When the AgNW solution is poured on the PUHU matrix, the surface of the PUHU film is swollen by ethanol, inducing the semi-embedded AgNW network on the PUHU film surface during the spin-coating process. Figure 5.15b shows a SEM image of the PUHU surface showing the semi-embedded AgNW networks on the surface of PUHU film after the AgNW coating process. A taping test is performed using a 3M scotch tape to confirm the adhesion between AgNW and PUHU. Figure 5.15c shows change in resistance of the AgNW electrodes coated on various substrates including glass, thermoplastic polyurethane (TPU), PEN, polydimethylsiloxane (PDMS), PUHU and humid-treated PUHU (95 °C, RH 80% for 5 min) during repeated taping cycles. The resistance of all the AgNW electrodes except the AgNW/PUHU electrode increased rapidly within a few times of taping cycles. However, the AgNW/PUHU electrode exhibited stable resistance after 1,000 taping cycles even after 5 min of humid treatment because of the strong adhesion of the semi-embedded AgNW structure on PUHU films. Figures 5.15d and e show the SEM images of AgNW networks before and after 1,000 taping tests, respectively. The AgNW networks coated on the PUHU maintain the dense conductive networks even after several taping cycles.

Moreover, the strong adhesion of AgNW networks on the PUHU film ensures mechanical stability of the electrodes. Figure 5.16a shows the change in resistance of the self-healable AgNW electrodes, depending on the variation of the bending radius. Thus, the electrode exhibits a minimal change in the resistance from 18.9 to 22.3 Ω for a change in the bending radius from 8 mm to 1.5 mm. The resistance value of self-healable AgNW electrode exhibits a negligible change from 21.6 to 23.6 Ω after 10,000 bending cycles with a bending radius of 5 mm, verifying the long-term stability of electrodes (Figure 5.16b). Figure 5.16c shows stable maintenance of the conductive network of the self-healable AgNW electrode that is connected to the LED for 10,000 bending cycles. Owing to their excellent mechanical and electrical stabilities (Figures 5.15 and 5.16), the proposed self-healable electrodes are applicable in flexible and damage-tolerant electrical devices.

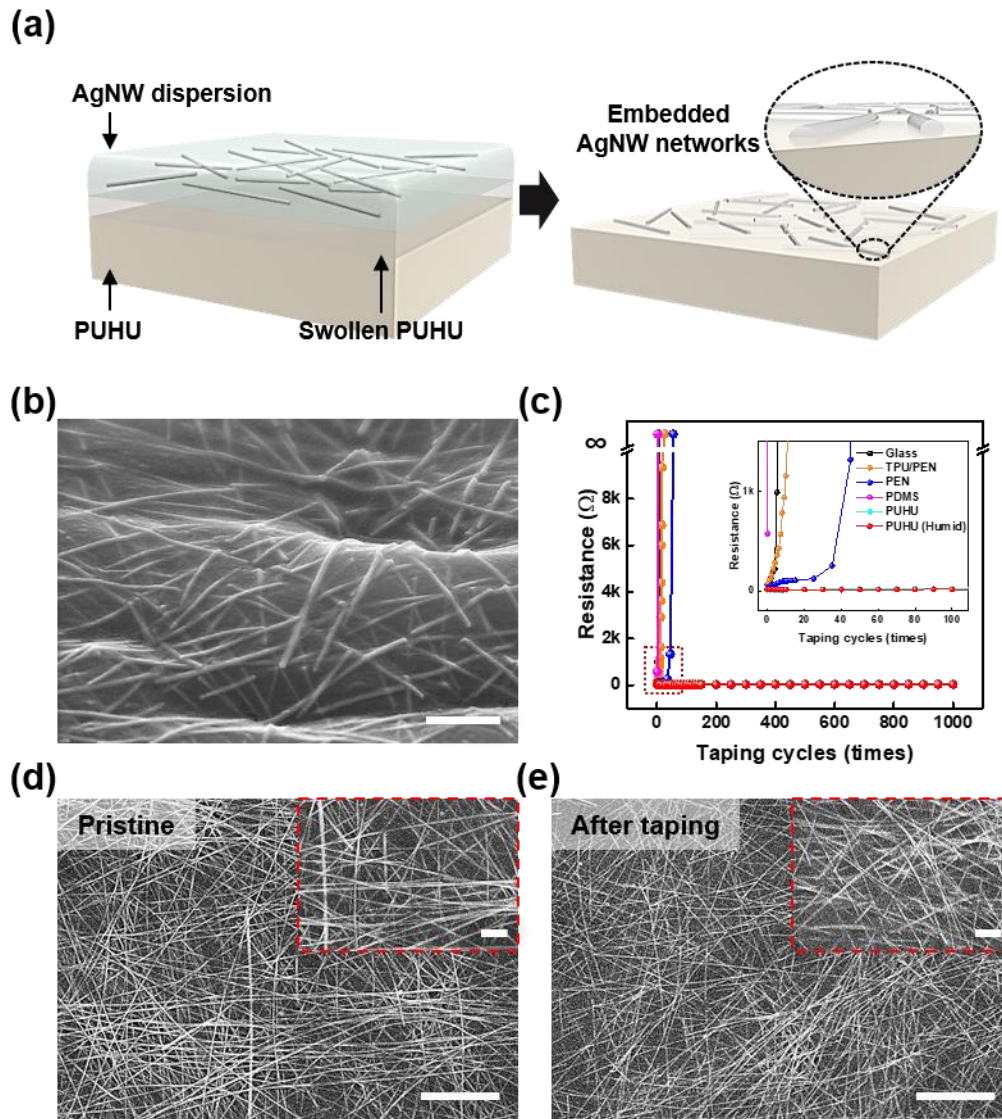


Figure 5.15 Adhesion properties of the AgNWs on the PUHU film. (a) Schematic illustration of the semi-embedded AgNW networks on the PUHU film surface. (b) SEM image of semi-embedded AgNW networks. The scale bar is 500 nm. (c) Change in the resistance of the AgNW networks on various substrates including glass, TPU, PEN, PDMS, and PUHU during the taping test for 1,000 times. (d,e) SEM images of the AgNW networks on the PUHU film (d) before and (e) after performing the taping test for 1,000 times. The scale bars are 2 μm . Insets show enlarged SEM images. The scale bars in insets are 500 nm.

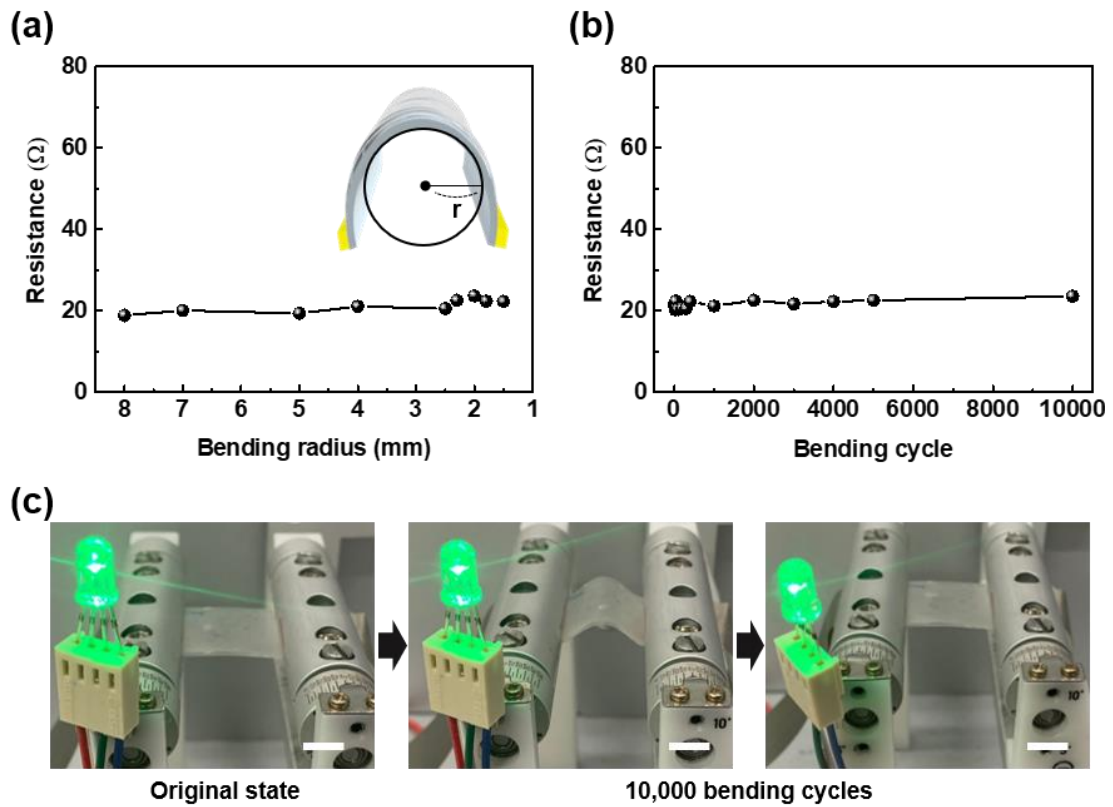


Figure 5.16 Mechanical properties of the self-healable AgNW/PUHU electrodes. (a) Plot of the change in resistance when the bending radius is changed from 8 to 1.4 mm. (b) Plot of the change in resistance when 10,000 bending cycles are performed at a fixed bending radius of 5 mm. (c) Photographs of self-healable AgNW/PUHU electrodes connected to the LED lamp during 10,000 bending cycles. The scale bars are 1 cm.

In this study, we fabricated transparent and self-healable TA loudspeakers to demonstrate the self-healable AgNW electrodes that exhibit scratch recoverability, transparency, and flexibility. Previously demonstrated TA loudspeakers were based on free-standing CNT,⁷² monolayered graphene,⁷¹ and graphene foam.²³⁹ However, such materials are vulnerable to losing their conductivity *via* surface damages, repetitive mechanical stresses, and delamination from substances. This problem can be mitigated by introducing a self-healing polymer into the TA loudspeaker allows a durable operating performance after the bending, taping, or surface damage on the conductive networks are healed. Figure 5.17a shows the fabricated self-healable TA loudspeaker comprising conductive AgNW networks ($1.5 \times 2.5 \text{ cm}^2$) on the PUHU-coated PEN substrate and the Cu electrodes at each end of the conductive AgNW networks. The working principle of the self-healable TA loudspeaker is illustrated in Figure 5.17b. First, the Joule-heating induces heat oscillation in the TA loudspeaker when the AC voltage is applied to it at a specific frequency. The heat oscillation from the TA loudspeaker vibrates the surrounding gas molecules, generating sound with doubled frequency from the frequency of the applied voltage. Figure 5.17c shows the scheme of an acoustic measurement system inside an anechoic chamber. The sinusoidal waveform of voltage input from the function generator is applied to the TA loudspeaker. Thereafter, a commercial microphone that is connected to a sound analyzer collects the emitted sound from the TA loudspeaker. As the sound pressure of the device is inversely proportional to the distance between the microphone and the TA loudspeaker,²³⁷ the experimental result follows the inversely proportional fitting (Figure 5.18). In our experiment, the microphone that collects sound is 2 cm away from the TA loudspeaker. The anechoic chamber has a background noise of below 25 dB, which can isolate the sound pressure from surrounding noise signals (Figure 5.19). Figure 5.17d shows the sound pressure produced by the self-healable TA loudspeaker as a function of the input power at 2, 10, and 20 kHz. In addition, the surface temperature of the TA loudspeaker increases linearly with the input power, indicating a reliable operation over different power range (Figure 5.17e). Figure 5.17f shows the SPL produced by the self-healable TA loudspeaker with the variation in the frequency from 2 to 20 kHz, before and after the scratching and healing processes. The TA loudspeaker exhibits SPL values ranging from 35.5 to 64.2 dB, which decrease below 25 dB after scratching. After the self-healing process, the TA loudspeaker exhibited SPL values ranging from 35.0 to 65.6 dB, which is similar to the range of the original SPL values before scratching; this indicates the damage-tolerant behavior of the AgNW/PUHU-based TA loudspeaker. Figure 5.20 shows that after the self-healing process of the surface scratch, the resistance of the self-healable TA loudspeaker has recovered, thereby allowing the damaged loudspeaker to operate properly.

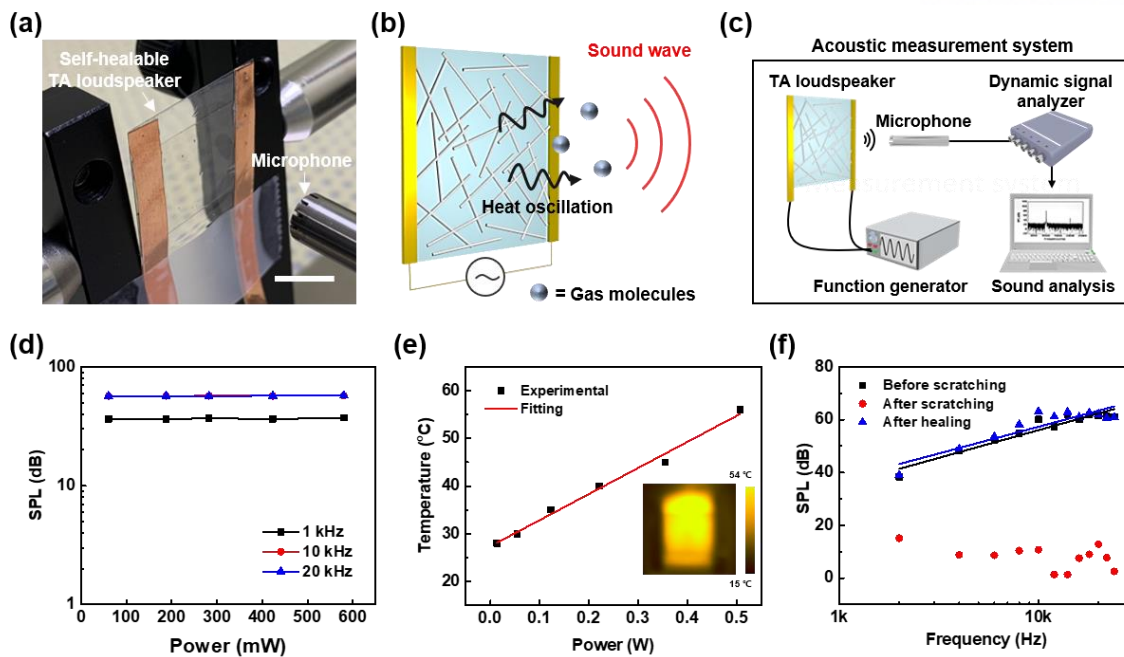


Figure 5.17 Self-healable AgNW/PUHU electrode-based TA loudspeakers. (a) Photograph of self-healable TA loudspeaker with microphone for sound measurements. The scale bar is 1 cm. (b) Schematic mechanism of the TA loudspeaker. (c) Schematic representation of the acoustic measurement system. (d) Variation in sound pressure level (SPL) generated from the self-healable TA loudspeaker as a function of input power at different frequencies. (e) Plot of temperature change of the TA loudspeaker against the increasing power input on the speaker device. Inset shows the infrared image of the TA loudspeaker while applying power. (f) Experimental values of the SPL versus sound frequency for the self-healable TA loudspeaker before scratching (pristine), after scratching, and after self-healing process.

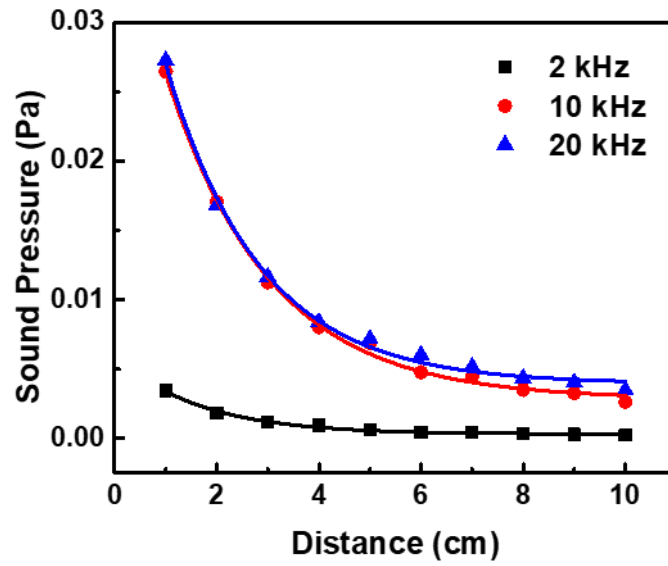


Figure 5.18 Plot of the sound pressure of the TA loudspeaker with different frequencies against varying distances, which is obtained by using a commercial microphone.

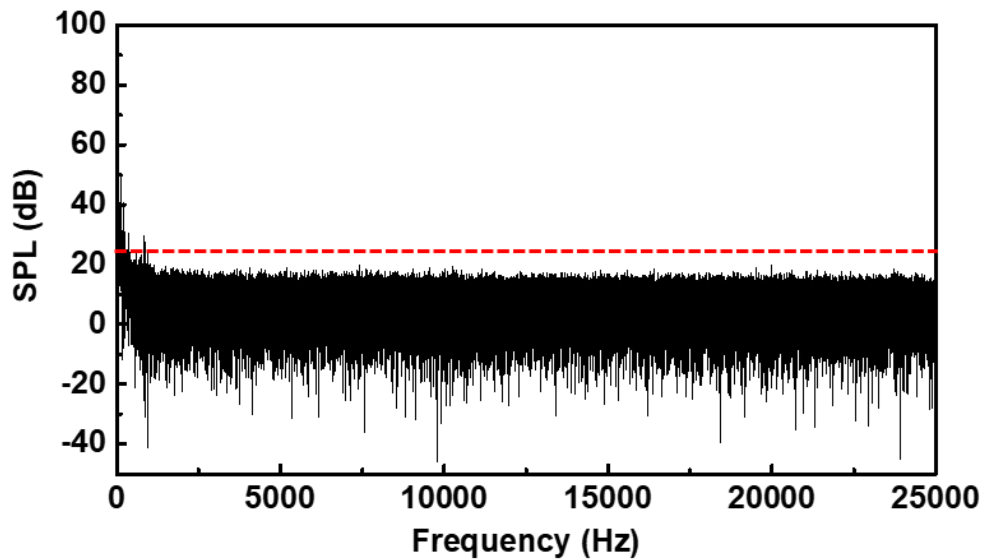


Figure 5.19 Plot of SPL inside an anechoic room without the TA loudspeaker, showing an ambient noise level of below 25 dB.

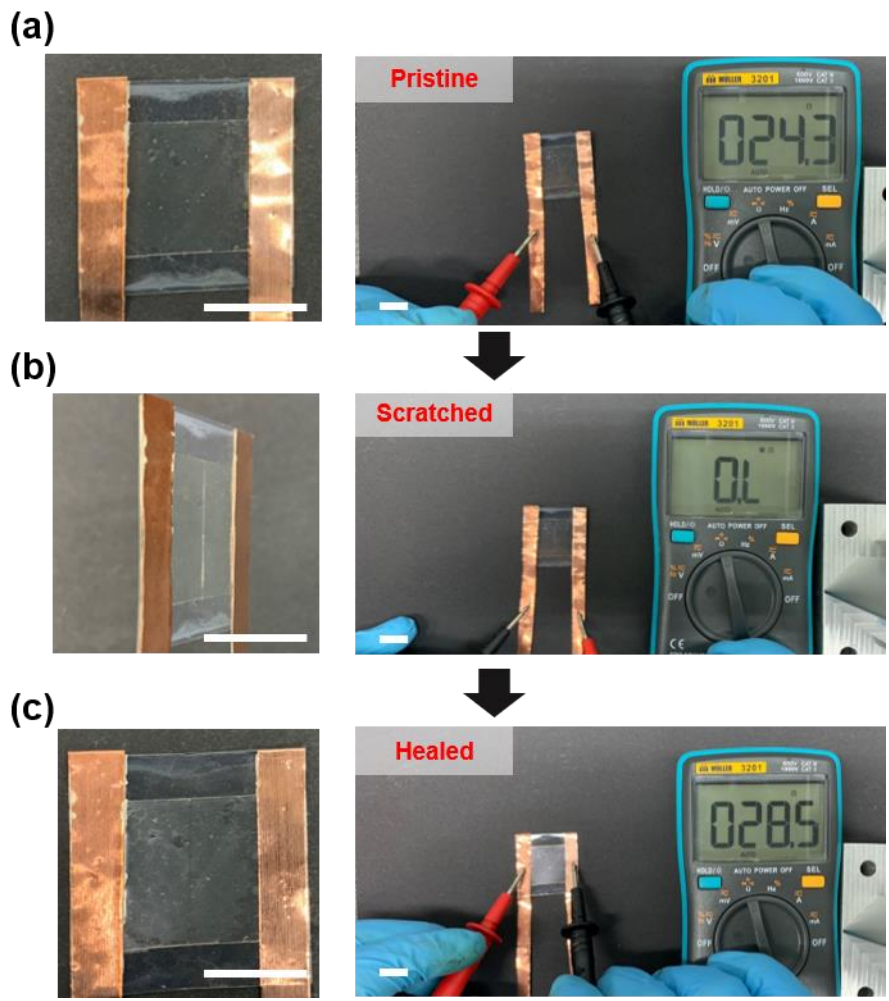


Figure 5.20 Photographs showing the surface and resistance of the TA loudspeaker at different stages: (a) before scratching, (b) after scratching, and (c) after scratching and self-healing. All scale bars are 1 cm.

5.4 Conclusions

In this study, we developed a transparent, flexible, and self-healable TA loudspeaker based on the PUHU self-healable polymer coated with the AgNW electrodes. While conventional AgNW networks are susceptible to surface damage, the self-healable AgNW/PUHU electrode can obtain a similar resistance to that of the initial resistance when it is healed at 95 °C and 80% RH. In addition, the AgNWs showed an excellent adhesion property on the PUHU polymer, which enhances the durability of the self-healable electrode. After the self-healing process of the damaged AgNW, our developed self-healable TA loudspeaker can recover its sound performance. Further, the TA speaker can be used for a different type of speaker application in various wearable electronic devices.

Chapter 6. Highly stretchable sound-in-display electronic devices with strain-insensitive AgNW electrodes

6.1 Introduction

The growing demand for bezel-less,²⁶⁴ interactive,²⁶⁵ and smart^{266, 267} displays, driven by the need to maximize user experience and the user-display interface, has inspired the integration of diverse functions (e.g., speakers, sensors, actuators, and cameras) into or under displays. For example, interactive displays with integrated sensors visualize various external stimuli such as touch,^{254, 268, 269} strain,²⁷⁰⁻²⁷² and pressure^{3, 42, 273, 274} and stimulate the human sense of vision to achieve their intuitive and instant perception. Prior research has mostly focused on the visualization of mechanical stimuli for tactile display and human-machine interface applications, leaving the visualization of sound waves underexplored. When visual stimuli are accompanied by acoustic ones or vice versa, they are easily perceived by humans via the auditory-visual synesthesia because of the synergistic effect of conscious and reliable perceptions.^{275, 276} Similarly, the integration of a loudspeaker and a display in a single device is expected to enable the generation of synchronized acoustic and visual information and thus allow the synesthetic perception of information and maximized user experience. Furthermore, sound-in-display technologies can be combined with stretchable and thin film form factors to afford stretchable sound-in-display solutions that can be widely applied in the internet of things (IoT), wearable devices, and human-machine interfaces attached on arbitrary curvilinear objects and body parts.

Although sound-emitting thin film electroluminescent (EL) devices can be fabricated using piezoelectric ceramics such as barium titanate,²⁷⁶ $\text{Pb}(\text{Mg}_{1/3}\text{Nb}_{2/3})\text{O}_{3-x}\text{PbTiO}_3$,²⁷⁷ and lead zirconate titanate²⁷⁸ with zinc sulfide-based phosphors as emitting layers, the applications of these devices in stretchable electronics are limited by the complicated fabrication processes requiring high temperatures, hard substrates, and rigid ceramic insulators. Kim *et al.*⁹³ demonstrated the simultaneous generation of color and sound in a soft photonic-crystal device with electro-actuation capability. However, even though this photonic skin showed the dual functionality of color tuning and sound generation in response to both direct-current (DC) and alternating-current (AC) biases, its practical usability in low-power and stretchable electronics was limited by the need for very high operating voltages (several kV) and the lack of stretchability. More recently, Kim *et al.*⁹⁴ have presented flexible artificial synesthesia electronic devices that employ inorganic EL phosphors to realize light emission and use piezoelectric polymer films to visualize input sound signals and generate sound. Despite the prominent brightness and sound performances of these thin film-based devices, their applications in stretchable electronics are limited by the inelasticity of conducting electrodes and piezoelectric materials. To have a wide

application scope, sound-generating displays should exhibit both bending capability and stretchability, i.e., should withstand large mechanical deformations and conformably wrap around arbitrary curvilinear surfaces and human bodies.

Stretchable AC electroluminescent (ACEL) devices have attracted much attention as next-generation light sources because of their high robustness and stable performance under large mechanical deformation, simple fabrication procedure, and high brightness.^{3, 87, 189, 191, 247, 279-281} Ionic hydrogels,^{3, 191} ionic conductors,^{189, 279} carbon nanotubes (CNTs),²⁸⁰ and silver nanowires (AgNWs)^{87, 247} have been widely used for the fabrication of stretchable electrodes to realize stretchable ACEL devices capable of stable operation under large strain. Among these devices, those based on hydrogels and ionic conductors show large stretchability but require overly high operating voltages because of the low conductivity of stretchable electrodes.^{3, 189, 191, 279} Conversely, stretchable ACEL devices with CNT- and AgNW-based stretchable electrodes show high luminance at relatively low operating voltages but exhibit low stretchability because of the inherent limitations of conducting materials.^{87, 279, 280} Despite the notable progress in the fabrication of stretchable ACEL devices, no attempts have been made to construct stretchable sound-in-display electronics using stretchable ACEL devices for the generation of synchronized sound and vision information, which can enhance the user experience and interface in diverse human-machine interface applications.

Herein, a stretchable sound-in-display device generating synchronized acoustic and visual information is fabricated using a stretchable EL loudspeaker with an emissive layer of copper-doped zinc sulfide (ZnS:Cu) and a dielectric elastomer actuator (DEA) matrix that are sandwiched between stretchable electrodes. When an AC bias is applied to this loudspeaker, EL occurs at the emissive layer, and an audible sound wave is generated through DEA matrix vibration. The intensities of light emission and output sound depend on the frequency and amplitude of the applied bias. In particular, light emission and sound-generation performances are invariant under significant tensile strain because of the stable electrical connection provided by strain-insensitive stretchable AgNW electrodes. As a result, the developed stretchable sound-in-display device synchronously generates light and sound even under the conditions of significant stretching.

6.2 Experimental Details

Fabrication of Strain-Insensitive AgNW Stretchable Electrodes: For elastic substrate preparation, a PDMS base (Sylgard 184, Dow Corning) and PDMS curing agent were thoroughly mixed in a 10:1 mass ratio, and the mixture was degassed in a vacuum desiccator for 30 min to remove bubbles and then evenly poured on a Petri dish. For the partial curing of PDMS, the Petri dish with PDMS was heated in an oven for 20 min at 80 °C. Prior to being coated with the AgNW dispersion, partially cured PDMS was pre-stretched using an in-house-made stretching stage and pre-treated with O₂ plasma (18 W, 5 min). The dispersion of AgNWs (average length = 22 μm, diameter = 21 nm; Flexiowire 2020, Flexio Co., Ltd.) was spun onto the partially cured and pre-stretched PDMS at a spin rate of 2000 rpm for 120 s, and the coated substrate was released and thermally cured at 80 °C for 2 h. Finally, Cu tapes and silver paste were applied to the edges of stretchable electrodes.

Fabrication of Stretchable EL Loudspeaker: The ZnS:Cu/PDMS composite was prepared by thoroughly mixing ZnS:Cu microparticle powder (Shanghai KPT Co.) with liquid PDMS in a 2:1 mass ratio using a planetary mixer (ARE-310, Thinky Corporation) at a mixing rate of 2000 rpm for 15 min. The thus obtained composite was spun onto the bottom stretchable electrode at a spin rate of 2000 rpm for 120 s, and the top electrode was then attached at the top of the composite layer. Finally, the assembled device was thermally cured at 80 °C for 2 h.

Characterization: The surface morphology of strain-insensitive stretchable electrodes was examined by optical microscopy (PSM-1000, Olympus) and field-emission SEM (Hitachi S4800, operating voltage = 10 kV). The latter technique was also used to probe the surface morphology of ZnS:Cu phosphors. Optical transmittance was determined using ultraviolet-visible spectroscopy (Carry 5000, Agilent), and electrical resistance was measured by a multimeter (3201, Müller). Stretching tests were performed using an in-house-made stretching apparatus. A function generator (AFG 3011C, Tektronix) connected with a power amplifier (T-700H, ElbaTech) was used to apply a square alternating voltage to the stretchable EL loudspeaker. For music playing, input sound waves of a sinusoidal waveform and an offset bias voltage were applied using LabVIEW software. Luminescence spectra of stretchable EL loudspeaker devices were recorded by a spectroradiometer (PR-655, PhotoResearch, Inc.). Luminance was measured in a dark chamber. A dynamic signal analyzer (National Instruments Corp.) integrated with a commercial microphone (40PH, GRAS) was used to capture the sound emitted by the stretchable EL loudspeaker. Sound tests were performed in an anechoic chamber with a cut-off frequency of 500 Hz and a sound transmission class of >30 dB (SMB-80, IDS-technology).

6.3 Results and Discussion

The concept of integrating a color module and a speaker in a single stretchable unit to afford a so-called stretchable sound-in-display device capable of light/sound synchronization is illustrated in Figure 6.1a. Figure 6.1b and 1c show the schematic structure and a cross-sectional scanning electron microscopy (SEM) image of a stretchable sound-in-display device consisting of a ZnS:Cu/polydimethylsiloxane (PDMS) EL layer sandwiched between stretchable AgNW electrodes on PDMS layers. The homogeneous size distribution (average size $\approx 18.2 \mu\text{m}$; Figure 6.2) of ZnS:Cu particles and their good dispersion in the PDMS matrix layer resulted in uniform light emission without device failure under high electric fields. The stretchable AgNW electrodes featured a percolative network of AgNWs (average diameter = $21 \pm 3 \text{ nm}$, average length = $22 \pm 5 \mu\text{m}$; Figure 6.3) conformally coated on the wrinkled PDMS matrix (Figure 6.1d), which enabled the maintenance of good electrical conductivity during mechanical deformation. Figure 6.4 shows a photograph of the semi-transparent stretchable EL loudspeaker that simultaneously generates sound (via vibration of the ZnS:Cu/PDMS composite DEA in the emitting layer) and light (via the field-induced EL of inorganic phosphors) under AC biases. Specifically, the loudspeaker emitted bright blue light and audible sound from both sides of the display under the application of a square pulse function (60 V, 5 kHz) even when subjected to mechanical deformations such as bending, twisting, and stretching during finger flexion (Figure 6.1e). DEA actuation resulted from the consecutive contraction and expansion of the DEA film in the thickness and lateral directions under the AC bias input for light emission, enabling the synesthetic perception of both color and sound (Figure 6.1f). Although single-functionality devices, i.e., those capable of light emission *or* sound generation, have been reported, the concept of stretchable sound-in-display electronics employing a stretchable EL loudspeaker for the generation of synchronized sound and visual information has not yet been explored (Table 6.1). In addition, our stretchable EL loudspeaker achieved high brightness (luminance $\approx 15.1 \text{ cd m}^{-2}$ at 120 V and 1 kHz), excellent sound-generation performance (sound pressure level (SPL) $\approx 83.3 \text{ dB}$ at 120 V and 10 kHz), and large stretchability (up to 150%), and was therefore favorably compared with previously reported devices listed in Table 6.1.

Stretchable electrodes are critically important for the realization of high-performance stretchable sound-in-display devices. During repetitive stretching or mechanical deformation, previously reported stretchable electrodes based on graphene,²⁸² conducting polymers,²⁸³ CNTs,²⁸⁴ and hybrid systems²⁴⁷ experience electrical conductivity degradation due to the damage of conducting networks. Attempts to solve this problem included the deposition of AgNW networks on elastomeric matrices; however, the resulting electrodes still exhibited limited stretchability.^{83, 285-288} Herein, strain-insensitive stretchable electrodes fabricated by the formation of AgNW networks conformally attached to a wrinkled PDMS substrate (Figure 6.5) were shown to maintain electrical conductivity at uniaxial

tensile strains of up to 150%. Partially cured PDMS (20 min at 80 °C) was stretched to 150%, released to form wrinkles, and subsequently treated with O₂ plasma to afford a hydrophilic surface bearing hydroxyl groups²⁸⁹ and thus enhance surface wettability and ensure the uniform coating of AgNWs. After the spin coating of AgNW dispersions, partially cured pre-strained PDMS was released and fully cured (2 h at 80 °C). The stiffness differences between the stiff AgNW layer and the soft bottom PDMS layer resulted in the formation of periodical wrinkles upon the release of pre-strained PDMS (Figure 6.6). In addition to wrinkles, cracks were formed in the direction parallel to that of the pre-strain because of the Poisson effect, as the release of pre-stretched PDMS resulted in its expansion in the direction transverse to that of stretching. The softness and stickiness of partially cured PDMS enabled the strong and conformal attachment of AgNW networks on the periodic wrinkles of stretchable electrodes (Figure 6.7a,b). In addition, the low Young's modulus of partially cured PDMS minimized the formation of surface cracks after the release of pre-stretched PDMS. On the contrary, the use of the less sticky and less elastic fully cured PDMS resulted in the poor attachment of AgNW networks on wrinkles, and protruded nanowires together with abundant cracks were observed (Figure 6.7c,d). The conformal adhesion of AgNW networks to partially cured PDMS endowed the corresponding stretchable AgNW electrodes with an ability to maintain electrical conductivity during repeated taping tests, while in the case of electrodes fabricated on fully cured PDMS, electrical conductivity decreased after several taping tests (Figure 6.8).

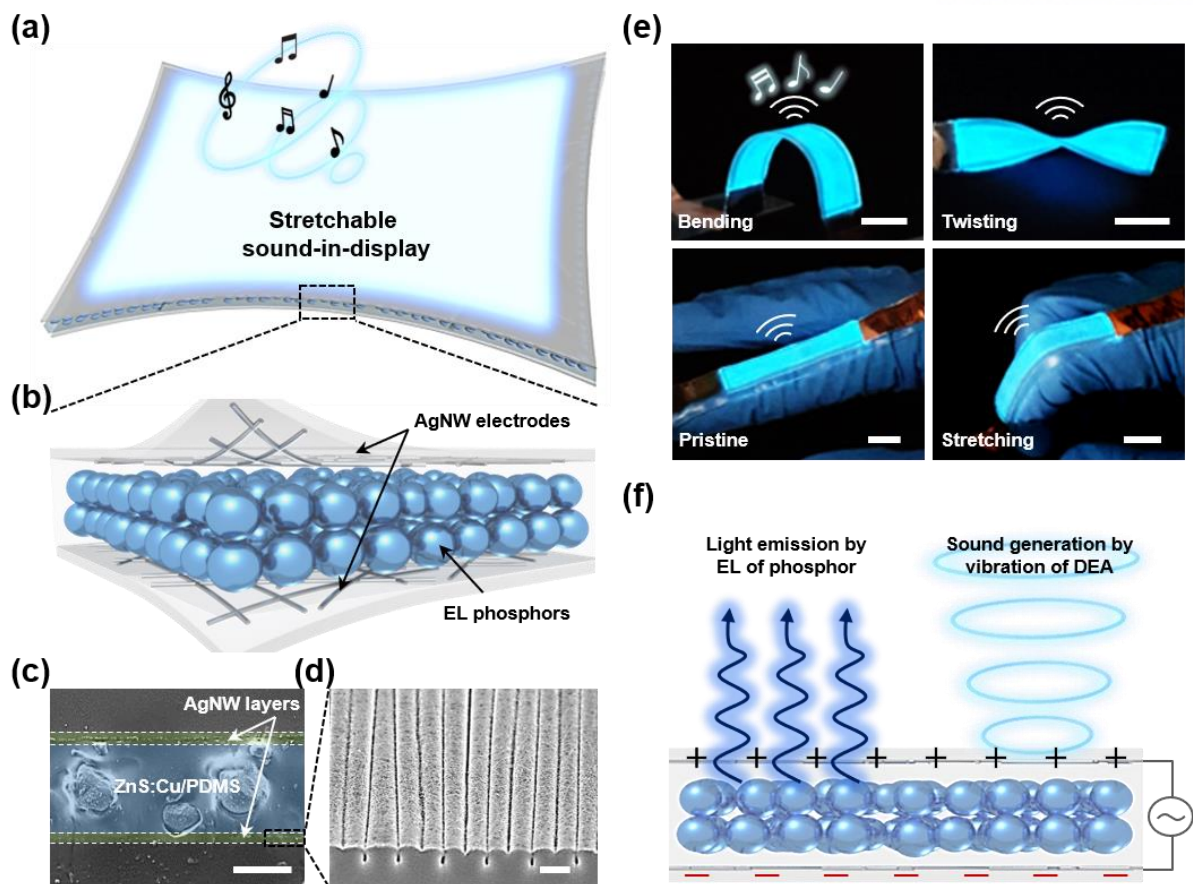


Figure 6.1 Stretchable sound-in-display electronics. (a) Concept of a stretchable sound-in-display device and (b) schematic image showing device geometry. (c) Cross-sectional SEM image of the device. Scale bar is 20 μm . (d) SEM image of stretchable AgNW electrode. Scale bar is 5 μm . (e) Operation of the sound-in-display device with sound-synchronized EL under bending, twisting, and stretching on the index finger. An audible sound and blue luminescence are generated (AC 60 V and 5 kHz). All scale bars are 1.5 cm. (f) Schematic operation mechanism of the sound-in-display device.

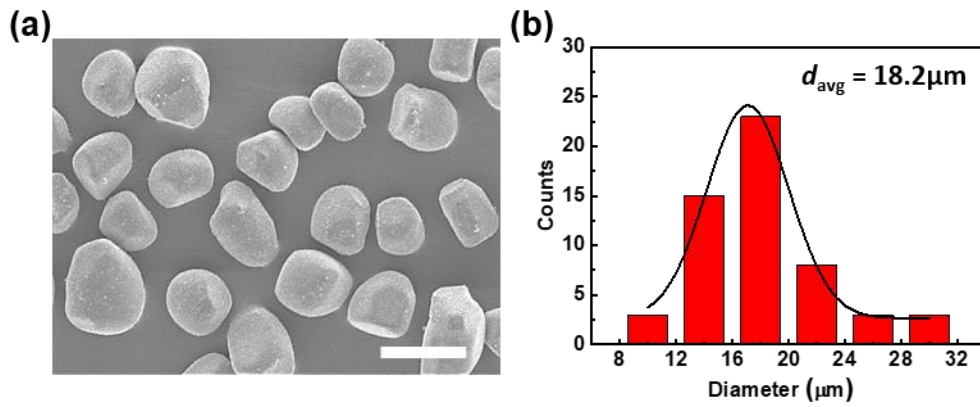


Figure 6.2 Investigation of size distribution of ZnS:Cu phosphors. (a) SEM images of ZnS:Cu phosphors. The scale bar is 25 μm. (b) Size distribution of ZnS:Cu phosphors. The average diameter of ZnS:Cu phosphors is around 18.2 μm.

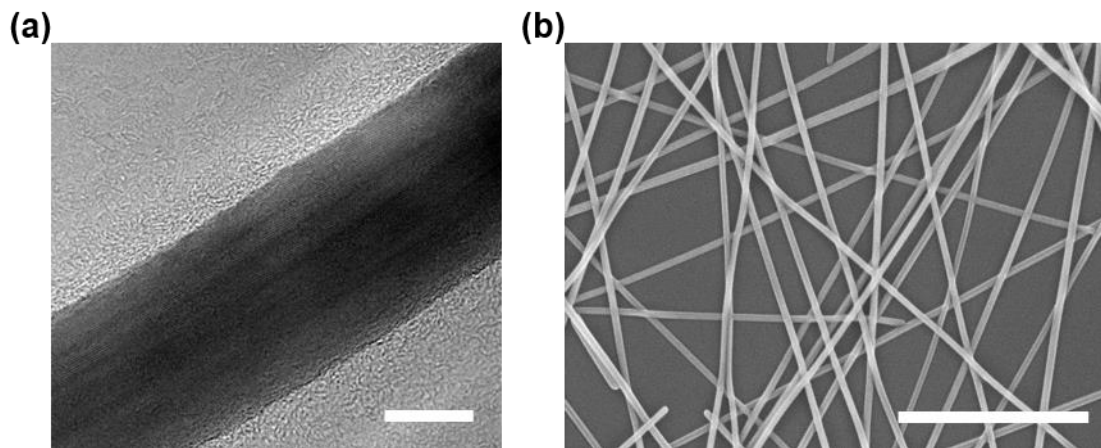


Figure 6.3 Investigation of AgNWs. (a) TEM images of single AgNW. The scale bar is 10 nm. (b) SEM images of AgNW networks. The scale bar is 1 μm.



Figure 6.4 Photograph of the fabricated stretchable EL loudspeaker device placed on the background UNIST logo. The scale bar is 1.5 cm.

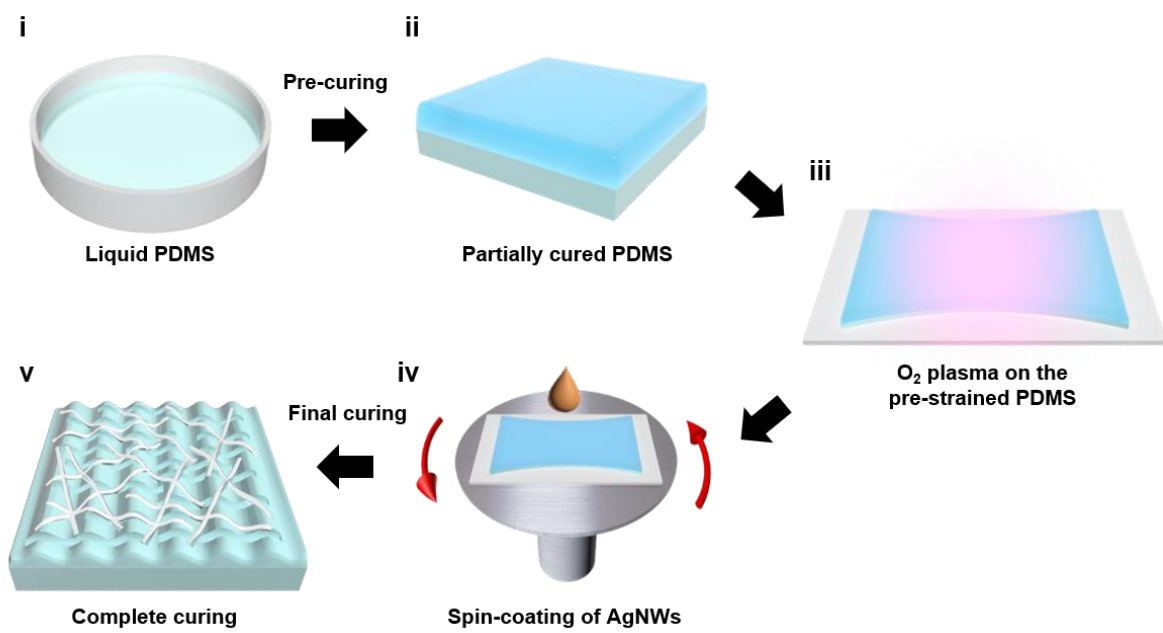


Figure 6.5 Schematic of an overall procedure for the fabrication of strain-insensitive stretchable AgNW electrodes. Firstly, the liquid state PDMS prepolymer is partially-cured. Before the coating of AgNWs, partially-cured PDMS was pre-strained and pre-treated with O₂ plasma. After the coating of AgNWs, pre-strained PDMS was released and cured completely.

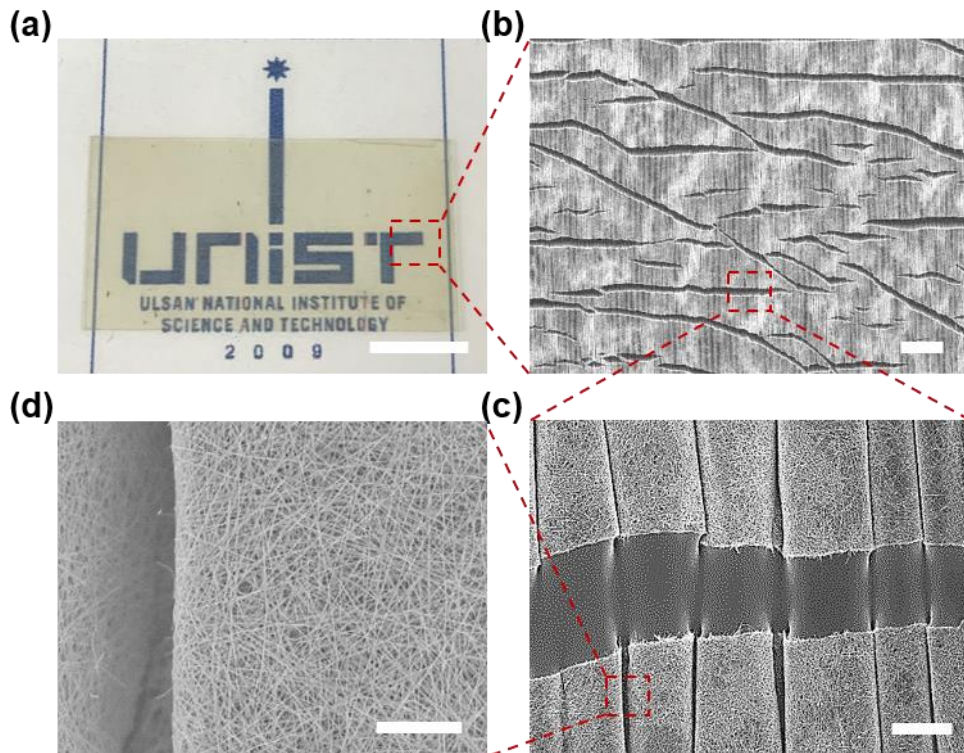


Figure 6.6 Observation of strain-insensitive stretchable AgNW electrodes. (a) A photograph of a stretchable and transparent AgNW electrode. (b) SEM image of stretchable AgNW electrode. The scale bar is 100 μm . (c, d) The magnified SEM images of the stretchable AgNW electrode. The scale bars are 10 μm and 3 μm , respectively.

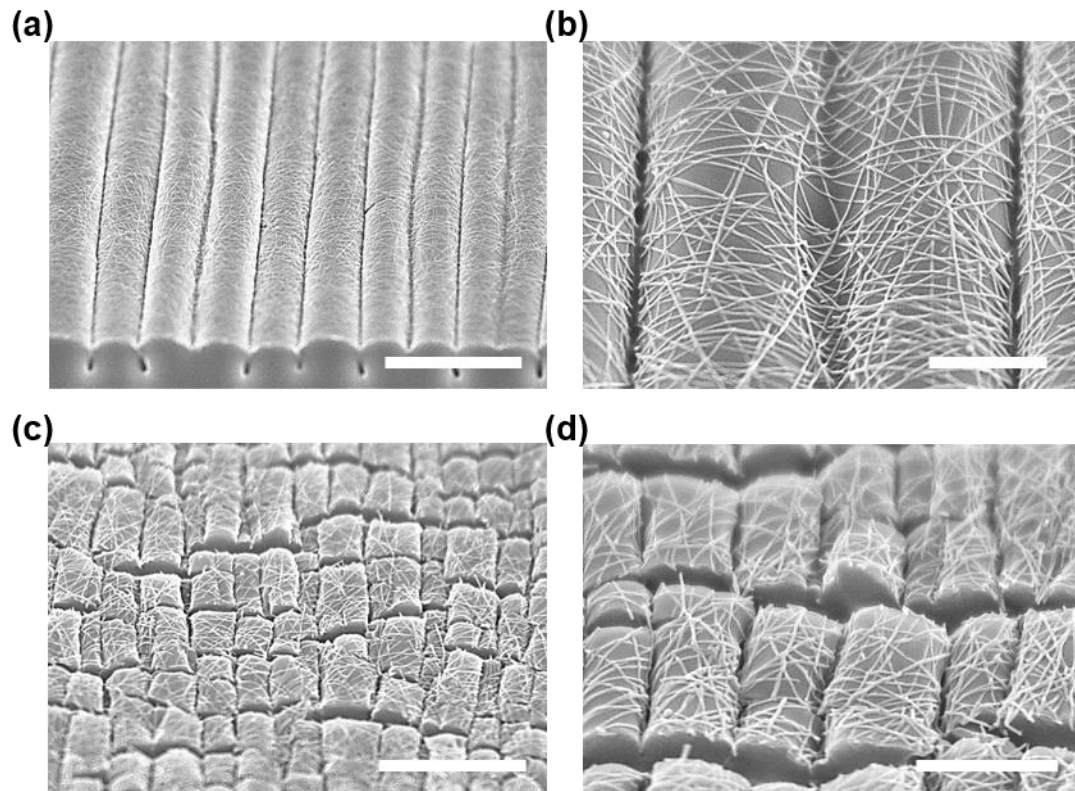


Figure 6.7 The SEM images for the comparison between stretchable AgNW electrodes fabricated by using partially-cured and fully-cured PDMS. (a, b) The SEM images of stretchable AgNW electrodes using partially-cured PDMS. The scale bars are 10 μm and 2 μm , respectively. (c, d) The SEM images of stretchable AgNW electrodes using fully-cured PDMS. The scale bars are 5 μm and 2 μm , respectively.

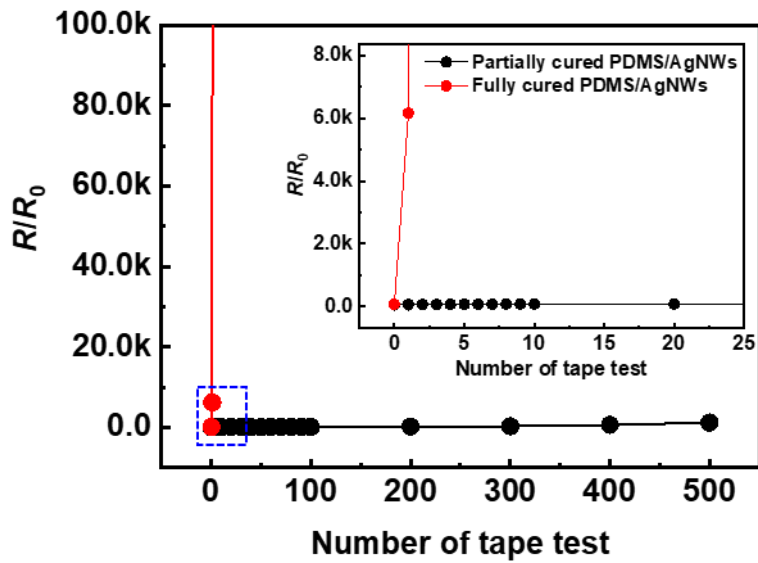


Figure 6.8 The taping test for the comparison of adhesion property between stretchable AgNW electrodes fabricated by using partially-cured and fully-cured PDMS. Compared to the partially-cured PDMS based electrodes, fully-cured PDMS based stretchable electrodes show dramatic increase in resistance after two times of taping tests.

Materials for			Stretchability	Luminance	SPL	Journal	Ref.
Electrode	Luminescence	Sound (Principle)					
AgNW/PDMS	ZnS	-	100%	> 12 cd/m ² (120 V, 1 kHz)	-	Adv. Mater. (2015)	[1]
AgNW/PDMS	ZnS	-	80%	> 5 cd/m ² (120 V, 0.4 kHz)	-	Adv. Mater. (2016)	[2]
Ionic gel/ VHB tape	ZnS	-	1500% (Area strain)	> 2 cd/m ² (900 V, 1 kHz)	-	Adv. Mater. (2016)	[3]
AgNW/PDMS	ZnS/QDs	-	60%	~ 1 cd/m ² (120 V, 1 kHz)	-	RSC Adv. (2017)	[4]
Polar solvent /Ag flake/PET	ZnS	-	-	~ 40 cd/m ² (120 V, 1 kHz)	-	Adv. Mater. (2017)	[5]
AgNW/PET	ZnS	-	-	~ 18 cd/m ² (120 V, 1 kHz)	-	Adv. Funct. Mater. (2019)	[6]
CNT	-	CNT (Thermoacoustic)	100%	-	> 100 dB (50 V, 10 kHz)	Nano Lett. (2008)	[7]
Galinstan	-	Galinstan/Nd (Vibration)	50%	-	> 50 dB (1 V, 10 kHz)	Sci. Rep. (2015)	[8]
Sputtered Ag	-	Polypropylene/ silicate particle (Ferroelectret)	-	-	> 90 dB (300 V, 10 kHz)	Nat. Commun. (2017)	[9]
Graphene	-	Graphene (Thermoacoustic)	-	-	> 45 dB (0.25 W, 10 kHz)	Adv. Mater. (2012)	[10]
PEDOT:PSS	SE-ZnS	PVDF-TrFE (Piezoelectric)	-	~ 35 cd/m ² (100V, 1 kHz)	> 60 dB (120 V, 10 kHz)	Nano Energy (2018)	[11]
Wrinkled AgNW/PDMS	ZnS	PDMS (Vibration)	150%	~ 15.1 cd/m² (120 V, 1 kHz)	~ 83.3 dB (120 V, 10 kHz)	This work	

Table 6.1 Summary of recently reported works related to the light emission or sound generation.

The stretchable electrodes showed almost no resistance variation under uniaxial tensile straining up to a pre-strain level of 150% regardless of their initial resistance (Figure 6.9), which could be easily controlled by adjusting the density of AgNW networks (Figure 6.10). The degree of pre-straining was a crucial parameter determining the performance of our stretchable electrodes, as their wrinkled surface could be stretched up to the applied pre-strain level without the formation of additional cracks. The reversibility and stability of resistance observed after 1000 stretch-release cycles for our electrodes were indicative of outstanding mechanical durability (Figure 6.9b). On the other hand, under the above conditions, electrodes fabricated in the absence of pre-straining showed a dramatic increase in resistance due to the failure and breakage of conducting networks (Figure 6.11). A light-emitting diode (LED) connected to our electrodes maintained a stable illumination intensity as the electrode was stretched to a strain of 150%, which was indicative of high electrode performance and insensitivity to strain (Figure 6.12).

Figure 6.11c and Figure 6.13 show changes in the micro- and macroscopic surface morphologies of stretchable AgNW electrodes during stretching to 150% strain. Stretchable electrodes can be fabricated using two different strategies based on the modification of structures or materials to be stretched.^{286, 290} The deposition of highly ductile AgNWs on wrinkled PDMS combines the advantages of these two strategies. The first strategy of using “structures that stretch” relies on the introduction of wrinkles to release the strain applied to the electrode during stretching. When tensile strain is applied to the electrode in a direction perpendicular to the wrinkle pattern, the wrinkle structures flatten to accommodate the applied strain (Figure 6.9c), and the wrinkle width increases with increasing tensile strain without the formation of additional cracks along parallel wrinkles. It is worth noting that the width of the original cracks formed because of the Poisson effect (Figure 6.6) decreased with increasing tensile strain, which resulted in the generation of more conducting pathways and, hence, in stable electrical conductivity during electrode elongation (Figure 6.9d). The second strategy of using “materials that stretch” relies on the intrinsically high ductility of nanosized AgNWs with a large aspect ratio and stretchability.^{245, 286} Consequently, the combination of these two strategies allowed our stretchable electrodes based on AgNW networks on wrinkled PDMS to provide a stable electrical conduction pathway during stretching without notable resistance change. Moreover, no resistance changes were observed at bending radii of down to 1 mm and during repeated bending for up to 1000 cycles, which indicated the excellent electrical and mechanical durability of our stretchable electrodes (Figure 6.14).

The sound-in-display concept was realized by using the EL of the inorganic phosphor for light emission and DEA vibration under the applied AC bias for sound generation (Figure 6.1a). In the stretchable EL loudspeaker, the ZnS:Cu phosphor/PDMS dielectric layer is sandwiched between the

top and bottom AgNW electrodes. Under a sufficiently high applied voltage, trapped electrons are injected from the PDMS–ZnS:Cu interface to the phosphor conduction band and are accelerated to induce light emission via the impact ionization and excitation of luminescent dopant centers followed by their radiative relaxation (Figure 6.15).^{218, 291} The light-emitting performance of the constructed device was examined using a spectroradiometer in a dark box at different voltages and frequencies controlled by a function generator connected to a voltage amplifier (Figure 6.16). The loudspeaker luminance intensity was investigated in various driving modes (sinusoidal, ramp, and square waveforms; Figure 6.17). Notably, the EL intensity under the square pulsed bias exceeded those under sinusoidal and ramp pulsed biases, as the effective working voltage of the square waveform ($0.5 V_{pp}$) exceeded those of sinusoidal ($0.35 V_{pp}$) and ramp ($0.29 V_{pp}$) waveforms.

Figure 6.18a shows the effects of voltage (20–180 V) and frequency (100 Hz – 50 kHz) on loudspeaker luminance, revealing that light emission intensity gradually increased with increasing voltage and frequency. The relationship between luminance (L) and applied voltage bias (V) at a certain frequency is given by¹⁹²

$$L=L_0\exp(-\beta/V^{0.5}) \quad (1)$$

where L_0 and β are device- and material-dependent constants. Within the whole range of applied frequencies, the experimental data were well fitted by Equation 1 (Figure 6.18a). To fit the relationship between EL intensity and applied voltage bias at a certain frequency (Equation 1), two experimental luminance values obtained at applied voltages of 20 and 180 V were used to determine the values of L_0 and β , which were calculated as 66.82 and 40.01 (100 Hz), 520.2 and 40.19 (1 kHz), 1457.3 and 40.2 (5 kHz), 1912.5 and 40.19 (10 kHz), 2428.7 and 40.18 (25 kHz), and 2637.7 and 40.18 (50 kHz), respectively. Luminance values (L) were calculated according to the determined values of L_0 , β , and applied voltages between 10 and 180 V. At low applied bias, the active layer acts as an insulator, becoming conductive at biases above the breakdown voltage, in which case electrons are accelerated to sufficiently high energies to excite the luminescent centers and induce a steep increase in luminance. At a frequency of 10 kHz, the luminance peak centered at 456 nm gained intensity with increasing voltage bias (Figure 6.18b). On the other hand, when the frequency was increased from 50 Hz to 20 kHz, the luminance peak shifted from 508 nm (green) to 460 nm (blue) at a fixed bias (Figure 6.19). The above voltage- and frequency-dependent emission changes can be clearly observed in the corresponding CIE 1931 chromaticity diagram (Figure 6.18c). As the applied bias increased from 20 to 180 V, the chromaticity coordinates shifted from the yellowish region to the green region at low frequencies, which indicated a gradual increase of illumination intensity, whereas the rapid shift from

the yellowish region to the deep blue region at high frequencies indicated a steep increase of illumination intensity. The coordinate points in the yellowish region indicate insufficient illumination intensity due to low applied bias. As the frequency increased from 100 Hz to 50 kHz, the chromaticity coordinates shifted from the green region to the deep blue region. This behavior was attributed to the presence of two dopant crystallographic sites with two different types of shallow and deep traps.²⁸⁸ Under the condition of low frequency and weak electron/hole injection, mostly shallow traps are occupied, and green emission is observed, whereas the occupation of deeper traps at higher frequencies due to the higher-energy injection induces a shift to blue emission. Under the same electric field strength and frequency, luminance increased with decreasing emission film thickness (Figure 6.20) because of the larger electric field experienced by ZnS:Cu phosphors in thinner devices. Specifically, a luminance of 51.5 cd m^{-2} was achieved at a film thickness of $28.3 \text{ }\mu\text{m}$ (100 V, 10 kHz).

Loudspeaker stretchability was tested by elongating the device in the uniaxial direction during EL operation (Figure 6.18d). Figure 6.18d and Figure 6.18e show that the loudspeaker could be stably operated with bright blue emission at tensile strains of up to 150% without noticeable changes in luminance. This robust performance originated from the stable supply of applied voltage bias and current to the loudspeaker via the strain-insensitive stretchable AgNW electrodes. As strain increased to 150%, luminance intensity also increased (Figure 6.18e), which was attributed to the concomitant decrease of emission layer thickness and the resulting increase in the strength of the electric field acting on the emission layer. In addition, the relative change in loudspeaker luminance after 5000 stretch-release cycles under a strain of 100% was less than 8% (Figure 6.18f), indicating the superior mechanical durability and stability of the tested device. Furthermore, the loudspeaker showed a negligible change in EL intensity even after 5000 on-off cycles, which was indicative of long-term stability (Figure 6.18g).

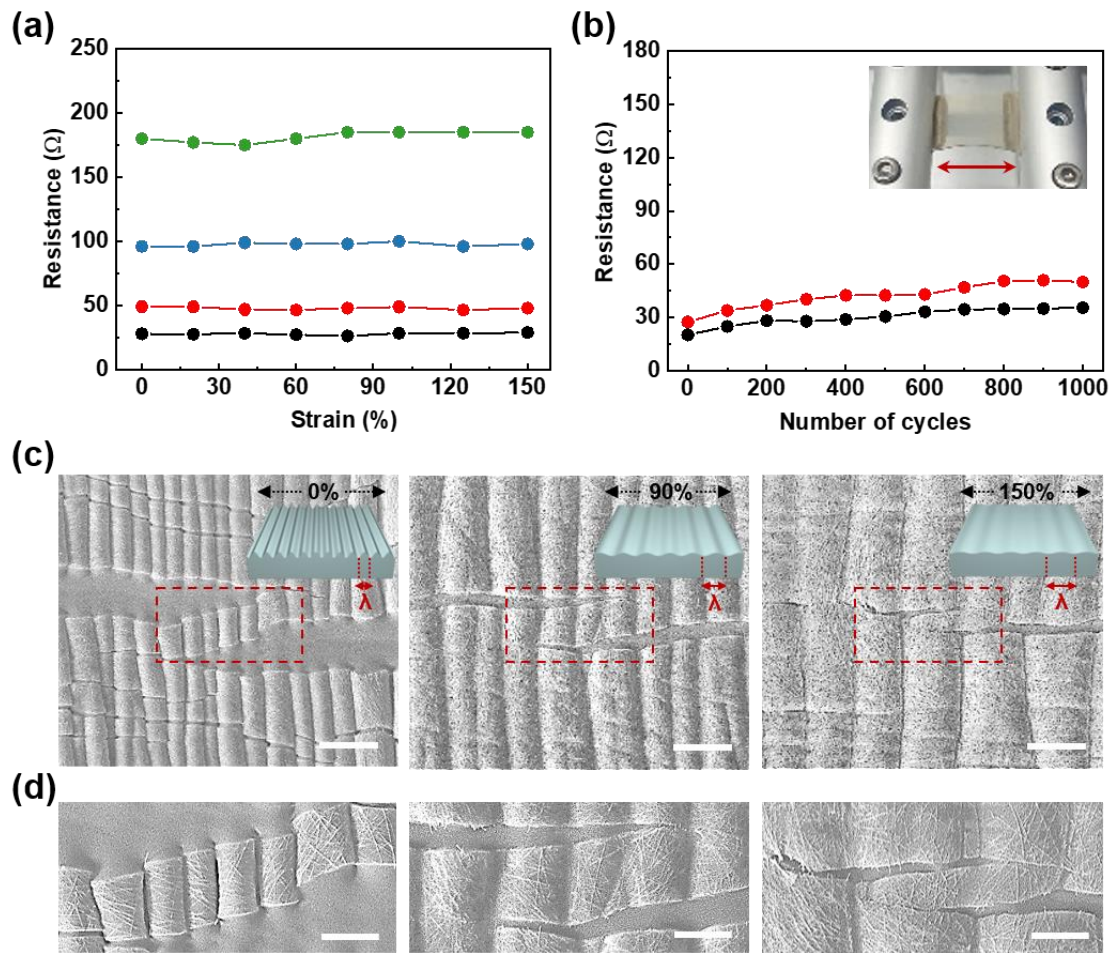


Figure 6.9 Characterization of strain-insensitive stretchable AgNW electrodes. (a) Resistance as a function of tensile strain for different initial resistances. (b) Resistance evolution during repetitive stretching to 100% for 1000 cycles. Inset: photograph of the stretching system. (c) SEM images of stretchable AgNW electrodes during stretching to 150%. All scale bars are 20 μm . Insets illustrate the wrinkle structures of stretched electrodes. (d) Enlarged SEM images of stretchable AgNW electrodes during stretching to 150%. All scale bars are 10 μm .

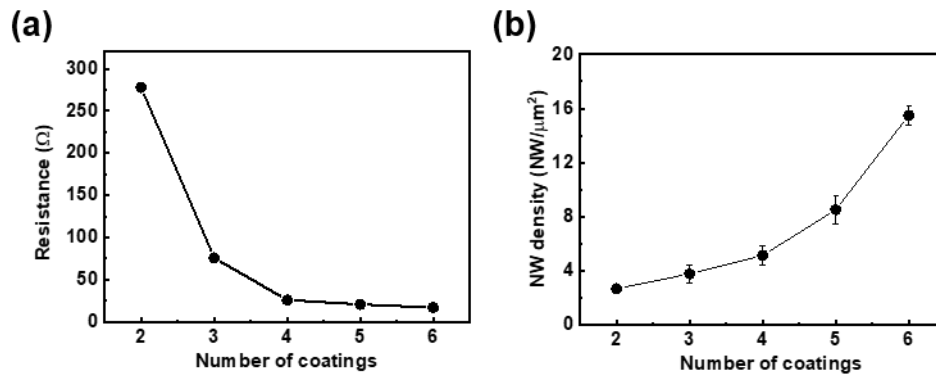


Figure 6.10 Effect of the number of coatings on (a) the electrical resistance of stretchable AgNW electrodes and (b) AgNW density.

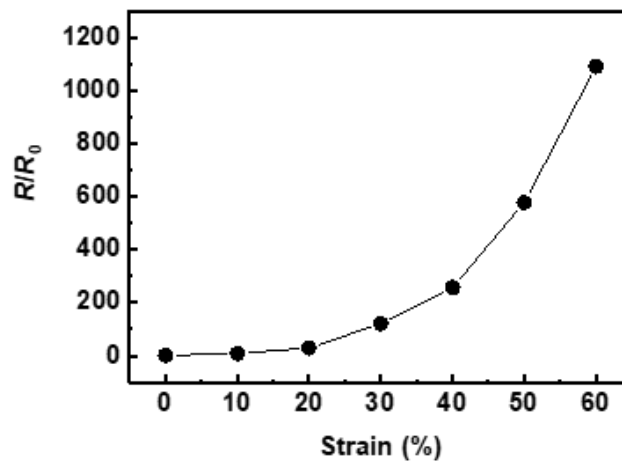


Figure 6.11 Effect of strain on the resistance of stretchable AgNW electrodes fabricated without pre-straining.

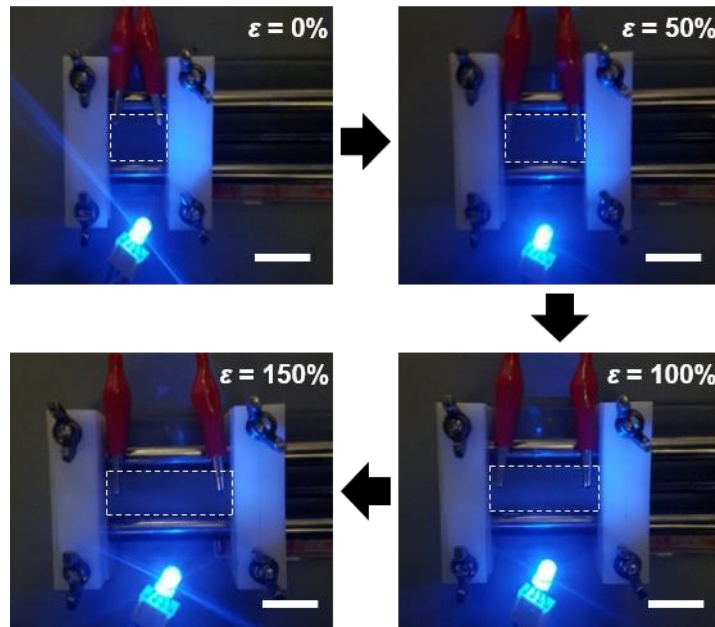


Figure 6.12 Photographs showing the behavior of LED circuits connected to strain-insensitive stretchable AgNW electrodes upon the increase of tensile strain up to 150%. All scale bars equal 2 cm.

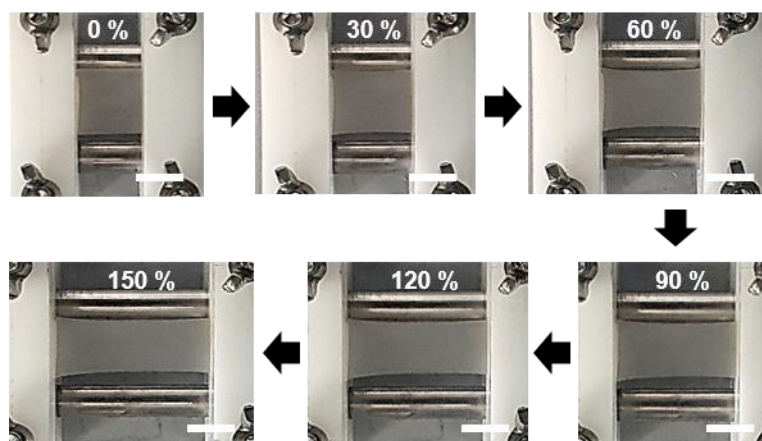


Figure 6.13 Photographs of a stretchable electrode during stretching to 150%. All scale bars equal 1 cm.

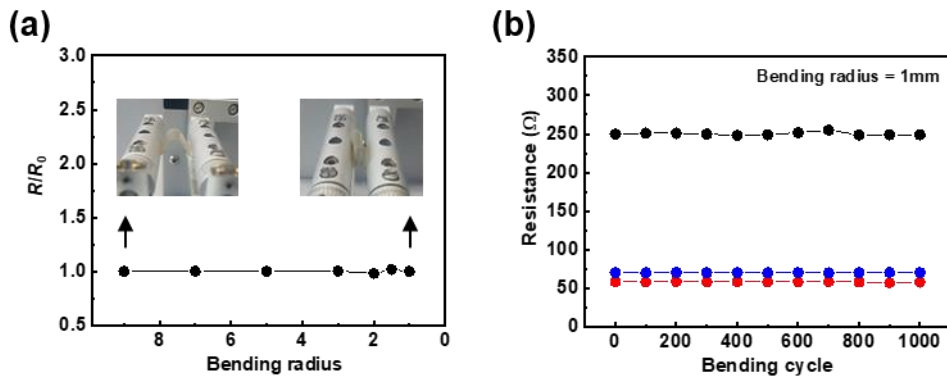


Figure 6.14 Mechanical stability of strain-insensitive stretchable AgNW electrodes. (a) Effect of bending radius on electrode resistance. (b) Electrode resistance change during 1000 bending cycles at a bending radius of 1 mm.

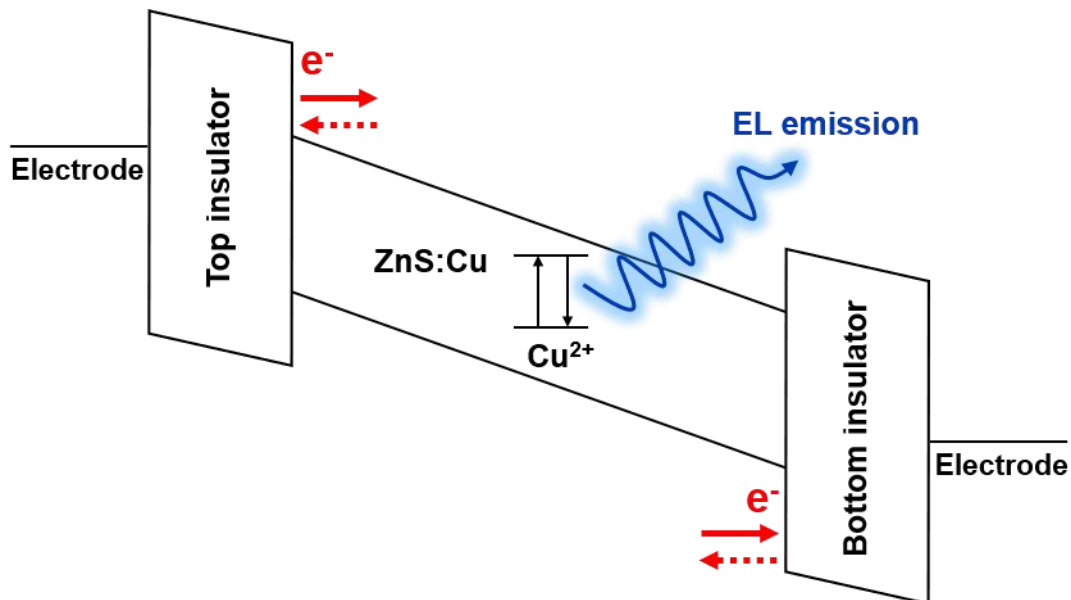


Figure 6.15 Band structure diagram showing the ACEL mechanism for the stretchable EL loudspeaker. Emission originates from the impact excitation of Cu^{2+} in ZnS:Cu phosphors.

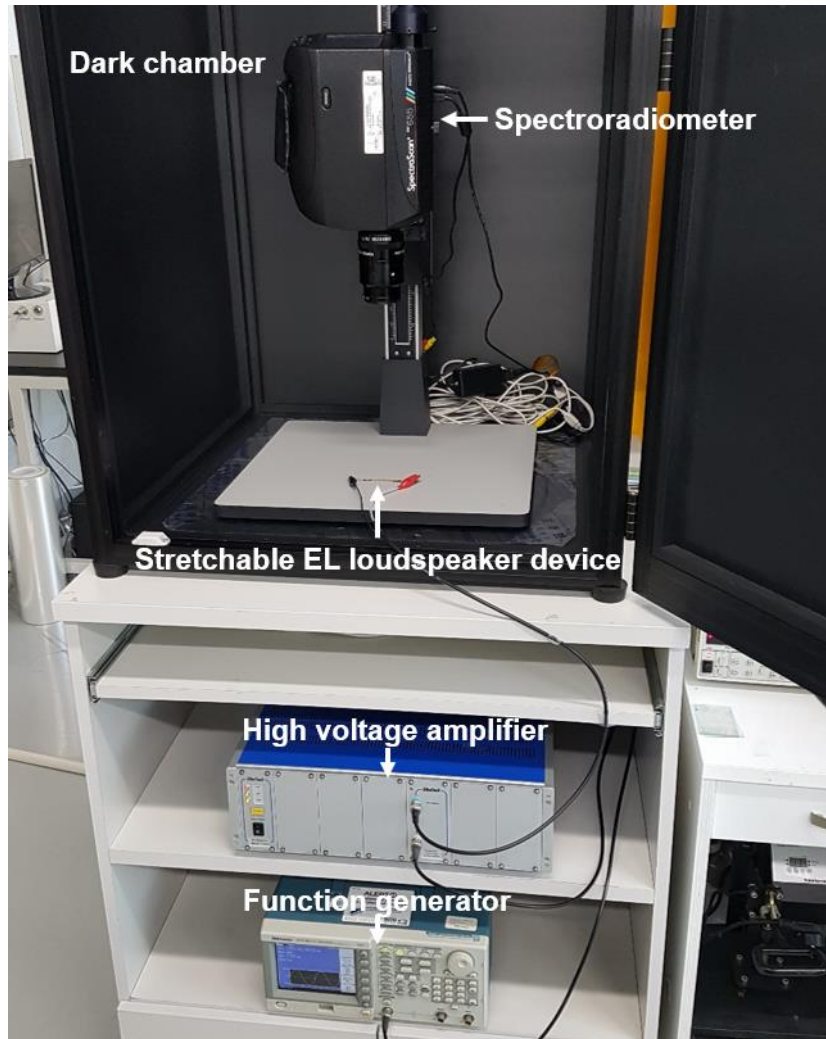


Figure 6.16 Photograph of the setup used to measure EL by a spectroradiometer. The applied AC voltage from the function generator was amplified by a high-voltage amplifier.

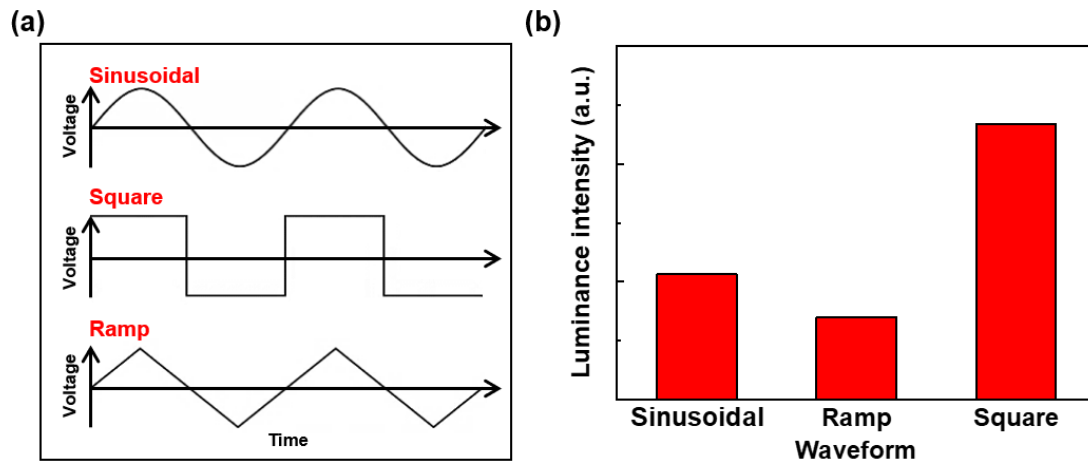


Figure 6.17 (a) Sinusoidal, square, and ramp waves. (b) Luminance intensity obtained for various excitation waveforms at 100 V and 10 kHz.

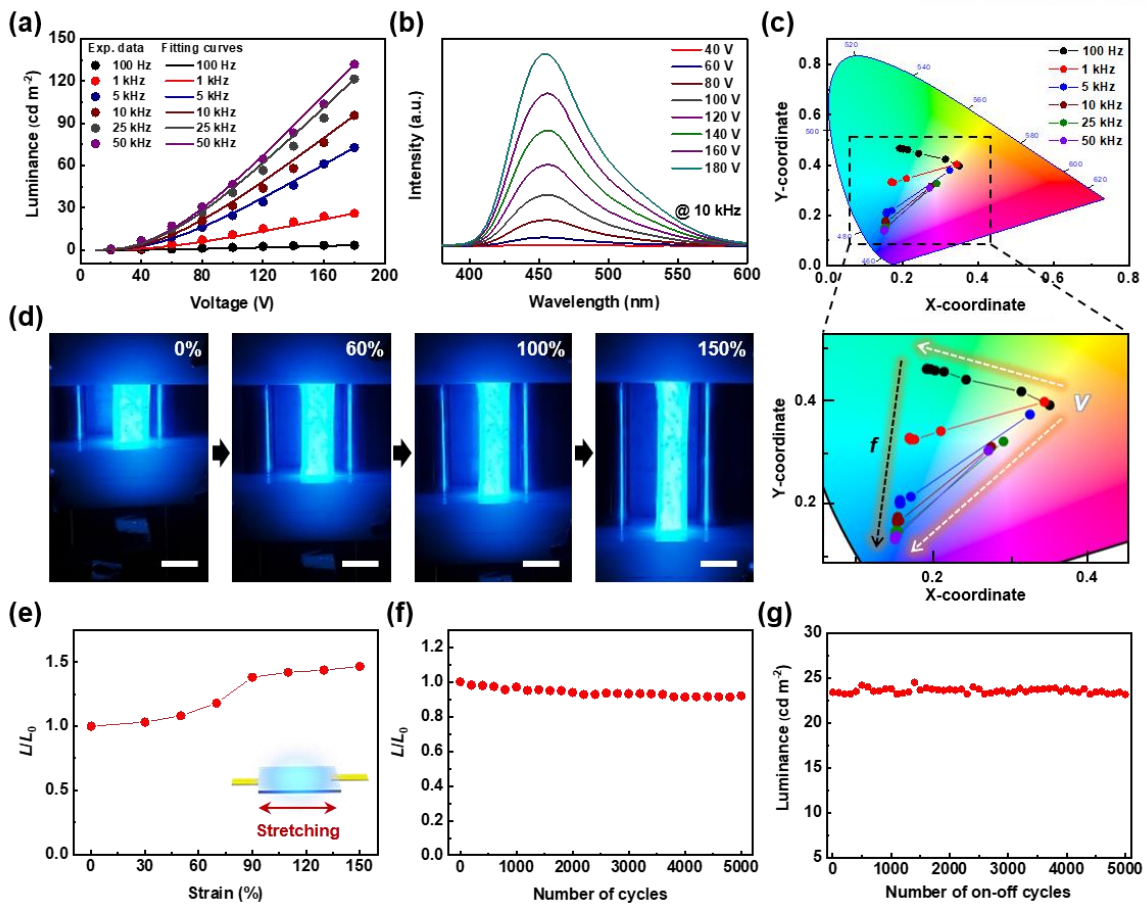


Figure 6.18 Light emission characteristics and mechanical properties of stretchable EL loudspeaker. (a) Effects of voltage on the luminance of stretchable EL loudspeaker at different frequencies and the corresponding fits. (b) EL spectra of stretchable EL loudspeaker recorded at different applied voltages and a fixed frequency of 10 kHz. (c) Representation of color coordinates in CIE 1931 color space according to voltage- and frequency-dependent emission color change. White arrows (*V*) indicate the change of color coordinates upon the increase of applied AC voltage from 20 to 180 V. Black arrow (*f*) indicates the change of color coordinates upon the increase of applied frequency from 100 Hz to 50 kHz. (d) Photographs of EL loudspeaker stretched to strains of 0, 60, 100, and 150% (AC 100 V, 10 kHz). All scale bars are 1.5 cm. (e) Effect of stretching strain on the relative emission intensity of the stretchable EL loudspeaker. (f) Stretching stability test of the stretchable EL loudspeaker under repetitive straining to 100%. (g) Emission stability test of the stretchable EL loudspeaker under 5000 on-off cycles.

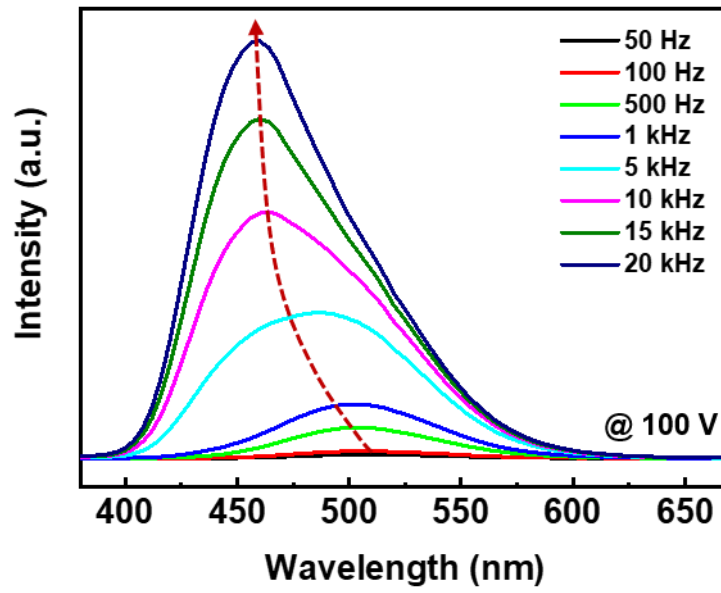


Figure 6.19 EL spectra as a function of applied frequency (50 Hz to 20 kHz) at a fixed applied voltage of 100 V.

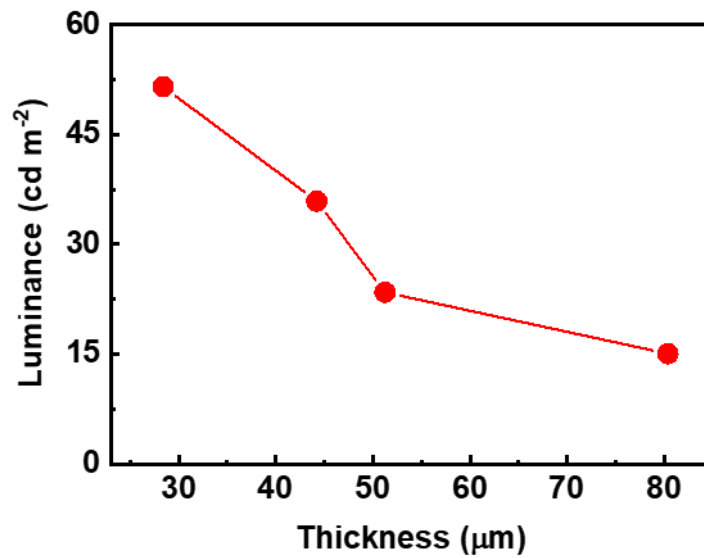


Figure 6.20 Luminance of stretchable EL loudspeaker as a function of emission layer thickness (100 V, 10 kHz).

Field-dependent light emission was due to the EL of ZnS:Cu phosphors, and sound waves were synchronously generated by the vibration of the DEA based on ZnS:Cu/PDMS composites under the same applied AC bias (Figure 6.1f). Whereas conventional speakers require complicated fabrication processes and a large volumetric speaker size for diaphragm vibration, the ZnS:Cu/PDMS DEA of our device could generate sound by converting electrical energy into the mechanical vibration of a thin film structure.²⁹²⁻²⁹⁵ Upon the application of an electric field, attractive forces between opposite charges on the top and bottom electrodes of the DEA provide compressive forces through Maxwell stress, inducing the contraction and expansion in the thickness and lateral directions of the DEA film, respectively. Figure 6.21a shows the stretchable EL loudspeaker generating sound in sync with the emitted light under an AC bias. Figure 6.21b shows the acoustic measurement system used to analyze the sound performance of the stretchable EL sound-in-display device inside an anechoic chamber upon the application of a voltage produced by a function generator and then amplified by an amplifier. The background noise floor inside the anechoic chamber was below 20 dB (Figure 6.22). A commercially available microphone was used to collect and record the sound produced by the stretchable loudspeaker, and the intensity of this sound was measured under various driving modes (sinusoidal, ramp, and square waveforms; Figure 6.23). As discussed in Figure 6.17, the highest SPL was observed for the square pulsed bias because its effective working voltage exceeded those of sinusoidal and ramp pulsed biases.

Figure 4c shows the SPL of sound generated by the stretchable EL loudspeaker as a function of applied voltage at a frequency of 10 kHz and a AC to DC voltage ratio of 3:1. Notably, sound pressure increased with increasing applied voltage, as the degree of actuation (S) on a dielectric elastomer film is proportional to the square of applied voltage (V):²⁹⁶

$$S = \varepsilon_r \varepsilon_0 V^2 h^{-2} Y^{-1} \quad (2)$$

where ε_r is the relative dielectric constant, ε_0 is the permittivity of free space, h is film thickness, and Y is Young's modulus. DEA-based loudspeakers are mainly operated using a combination of DC and AC voltages, similarly to electrostatic speakers.²⁹⁷ When the merged voltage (V) applied to the DEA loudspeaker is given by $V = B + A \sin(\omega t)$, where B is the DC bias and A is the amplitude of the AC drive voltage, the time-dependent actuation amplitude (S_{AC}) in Equation 2 can be expressed as

$$S_{AC} = \frac{\varepsilon_r \varepsilon_0}{h^2 Y} (2BA + A^2) \quad (3)$$

Equation 3 suggests that the sound performance of the stretchable EL loudspeaker depends on both DC bias and AC drive voltages. Figure 6.21d shows the SPL of output sound at different DC to AC voltage

ratios and a frequency of 10 kHz, revealing that SPL increased as DC bias was added to the AC voltage, saturating at DC biases above 100 V. Note that the maximum combined AC-DC voltage (V_{\max}) was limited to 400 V because of the specifications of our equipment. As sound performance is related to DEA film vibration, the acoustic response is proportional to the square of the applied voltage (as indicated in Equation 3), which always results in the generation of a harmonic distortion. The DC-AC combined voltage (V) applied to the DEA-based loudspeaker can be expressed as $V = B + A\sin(\omega t)$, where B is the DC bias and A is the AC drive voltage. As indicated in Equation 2, sound performance is related to film strain and is proportional to the square of applied voltage, which is given by $V^2 = B^2 + 2BA\sin(\omega t) + A^2\sin^2(\omega t)$. The above relationship can be re-written as $V^2 = B^2 + 2BA\sin(\omega t) + 0.5A^2[1 - \cos(2\omega t)]$, where the $\cos(2\omega t)$ term implies the generation of second harmonics with doubled frequency. The harmonic distortion primarily depends on the amplitude of AC drive voltage (A) compared to the DC voltage bias (B). Therefore, with increasing DC to AC voltage ratio, the amplitude of the harmonic peak decreases, which results in better sound performance and higher fidelity. With increasing DC to AC voltage ratio at constant maximum voltage, the intensity of SPL at the fundamental frequency (first harmonic, 10 kHz) increased, while the intensity of the second harmonic peak (20 kHz) decreased, which indicated an improvement of fidelity in the sound of stretchable EL loudspeakers (Figure 6.24).

However, as the DC voltage increased above 280 V, SPL steeply decreased because of the insufficient AC drive voltage. At a fixed applied bias, SPL gradually increased with increasing frequency for the range of 1–25 kHz (Figure 6.25). Moreover, at a constant electric field and frequency, SPL increased with decreasing thickness of the emission layer because of the concomitant increase in the concentration of the electric field on ZnS:Cu phosphors (Figure 6.26). Variation of the distance between the microphone and loudspeaker between 2 and 30 cm showed that output sound pressure was well maintained over a long distance (Figure 6.21e), which was indicative of superior loudspeaker performance. The SPL-distance relationship is known to follow the inverse square law, i.e., SPL decreases by 6 dB upon the doubling of the distance from the sound source. However, this relationship holds for distances of greater than 1 m, as at shorter distances, near-field effects result in a complex sound field close to the sound source.²⁹⁸ In our case, the invariability of loudspeaker sound performance with distance was ascribed to the fact that the measurement system was located in the near-field region, i.e., at a distance of <1 m. In contrast, a linear decrease in SPL with increasing distance between the loudspeaker and microphone is observed for thermoacoustic loudspeakers even in the near-field region because of the rapid concomitant decrease of the temperature wave amplitude.^{72, 245} One of the potential issues of stretchable and bendable sound-in-display devices is the non-uniform sound generation toward the listener at different off-axis locations. Omnidirectional loudspeakers generate sound evenly in all directions, which is a significant advantage for the practical applications of sound-in-display devices.

Our stretchable EL loudspeaker exhibited an omnidirectional sound-generation performance (Figure 6.21f), i.e., a sound wave with uniform SPL was generated irrespective of the detection angle, which was attributed to the isotropic vibration of the DEA film.

The stretchability of our loudspeaker was probed by measuring its output sound pressure upon increasing tensile strain up to 150% (Figure 6.21g), and the elongation-induced sound performance change was found to be negligible because of the stable electrical connection provided by the stretchable AgNW electrodes. Loudspeaker stability and durability were probed by recording SPL during 5000 stretching cycles (Figure 6.21h), and the negligible SPL change was ascribed to the presence of highly robust and strain-insensitive stretchable AgNW electrodes and the ZnS:Cu/PDMS emitting layer. The practical utility of sound-in-display devices based on our stretchable EL loudspeaker was demonstrated by playing Mozart's "*Le Nozze di Figaro*" in the dark anechoic chamber. During this experiment, the stretchable EL loudspeaker emitted luminescence light synchronized with music, and the stable generation of sound from the highly stretchable loudspeaker resulted in high sound quality even when the loudspeaker was stretched and twisted. Moreover, our loudspeaker showed negligible changes in sound quality and performance even after 5000 on-off cycles and was therefore concluded to exhibit high long-term stability (Figure 6.21i).

As a proof of concept application, we fabricated wearable sound-in-display electronics using the stretchable EL loudspeaker, which offered a synesthetic stimulus with synchronous light and sound during music playing. The AC to DC applied voltage ratio was optimized to ensure the best light and sound-generation performances. Figure 6.27a shows the luminance and SPL of the stretchable EL loudspeaker as functions of the AC to DC ratio at constant combined maximum voltage (400 V) and frequency (10 kHz) before and after the application of tensile strain (150%). Whereas luminance continuously decreased with decreasing proportion of AC voltage because of the insufficiency of this voltage for phosphor excitation, SPL initially increased with increasing DC bias fraction because of the concomitant improvement of DEA actuation. However, overly high proportions of DC bias led to a decrease in SPL due to the lack of AC drive voltage. Besides, the stretchable EL loudspeaker showed negligible change in luminance and SPL during stretching, and was therefore concluded to be well suited for use in stretchable sound-in-display electronics. To demonstrate the ability of the EL loudspeaker to stably play music under stretching conditions, the input signal of the music sound wave was merged with the DC bias (Figure 6.27b). When the wearable EL loudspeaker was attached to a human finger in the straightened state (Figure 6.27c), synchronous light and sound were produced along with the input sound wave signal. Thus, the EL loudspeaker provided an intuitive perception of auditory-visual stimuli by visualizing the sound wave using emitted light. The loudspeaker could be stably operated even during finger flexion because of its high stretchability (Figure 6.27d). Figure 5e

shows the input sound signal (*Le Nozze di Figaro*) applied to the wearable EL loudspeaker. Here, the offset DC bias could be controlled to improve sound quality by enhancing the vibration of the DEA matrix during music playing. Figure 6.27f and Figure 6.27g show the output sound waveforms and short-time Fourier transform (STFT) spectrograms of the music sound played by the wearable EL loudspeaker before and after finger flexion, respectively, revealing that this flexion did not significantly affect the output sound waves and STFT spectrograms and thus indicating the maintenance of sound quality, excellent stretchability, and reliability of our device. When “*Le Nozze di Figaro*” was played during repeated finger bending, no noticeable change in sound and emitted light were observed, which indicated the high performance stability of our wearable EL loudspeaker.

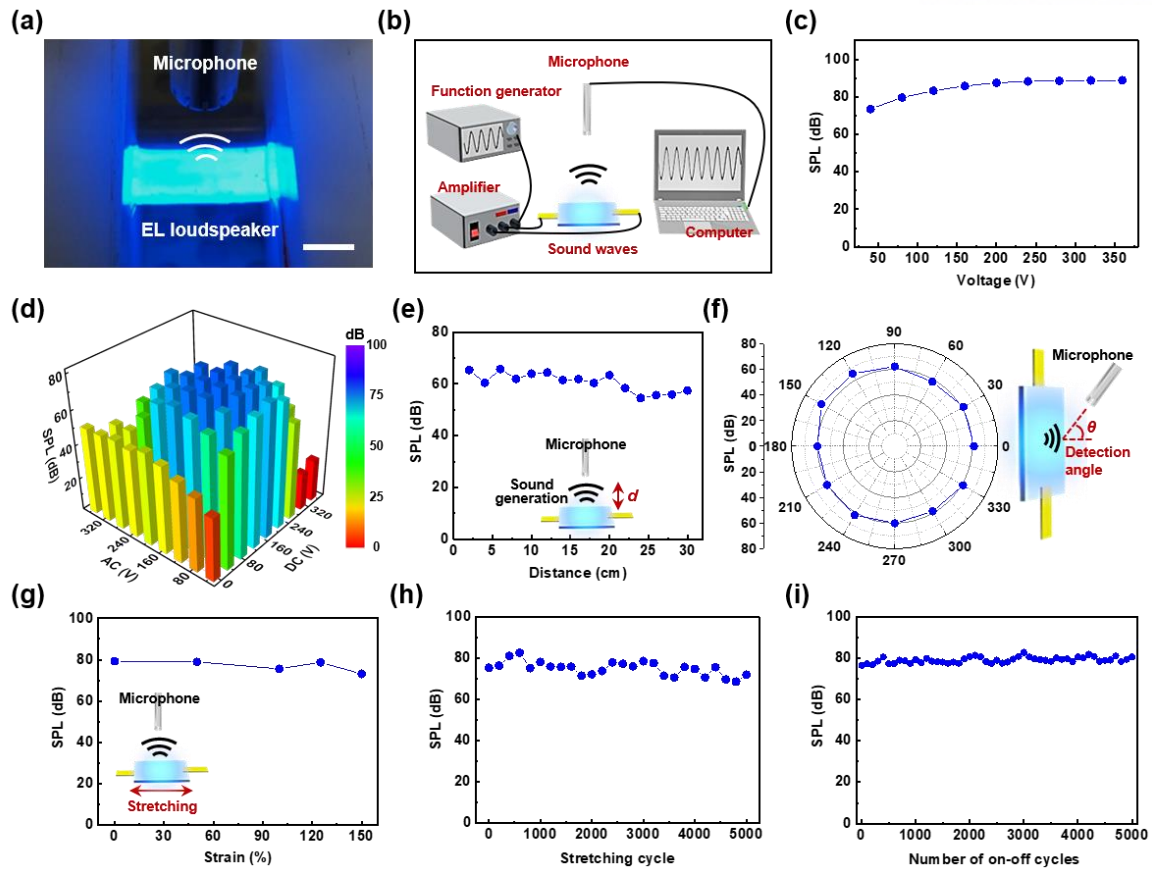


Figure 6.21 Characterization of the stretchable EL loudspeaker. (a) Photograph of the stretchable EL loudspeaker during sound recording using a microphone. Scale bar is 1.5 cm. (b) Acoustic measurement system in which sound emitted from the stretchable EL loudspeaker is collected by a microphone. (c) Effect of applied voltage on the SPL generated by the stretchable EL loudspeaker at an AC to DC voltage ratio of 3:1. (d) Sound performance of stretchable EL loudspeaker for different AC to DC voltage ratios. (e) Dependence of SPL on the distance between the microphone and the stretchable EL loudspeaker. (f) Effect of angle on the SPL of the stretchable EL loudspeaker at 100 V and 10 kHz. The distance between the loudspeaker and the microphone equaled 2.5 cm. (g) Dependence of loudspeaker SPL on tensile strain. (h) Stability of sound performance during 5000 cycles of stretching to 100% strain. (i) Sound performance stability of the stretchable EL loudspeaker during repeated 5000 on-off cycles.

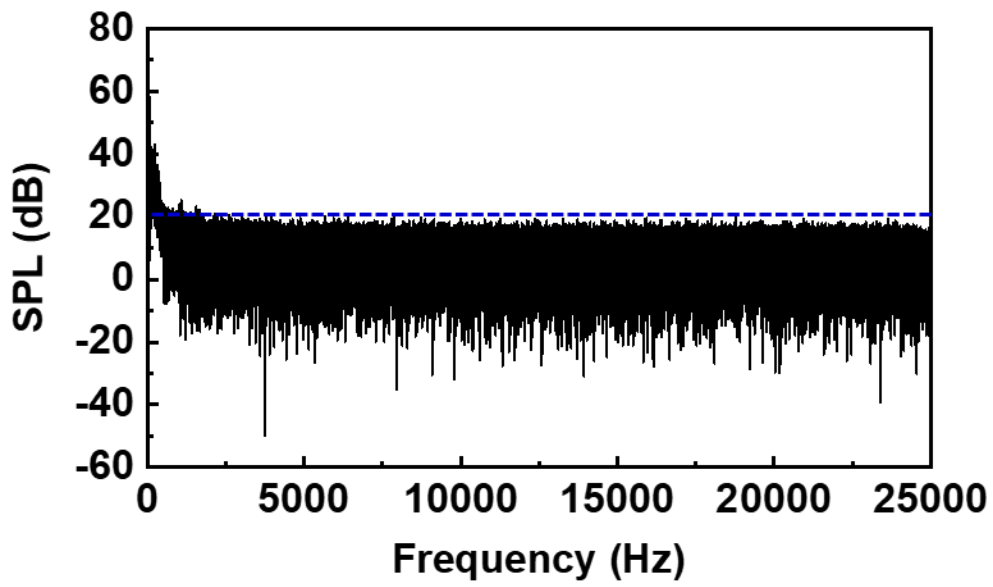


Figure 6.22 Power spectrum of the background noise in the anechoic room.

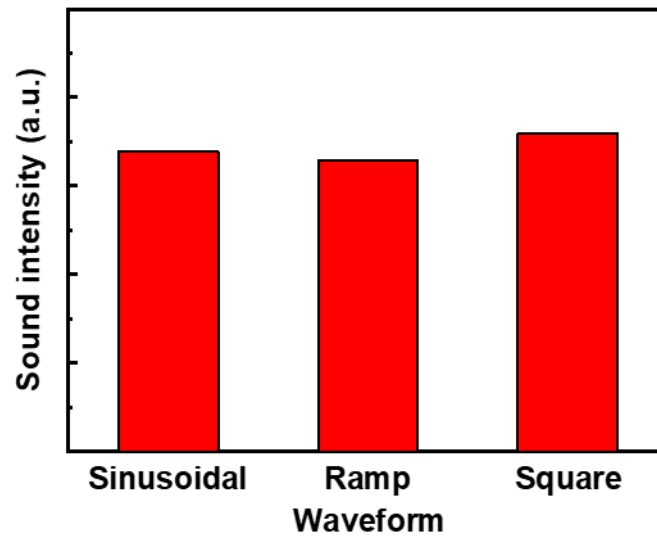


Figure 6.23 Sound intensity under varying excitation waveforms (100 V, 10 kHz).

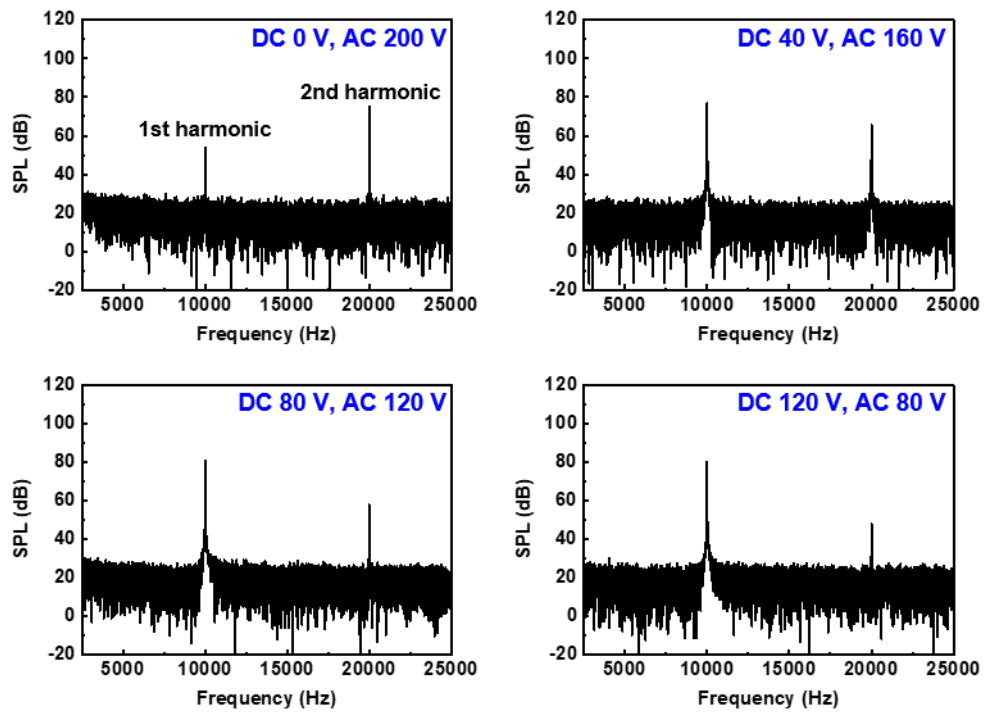


Figure 6.24 Sound performance under different DC to AC bias ratio ($V_{\max} = 200$ V, 10 kHz).

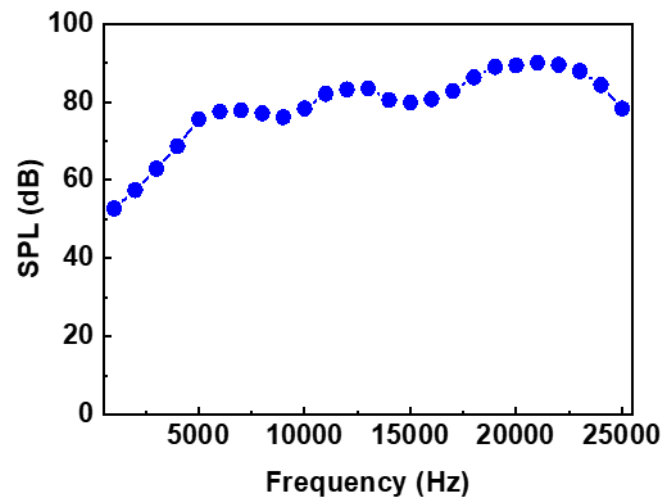


Figure 6.25 Experimental values of SPL versus sound frequencies for stretchable EL loudspeaker.

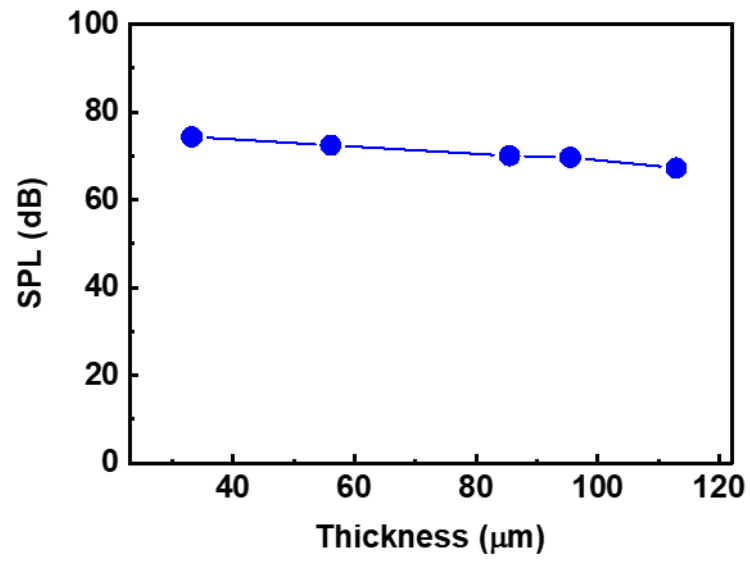


Figure 6.26 Sound intensity of stretchable EL loudspeaker as a function of emission layer thickness (100 V, 10 kHz).

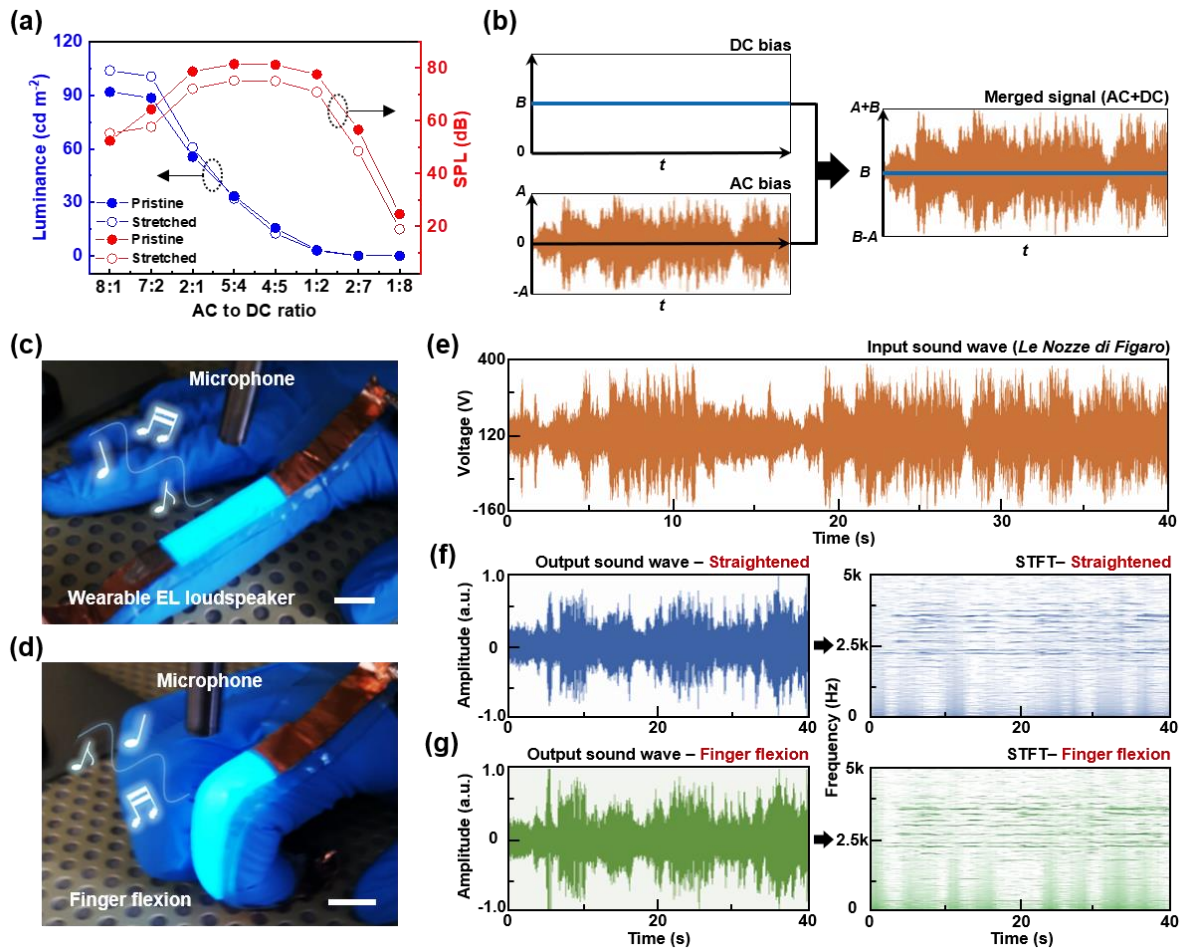


Figure 6.27 Stretchable sound-in-display electronics. (a) Luminance and SPL as functions of the AC to DC voltage ratio ($V_{\max} = 360$ V, frequency = 10 kHz) before and after the application of tensile strain (150%). (b) Schematic diagram showing the waveform of AC-DC combined signals used for music playing. (c) Wearable EL loudspeaker attached to a gloved index finger during music playing. Music sound was recorded by a commercial microphone. Scale bar is 1.5 cm. (d) Wearable EL loudspeaker during finger flexion. Scale bar is 1.5 cm. (e) Input signal of the sound wave (*Le Nozze di Figaro*). (f) Analyzed output sound wave (left) and its short-time Fourier transform (right) in the straightened state and (g) in the state of finger flexion.

6.4 Conclusions

In summary, synchronized generation of color and sound in a single sound-in-display device was realized using a stretchable EL loudspeaker comprising ZnS:Cu EL phosphors dispersed in a stretchable PDMS DEA layer sandwiched between stretchable AgNW electrodes. The loudspeaker simultaneously emitted light by the EL of ZnS:Cu phosphors and generated sound waves by the vibration of the PDMS DEA under the same AC bias input, allowing the synesthetic perception of both color and sound. The intensity of light emission and output sound generation could be easily controlled by the frequency and amplitude of the applied AC bias. Importantly, the stable electrical connection provided by strain-insensitive stretchable AgNW electrodes resulted in highly robust and reliable EL and sound emission performances even under significant tensile strains of up to 150% and 5000 stretch-release cycles. As a proof of concept application, our loudspeaker was integrated in a stretchable sound-in-display device that could be worn on a human finger and provided a synesthetic vision and hearing stimulus with synchronous light and sound generation even when significantly stretched during finger flexion. Thus, the presented loudspeaker with the capability of synchronized sound generation and visual display in a single sound-in-display device is a robust platform for the further development of human-machine interfaces in the visualization of auditory systems and IoT devices.

Chapter 7. Summary and Future Perspective

7.1 Summary

With increasing importance of human-machine interface along with the rapid growth of IoT, various flexible and stretchable electronic and optoelectronic devices have been developed for the wide range of multifunctional and wearable applications. In this thesis, we suggest high-performance soft transparent electrodes based on AgNW network to replace conventional ITO film. Firstly, we demonstrated large-area alignment technique using bar coating method for the fabrication of large-scale and cross-aligned AgNW networks, which provide large improvements in electrical conductivity and optical transparency because of lower percolation threshold compared to the random AgNW network. The highly flexible and high-performance optoelectronic and electronic devices, such as force-sensitive touch screen, microphone, loudspeaker, and EL device were successfully demonstrated based on cross-aligned AgNW electrodes. In addition, highly robust self-healable AgNW electrode was demonstrated by integrating AgNW networks with self-healing polymer matrix, which shows multiple healing capability.

Moreover, with the demand for next-generation electronics, which calls for the development of stretchable and transparent electronic devices, we fabricated strain-insensitive stretchable AgNW electrodes. As a proof of concept demonstration, the stretchable sound-in-display electronic device generating synchronized acoustic and visual information was successfully demonstrated using a stretchable EL loudspeaker based on strain-insensitive AgNW electrodes, which can be applied to the visualization of auditory systems and IoT devices.

In chapter 2, we reported the simple, fast, and large-scale ($>20 \times 20 \text{ cm}^2$) NW assembly strategy for the fabrication of flexible TCEs based on cross-aligned AgNW networks. In this study, the alignment of AgNWs by bar coating assembly is simply carried out by dragging the Meyer rod at the predefined rod-substrate gap distance over a AgNW solution on the amine-modified target substrate. The highly cross-aligned AgNW networks for transparent electrode show sheet resistance of $21.0 \Omega \text{ sq}^{-1}$ at 95.0% of optical transmittance, which compares favorably with that of random AgNW networks (Sheet resistance of $21.0 \Omega \text{ sq}^{-1}$ at 90.4% of optical transmittance). As a proof of concept demonstration, we fabricated flexible, transparent, and force-sensitive touch screens using cross-aligned AgNW electrodes integrated with mechanochromic SP-PDMS composite film. Our force-sensitive touch screens enable the precise monitoring of dynamic writings, tracing and drawing of underneath pictures, and perception of handwriting patterns with locally different writing forces. In this study, we expect

that the suggested technique provides a robust and powerful platform for the controllable assembly of NWs beyond the scale of conventional fabrication techniques, which can find diverse applications in multifunctional flexible electronic and optoelectronic devices.

In chapter 3, we demonstrated ultrathin, transparent, and conductive hybrid NMs with nanoscale thickness down to 100 nm, consisting of the orthogonal AgNW arrays embedded in the polymer matrix. Hybrid NMs significantly enhance the electrical and mechanical properties of ultrathin polymer NMs, which can be intimately attached to human skin and curvilinear surfaces. For the applications, we presented the skin-attachable NM loudspeaker, which exhibits the significant enhancement in thermoacoustic capabilities without any significant heat loss from the substrate. Furthermore, we presented wearable transparent NM-based microphone combined with a micropyramid-patterned PDMS film, which provides excellent acoustic sensing capabilities based on the triboelectric voltage signals. The user interface for a personal voice-based security system was demonstrated using NM microphone that can accurately recognize the user's voice. This study addressed the NM-based conformal electronics required for acoustic device platforms, which could be further expanded for application to conformal wearable sensors and health care devices.

In chapter 4, solution-processed high- k BTO:La nanocuboids (~ 150 nm) were presented as high dielectric constant nanodielectrics, which can enhance the dielectric constant of the ACEL devices from 2.6 to 21 (at 1 kHz of frequency), enabling the fabrication of high-performance flexible ACEL devices with the lower operating voltage as well as higher luminance (~ 57.54 cd m⁻² at 240 V, 1 kHz) than devices using undoped BTO nanodielectrics (~ 14.3 cd m⁻² at 240 V, 1 kHz). Furthermore, the uniform brightness across the whole panel surface of the flexible ACEL devices and excellent device reliability are achieved via the use of uniform networks of cross-aligned AgNWs as highly conductive and flexible electrodes. The results offer experimental validation of high-brightness flexible ACELs using solution-processed BTO:La nanodielectrics, which constitutes the important milestone toward the implementation of high- k nanodielectrics in flexible displays.

In chapter 5, we presented transparent, flexible, and self-healable TA loudspeakers based on AgNW-PUHU conductive electrodes. The self-healable AgNW/PUHU electrodes exhibit significant self-healing for repairing the surface damages that are caused due to the dynamic reconstruction of reversible bulky urea bonds in PUHU. The fabricated self-healable TA loudspeakers generate a sound pressure level of 61 dB at 10 kHz frequency (AC 7V/DC 1V). In particular, the TA speakers are able to recover the original sound after healing the surface damages of electrodes at 95°C and 80% RH within 5 min. We believe that the technique proposed in this study provides a robust and powerful platform for

the fabrication of transparent and flexible TA loudspeakers with excellent self-healing, which can be applied in flexible and wearable acoustic electronics.

In chapter 6, the synchronized generation of sound and color is demonstrated for the stretchable sound-in-display device with electrodes of strain-insensitive AgNW electrodes and emissive layers of field-induced inorganic EL phosphors. In this device, EL phosphors embedded in the DEA emit light under AC bias, while audible sound waves are simultaneously generated via DEA actuation along with input sound signals. The electroluminescence and sound-generation performances of the fabricated device are highly robust and reliable, being relatively insensitive to stretch-release cycling because of the presence of the above stretchable electrodes. The presented principle of integrating light emission and acoustic systems in a single stretchable device can be further expanded to realize sound-in-display electronics for IoT and human-machine interface applications.

In summary, this thesis presents the novel techniques for the fabrication of flexible/stretchable AgNW electrodes and their applications in the diverse soft optoelectronic and functional electronic devices. In particular, highly flexible and transparent AgNW electrodes are demonstrated using simple large-scale alignment technique based on the bar coating method, which are applied to the fabrication of soft optoelectronic and electronic devices, such as transparent and flexible force-sensitive touch screens, skin-attachable loudspeakers, skin-attachable microphones, and high-performance EL devices. In addition, strain-invariant stretchable AgNW electrodes are fabricated with the growing importance of stretchable electronics, enabling the conformal integration of sound-in-display devices with skin or nonplanar surfaces. With the development of high-performance flexible or stretchable transparent conductor based on AgNWs, our researches are expected to serve as one of the most critical roles for the realization of highly robust and reliable future soft optoelectronic and electronic devices.

7.2 Future perspective

In the last decade, there have been numerous advances in flexible/stretchable and transparent electronics, enabling the development of new soft device applications that were not feasible in the past. Especially, significant progresses in soft electronics based on conducting percolation network of 1D nanomaterials including CNTs, metallic NWs, and hybrid of them have been achieved. As discussed in the chapter 6, two strategies have been researched to develop highly stretchable electrodes; the one is the materials innovation strategy and the other is the structural modification strategy. Moreover, integration of both strategies provides more powerful solution for developing highly stretchable electrodes with stability and reliability. These soft and transparent electronics are expected to brighten up the way of our life enabled by the realization of future user-interactive wearable devices. However, there are still several challenges in the fabrication of stretchable and transparent electrodes having scalability, enough performance, and reliability.

First, the scalable and cost-efficient manufacturing of stretchable electrodes based on 1D nanomaterials should be realized. The solution-processable top-down approach has been achieved by AgNW-based transparent conducting films. Despite the recent progress in the manufacturing of flexible/stretchable transparent AgNW networks, some of lab-scale synthesis methods still limit the commercialization of high-performance AgNW TCEs. For large-area applications, various coating methods, such as spray coating,^{37, 101, 103, 143} screen printing,²⁹⁹⁻³⁰¹ and bar coating^{42, 302, 303} have been researched and shown great promise to overcome the current challenges with cost-effective way.

Second, the fabrication of strain-insensitive stretchable and transparent electrodes showing negligible change in electrical conductivity is still challenging. The simple hybrid of 1D conducting nanomaterials and elastomeric substrates can provide stretchability with high optical transparency.^{81, 83, 304} However, the thin conducting film on the elastomer inevitably leads to cracking or breakage, resulting in the increase of electrical resistance under tensile strain. To avoid the cracking or breakage of conducting percolation networks, the surface structure modifications, such as wavy or wrinkle have been introduced with minimal change in electrical resistance during tensile strain.^{285, 287, 305, 306} However, the modification of surface structures may causes serious loss in the optical transparency because of the light scattering from the nonplanar surfaces. Therefore, for future transparent and stretchable electronics, integration of 1D conducting nanomaterials and modifications of surface structure should be carefully optimized with minimized loss in optical transparency and electrical conductivity under tensile strain.

Third, most of recently reported stretchable electrodes are lack of diversity in the direction of stretchability. The strain-insensitive stretchable AgNW electrodes are mostly depending on the pre-strain method, resulting in the only unidirectional stretchability of devices.^{285, 307, 308} The biaxially

stretchable electrodes have been demonstrated using two direction of pre-strain to overcome previous unidirectionally stretchable electrodes.³⁰⁹⁻³¹² However, the performance of biaxially stretchable electrodes are still not good and omnidirectional stretching ability is needed to construct isotropically stretchable electrodes. Accordingly, omnidirectionally stretchable electrode using waved or buckled AgNWs have been reported.^{313, 314} However, the fabricated stretchable electrodes are not perfectly omnidirectionally stretchable and still need more improvement in optoelectronic properties and stability.

In this thesis, we discussed recent progress in flexible/stretchable electronics mainly based on the AgNW networks. The high-aspect ratio of AgNW provides the excellent electrical conductivity with high optical transparency. Moreover, ultrathin NWs enable the fabrication of the highly flexible and even stretchable transparent electrodes. The suggested large-area alignment technique provides the efficient platform for the controllable assembly of NWs beyond the scale of conventional fabrication techniques with superior optoelectronic properties, which can be utilized in variety of high-performance flexible applications including flexible force-sensitive touch screens, skin-attachable loudspeakers and microphones, and flexible EL displays. Furthermore, the strain-insensitive stretchable AgNW electrodes are demonstrated to accommodate the special needs resulted from the future soft and wearable electronic devices. As a new concept of electronic applications, stretchable sound-in-display electronics is demonstrated that generates synchronized acoustic and visual information using the stretchable EL loudspeakers. To sum up, we anticipate that the suggested techniques regarding AgNWs are beneficial to the development of next-generation soft optoelectronic and electronic applications.

References

1. D.-H. Kim, N. Lu, R. Ma, Y.-S. Kim, R.-H. Kim, S. Wang, J. Wu, S. M. Won, H. Tao, A. Islam, K. J. Yu, T.-I. Kim, R. Chowdhury, M. Ying, L. Xu, M. Li, H.-J. Chung, H. Keum, M. McCormick, P. Liu, Y.-W. Zhang, F. G. Omenetto, Y. Huang, T. Coleman, J. A. Rogers, Epidermal Electronics. *Science* **2011**, 333, 838-843.
2. A. M. Hussain, M. M. Hussain, CMOS-Technology-Enabled Flexible and Stretchable Electronics for Internet of Everything Applications. *Adv. Mater.* **2016**, 28, 4219-4249.
3. C. Larson, B. Peele, S. Li, S. Robinson, M. Totaro, L. Beccai, B. Mazzolai, R. Shepherd, Highly Stretchable Electroluminescent Skin for Optical Signaling and Tactile Sensing. *Science* **2016**, 351, 1071-1074.
4. M. S. Lim, M. Nam, S. Choi, Y. Jeon, Y. H. Son, S.-M. Lee, K. C. Choi, Two-Dimensionally Stretchable Organic Light-Emitting Diode with Elastic Pillar Arrays for Stress Relief. *Nano Lett.* **2020**, 20, 1526-1535.
5. X. Zhang, V. A. Oberg, J. Du, J. Liua, E. M. J. Johansson, Extremely Lightweight and Ultra-Flexible Infrared Light-Converting Quantum Dot Solar Cells with High Power-Per-Weight Output Using a Solution-Processed Bending Durable Silver Nanowire-Based Electrode. *Energ Environ. Sci.* **2018**, 11, 354-364.
6. J. Lee, P. Lee, H. Lee, D. Lee, S. S. Lee, S. H. Ko, Very Long Ag Nanowire Synthesis and Its Application in a Highly Transparent, Conductive and Flexible Metal Electrode Touch Panel. *Nanoscale* **2012**, 4, 6408-6414.
7. L.-Q. Tao, H. Tian, Y. Liu, Z.-Y. Ju, Y. Pang, Y.-Q. Chen, D.-Y. Wang, X.-G. Tian, J.-C. Yan, N.-Q. Deng, Y. Yang, T.-L. Ren, An Intelligent Artificial Throat with Sound-Sensing Ability Based on Laser Induced Graphene. *Nat. Commun.* **2017**, 8, 14579.
8. A. G. Nasibulin, A. Kaskela, K. Mustonen, A. S. Anisimov, V. Ruiz, S. Kivisto, S. Rackauskas, M. Y. Timmermans, M. Pudas, B. Aitchison, M. Kauppinen, D. P. Brown, O. G. Okhotnikov, E. I. Kauppinen, Multifunctional Free-Standing Single-Walled Carbon Nanotube Films. *ACS Nano* **2011**, 5, 3214-3221.
9. T. Kim, Y. W. Kim, H. S. Lee, H. Kim, W. S. Yang, K. S. Suh, Uniformly Interconnected Silver-Nanowire Networks for Transparent Film Heaters. *Adv. Funct. Mater.* **2013**, 23, 1250-1255.
10. A. Miyamoto, S. Lee, N. F. Cooray, S. Lee, M. Mori, N. Matsuhisa, H. Jin, L. Yoda, T. Yokota, A. Itoh, M. Sekino, H. Kawasaki, T. Ebihara, M. Amagai, T. Someya, Inflammation-Free, Gas-Permeable, Lightweight, Stretchable On-Skin Electronics with Nanomeshes. *Nat. Nanotechnol.* **2017**, 12, 907-913.

11. T. Q. Trung, N.-E. Lee, Materials and Devices for Transparent Stretchable Electronics. *J. Mater. Chem. C* **2017**, *5*, 2202-2222.
12. K. Alzoubi, M. M. Hamasha, S. Lu, B. Sammakia, Bending Fatigue Study of Sputtered ITO on Flexible Substrate. *J. Disp. Technol.* **2011**, *7*, 593-600.
13. S. Ye, A. R. Rathmell, Z. Chen, I. E. Stewart, B. J. Wiley, Metal Nanowire Networks: The Next Generation of Transparent Conductors. *Adv. Mater.* **2014**, *26*, 6670-6687.
14. N. Kim, S. Kee, S. H. Lee, B. H. Lee, Y. H. Kahng, Y.-R. Jo, B.-J. Kim, K. Lee, Highly Conductive PEDOT: PSS Nanofibrils Induced by Solution-Processed Crystallization. *Adv. Mater.* **2014**, *26*, 2268-2272.
15. J. C. Meyer, A. K. Geim, M. I. Katsnelson, K. S. Novoselov, T. J. Booth, S. Roth, The Structure of Suspended Graphene Sheets. *Nature* **2007**, *446*, 60-63.
16. A. Khan, S. Lee, T. Jang, Z. Xiong, C. Zhang, J. Tang, L. J. Guo, W.-D. Li, High-Performance Flexible Transparent Electrode with an Embedded Metal Mesh Fabricated by Cost-Effective Solution Process. *Small* **2016**, *12*, 3021-3030.
17. F. Mirri, A. W. K. Ma, T. T. Hsu, N. Behabtu, S. L. Eichmann, C. C. Young, D. E. Tsentalovich, M. Pasquali, High-Performance Carbon Nanotube Transparent Conductive Films by Scalable Dip Coating. *ACS Nano* **2012**, *6*, 9737-9744.
18. B. W. An, E.-J. Gwak, K. Kim, Y.-C. Kim, J. Jang, J.-Y. Kim, J.-U. Park, Stretchable, Transparent Electrodes as Wearable Heaters Using Nanotrough Networks of Metallic Glasses with Superior Mechanical Properties and Thermal Stability. *Nano Lett.* **2016**, *16*, 471-478.
19. Y. Sun, M. Chang, L. Meng, X. Wan, H. Gao, Y. Zhang, K. Zhao, Z. Sun, C. Li, S. Liu, H. Wang, J. Liang, Y. Chen, Flexible Organic Photovoltaics Based on Water-Processed Silver Nanowire Electrodes. *Nat. Electron.* **2019**, *2*, 513-520.
20. S.-I. Na, S.-S. Kim, J. Jo, D.-Y. Kim, Efficient and Flexible ITO-Free Organic Solar Cells Using Highly Conductive Polymer Anodes. *Adv. Mater.* **2008**, *20*, 4061-4067.
21. K. S. Novoselov, A. K. Geim, S. V. Morozov, D. Jiang, Y. Zhang, S. V. Dubonos, I. V. Grigorieva, A. A. Firsov, Electric Field Effect in Atomically Thin Carbon Films. *Science* **2004**, *306*, 666-669.
22. S. Bae, H. Kim, Y. Lee, X. Xu, J.-S. Park, Y. Zheng, J. Balakrishnan, T. Lei, H. R. Kim, Y. I. Song, Y.-J. Kim, K. S. Kim, B. Ozyilmaz, J.-H. Ahn, B. H. Hong, S. Iijima, Roll-to-Roll Production of 30-Inch Graphene Films for Transparent Electrodes. *Nat. Nanotechnol.* **2010**, *5*, 574-578.
23. M.-G. Kang, L. J. Guo, Nanoimprinted Semitransparent Metal Electrodes and Their Application in Organic Light-Emitting Diodes. *Adv. Mater.* **2007**, *19*, 1391-1396.

24. H. B. Lee, W.-Y. Jin, M. M. Ovhall, N. Kumar, J.-W. Kang, Flexible Transparent Conducting Electrodes Based on Metal Meshes for Organic Optoelectronic Device Applications: a Review. *J. Mater. Chem. C* **2019**, *7*, 1087-1110.
25. I. Jeon, J. Yoon, U. Kim, C. Lee, R. Xiang, A. Shawky, J. Xi, J. Byeon, H. M. Lee, M. Choi, S. Maruyama, Y. Matsuo, High-Performance Solution-Processed Double-Walled Carbon Nanotube Transparent Electrode for Perovskite Solar Cells. *Adv. Energy Mater.* **2019**, *9*, 1901204.
26. H. Wu, D. Kong, Z. Ruan, P.-C. Hsu, S. Wang, Z. Yu, T. J. Carney, L. Hu, S. Fan, Y. Cui, A Transparent Electrode Based on a Metal Nanotrough Network. *Nat. Nanotechnol.* **2013**, *8*, 421-425.
27. P.-C. Hsu, S. Wang, H. Wu, V. K. Narasimhan, D. Kong, H. R. Lee, Y. Cui, Performance Enhancement of Metal Nanowire Transparent Conducting Electrodes by Mesoscale Metal Wires. *Nat. Commun.* **2013**, *4*, 2522.
28. H. Guo, N. Lin, Y. Z. Chen, Z. W. Wang, Q. S. Xie, T. Zheng, N. Gao, S. Li, J. Kang, D. Cai, D.-L. Peng, Copper Nanowires as Fully Transparent Conductive Electrodes. *Sci. Rep.* **2013**, *3*, 2323.
29. D. Zhang, R. Wang, M. Wen, D. Weng, X. Cui, J. Sun, H. Li, Y. Lu, Synthesis of Ultralong Copper Nanowires for High-Performance Transparent Electrodes. *J. Am. Chem. Soc.* **2012**, *134*, 14283-14286.
30. H.-G. Im, S.-H. Jung, J. Jin, D. Lee, J. Lee, D. Lee, J.-Y. Lee, I.-D. Kim, B.-S. Bae, Flexible Transparent Conducting Hybrid Film Using a Surface-Embedded Copper Nanowire Network: A Highly Oxidation-Resistant Copper Nanowire Electrode for Flexible Optoelectronics. *ACS Nano* **2014**, *8*, 10973-10979.
31. L. Hu, H. S. Kim, J.-Y. Lee, P. Peumans, Y. Cui, Scalable Coating and Properties of Transparent, Flexible, Silver Nanowire Electrodes. *ACS Nano* **2010**, *4*, 2955-2963.
32. S. Kang, T. Kim, S. Cho, Y. Lee, A. Choe, B. Walker, S.-J. Ko, J. Y. Kim, H. Ko, Capillary Printing of Highly Aligned Silver Nanowire Transparent Electrodes for High-Performance Optoelectronic Devices. *Nano Lett.* **2015**, *15*, 7933-7942.
33. J. V. van de Groep, P. Spinelli, A. Polman, Transparent Conducting Silver Nanowire Networks. *Nano Lett.* **2012**, *12*, 3138-3144.
34. Y. Sun, B. Gates, B. Mayers, Y. Xia, Crystalline Silver Nanowires by Soft Solution Processing. *Nano Lett.* **2002**, *2*, 165-168.
35. Y. Sun, Y. Xia, Large-Scale Synthesis of Uniform Silver Nanowires Through a Soft, Self-Seeding, Polyol Process. *Adv. Mater.* **2002**, *14*, 833-837.

36. X. Guo, X. Liu, J. Luo, Z. Gan, Z. Meng, N. Zhang, Silver Nanowire/Polyimide Composite Transparent Electrodes for Reliable Flexible Polymer Solar Cells Operating at High and Ultra-Low Temperature. *RSC Adv.* **2015**, *5*, 24953-24959.
37. D. Y. Choi, H. W. Kang, H. J. Sung, S. S. Kim, Annealing-Free, Flexible Silver Nanowire-Polymer Composite Electrodes via a Continuous Two-Step Spray-Coating Method. *Nanoscale* **2013**, *5*, 977-983.
38. S. Xie, Z. Ouyang, B. Jia, M. Gu, Large-Size, High-Uniformity, Random Silver Nanowire Networks as Transparent Electrodes for Crystalline Silicon Wafer Solar Cells. *Opt. Express* **2013**, *21*, A355-A362.
39. W. Xiong, H. Liu, Y. Chen, M. Zheng, Y. Zhao, X. Kong, Y. Wang, X. Zhang, X. Kong, P. Wang, L. Jiang, Highly Conductive, Air-Stable Silver Nanowire@Iongel Composite Films toward Flexible Transparent Electrodes. *Adv. Mater.* **2016**, *28*, 7167-7172.
40. X. Zhang, J. Wu, J. Wang, Q. Yang, B. Zhang, Z. Xie, Low-Temperature All-Solution-Processed Transparent Silver Nanowire-Polymer/AZO Nanoparticles Composite Electrodes for Efficient ITO-Free Polymer Solar Cells. *ACS Appl. Mater. Interfaces* **2016**, *8*, 34630-34637.
41. A. R. Madaria, A. Kumar, C. Zhou, Large Scale, Highly Conductive and Patterned Transparent Films of Silver Nanowires on Arbitrary Substrates and Their Application in Touch Screens. *Nanotechnology* **2011**, *22*, 245201.
42. S. Cho, S. Kang, A. Pandya, R. Shanker, Z. Khan, Y. Lee, J. Park, S. L. Craig, H. Ko, Large-Area Cross-Aligned Silver Nanowire Electrodes for Flexible, Transparent, and Force-Sensitive Mechanochromic Touch Screens. *ACS Nano* **2017**, *11*, 4346-4357.
43. M. Jagota, N. Tansu, Conductivity of Nanowire Arrays under Random and Ordered Orientation Configurations. *Sci. Rep.* **2015**, *5*, 10219.
44. L. Hu, D. S. Hecht, G. Gruner, Percolation in Transparent and Conducting Carbon Nanotube Networks. *Nano Lett.* **2004**, *4*, 2513-2517.
45. S. De, P. J. King, P. E. Lyons, U. Khan, J. N. Coleman, Size Effects and the Problem with Percolation in Nanostructured Transparent Conductors. *ACS Nano* **2010**, *4*, 7064-7072.
46. C. G. da Rocha, H. G. Manning, C. O'Callaghan, C. Ritter, A. T. Bellew, J. J. Bolandd, M. S. Ferreira, Ultimate Conductivity Performance in Metallic Nanowire Networks. *Nanoscale* **2015**, *7*, 13011-13016.
47. F. Selzer, C. Floresca, D. Knepe, L. Bormann, C. Sachse, N. Weiss, A. Eychmuller, A. Amassian, L. Muller-Meskamp, K. Leo, Electrical Limit of Silver Nanowire Electrodes: Direct Measurement of the Nanowire Junction Resistance. *Appl. Phys. Lett.* **2016**, *108*, 163302.

48. T. Tokuno, M. Nogi, M. Karakawa, J. Jiu, T. T. Nge, Y. Aso, K. Suganuma, Fabrication of Silver Nanowire Transparent Electrodes at Room Temperature. *Nano Res.* **2011**, *4*, 1215-1222.
49. E. C. Garnett, W. Cai, J. J. Cha, F. Mahmood, S. T. Connor, M. G. Christoforo, Y. Cui, M. D. McGehee, M. L. Brongersma, Self-Limited Plasmonic Welding of Silver Nanowire Junctions. *Nat. Mater.* **2012**, *11*, 241-249.
50. D. P. Langley, M. Lagrange, G. Giusti, C. Jimenez, Y. Brechet, N. D. Nguyen, D. Bellet, Metallic Nanowire Networks: Effects of Thermal Annealing on Electrical Resistance. *Nanoscale* **2014**, *6*, 13535-13543.
51. Y. Liu, J. Zhang, H. Gao, Y. Wang, Q. Liu, S. Huang, C. F. Guo, Z. F. Ren, Capillary-Force-Induced Cold Welding in Silver-Nanowire-Based Flexible Transparent Electrodes. *Nano Lett.* **2017**, *17*, 1090-1096.
52. H.-J. Lee, S. Oh, K.-Y. Cho, W.-L. Jeong, D.-S. Lee, S.-J. Park, Spontaneous and Selective Nanowelding of Silver Nanowires by Electrochemical Ostwald Ripening and High Electrostatic Potential at the Junctions for High-Performance Stretchable Transparent Electrodes. *ACS Appl. Mater. Interfaces* **2018**, *10*, 14124-14131.
53. A. Tao, F. Kim, C. Hess, J. Goldberger, R. He, Y. Sun, Y. Xia, P. Yang, Langmuir-Blodgett Silver Nanowire Monolayers for Molecular Sensing Using Surface-Enhanced Raman Spectroscopy. *Nano Lett.* **2003**, *3*, 1229-1233.
54. S.-K. Duan, Q.-L. Niu, J.-F. Wei, J.-B. He, Y.-A. Yin, Y. Zhang, Water-Bath Assisted Convective Assembly of Aligned Silver Nanowire Films for Transparent Electrodes. *Phys. Chem. Chem. Phys.* **2015**, *17*, 8106-8112.
55. B. Park, I.-G. Bae, Y. H. Huh, Aligned Silver Nanowire-Based Transparent Electrodes for Engineering Polarisation-Selective Optoelectronics. *Sci. Rep.* **2016**, *6*, 19485.
56. H. Hu, M. Pauly, O. Felix, G. Decher, Spray-Assisted Alignment of Layer-by-Layer Assembled Silver Nanowires: A General Approach for the Preparation of Highly Anisotropic Nano-Composite Films. *Nanoscale* **2017**, *9*, 1307-1314.
57. L. Meng, R. Bian, C. Guo, B. Xu, H. Liu, L. Jiang, Aligning Ag Nanowires by a Facile Bioinspired Directional Liquid Transfer: Toward Anisotropic Flexible Conductive Electrodes. *Adv. Mater.* **2018**, *30*, 1706938.
58. H. Hu, S. Wang, S. Wang, G. Liu, T. Cao, Y. Long, Aligned Silver Nanowires Enabled Highly Stretchable and Transparent Electrodes with Unusual Conductive Property. *Adv. Funct. Mater.* **2019**, *29*, 1902922.

59. Y. Jia, C. Chen, D. Jia, S. Li, S. Ji, C. Ye, Silver Nanowire Transparent Conductive Films with High Uniformity Fabricated via a Dynamic Heating Method. *ACS Appl. Mater. Interfaces* **2016**, *8*, 9865-9871.
60. J. Jang, H.-G. Im, J. Jin, J. Lee, J.-Y. Lee, B.-S. Bae, A Flexible and Robust Transparent Conducting Electrode Platform Using an Electroplated Silver Grid/Surface-Embedded Silver Nanowire Hybrid Structure. *ACS Appl. Mater. Interfaces* **2016**, *8*, 27035-27043.
61. J.-S. Bae, Y.-S. Lee, J. Li, J. Liang, D. Chen, Q. Pei, S.-B. Lee, The Feasibility of Healable Electronics and Mechanical Behavior of Silver Nanowire (AgNW)/Healable Polymer Composite. *Adv. Mater. Technol.* **2018**, *3*, 1700364.
62. C. Mayousse, C. Celle, E. Moreau, J.-F. Mainguet, A. Carella, J.-P. Simonato, Improvements in Purification of Silver Nanowires by Decantation and Fabrication of Flexible Transparent Electrodes. Application to Capacitive Touch Sensors. *Nanotechnology* **2013**, *24*, 215501.
63. S. Hong, J. Yeo, J. Lee, H. Lee, P. Lee, S. S. Lee, S. H. Ko, Selective Laser Direct Patterning of Silver Nanowire Percolation Network Transparent Conductor for Capacitive Touch Panel. *J. Nanosci. Nanotechnol.* **2015**, *15*, 2317-2323.
64. S. Yao, Y. Zhu, Wearable Multifunctional Sensors Using Printed Stretchable Conductors Made of Silver Nanowires. *Nanoscale* **2014**, *6*, 2345-2352.
65. H. Lee, K. Lee, J. T. Park, W. C. Kim, H. Lee, Well-Ordered and High Density Coordination-Type Bonding to Strengthen Contact of Silver Nanowires on Highly Stretchable Polydimethylsiloxane. *Adv. Funct. Mater.* **2014**, *24*, 3276-3283.
66. J. Li, J. Liang, L. Li, F. Ren, W. Hu, J. Li, S. Qi, Q. Pei, Healable Capacitive Touch Screen Sensors Based on Transparent Composite Electrodes Comprising Silver Nanowires and a Furan/Maleimide Diels-Alder Cycloaddition Polymer. *ACS Nano* **2014**, *8*, 12874-12882.
67. T. Y. Choi, B.-U. Hwang, B.-Y. Kim, T. Q. Trung, Y. H. Nam, D.-N. Kim, K. Eom, N.-E. Lee, Stretchable, Transparent, and Stretch-Unresponsive Capacitive Touch Sensor Array with Selectively Patterned Silver Nanowires/Reduced Graphene Oxide Electrodes. *ACS Appl. Mater. Interfaces* **2017**, *9*, 18022-18030.
68. S. Xu, B. Man, S. Jiang, M. Liu, C. Yang, C. S. Chen, C. Zhang, Graphene-Silver Nanowire Hybrid Films as Electrodes for Transparent and Flexible Loudspeakers. *CrystEngComm* **2014**, *16*, 3532-3539.
69. H. Tian, D. Xie, Y. Yang, T.-L. Ren, Y.-X. Lin, Y. Chen, Y.-F. Wang, C.-J. Zhou, P.-G. Peng, L.-G. Wang, L.-T. Liu, Flexible, Ultrathin, and Transparent Sound-Emitting Devices Using Silver Nanowires Film. *Appl. Phys. Lett.* **2011**, *99*, 253507.

70. P. La Torraca, L. Larcher, M. Bobinger, P. Pavan, B. Seeber, P. Lugli, Physical Modeling and Characterization of Thermo-Acoustic Loudspeakers Made of Silver Nano-Wire Films. *J. Appl. Phys.* **2017**, *121*, 214502.
71. J. W. Suk, K. Kirk, Y. Hao, N. A. Hall, R. S. Ruoff, Thermoacoustic Sound Generation from Monolayer Graphene for Transparent and Flexible Sound Sources. *Adv. Mater.* **2012**, *24*, 6342-6347.
72. L. Xiao, Z. Chen, C. Feng, L. Liu, Z.-Q. Bai, Y. Wang, L. Qian, Y. Zhang, Q. Li, K. Jiang, S. Fan, Flexible, Stretchable, Transparent Carbon Nanotube Thin Film Loudspeakers. *Nano Lett.* **2008**, *8*, 4539-4545.
73. H. S. Lee, J. Chung, G.-T. Hwang, C. K. Jeong, Y. Jung, J.-H. Kwak, H. Kang, M. Byun, W. D. Kim, S. Hur, S.-H. Oh, K. J. Lee, Flexible Inorganic Piezoelectric Acoustic Nanosensors for Biomimetic Artificial Hair Cells. *Adv. Funct. Mater.* **2014**, *24*, 6914-6921.
74. J. Jang, J. Lee, J. H. Jang, H. Choi, A Triboelectric-Based Artificial Basilar Membrane to Mimic Cochlear Tonotopy. *Adv. Healthcare Mater.* **2016**, *5*, 2481-2487.
75. H. Guo, X. Pu, J. Chen, Y. Meng, M.-H. Yeh, G. Liu, Q. Tang, B. Chen, D. Liu, S. Qi, C. Wu, C. Hu, J. Wang, Z. L. Wang, A Highly Sensitive, Self-Powered Triboelectric Auditory Sensor for Social Robotics and Hearing Aids. *Sci. Robot.* **2018**, *3*, eaat2516.
76. W. Li, D. Torres, R. Diaz, Z. Wang, C. Wu, C. Wang, Z. L. Wang, N. Sepulveda, Nanogenerator-Based Dual-Functional and Self-Powered Thin Patch Loudspeaker or Microphone for Flexible Electronics. *Nat. Commun.* **2017**, *8*, 15310.
77. S. Lee, J. Kim, I. Yun, G. Y. Bae, D. Kim, S. Park, I.-M. Yi, W. Moon, Y. Chung, K. Cho, An Ultrathin Conformable Vibration-Responsive Electronic Skin for Quantitative Vocal Recognition. *Nat. Commun.* **2019**, *10*, 2468.
78. W. Chen, L.-X. Liu, H.-B. Zhang, Z.-Z. Yu, Flexible, Transparent and Conductive $Ti_3C_2T_x$ MXene-Silver Nanowire Films with Smart Acoustic Sensitivity for High-Performance Electromagnetic Interference Shielding. *ACS Nano* **2020**, DOI:10.1021/acsnano.0c01635.
79. Q. Zhang, C. Ji, L. C. Lv, D. Zhao, J. Ji, K. Zhuo, Z. Yuan, W. Zhang, S. Sang, A Flexible, Acoustic Localized Sensor with Mass Block-Beam Structure Based on Polydimethylsiloxane-Silver Nanowires. *Soft Robot.* **2020**, DOI:10.1089/soro.2020.0030.
80. C. Wang, C. Wang, Z. Huang, S. Xu, Materials and Structures toward Soft Electronics. *Adv. Mater.* **2018**, *30*, 1801368.
81. W. Hu, X. Niu, L. Li, S. Yun, Z. Yu, Q. Pei, Intrinsically Stretchable Transparent Electrodes Based on Silver-Nanowire-Crosslinked-Polyacrylate Composites. *Nanotechnology* **2012**, *23*, 344002.

82. M.-S. Lee, K. Lee, S.-Y. Kim, H. Lee, J. Park, K.-H. Choi, H.-K. Kim, D.-G. Kim, D.-Y. Lee, S. Nam, J.-U. Park, High-Performance, Transparent, and Stretchable Electrodes Using Graphene-Metal Nanowire Hybrid Structures. *Nano Lett.* **2013**, *13*, 2814-2821.
83. S. Hong, H. Lee, J. Lee, J. Kwon, S. Han, Y. D. Suh, H. Cho, J. Shin, J. Yeo, S. H. Ko, Highly Stretchable and Transparent Metal Nanowire Heater for Wearable Electronics Applications. *Adv. Mater.* **2015**, *27*, 4744-4751.
84. J.-H. Kim, S.-R. Kim, H.-J. Kil, Y.-C. Kim, J.-W. Park, Highly Conformable, Transparent Electrodes for Epidermal Electronics. *Nano Lett.* **2018**, *18*, 4531-4540.
85. J. Wang, C. Yan, K. J. Chee, P. S. Lee, Highly Stretchable and Self-Deformable Alternating Current Electroluminescent Devices. *Adv. Mater.* **2015**, *27*, 2876-2882.
86. B. You, Y. Kim, B.-K. Ju, J.-W. Kim, Highly Stretchable and Waterproof Electroluminescence Device Based on Superstable Stretchable Transparent Electrode. *ACS Appl. Mater. Interfaces* **2017**, *9*, 5486-5494.
87. F. Stauffer, K. Tybrandt, Bright Stretchable Alternating Current Electroluminescent Displays Based on High Permittivity Composites. *Adv. Mater.* **2016**, *28*, 7200-7203.
88. Y. Zhou, S. Cao, J. Wang, H. Zhu, J. Wang, S. Yang, X. Wang, D. Kong, Bright Stretchable Electroluminescent Devices based on Silver Nanowire Electrodes and High-k Thermoplastic Elastomers. *ACS Appl. Mater. Interfaces* **2018**, *10*, 44760-44767.
89. Q. Sun, S. J. Lee, H. Kang, Y. Gim, H. S. Park, J. H. Cho, Positively-Charged Reduced Graphene Oxide as an Adhesion Promoter for Preparing a Highly-Stable Silver Nanowire Film. *Nanoscale* **2015**, *7*, 6798-6804.
90. T. Akter, W. S. Kim, Reversibly Stretchable Transparent Conductive Coatings of Spray-Deposited Silver Nanowires. *ACS Appl. Mater. Interfaces* **2012**, *4*, 1855-1859.
91. H. Fan, K. Li, Q. Li, C. Hou, Q. Zhang, Y. Li, W. Jin, H. Wang, Prepolymerization-Assisted Fabrication of an Ultrathin Immobilized Layer to Realize a Semi-Embedded Wrinkled AgNW Network for a Smart Electrothermal Chromatic Display and Actuator. *J. Mater. Chem. C* **2017**, *5*, 9778-9785.
92. H.-G. Im, J. Jin, J.-H. Ko, J. Lee, J.-Y. Lee, B.-S. Bae, Flexible Transparent Conducting Composite Films Using a Monolithically Embedded AgNW Electrode with Robust Performance Stability. *Nanoscale* **2014**, *6*, 711-715.
93. D. Y. Kim, S. Choi, H. Cho, J.-Y. Sun, Electroactive Soft Photonic Devices for the Synesthetic Perception of Color and Sound. *Adv. Mater.* **2019**, *31*, 1804080.

94. J. S. Kim, S. H. Cho, K. L. Kim, G. Kim, S. W. Lee, E. H. Kim, B. Jeong, I. Hwang, H. Han, W. Shim, T.-W. Lee, C. Park, Flexible Artificial Synesthesia Electronics with Sound-Synchronized Electroluminescence. *Nano Energy* **2019**, *59*, 773-783.
95. M. Kaltenbrunner, M. S. White, E. D. Glowacki, T. Sekitani, T. Someya, N. S. Sariciftci, S. Bauer, Ultrathin and Lightweight Organic Solar Cells with High Flexibility. *Nat. Commun.* **2012**, *3*, 770.
96. H. Kang, S. Jung, S. Jeong, G. Kim, K. Lee, Polymer-Metal Hybrid Transparent Electrodes for Flexible Electronics. *Nat. Commun.* **2015**, *6*, 6503.
97. T.-H. Han, Y. Lee, M.-R. Choi, S.-H. Woo, S.-H. Bae, B. H. Hong, J.-H. Ahn, T.-W. Lee, Extremely Efficient Flexible Organic Light-Emitting Diodes with Modified Graphene Anode. *Nat. Photonics* **2012**, *6*, 105-110.
98. N. Li, S. Oida, G. S. Tulevski, S.-J. Han, J. B. Hannon, D. K. Sadana, T.-C. Chen, Efficient and Bright Organic Light-Emitting Diodes on Single-Layer Graphene Electrodes. *Nat. Commun.* **2013**, *4*, 2294.
99. C. F. Guo, Z. Ren, Flexible Transparent Conductors Based on Metal Nanowire Networks. *Mater. Today* **2015**, *18*, 143-154.
100. D. S. Hecht, L. Hu, G. Irvin, Emerging Transparent Electrodes Based on Thin Films of Carbon Nanotubes, Graphene, and Metallic Nanostructures. *Adv. Mater.* **2011**, *23*, 1482-1513.
101. C. Mayousse, C. Celle, A. Fraczkiewicz, J.-P. Simonato, Stability of Silver Nanowire Based Electrodes under Environmental and Electrical Stresses. *Nanoscale* **2015**, *7*, 2107-2115.
102. M. Song, D. S. You, K. Lim, S. Park, S. Jung, C. S. Kim, D.-H. Kim, D.-G. Kim, J.-K. Kim, J. Park, Y.-C. Kang, J. Heo, S.-H. Jin, J. H. Park, J.-W. Kang, Highly Efficient and Bendable Organic Solar Cells with Solution-Processed Silver Nanowire Electrodes. *Adv. Funct. Mater.* **2013**, *23*, 4177-4184.
103. F. Selzer, N. Weiss, D. Knepe, L. Bormann, C. Sachse, N. Gaponik, A. Eychmuller, K. Leo, L. Muller-Meskamp, A Spray-Coating Process for Highly Conductive Silver Nanowire Networks as the Transparent Top-Electrode for Small Molecule Organic Photovoltaics. *Nanoscale* **2015**, *7*, 2777-2783.
104. S. J. Lee, Y.-H. Kim, J. K. Kim, H. Baik, J. H. Park, J. Lee, J. Nam, J. H. Park, T.-W. Lee, G.-R. Yi, J. H. Cho, A Roll-to-Roll Welding Process for Planarized Silver Nanowire Electrodes. *Nanoscale* **2014**, *6*, 11828-11834.
105. H. Sim, S. Bok, B. Kim, M. Kim, G.-H. Lim, S. M. Cho, B. Lim, Organic-Stabilizer-Free Polyol Synthesis of Silver Nanowires for Electrode Applications. *Angew. Chem. Int. Ed.* **2016**, *55*, 11814-11818.

106. Y. Lee, S.-Y. Min, T.-S. Kim, S.-H. Jeong, J. Y. Won, H. Kim, W. Xu, J. K. Jeong, T.-W. Lee, Versatile Metal Nanowiring Platform for Large-Scale Nano- and Opto-Electronic Devices. *Adv. Mater.* **2016**, *28*, 9109-9116.
107. A. R. Rathmell, S. M. Bergin, Y.-L. Hua, Z.-Y. Li, B. J. Wiley, The Growth Mechanism of Copper Nanowires and Their Properties in Flexible, Transparent Conducting Films. *Adv. Mater.* **2010**, *22*, 3558-3563.
108. P.-C. Hsu, D. Kong, S. Wang, H. Wang, A. J. Welch, H. Wu, Y. Cui, Electrolessly Deposited Electrospun Metal Nanowire Transparent Electrodes. *J. Am. Chem. Soc.* **2014**, *136*, 10593-10596.
109. H. Koga, M. Nogi, N. Komoda, T. T. Nge, T. Sugahara, K. Suganuma, Uniformly Connected Conductive Networks on Cellulose Nanofiber Paper for Transparent Paper Electronics. *NPG Asia Mater.* **2014**, *6*, e93.
110. J.-Y. Lee, S. T. Connor, Y. Cui, P. Peumans, Solution-Processed Metal Nanowire Mesh Transparent Electrodes. *Nano Lett.* **2008**, *8*, 689-692.
111. S. M. Bergin, Y.-H. Chen, A. R. Rathmell, P. Charbonneau, Z.-Y. Li, B. J. Wiley, The Effect of Nanowire Length and Diameter on the Properties of Transparent, Conducting Nanowire Films. *Nanoscale* **2012**, *4*, 1996-2004.
112. R. M. Mutiso, M. C. Sherrott, A. R. Rathmell, B. J. Wiley, K. I. Winey, Integrating Simulations and Experiments To Predict Sheet Resistance and Optical Transmittance in Nanowire Films for Transparent Conductors. *ACS Nano* **2013**, *7*, 7654-7663.
113. J. Yao, H. Yan, C. M. Lieber, A Nanoscale Combing Technique for the Large-Scale Assembly of Highly Aligned Nanowires. *Nat. Nanotechnol.* **2013**, *8*, 329-335.
114. Z. Fan, J. C. Ho, Z. A. Jacobson, R. Yerushalmi, R. L. Alley, H. Razavi, A. Javey, Wafer-Scale Assembly of Highly Ordered Semiconductor Nanowire Arrays by Contact Printing. *Nano Lett.* **2008**, *8*, 20-25.
115. X. Zhou, Y. Zhou, J. C. Ku, C. Zhang, C. A. Mirkin, Capillary Force-Driven, Large-Area Alignment of Multi-segmented Nanowires. *ACS Nano* **2014**, *8*, 1511-1516.
116. W. Han, Z. Lin, Learning from "Coffee Rings": Ordered Structures Enabled by Controlled Evaporative Self-Assembly. *Angew. Chem. Int. Ed.* **2012**, *51*, 1534-1546.
117. Y. Huang, X. Duan, Q. Wei, C. M. Lieber, Directed Assembly of One-Dimensional Nanostructures into Functional Networks. *Science* **2001**, *291*, 630-633.
118. B. Li, C. C. Zhang, B. B. Jiang, W. Han, Z. Q. Lin, Flow-Enabled Self-Assembly of Large-Scale Aligned Nanowires. *Angew Chem Int Edit* **2015**, *54*, 4250-4254.
119. B. Li, W. Han, B. Jiang, Z. Lin, Crafting Threads of Diblock Copolymer Micelles via Flow-Enabled Self-Assembly. *ACS Nano* **2014**, *8*, 2936-2942.

120. B. Li, B. B. Jiang, W. Han, M. He, X. Li, W. Wang, S. W. Hong, M. Byun, S. Lin, Z. Lin, Harnessing Colloidal Crack Formation by Flow-Enabled Self-Assembly. *Angew. Chem. Int. Ed.* **2017**, *56*, 4554-4559.
121. P. A. Smith, C. D. Nordquist, T. N. Jackson, T. S. Mayer, B. R. Martin, J. Mbindyo, T. E. Mallouk, Electric-Field Assisted Assembly and Alignment of Metallic Nanowires. *Appl. Phys. Lett.* **2000**, *77*, 1399-1401.
122. H.-Y. Shi, B. Hu, X.-C. Yu, R.-L. Zhao, X.-F. Ren, S.-L. Liu, J.-W. Liu, M. Feng, A.-W. Xu, S.-H. Yu, Ordering of Disordered Nanowires: Spontaneous Formation of Highly Aligned, Ultralong Ag Nanowire Films at Oil-Water-Air Interface. *Adv. Funct. Mater.* **2010**, *20*, 958-964.
123. J. Huang, R. Fan, S. Connor, P. Yang, One-Step Patterning of Aligned Nanowire Arrays by Programmed Dip Coating. *Angew. Chem. Int. Ed.* **2007**, *46*, 2414-2417.
124. H. Lee, B. Seong, J. Kim, Y. Jang, D. Byun, Direct Alignment and Patterning of Silver Nanowires by Electrohydrodynamic Jet Printing. *Small* **2014**, *10*, 3918-3922.
125. Y. Ko, S. K. Song, N. H. Kim, S. T. Chang, Highly Transparent and Stretchable Conductors Based on a Directional Arrangement of Silver Nanowires by a Microliter-Scale Solution Process. *Langmuir* **2016**, *32*, 366-373.
126. M. Le Berre, Y. Chen, D. Baigl, From Convective Assembly to Landau-Levich Deposition of Multilayered Phospholipid Films of Controlled Thickness. *Langmuir* **2009**, *25*, 2554-2557.
127. E. M. Freer, O. Grachev, X. Duan, S. Martin, D. P. Stumbo, High-Yield Self-Limiting Single-Nanowire Assembly with Dielectrophoresis. *Nat. Nanotechnol.* **2010**, *5*, 525-530.
128. H. Ko, S. Peleshanko, V. V. Tsukruk, Combing and Bending of Carbon Nanotube Arrays with Confined Microfluidic Flow on Patterned Surfaces. *J. Phys. Chem. B* **2004**, *108*, 4385-4393.
129. Q. N. Luu, J. M. Doorn, M. T. Berry, C. Jiang, C. Lin, P. S. May, Preparation and Optical Properties of Silver Nanowires and Silver-Nanowire Thin Films. *J. Colloid Interface Sci.* **2011**, *356*, 151-158.
130. S. Badoga, S. K. Pattanayek, A. Kumar, L. M. Pandey, Effect of Polymer-Surfactant Structure on Its Solution Viscosity. *Asia-Pac. J. Chem. Eng.* **2011**, *6*, 78-84.
131. D. Kowalski, P. Schmuki, Polypyrrole Self-Organized Nanopore Arrays Formed by Controlled Electropolymerization in TiO₂ Nanotube Template. *Chem. Commun.* **2010**, *46*, 8585-8587.
132. S. W. Huang, K. G. Neoh, E. T. Kang, H. S. Han, K. L. Tan, Palladium-Containing Polyaniline and Polypyrrole Microparticles. *J. Mater. Chem.* **1998**, *8*, 1743-1748.
133. P. Jiang, S.-Y. Li, S.-S. Xie, Y. Gao, L. Song, Machinable Long PVP-Stabilized Silver Nanowires. *Chem. Eur. J.* **2004**, *10*, 4817-4821.

134. J.-W. Liu, J.-L. Wang, Z.-H. Wang, W.-R. Huang, S.-H. Yu, Manipulating Nanowire Assembly for Flexible Transparent Electrodes. *Angew. Chem. Int. Ed.* **2014**, *53*, 13477-13482.
135. C.-H. Choi, C.-J. Kim, Large Slip of Aqueous Liquid Flow over a Nanoengineered Superhydrophobic Surface. *Phys. Rev. Lett.* **2006**, *96*, 066001.
136. H. Yu, P. Zhang, A Kinetic-Hydrodynamic Simulation of Microstructure of Liquid Crystal Polymers in Plane Shear Flow. *J. Non-Newtonian Fluid Mech.* **2007**, *141*, 116-127.
137. D. M. Kuncicky, R. R. Naik, O. D. Velev, Rapid Deposition and Long-Range Alignment of Nanocoatings and Arrays of Electrically Conductive Wires from Tobacco Mosaic Virus. *Small* **2006**, *2*, 1462-1466.
138. R. Janneck, F. Vercesi, P. Heremans, J. Genoe, C. Rolin, Predictive Model for the Meniscus-Guided Coating of High-Quality Organic Single-Crystalline Thin Films. *Adv. Mater.* **2016**, *28*, 8007-8013.
139. D. Khim, H. Han, K.-J. Baeg, J. Kim, S.-W. Kwak, D.-Y. Kim, Y.-Y. Noh, Simple Bar-Coating Process for Large-Area, High-Performance Organic Field-Effect Transistors and Ambipolar Complementary Integrated Circuits. *Adv. Mater.* **2013**, *25*, 4302-4308.
140. A. K. Doolittle, Studies in Newtonian Flow .1. The Dependence of the Viscosity of Liquids on Temperature. *J. Appl. Phys.* **1951**, *22*, 1031-1035.
141. C. Zhang, X. Zhang, X. Zhang, X. Fan, J. Jie, J. C. Chang, C.-S. Lee, W. Zhang, S.-T. Lee, Facile One-step Growth and Patterning of Aligned Squaraine Manowires via Evaporation-Induced Self-Assembly. *Adv. Mater.* **2008**, *20*, 1716-1720.
142. B. Li, S. Ye, I. E. Stewart, S. Alvarez, B. J. Wiley, Synthesis and Purification of Silver Nanowires To Make Conducting Films with a Transmittance of 99%. *Nano Lett.* **2015**, *15*, 6722-6726.
143. T. Kim, A. Canlier, G. H. Kim, J. Choi, M. Park, S. M. Han, Electrostatic Spray Deposition of Highly Transparent Silver Nanowire Electrode on Flexible Substrate. *ACS Appl. Mater. Interfaces* **2013**, *5*, 788-794.
144. A. R. Madaria, A. Kumar, F. N. Ishikawa, C. Zhou, Uniform, Highly Conductive, and Patterned Transparent Films of a Percolating Silver Nanowire Network on Rigid and Flexible Substrates Using a Dry Transfer Technique. *Nano Res.* **2010**, *3*, 564-573.
145. J. Liang, L. Li, K. Tong, Z. Ren, W. Hu, X. Niu, Y. Chen, Q. Pei, Silver Nanowire Percolation Network Soldered with Graphene Oxide at Room Temperature and Its Application for Fully Stretchable Polymer Light-Emitting Diodes. *ACS Nano* **2014**, *8*, 1590-1600.
146. J. Lee, P. Lee, H. B. Lee, S. Hong, I. Lee, J. Yeo, S. S. Lee, T.-S. Kim, D. Lee, S. H. Ko, Room-Temperature Nanosoldering of a Very Long Metal Nanowire Network by Conducting-Polymer-Assisted Joining for a Flexible Touch-Panel Application. *Adv. Funct. Mater.* **2013**, *23*, 4171-4176.

147. J. Wu, X. Que, Q. Hu, D. Luo, T. Liu, F. Liu, T. P. Russell, R. Zhu, Q. Gong, Multi-Length Scaled Silver Nanowire Grid for Application in Efficient Organic Solar Cells. *Adv. Funct. Mater.* **2016**, *26*, 4822-4828.
148. D. A. Davis, A. Hamilton, J. Yang, L. D. Cremar, D. Van Gough, S. L. Potisek, M. T. Ong, P. V. Braun, T. J. Martinez, S. R. White, J. S. Moore, N. R. Sottos, Force-Induced Activation of Covalent Bonds in Mechanoresponsive Polymeric Materials. *Nature* **2009**, *459*, 68-72.
149. G. R. Gossweiler, G. B. Hewage, G. Soriano, Q. Wang, G. W. Welshofer, X. Zhao, S. L. Craig, Mechanochemical Activation of Covalent Bonds in Polymers with Full and Repeatable Macroscopic Shape Recovery. *ACS Macro Lett.* **2014**, *3*, 216-219.
150. Q. Wang, G. R. Gossweiler, S. L. Craig, X. Zhao, Cephalopod-Inspired Design of Electro-Mechano-Chemically Responsive Elastomers for On-Demand Fluorescent Patterning. *Nat. Commun.* **2014**, *5*, 4899.
151. G. R. Gossweiler, C. L. Brown, G. B. Hewage, E. Sapiro-Gheiler, W. J. Trautman, G. W. Welshofer, S. L. Craig, Mechanochemically Active Soft Robots. *ACS Appl. Mater. Interfaces* **2015**, *7*, 22431-22435.
152. X. Fang, H. Zhang, Y. Chen, Y. Lin, Y. Xu, W. Weng, Biomimetic Modular Polymer with Tough and Stress Sensing Properties. *Macromolecules* **2013**, *46*, 6566-6574.
153. X. Wang, H. Zhang, R. Yu, L. Dong, D. Peng, A. Zhang, Y. Zhang, H. Liu, C. Pan, Z. L. Wang, Dynamic Pressure Mapping of Personalized Handwriting by a Flexible Sensor Matrix Based on the Mechanoluminescence Process. *Adv. Mater.* **2015**, *27*, 2324-2331.
154. L. Pan, A. Chortos, G. Yu, Y. Wang, S. Isaacson, R. Allen, Y. Shi, R. Dauskardt, Z. Bao, An Ultra-Sensitive Resistive Pressure Sensor Based on Hollow-Sphere Microstructure Induced Elasticity in Conducting Polymer Film. *Nat. Commun.* **2014**, *5*, 3002.
155. J. Park, M. Kim, Y. Lee, H. S. Lee, H. Ko, Fingertip Skin-Inspired Microstructured Ferroelectric Skins Discriminate Static/Dynamic Pressure and Temperature Stimuli. *Sci. Adv.* **2015**, *1*, e1500661.
156. J. Park, Y. Lee, J. Hong, M. Ha, Y.-D. Jung, H. Lim, S. Y. Kim, H. Ko, Giant Tunneling Piezoresistance of Composite Elastomers with Interlocked Microdome Arrays for Ultrasensitive and Multimodal Electronic Skins. *ACS Nano* **2014**, *8*, 4689-4697.
157. A. Bertrand In *Applications and trends in wireless acoustic sensor networks: A signal processing perspective*, 2011 18th IEEE symposium on communications and vehicular technology in the Benelux (SCVT), IEEE: **2011**; pp 1-6.
158. C. L. Sidner, C. D. Kidd, C. Lee, N. Lesh In *Where to look: a study of human-robot engagement*, Proceedings of the 9th international conference on Intelligent user interfaces, **2004**; pp 78-84.

159. J. Yang, J. Chen, Y. Liu, W. Yang, Y. Su, Z. L. Wang, Triboelectrification-Based Organic Film Nanogenerator for Acoustic Energy Harvesting and Self-Powered Active Acoustic Sensing. *ACS Nano* **2014**, *8*, 2649-2657.
160. C. Lang, J. Fang, H. Shao, X. Ding, T. Lin, High-Sensitivity Acoustic Sensors from Nanofibre Webs. *Nat. Commun.* **2016**, *7*, 11108.
161. B. Park, J. Kim, D. Kang, C. Jeong, K. S. Kim, J. U. Kim, P. J. Yoo, T.-I. Kim, Dramatically Enhanced Mechanosensitivity and Signal-to-Noise Ratio of Nanoscale Crack-Based Sensors: Effect of Crack Depth. *Adv. Mater.* **2016**, *28*, 8130-8137.
162. O. J. Cheong, J. S. Lee, J. H. Kim, J. Jang, High Performance Flexible Actuator of Urchin-Like ZnO Nanostructure/Polyvinylene fluoride Hybrid Thin Film with Graphene Electrodes for Acoustic Generator and Analyzer. *Small* **2016**, *12*, 2567-2574.
163. X. Fan, J. Chen, J. Yang, P. Bai, Z. Li, Z. L. Wang, Ultrathin, Rollable, Paper-Based Triboelectric Nanogenerator for Acoustic Energy Harvesting and Self-Powered Sound Recording. *ACS Nano* **2015**, *9*, 4236-4243.
164. T. Q. Trung, N.-E. Lee, Flexible and Stretchable Physical Sensor Integrated Platforms for Wearable Human-Activity Monitoring and Personal Healthcare. *Adv. Mater.* **2016**, *28*, 4338-4372.
165. M. Kaltenbrunner, T. Sekitani, J. Reeder, T. Yokota, K. Kuribara, T. Tokuhara, M. Drack, R. Schwodiauer, I. Graz, S. Bauer-Gogonea, S. Bauer, T. Someya, An Ultra-Lightweight Design for Imperceptible Plastic Electronics. *Nature* **2013**, *499*, 458-463.
166. M. Melzer, M. Kaltenbrunner, D. Makarov, D. Karnaushenko, D. Karnaushenko, T. Sekitani, T. Someya, O. G. Schmidt, Imperceptible Magnetoelectronics. *Nat. Commun.* **2015**, *6*, 6080.
167. T. Yokota, P. Zalar, M. Kaltenbrunner, H. Jinno, N. Matsuhisa, H. Kitanosako, Y. Tachibana, W. Yukita, M. Koizumi, T. Someya, Ultraflexible Organic Photonic Skin. *Sci. Adv.* **2016**, *2*, e1501856.
168. M. S. White, M. Kaltenbrunner, E. D. Glowacki, K. Gutnichenko, G. Kettlgruber, I. Graz, S. Aazou, C. Ulbricht, D. A. M. Egbe, M. C. Miron, Z. Major, M. C. Scharber, T. Sekitani, T. Someya, S. Bauer, N. S. Sariciftci, Ultrathin, Highly Flexible and Stretchable PLEDs. *Nat. Photonics* **2013**, *7*, 811-816.
169. D.-H. Kim, J. Viventi, J. J. Amsden, J. Xiao, L. Vigeland, Y.-S. Kim, J. A. Blanco, B. Panilaitis, E. S. Frechette, D. Contreras, D. L. Kaplan, F. G. Omenetto, Y. Huang, K.-C. Hwang, M. R. Zakin, B. Litt, J. A. Rogers, Dissolvable Films of Silk Fibroin for Ultrathin Conformal Bio-Integrated Electronics. *Nat. Mater.* **2010**, *9*, 511-517.
170. M. Park, Y. J. Park, X. Chen, Y.-K. Park, M.-S. Kim, J.-H. Ahn, MoS₂-Based Tactile Sensor for Electronic Skin Applications. *Adv. Mater.* **2016**, *28*, 2556-2562.

171. Y. J. Park, S.-K. Lee, M.-S. Kim, H. Kim, J.-H. Ahn, Graphene-Based Conformal Devices. *ACS Nano* **2014**, *8*, 7655-7662.
172. C. Pang, J. H. Koo, A. Nguyen, J. M. Caves, M.-G. Kim, A. Chortos, K. Kim, P. J. Wang, J. B. - H. Tok, Z. Bao, Highly Skin-Conformal Microhairy Sensor for Pulse Signal Amplification. *Adv. Mater.* **2015**, *27*, 634-640.
173. M. K. Kwak, H.-E. Jeong, K. Y. Suh, Rational Design and Enhanced Biocompatibility of a Dry Adhesive Medical Skin Patch. *Adv. Mater.* **2011**, *23*, 3949-3953.
174. C. Jiang, S. Markutsya, Y. Pikus, V. V. Tsukruk, Freely Suspended Nanocomposite Membranes as Highly Sensitive Sensors. *Nat. Mater.* **2004**, *3*, 721-728.
175. J. A. Rogers, M. G. Lagally, R. G. Nuzzo, Synthesis, Assembly and Applications of Semiconductor Nanomembranes. *Nature* **2011**, *477*, 45-53.
176. R. Gunawidjaja, C. Jiang, S. Peleshanko, M. Ornatska, S. Singamaneni, V. V. Tsukruk, Flexible and Robust 2D Arrays of Silver Nanowires Encapsulated within Freestanding Layer-by-Layer Films. *Adv. Funct. Mater.* **2006**, *16*, 2024-2034.
177. D. D. Kulkarni, I. Choi, S. Singamaneni, V. V. Tsukruk, Graphene Oxide-Polyelectrolyte Nanomembranes. *ACS Nano* **2010**, *4*, 4667-4676.
178. A. A. Mamedov, N. A. Kotov, M. Prato, D. M. Guldi, J. P. Wicksted, A. Hirsch, Molecular Design of Strong Single-Wall Carbon Nanotube/Polyelectrolyte Multilayer Composites. *Nat. Mater.* **2002**, *1*, 190-194.
179. S. Lee, S. Shin, S. Lee, J. Seo, J. Lee, S. Son, H. J. Cho, H. Algadi, S. Al-Sayari, D. E. Kim, T. Lee, Ag Nanowire Reinforced Highly Stretchable Conductive Fibers for Wearable Electronics. *Adv. Funct. Mater.* **2015**, *25*, 3114-3121.
180. R. Gunawidjaja, H. Ko, C. Jiang, V. V. Tsukruk, Buckling Behavior of Highly Oriented Silver Nanowires Encapsulated within Layer-by-Layer Films. *Chem. Mater.* **2007**, *19*, 2007-2015.
181. C. Hassler, T. Boretius, T. Stieglitz, Polymers for Neural Implants. *J. Polym. Sci. Polym. Phys.* **2011**, *49*, 18-33.
182. D. Qian, E. C. Dickey, R. Andrews, T. Rantell, Load Transfer and Deformation Mechanisms in Carbon Nanotube-Polystyrene Composites. *Appl. Phys. Lett.* **2000**, *76*, 2868-2870.
183. P. Podsiadlo, A. K. Kaushik, E. M. Arruda, A. M. Waas, B. S. Shim, J. Xu, H. Nandivada, B. G. Pumplin, J. Lahann, A. Ramamoorthy, N. A. Kotov, Ultrastrong and Stiff Layered Polymer Nanocomposites. *Science* **2007**, *318*, 80-83.
184. H. Jang, W. Lee, S. M. Won, S. Y. Ryu, D. Lee, J. B. Koo, S.-D. Ahn, C.-W. Yang, M.-H. Jo, J. H. Cho, J. A. Rogers, J.-H. Ahn, Quantum Confinement Effects in Transferrable Silicon Nanomembranes and Their Applications on Unusual Substrates. *Nano Lett.* **2013**, *13*, 5600-5607.

185. J. Huang, M. Juskiewicz, W. H. de Jeu, E. Cerda, T. Emrick, N. Menon, T. P. Russell, Capillary Wrinkling of Floating Thin Polymer Films. *Science* **2007**, *317*, 650-653.
186. C. S. Kim, S. K. Hong, J.-M. Lee, D.-S. Kang, B. J. Cho, J.-W. Choi, Free-Standing Graphene Thermophone on a Polymer-Mesh Substrate. *Small* **2016**, *12*, 185-189.
187. L. Lin, Y. Xie, S. Wang, W. Wu, S. Niu, X. Wen, Z. L. Wang, Triboelectric Active Sensor Array for Self-Powered Static and Dynamic Pressure Detection and Tactile Imaging. *ACS Nano* **2013**, *7*, 8266-8274.
188. S. Niu, S. Wang, L. Lin, Y. Liu, Y. S. Zhou, Y. Hu, Z. L. Wang, Theoretical Study of Contact-Mode Triboelectric Nanogenerators as an Effective Power Source. *Energ Environ. Sci.* **2013**, *6*, 3576-3583.
189. C. H. Yang, B. Chen, J. Zhou, Y. M. Chen, Z. Suo, Electroluminescence of Giant Stretchability. *Adv. Mater.* **2016**, *28*, 4480-4484.
190. X. Xu, D. Hu, L. J. Yan, S. Fang, C. Shen, Y.-L. Loo, Y. Lin, C. S. Haines, N. Li, A. A. Zakhidov, H. Meng, R. H. Baughman, W. Huang, Polar-Electrode-Bridged Electroluminescent Displays: 2D Sensors Remotely Communicating Optically. *Adv. Mater.* **2017**, *29*, 1703552.
191. S. Li, B. N. Peele, C. M. Larson, H. Zhao, R. F. Shepherd, A Stretchable Multicolor Display and Touch Interface Using Photopatterning and Transfer Printing. *Adv. Mater.* **2016**, *28*, 9770-9775.
192. D. Vij, *Handbook of electroluminescent materials*. CRC press: **2004**.
193. J. Yu, R. Huo, C. Wu, X. Wu, G. Wang, P. Jiang, Influence of Interface Structure on Dielectric Properties of Epoxy/Alumina Nanocomposites. *Macromol. Res.* **2012**, *20*, 816-826.
194. V. S. Nisa, S. Rajesh, K. P. Murali, V. Priyadarsini, S. N. Potty, R. Ratheesh, Preparation, Characterization and Dielectric Properties of Temperature Stable SrTiO₃/PEEK Composites for Microwave Substrate Applications. *Compos. Sci. Technol.* **2008**, *68*, 106-112.
195. X. Huang, P. Jiang, T. Tanaka, A Review of Dielectric Polymer Composites With High Thermal Conductivity. *IEEE Electr. Insul. Mag.* **2011**, *27*, 8-16.
196. Prateek, V. K. Thakur, R. K. Gupta, Recent Progress on Ferroelectric Polymer-Based Nanocomposites for High Energy Density Capacitors: Synthesis, Dielectric Properties, and Future Aspects. *Chem. Rev.* **2016**, *116*, 4260-4317.
197. R. P. Ortiz, A. Facchetti, T. J. Marks, High-k Organic, Inorganic, and Hybrid Dielectrics for Low-Voltage Organic Field-Effect Transistors. *Chem. Rev.* **2010**, *110*, 205-239.
198. M. Bredol, H. S. Dieckhoff, Materials for Powder-Based AC-Electroluminescence. *Materials* **2010**, *3*, 1353-1374.
199. A. V. Hippel, Ferroelectricity, Domain Structure, and Phase Transitions of Barium Titanate. *Rev. Mod. Phys.* **1950**, *22*, 221-237.

200. S. M. Bobade, D. D. Gulwade, A. R. Kulkarni, P. Gopalan, Dielectric Properties of A- and B-Site-Doped BaTiO₃(I): La- and Al-Doped Solid Solutions. *J. Appl. Phys.* **2005**, *97*, 074105.
201. F. D. Morrison, D. C. Sinclair, J. M. S. Skakle, A. R. West, Novel doping mechanism for very-high-permittivity barium titanate ceramics. *J Am Ceram Soc* **1998**, *81*, 1957-1960.
202. M. Ganguly, S. K. Rout, T. P. Sinha, S. K. Sharma, H. Y. Park, C. W. Ahn, I. W. Kim, Characterization and Rietveld Refinement of A-Site Deficient Lanthanum Doped Barium Titanate. *J. Alloys Compd.* **2013**, *579*, 473-484.
203. T. Sareein, N. Albutt, M. Unruan, N. Funsueb, A. Ngamjarurojana, R. Yimnirun, Effect of Hybrid Doping on Dielectric Behavior of Barium Titanate Ceramics. *Integr. Ferroelectr.* **2016**, *175*, 96-101.
204. F. D. Morrison, D. C. Sinclair, A. R. West, Electrical and Structural Characteristics of Lanthanum-Doped Barium Titanate Ceramics. *J. Appl. Phys.* **1999**, *86*, 6355-6366.
205. H.-P. Wang, D. Periyangounder, A.-C. Li, J.-H. He, Fabrication of Silicon Hierarchical Structures for Solar Cell Applications. *IEEE Access* **2019**, *7*, 19395-19400.
206. A. Alarawi, V. Ramalingam, H.-C. Fu, P. Varadhan, R. Yang, J.-H. He, Enhanced Photoelectrochemical Hydrogen Production Efficiency of MoS₂-Si Heterojunction. *Opt. Express* **2019**, *27*, A352-A363.
207. C. Schrage, S. Kaskel, Flexible and Transparent SWCNT Electrodes for Alternating Current Electroluminescence Devices. *ACS Appl. Mater. Interfaces* **2009**, *1*, 1640-1644.
208. Z.-G. Wang, Y.-F. Chen, P.-J. Li, X. Hao, J.-B. Liu, R. Huang, Y.-R. Li, Flexible Graphene-Based Electroluminescent Devices. *ACS Nano* **2011**, *5*, 7149-7154.
209. V.-Q. Le, T.-H. Do, J. R. D. Retamal, P.-W. Shao, Y.-H. Lai, W.-W. Wu, J.-H. He, Y.-L. Chueh, Y.-H. Chu, Van der Waals Heteroepitaxial AZO/NiO/AZO/Muscovite (ANA/muscovite) Transparent Flexible Memristor. *Nano Energy* **2019**, *56*, 322-329.
210. Z. Zhou, C. Lan, R. Wei, J. C. Ho, Transparent Metal-Oxide Nanowires and Their Applications in Harsh Electronics. *J. Mater. Chem. C* **2019**, *7*, 202-217.
211. J.-Y. Tseng, L. Lee, Y.-C. Huang, J.-H. Chang, T.-Y. Su, Y.-C. Shih, H.-W. Lin, Y.-L. Chueh, Pressure Welding of Silver Nanowires Networks at Room Temperature as Transparent Electrodes for Efficient Organic Light-Emitting Diodes. *Small* **2018**, *14*, 1800541.
212. S. M. Jeong, S. Song, H. Kim, S.-H. Baek, J. S. Kwak, Stretchable, Alternating-Current-Driven White Electroluminescent Device Based on Bilayer-Structured Quantum-Dot-Embedded Polydimethylsiloxane Elastomer. *RSC Adv.* **2017**, *7*, 8816-8822.

213. D. Wang, R. Yu, S. Feng, W. Zheng, T. Takei, N. Kumada, N. Kinomura, Hydrothermal Synthesis of Perovskite-Type Solid Solution of $(1-x)\text{BaTiO}_3 \cdot x\text{La}_{2/3}\text{TiO}_3$. *Solid State Ionics* **2002**, *151*, 329-333.
214. H.-W. Lee, S. Moon, C.-H. Choi, D. K. Kim, Synthesis and Size Control of Tetragonal Barium Titanate Nanopowders by Facile Solvothermal Method. *J. Am. Ceram. Soc.* **2012**, *95*, 2429-2434.
215. H.-W. Lin, C.-P. Chang, W.-H. Hwu, M.-D. Ger, The Rheological Behaviors of Screen-Printing Pastes. *J. Mater. Process. Tech.* **2008**, *197*, 284-291.
216. P. F. Moonen, I. Yakimets, J. Huskens, Fabrication of Transistors on Flexible Substrates: from Mass-Printing to High-Resolution Alternative Lithography Strategies. *Adv. Mater.* **2012**, *24*, 5526-5541.
217. Y. Aleeva, B. Pignataro, Recent Advances in Upscalable Wet Methods and Ink Formulations for Printed Electronics. *J. Mater. Chem. C* **2014**, *2*, 6436-6453.
218. M. Dur, S. M. Goodnick, S. S. Pennathur, J. F. Wager, M. Reigrotzki, R. Redmer, High-Field Transport and Electroluminescence in ZnS Phosphor Layers. *J. Appl. Phys.* **1998**, *83*, 3176-3185.
219. R. Ashiri, A. Moghtada, A. Shahrouzianfar, R. Ajami, Low Temperature Synthesis of Carbonate-Free Barium Titanate Nanoscale Crystals: Toward a Generalized Strategy of Titanate-Based Perovskite Nanocrystals Synthesis. *J. Am. Ceram. Soc.* **2014**, *97*, 2027-2031.
220. B. Jiang, L. A. Bursill, Phenomenological Theory of Size Effects in Ultrafine Ferroelectric Particles of Lead Titanate. *Phys. Rev. B* **1999**, *60*, 9978-9982.
221. B. Ding, C. Han, L. Zheng, J. Zhang, R. Wang, Z. L. Tang, Tuning Oxygen Vacancy Photoluminescence in Monoclinic Y_2WO_6 by Selectively Occupying Yttrium Sites Using Lanthanum. *Sci. Rep.* **2015**, *5*, 9443.
222. S. P. Culver, V. Stepanov, M. Mecklenburg, S. Takahashi, R. L. Brutchey, Low Temperature Synthesis and Characterization of Lanthanide-Doped BaTiO_3 Nanocrystals. *Chem. Commun.* **2014**, *50*, 3480-3483.
223. S. Guillemet-Fritsch, Z. Valdez-Nava, C. Tenailleau, T. Lebey, B. Durand, J.-Y. Chane-Ching, Colossal Permittivity in Ultrafine Grain Size BaTiO_{3-x} and $\text{Ba}_{0.95}\text{La}_{0.05}\text{TiO}_{3-x}$ Materials. *Adv. Mater.* **2008**, *20*, 551-555.
224. M. T. Buscaglia, V. Buscaglia, M. Viviani, P. Nanni, M. Hanuskova, Influence of Foreign Ions on the Crystal Structure of BaTiO_3 . *J. Eur. Ceram. Soc.* **2000**, *20*, 1997-2007.
225. N. Kurata, M. Kuwabara, Semiconducting Insulating Transition for Highly Donor-Doped Barium-Titanate Ceramics. *J. Am. Ceram. Soc.* **1993**, *76*, 1605-1608.
226. F. A. Rabuffetti, S. P. Culver, J. S. Lee, R. L. Brutchey, Local Structural Investigation of Eu^{3+} -Doped BaTiO_3 Nanocrystals. *Nanoscale* **2014**, *6*, 2909-2914.

227. J. C. Hitt, J. P. Bender, J. F. Wager, Thin-Film Electroluminescent Device Physics Modeling. *Crit. Rev. Solid State Mater. Sci.* **2000**, *25*, 29-85.
228. J. C. Hitt, J. F. Wager, Insulator Issues in Alternating-Current Thin-Film Electroluminescent Devices. *J. Appl. Phys.* **2001**, *90*, 2711-2717.
229. K. Laxman, M. T. Z. Myint, R. Khan, T. Pervez, J. Dutta, Effect of a Semiconductor Dielectric Coating on the Salt Adsorption Capacity of a Porous Electrode in a Capacitive Deionization Cell. *Electrochim. Acta* **2015**, *166*, 329-337.
230. T. Furukawa, K. Fujino, E. Fukada, Electromechanical Properties in Composites of Epoxy-Resin and Pzt Ceramics. *Jpn. J. Appl. Phys.* **1976**, *15*, 2119-2129.
231. A. Goswami, A. P. Goswami, Dielectric and Optical Properties of Zns Films. *Thin Solid Films* **1973**, *16*, 175-185.
232. Y. S. Chen, D. C. Krupka, Limitation Imposed by Field Clamping on Efficiency of High-Field Ac Electroluminescence in Thin-Films. *J. Appl. Phys.* **1972**, *43*, 4089.
233. P. Peka, H.-J. Schulz, Empirical One-Electron Model of Optical-Transitions in Cu-Doped ZnS and CdS. *Physica B* **1994**, *193*, 57-65.
234. Y. P. Chukova, Electroluminescent Capacitors as Systems with Distribution Parameters. *J. Appl. Spectrosc.* **1967**, *7*, 185-188.
235. E. T. Alonso, G. Karkera, G. F. Jones, M. F. Craciun, S. Russo, Homogeneously Bright, Flexible, and Foldable Lighting Devices with Functionalized Graphene Electrodes. *ACS Appl. Mater. Interfaces* **2016**, *8*, 16541-16545.
236. H. Arnold, I. B. Crandall, The Thermophone as a Precision Source of Sound. *Phys. Rev.* **1917**, *10*, 22.
237. L. Xiao, P. Liu, L. Liu, Q. Li, Z. Feng, S. Fan, K. Jiang, High Frequency Response of Carbon Nanotube Thin Film Speaker in Gases. *J. Appl. Phys.* **2011**, *110*, 084311.
238. A. G. Yeklangi, S. E. Khadem, S. Darbari, Fabrication and Investigation of a Thermoacoustic Loudspeaker Based on Carbon Nanotube Coated Laser-Scribed Graphene. *J. Appl. Phys.* **2018**, *124*, 224501.
239. W. Fei, J. Zhou, W. Guo, Low-Voltage Driven Graphene Foam Thermoacoustic Speaker. *Small* **2015**, *11*, 2252-2256.
240. C. S. Kim, K. E. Lee, J.-M. Lee, S. O. Kim, B. J. Cho, J.-W. Choi, Application of N-Doped Three-Dimensional Reduced Graphene Oxide Aerogel to Thin Film Loudspeaker. *ACS Appl. Mater. Interfaces* **2016**, *8*, 22295-22300.

241. P. La Torraca, M. Bobinger, P. Pavan, M. Becherer, S. Zhao, M. Koebel, L. Cattani, P. Lugli, L. Larcher, High Efficiency Thermoacoustic Loudspeaker Made with a Silica Aerogel Substrate. *Adv. Mater. Technol.* **2018**, *3*, 1800139.
242. M. Bobinger, P. La Torraca, J. Mock, M. Becherer, L. Cattani, D. Angeli, L. Larcher, P. Lugli, Solution-Processing of Copper Nanowires for Transparent Heaters and Thermo-Acoustic Loudspeakers. *IEEE Trans. Nanotechnol.* **2018**, *17*, 940-947.
243. H. Tian, D. Xie, Y. Yang, T.-L. Ren, T.-T. Feng, Y.-F. Wang, C.-J. Zhou, P.-G. Peng, L.-G. Wang, L.-T. Liu, Poly(3,4-ethylenedioxythiophene):Poly(styrenesulfonate)-Based Organic, Ultrathin, and Transparent Sound-Emitting Device. *Appl. Phys. Lett.* **2011**, *99*, 233503.
244. G.-Y. Gou, M. L. Jin, B.-J. Lee, H. Tian, F. Wu, Y.-T. Li, Z.-Y. Ju, J.-M. Jian, X.-S. Geng, J. Ren, Y. Wei, G.-Y. Jiang, Y. Qiao, X. Li, S. J. Kim, M. Gao, H.-T. Jung, C. W. Ahn, Y. Yang, T.-L. Ren, Flexible Two-Dimensional Ti_3C_2 MXene Films as Thermoacoustic Devices. *ACS Nano* **2019**, *13*, 12613-12620.
245. S. Kang, S. Cho, R. Shanker, H. Lee, J. Park, D.-S. Um, Y. Lee, H. Ko, Transparent and Conductive Nanomembranes with Orthogonal Silver Nanowire Arrays for Skin-Attachable Loudspeakers and Microphones. *Sci. Adv.* **2018**, *4*, eaas8772.
246. Y. Wei, X. Lin, K. Jiang, P. Liu, Q. Li, S. Fan, Thermoacoustic Chips with Carbon Nanotube Thin Yarn Arrays. *Nano Lett.* **2013**, *13*, 4795-4801.
247. E. Roh, B.-U. Hwang, D. Kim, B.-Y. Kim, N.-E. Lee, Stretchable, Transparent, Ultrasensitive, and Patchable Strain Sensor for Human-Machine Interfaces Comprising a Nanohybrid of Carbon Nanotubes and Conductive Elastomers. *ACS Nano* **2015**, *9*, 6252-6261.
248. X. Yu, R. Rajamani, K. A. Stelson, T. Cui, Carbon Nanotube-Based Transparent Thin Film Acoustic Actuators and Sensors. *Sensors Actuat. A-Phys.* **2006**, *132*, 626-631.
249. Y. Yang, M. W. Urban, Self-Healing Polymeric Materials. *Chem. Soc. Rev.* **2013**, *42*, 7446-7467.
250. Z. Wei, J. H. Yang, J. Zhou, F. Xu, M. Zrinyi, P. H. Dussault, Y. Osada, Y. M. Chen, Self-Healing Gels Based on Constitutional Dynamic Chemistry and Their Potential Applications. *Chem. Soc. Rev.* **2014**, *43*, 8114-8131.
251. J. Kang, D. Son, G.-J. N. Wang, Y. Liu, J. Lopez, Y. Kim, J. Y. Oh, T. Katsumata, J. Mun, Y. Lee, L. Jin, J. B.-H. Tok, Z. Bao, Tough and Water-Insensitive Self-Healing Elastomer for Robust Electronic Skin. *Adv. Mater.* **2018**, *30*, 1706846.
252. J. Sun, X. Pu, M. M. Liu, A. Yu, C. Du, J. Zhai, W. Hu, Z. L. Wang, Self-Healable, Stretchable, Transparent Triboelectric Nanogenerators as Soft Power Sources. *ACS Nano* **2018**, *12*, 6147-6155.

253. Q. Zhang, S. Niu, L. Wang, J. Lopez, S. Chen, Y. Cai, R. Du, Y. Liu, J.-C. Lai, L. Liu, C.-H. Li, X. Yan, C. Liu, J. B.-H. Tok, X. Jia, Z. Bao, An Elastic Autonomous Self-Healing Capacitive Sensor Based on a Dynamic Dual Crosslinked Chemical System. *Adv. Mater.* **2018**, *30*, 1801435.
254. J. H. Pikul, S. Li, H. Bai, R. T. Hanlon, I. Cohen, R. F. Shepherd, Stretchable Surfaces with Programmable 3D Texture Morphing for Synthetic Camouflaging Skins. *Science* **2017**, *358*, 210-214.
255. X. Dai, Y. Zhang, L. Gao, T. Bai, W. Wang, Y. Cui, W. Liu, A Mechanically Strong, Highly Stable, Thermoplastic, and Self-Healable Supramolecular Polymer Hydrogel. *Adv. Mater.* **2015**, *27*, 3566-3571.
256. G. Gao, G. Du, Y. Sun, J. Fu, Self-Healable, Tough, and Ultrastretchable Nanocomposite Hydrogels Based on Reversible Polyacrylamide/Montmorillonite Adsorption. *ACS Appl. Mater. Interfaces* **2015**, *7*, 5029-5037.
257. J. A. Yoon, J. Kamada, K. Koynov, J. Mohin, R. Nicolay, Y. Zhang, A. C. Balazs, T. Kowalewski, K. Matyjaszewski, Self-Healing Polymer Films Based on Thiol-Disulfide Exchange Reactions and Self-Healing Kinetics Measured Using Atomic Force Microscopy. *Macromolecules* **2012**, *45*, 142-149.
258. H. Ying, Y. Zhang, J. Cheng, Dynamic Urea Bond for the Design of Reversible and Self-Healing Polymers. *Nat. Commun.* **2014**, *5*, 3218.
259. J. I. Park, A. Choe, M. P. Kim, H. Ko, T. H. Lee, S. M. Noh, J. C. Kim, I. W. Cheong, Water-Adaptive and Repeatable Self-Healing Polymers Bearing Bulky Urea Bonds. *Polym. Chem.* **2018**, *9*, 11-19.
260. Z. Q. Lei, H. P. Xiang, Y. J. Yuan, M. Z. Rong, M. Q. Zhang, Room-Temperature Self-Healable and Remoldable Cross-linked Polymer Based on the Dynamic Exchange of Disulfide Bonds. *Chem. Mater.* **2014**, *26*, 2038-2046.
261. H. Meng, P. Xiao, J. Gu, X. Wen, J. Xu, C. Zhao, J. Zhang, T. Chen, Self-Healable Macro-/Microscopic Shape Memory Hydrogels Based on Supramolecular Interactions. *Chem. Commun.* **2014**, *50*, 12277-12280.
262. G. Y. Kim, S. Sung, M. P. Kim, S. C. Kim, S.-H. Lee, Y. I. Park, S. M. Noh, I. W. Cheong, J. C. Kim, Reversible Polymer Networks Based on the Dynamic Hindered Urea Bond for Scratch Healing in Automotive Clearcoats. *Appl. Surf. Sci.* **2020**, *505*, 144546.
263. H. Ying, J. Cheng, Hydrolyzable Polyureas Bearing Hindered Urea Bonds. *J. Am. Chem. Soc.* **2014**, *136*, 16974-16977.

264. H. S. Jang, G.-G. Kim, S. H. Kang, Y. Kim, J. I. Yoo, S. Yoo, K.-K. Kim, C. Jung, H. C. Ko, A Bezel-Less Tetrahedral Image Sensor Formed by Solvent-Assisted Plasticization and Transformation of an Acrylonitrile Butadiene Styrene Framework. *Adv. Mater.* **2018**, *30*, 1801256.
265. D. Ge, E. Lee, L. L. Yang, Y. Cho, M. Li, D. S. Gianola, S. Yang, A Robust Smart Window: Reversibly Switching from High Transparency to Angle-Independent Structural Color Display. *Adv. Mater.* **2015**, *27*, 2489-2495.
266. J. H. Koo, D. C. Kim, H. J. Shim, T.-H. Kim, D.-H. Kim, Flexible and Stretchable Smart Display: Materials, Fabrication, Device Design, and System Integration. *Adv. Funct. Mater.* **2018**, *28*, 1801834.
267. H.-H. Chou, A. Nguyen, A. Chortos, J. W. F. To, C. Lu, J. Mei, T. Kurosawa, W.-G. Bae, J. B.-H. Tok, Z. Bao, A Chameleon-Inspired Stretchable Electronic Skin with Interactive Colour Changing Controlled by Tactile Sensing. *Nat. Commun.* **2015**, *6*, 8011.
268. C.-C. Kim, H.-H. Lee, K. H. Oh, J.-Y. Sun, Highly Stretchable, Transparent Ionic Touch Panel. *Science* **2016**, *353*, 682-687.
269. E. H. Kim, S. H. Cho, J. H. Lee, B. Jeong, R. H. Kim, S. Yu, T.-W. Lee, W. Shim, C. Park, Organic Light Emitting Board for Dynamic Interactive Display. *Nat. Commun.* **2017**, *8*, 14964.
270. C. Yu, Y. Zhang, D. Cheng, X. Li, Y. Huang, J. A. Rogers, All-Elastomeric, Strain-Responsive Thermochromic Color Indicators. *Small* **2014**, *10*, 1266-1271.
271. S. M. Jeong, S. Song, S.-K. Lee, N. Y. Ha, Color Manipulation of Mechanoluminescence from Stress-Activated Composite Films. *Adv. Mater.* **2013**, *25*, 6194-6200.
272. C. Wang, D. Hwang, Z. Yu, K. Takei, J. Park, T. Chen, B. Ma, A. Javey, User-Interactive Electronic Skin for Instantaneous Pressure Visualization. *Nat. Mater.* **2013**, *12*, 899-904.
273. X. Y. Wei, X. Wang, S. Y. Kuang, L. Su, H. Y. Li, Y. Wang, C. Pan, Z. L. Wang, G. Zhu, Dynamic Triboelectrification-Induced Electroluminescence and its Use in Visualized Sensing. *Adv. Mater.* **2016**, *28*, 6656-6664.
274. A. I. Goller, L. J. Otten, J. Ward, Seeing Sounds and Hearing Colors: An Event-Related Potential Study of Auditory-Visual Synesthesia. *J. Cognitive Neurosci.* **2009**, *21*, 1869-1881.
275. G. Beeli, M. Esslen, L. Jancke, Time Course of Neural Activity Correlated with Colored-Hearing Synesthesia. *Cereb. Cortex* **2008**, *18*, 379-385.
276. T. Minami, T. Miyata, K. Kitamura, S. Takata, I. Fukuda, Flat Panel Light-Emitting Sounder Using Thin-Film El-Devices with a Ceramic Insulating Layer. *Jpn. J. Appl. Phys.* **1990**, *29*, L315-L318.

277. Y. Zhang, G. Gao, H. L. W. Chan, J. Dai, Y. Wang, J. Hao, Piezo-Phototronic Effect-Induced Dual-Mode Light and Ultrasound Emissions from ZnS:Mn/PMN-PT Thin-Film Structures. *Adv. Mater.* **2012**, *24*, 1729-1735.
278. S. Lee, T. Kang, W. Lee, M. M. Afandi, J. Ryu, J. Kim, Multifunctional Device Based on Phosphor-Piezoelectric PZT: Lighting, Speaking, and Mechanical Energy Harvesting. *Sci. Rep.* **2018**, *8*, 301.
279. J. Wang, C. Yan, G. Cai, M. Cui, A. L.-S. Eh, P. S. Lee, Extremely Stretchable Electroluminescent Devices with Ionic Conductors. *Adv. Mater.* **2016**, *28*, 4490-4496.
280. Z. Yu, X. Niu, Z. Liu, Q. Pei, Intrinsically Stretchable Polymer Light-Emitting Devices Using Carbon Nanotube-Polymer Composite Electrodes. *Adv. Mater.* **2011**, *23*, 3989-3994.
281. J. Wang, P. S. Lee, Progress and Prospects in Stretchable Electroluminescent Devices. *Nanophotonics* **2017**, *6*, 435-451.
282. K. S. Kim, Y. Zhao, H. Jang, S. Y. Lee, J. M. Kim, K. S. Kim, J.-H. Ahn, P. Kim, J.-Y. Choi, B. H. Hong, Large-Scale Pattern Growth of Graphene Films for Stretchable Transparent Electrodes. *Nature* **2009**, *457*, 706-710.
283. Y. Wang, C. Zhu, R. Pfattner, H. Yan, L. Jin, S. Chen, F. Molina-Lopez, F. Lissel, J. Liu, N. I. Rabiah, Z. Chen, J. W. Chung, C. Linder, M. F. Toney, B. Murmann, Z. Bao, A Highly Stretchable, Transparent, and Conductive Polymer. *Sci. Adv.* **2017**, *3*, e1602076.
284. D. J. Lipomi, M. Vosgueritchian, B. C.-K. Tee, S. L. Hellstrom, J. A. Lee, C. H. Fox, Z. Bao, Skin-Like Pressure and Strain Sensors Based on Transparent Elastic Films of Carbon Nanotubes. *Nat. Nanotechnol.* **2011**, *6*, 788-792.
285. F. Xu, Y. Zhu, Highly Conductive and Stretchable Silver Nanowire Conductors. *Adv. Mater.* **2012**, *24*, 5117-5122.
286. P. Lee, J. Lee, H. Lee, J. Yeo, S. Hong, K. H. Nam, D. Lee, S. S. Lee, S. H. Ko, Highly Stretchable and Highly Conductive Metal Electrode by Very Long Metal Nanowire Percolation Network. *Adv. Mater.* **2012**, *24*, 3326-3332.
287. M. Amjadi, A. Pichitpajongkit, S. Lee, S. Ryu, I. Park, Highly Stretchable and Sensitive Strain Sensor Based on Silver Nanowire-Elastomer Nanocomposite. *ACS Nano* **2014**, *8*, 5154-5163.
288. S. Choi, J. Park, W. Hyun, J. Kim, J. Kim, Y. B. Lee, C. Song, H. J. Hwang, J. H. Kim, T. Hyeon, D.-H. Kim, Stretchable Heater Using Ligand-Exchanged Silver Nanowire Nanocomposite for Wearable Articular Thermotherapy. *ACS Nano* **2015**, *9*, 6626-6633.
289. J. Tang, H. Guo, M. Zhao, J. Yang, D. Tsoukalas, B. Zhang, J. Liu, C. Xue, W. Zhang, Highly Stretchable Electrodes on Wrinkled Polydimethylsiloxane Substrates. *Sci. Rep.* **2015**, *5*, 16527.

290. J. A. Rogers, T. Someya, Y. G. Huang, Materials and Mechanics for Stretchable Electronics. *Science* **2010**, *327*, 1603-1607.
291. R. Shanker, S. Cho, A. Choe, M. P. Kim, Z. Khan, S. Kang, H. Ko, Solution-Processable, High-Performance Flexible Electroluminescent Devices Based on High-k Nanodielectrics. *Adv. Funct. Mater.* **2019**, *29*, 1904377.
292. M. Molberg, Y. Leterrier, C. J. G. Plummer, C. Walder, C. Lowe, D. M. Opris, F. A. Nuesch, S. Bauer, J. A. E. Manson, Frequency Dependent Dielectric and Mechanical Behavior of Elastomers for Actuator Applications. *J. Appl. Phys.* **2009**, *106*, 054112.
293. D. M. Opris, M. Molberg, C. Walder, Y. S. Ko, B. Fischer, F. A. Nuesch, New Silicone Composites for Dielectric Elastomer Actuator Applications In Competition with Acrylic Foil. *Adv. Funct. Mater.* **2011**, *21*, 3531-3539.
294. M. Molberg, D. Crespy, P. Rupper, F. Nuesch, J.-A. E. Manson, C. Lowe, D. M. Opris, High Breakdown Field Dielectric Elastomer Actuators Using Encapsulated Polyaniline as High Dielectric Constant Filler. *Adv. Funct. Mater.* **2010**, *20*, 3280-3291.
295. M. Panahi-Sarmad, M. Razzaghi-Kashani, Actuation Behavior of PDMS Dielectric Elastomer Composites Containing Optimized Graphene Oxide. *Smart Mater. Struct.* **2018**, *27*, 085021.
296. R. Pelrine, R. Kornbluh, Q. Pei, J. Joseph, High-Speed Electrically Actuated Elastomers with Strain Greater Than 100%. *Science* **2000**, *287*, 836-839.
297. R. Heydt, R. Kornbluh, J. Eckerle, R. Pelrine In *Sound radiation properties of dielectric elastomer electroactive polymer loudspeakers*, Smart structures and materials 2006: Electroactive polymer actuators and devices (eapad), International Society for Optics and Photonics: **2006**; p 61681M.
298. B. Goelzer, C. H. Hansen, G. Sehrndt, *Occupational exposure to noise: evaluation, prevention and control*. World Health Organisation: **2001**.
299. J. Liang, K. Tong, Q. Pei, A Water-Based Silver-Nanowire Screen-Print Ink for the Fabrication of Stretchable Conductors and Wearable Thin-Film Transistors. *Adv. Mater.* **2016**, *28*, 5986-5996.
300. X. He, R. He, Q. Lan, W. Wu, F. Duan, J. Xiao, M. Zhang, Q. Zeng, J. Wu, J. Liu, Screen-Printed Fabrication of PEDOT: PSS/Silver Nanowire Composite Films for Transparent Heaters. *Materials* **2017**, *10*, 220.
301. D. Angmo, T. R. Andersen, J. J. Bentzen, M. Helgesen, R. R. Sondergaard, M. Jorgensen, J. E. Carle, E. Bundgaard, F. C. Krebs, Roll-to-Roll Printed Silver Nanowire Semitransparent Electrodes for Fully Ambient Solution-Processed Tandem Polymer Solar Cells. *Adv. Funct. Mater.* **2015**, *25*, 4539-4547.

302. M. M. Menamparambath, C. M. Ajmal, K. H. Kim, D. Yang, J. Roh, H. C. Park, C. Kwak, J.-Y. Choi, S. Baik, Silver Nanowires Decorated with Silver Nanoparticles for Low-Haze Flexible Transparent Conductive Films. *Sci. Rep.* **2015**, *5*, 16371.
303. D. C. Choo, S. K. Bae, T. W. Kim, Flexible, Transparent Patterned Electrodes Based on Graphene Oxide/Silver Nanowire Nanocomposites Fabricated Utilizing an Accelerated Ultraviolet/Ozone Process to Control Silver Nanowire Degradation. *Sci. Rep.* **2019**, *9*, 5527.
304. J. Kim, J. Park, U. Jeong, J.-W. Park, Silver Nanowire Network Embedded in Polydimethylsiloxane as Stretchable, Transparent, and Conductive Substrates. *J. Appl. Polym. Sci.* **2016**, *133*, 43830.
305. S. Wu, S. Yao, Y. Liu, X. Hu, H. H. Huang, Y. Zhu, Buckle-Delamination-Enabled Stretchable Silver Nanowire Conductors. *ACS Appl. Mater. Interfaces* **2020**, *12*, 41696-41703.
306. B. S. Kim, H. Kwon, H. J. Kwon, J. B. Pyo, J. Oh, S. Y. Hong, J. H. Park, K. Char, J. S. Ha, J. G. Son, S.-S. Lee, Buckling Instability Control of 1D Nanowire Networks for a Large-Area Stretchable and Transparent Electrode. *Adv. Funct. Mater.* **2020**, *30*, 1910214.
307. K. K. Kim, S. Hong, H. M. Cho, J. Lee, Y. D. Suh, J. Ham, S. H. Ko, Highly Sensitive and Stretchable Multidimensional Strain Sensor with Prestrained Anisotropic Metal Nanowire Percolation Networks. *Nano Lett.* **2015**, *15*, 5240-5247.
308. F. Fang, Y.-Q. Li, G.-W. Huang, H.-M. Xiao, Q.-P. Feng, N. Hu, S.-Y. Fu, Electrical Anisotropy and Multidimensional Pressure Sensor of Aligned Fe₃O₄@Silver Nanowire/Polyaniline Composite Films under an Extremely Low Magnetic Field. *RSC Adv.* **2017**, *7*, 4260-4268.
309. X. Ho, J. N. Tey, W. Liu, C. K. Cheng, J. Wei, Biaxially Stretchable Silver Nanowire Transparent Conductors. *J. Appl. Phys.* **2013**, *113*, 044311.
310. X. Ho, C. K. Cheng, J. N. Tey, J. Wei, Biaxially Stretchable Transparent Conductors That Use Nanowire Networks. *J. Mater. Res.* **2014**, *29*, 2965-2972.
311. C. Wu, J. Jiu, T. Araki, H. Koga, T. Sekitani, H. Wang, K. Suganuma, Biaxially Stretchable Silver Nanowire Conductive Film Embedded in a Taro Leaf-Templated PDMS Surface. *Nanotechnology* **2017**, *28*, 01LT01.
312. B. S. Kim, J. B. Pyo, J. G. Son, G. Zi, S.-S. Lee, J. H. Park, J. Lee, Biaxial Stretchability and Transparency of Ag Nanowire 2D Mass-Spring Networks Prepared by Floating Compression. *ACS Appl. Mater. Interfaces* **2017**, *9*, 10865-10873.
313. C. Ding, Q. Li, Y. Lin, X. Wu, Z. Wang, W. Yuan, W. Su, W. Chen, Z. Cui, Omnidirectionally Stretchable Electrodes Based on Wrinkled Silver Nanowires Through the Shrinkage of Electrospun Polymer Fibers. *J. Mater. Chem. C* **2020**, DOI:10.1039/d0tc03052j.

314. G. Lee, S. G. Lee, Y. Chung, G. Y. Bae, S. Lee, S. Ryu, K. Cho, Omnidirectionally and Highly Stretchable Conductive Electrodes Based on Noncoplanar Zigzag Mesh Silver Nanowire Arrays. *Adv. Electron. Mater.* **2016**, *2*, 1600158.

*Chapter 2 is reproduced in part with permission of “Large-Area Cross-Aligned Silver Nanowire Electrodes for Flexible, Transparent, and Force-Sensitive Mechanochromic Touch Screens, *ACS Nano* **2017**, *11*, 4346-4357”. Copyright 2017 American Chemical Society.

*Chapter 3 is reproduced in part with permission of “Ultrathin, Transparent, and Conductive Nanomembranes with Orthogonal Silver Nanowire Arrays for Skin-Attachable Loudspeakers and Microphones, *Sci. Adv.* **2018** 4:eaas8772”. Copyright 2018 American Association for the Advancement of Science.

*Chapter 4 is reproduced in part with permission of “Solution-Processable, High-Performance Flexible Electroluminescent Devices Based on High-*k* Nanodielectrics, *Adv. Funct. Mater.* **2019**, *29*, 1904377”. Copyright 2019 Wiley-VCH GmbH.

*Chapter 5 is reproduced in part with permission of “Highly Transparent, Flexible, and Self-Healable Thermoacoustic Loudspeakers, *ACS Appl. Mater. Interfaces* **2020**, *12*, 53184-53192”. Copyright 2020 American Chemical Society.

*Chapter 6 is reproduced in part with permission of “Highly Stretchable Sound-in-Display Electronics Based on Strain-Insensitive Metallic Nanonetworks, *Adv. Sci.* **2020**, 2001647”. Copyright 2020 Wiley-VCH GmbH.

Appendix A: List of Achievements

The results of this dissertation have been published in: (†: equal contribution)

1. **Seungse Cho**[†], Saewon Kang[†], Ashish Pandya, Ravi Shanker, Ziyauddin Khan, Youngsu Lee, Jonghwa Park, Stephen L. Craig, and Hyunhyub Ko, Large-Area Cross-Aligned Silver Nanowire Electrodes for Flexible, Transparent, and Force-Sensitive Mechanochromic Touch Screens, *ACS Nano* **2017**, *11*, 4346-4357.
2. Saewon Kang[†], **Seungse Cho**[†] (co-first author), Ravi Shanker, Hochan Lee, Jonghwa Park, Doo-Seung Um, Yougoh Lee, and Hyunhyub Ko, Ultrathin, Transparent, and Conductive Nanomembranes with Orthogonal Silver Nanowire Arrays for Skin-Attachable Loudspeakers and Microphones, *Sci. Adv.* **2018**, *4*:eaas8772.
3. Ravi Shanker[†], **Seungse Cho**[†] (co-first author), Ayoung Choe, Minsoo P. Kim, Ziyauddin Khan, and Hyunhyub Ko, Solution-Processable, High-Performance Flexible Electroluminescent Devices Based on High-*k* Nanodielectrics, *Adv. Funct. Mater.* **2019**, *29*, 1904377.
4. Dong-hee Kang[†], **Seungse Cho**[†] (co-first author), Sujin Sung[†], Young-Ryul Kim, Hyejin Lee, Ayoung Choe, Jeonghee Yeom, Minsoo P. Kim, Jin Chul Kim, Seung Man Noh, and Hyunhyub Ko, Highly Transparent, Flexible, and Self-Healable Thermoacoustic Loudspeakers, *ACS Appl. Mater. Interfaces* **2020**, *12*, 53184-53192.
5. **Seungse Cho**, Dong-hee Kang, Hyejin Lee, Minsoo P. Kim, Saewon Kang, Ravi Shanker, and Hyunhyub Ko, Highly Stretchable Sound-in-Display Electronics Based on Strain-Insensitive Metallic Nanonetworks, *Adv. Sci.* **2020**, 2001647.

The other related results have been published in:

1. Saewon Kang[†], Taehyo Kim[†], **Seungse Cho**, Youngoh Lee, Ayoung Choe, Bright Walker, Seo-Jin Ko, Jin Young Kim, and Hyunhyub Ko, Capillary Printing of Highly Aligned Silver Nanowire Transparent Electrodes for High-Performance Optoelectronic Devices, *Nano Lett.* **2015**, *15*, 7933-7942.
2. Jonghwa Park, Youngoh Lee, Minjeong Ha, **Seungse Cho**, and Hyunhyub Ko, Micro/Nanostructured Surfaces for Self-Powered and Multifunctional Electronic Skins *J. Mater.*

- Chem. B* **2016**, *4*, 2999-3018.
3. Jonghwa Park[†], Jinyoung Kim[†], Jaehyung Hong[†], Hochan Lee, Youngoh Lee, **Seungse Cho**, Sung-Woo Kim, Jae Joon Kim, Sung Youb Kim, and Hyunhyub Ko, Tailoring Force Sensitivity and Selectivity by Microstructure Engineering of Multidirectional Electronic Skins, *NPG Asia Mater.* **2018**, *10*, 163-176.
 4. Youngoh Lee[†], Jonghwa Park[†], Soowon Cho, Young-Eun Shin, Hochan Lee, Jinyoung Kim, Jinyoung Myoung, **Seungse Cho**, Saewon Kang, Chunggi Baig, and Hyunhyub Ko, Flexible Ferroelectric Sensors with Ultrahigh Pressure Sensitivity and Linear Response over Exceptionally Broad Pressure Range, *ACS Nano*, **2018**, *12*, 4045-4054.
 5. Taehyo Kim[†], Saewon Kang[†], Jungwoo Heo, **Seungse Cho**, Jae Won Kim, Ayoung Choe, Bright Walker, Ravi Shanker, Hyunhyub Ko, and Jin Young Kim, Nanoparticle-Enhanced Silver-Nanowire Plasmonic Electrodes for High-Performance Organic Optoelectronic Devices, *Adv. Mater.* **2018**, *30*, 1800659.
 6. Saewon Kang[†], Jaeki Jeong[†], **Seungse Cho**, Yung Jin Yoon, Seungyoung Park, Seongdong Lim, Jin Young Kim, and Hyunhyub Ko, Ultrathin, Lightweight, and Flexible Perovskite Solar Cells with an Excellent Power-Per-Weight Performance, *J. Mater. Chem. A*, **2019**, *7*, 1107-1114.
 7. Jonghwa Park[†], Youngoh Lee[†], Meredith H. Barbee, Soowon Cho, **Seungse Cho**, Ravi Shanker, Jinyoung Kim, Jinyoung Myoung, Minsoo P. Kim, Chunggi Baig, Stephen L. Craig, and Hyunhyub Ko, A Hierarchical Nanoparticle-in-Micropore Architecture for Enhanced Mechanosensitivity and Stretchability in Mechanochromic Electronic Skins, *Adv. Mater.* **2019**, 1808148.
 8. Youngoh Lee[†], Jonghwa Park[†], Ayoung Choe, **Seungse Cho**, Jinyoung Kim, and Hyunhyub Ko, Mimicking Human and Biological Skins for Multifunctional Skin Electronics, *Adv. Funct. Mater.* **2019**, *30*, 1904523.
 9. Kwangmuk Lee, Hee Young Chae, Kyeonghwan Park, Youngoh Lee, **Seungse Cho**, Hyunhyub Ko, and Jae Joon Kim, A Multi-Functional Physiological Hybrid-Sensing E-Skin Integrated Interface for Wearable IoT Applications, *IEEE Trans. Biomed. Circuits Syst.* **2019**, *13*, 1535-1544.
 10. Yang-Seok Park, Junyoung Kim, Jung Min Oh, Seungyoung Park, **Seungse Cho**, Hyunhyub Ko, and Yoon-Kyoung Cho, Near-Field Electrospinning for Three-Dimensional Stacked Nanoarchitectures with High Aspect Ratios, *Nano Lett.* **2020**, *20*, 441-448.
 11. Sunyoung Yoon, Hyeong-Min Sim, **Seungse Cho**, Hyunhyub Ko, Yeehyun Park, Yunseok Kim, and Han-Ki Kim, Highly Stretchable, Conductive Polymer Electrodes with a Mixed AgPdCu and PTFE Network Interlayer for Stretchable Electronics, *Adv. Mater. Interfaces*, **2020**, 2001500.

Conference Presentation:

1. **Seungse Cho**, Saewon Kang, and Hyunhyub Ko, Large-Scale Bar-Coating Alignment of Silver Nanowires for High Performance Transparent Electrodes, *IMID 2016*, Jeju, South Korea.
2. **Seungse Cho**, Saewon Kang, and Hyunhyub Ko, Large Scale Alignment of Metallic Nanowires by Bar Coating Assembly for High Performance Transparent Electrodes, *The Materials Research Society of Korea 2016*, Yeosu, South Korea.
3. **Seungse Cho**, Saewon Kang, and Hyunhyub Ko, Large-Area Cross-Aligned Silver Nanowire Electrodes for Flexible, Transparent, and Force-Sensitive Mechanochromic Touch Screens, *ICAE 2017*, Jeju, South Korea.
4. **Seungse Cho**, Saewon Kang, and Hyunhyub Ko, Cross-Aligned Silver Nanowire Transparent Electrodes for Flexible and Force-Sensitive Mechanochromic Touch Screens, *The Polymer Society of Korea 2018*, Deajeon, South Korea.
5. Saewon Kang, **Seungse Cho**, and Hyunhyub Ko, Highly Transparent, Robust, and Well-Ordered AgNW Composite Nano-Membrane for the Fabrication of Conformal Electronics, *Nano Korea 2018*, Goyang, South Korea.
6. **Seungse Cho**, Saewon Kang, Ashish Pandya, Ravi Shanker, Ziyauddin Khan, Youngsu Lee, Stephene L. Craig, and Hyunhyub Ko, Cross-Aligned Silver Nanowire Electrodes by Bar-Coating Assembly for Flexible and Transparent Mechanochromic Touch Screens, *IMID 2018*, Busan, South Korea.
7. **Seungse Cho**, Dong-hee Kang, Hyejin Lee, Saewon Kang, Ravi Shanker, and Hyunhyub Ko, Stretchable Electroluminescent Device with Strain-Insensitive Silver Nanowire Electrodes, *Fall MRS Meeting 2019*, Boston, USA.

Honors and Awards:

1. The Outstanding Graduate Student Award presented by the Energy and Chemical Engineering Department of UNIST. December 2017.
2. The Outstanding Graduate Student Award presented by the Energy and Chemical Engineering Department of UNIST. December 2019.
3. 박사과정생 연구장려금지원, National Research Foundation of Korea, 2019-2020.

Acknowledgements

I would like to begin by expressing my genuine gratitude to Prof. Hyunhyub Ko who is my principal investigator during my combined master's and doctoral course. I'm very grateful for his sincere support, encouragements, helpful comments, and words of wisdom, which have helped me not only in successfully completing Ph.D course but in becoming a better person. I couldn't finish my Ph.D course without his guidance and constant feedbacks. It was a great honor to be able to become a professor's student and I would like to say that "Prof. Ko has always been not only a good *Scientist* but a great *Mentor* and I really respect you. Thank you".

I would also like to thank the committee members, Prof. Jin Young Kim, Prof. Myoung Hoon Song, Prof. Jiseok Lee, and Prof. Moon Kee Choi, *Ulsan National Institute of Science and Technology (UNIST)*, for their kind and constructive comments to improve my doctoral thesis and collaboration works. I would like to express my deep gratitude to the committee members for becoming my committee members.

I would like to thank the all of FNL members; my previous colleagues Dr. Jiwon Lee, Dr. Doo-Seung Um, Dr. Saewon Kang, Dr. Ziyauddin Khan, Dr. Ravi Shanker, Dr. Seongdong Lim, Dr. Minjeong Ha, Dr. Seungyoung Park, Dr. Hochan Lee, Sehee Ahn, Jinyoung Myoung, Yoojeong Park and current members Dr. Minsoo P. Kim, Dr. Jonghwa Park, Dr. Sujoy Kumar Ghosh, Dr. Yun Goo Ro, Dr. Yongoh Lee, Dr. Young-Eun Shin, Dr. Ayoung Choe, Youngsu Lee, Young-Ryul Kim, Jeonghee Yeom, Jinyoung Kim, Young-Jin Park, Sangyun Na, Dong-hee Kang, Yeju Kwon, Hyejin Lee, Seungjae Lee, Yujung Ko, Geonyoung Jeong, and Haryeong Cho.

Especially, I would like to say great thanks to Saewon Kang who is my *immediate supervisor and great mentor* for his kind and elaborate supports. I have learned a lot of things from him and couldn't complete my achievements without his sincere supports. Thank you.

Moreover, I feel great thanks to my lab colleagues, Jonghwa Park who is my *first lab-life mentor* and Yongoh Lee who is my *second lab-life mentor*. I have learned lots of things from them not only scientific knowledges but also the course of my life. Besides, I would like to say thank to my team members, Dong-hee Kang, *pizza boy*, and Hyejin Lee, *my scary subordinate*, for their support during my Ph.D course. In addition, I also specially thank to Jiwon, *the first lab leader*, Doo-Seung, *diligent older brother*, Ziyauddin Khan, *kind postdoc*, Ravi, *intelligent dude*, Hochan, *strict older brother*, Ayoung, *the first traveling companion*, Youngsu, *my target*, Jeonghee, *the second traveling companion*, Jinyoung, *earth corps senior*. So, thank you everyone.

I would also like to special thank to my room mates and friends in UNIST, 재형, 지홍, 태양, 세원,

규진, and 지정 who have played soccer together in the last 10 years. I was able to finish my works thanks to my friends. In addition, I really appreciate my hometown friends, 병욱, 인철, 재훈, 전경, 주현, 동연, 석찬, 병호, 정현, 재욱, 혜원, 수희. Their friendship means a lot to me. Thank you. Lastly, I would like to appreciate my parents and family for their love, immense support, and encouragement. Their permanent love has encouraged me to go ahead in my study and career. I would never be able to pay back their love and affection during my life. Thank you again. Especially, I would like to say great appreciate to my grandmother who passed away in October 2018. I wish I had shown my graduation to her; however, I couldn't. It's so sad and I do miss you so much. Rest in peace, grandma. The present thesis, resulting of six-year researches, would not have been possible without guidance, encouragements, and supports of many other people. I thank all of them and I present them all my gratitude.

Seungse Cho